Title
Microfluidic Modules for Enabling Point-of-Care Biopsy-based Cancer Diagnostics

Author
Mitra, Debkishore

Publication Date
2013

Peer reviewed|Thesis/dissertation

Microfluidic Modules for Enabling Point-of-Care Biopsy-based Cancer Diagnostics

by

Debkishore Mitra

A dissertation submitted in partial satisfaction of the

requirements for the degree of

Joint Doctor of Philosophy
with University of California, San Francisco

in

Bioengineering

in the

Graduate Division

of the

University of California, Berkeley

Committee in charge:

Professor Luke P. Lee, Chair
Professor Shuvo Roy
Professor Lee W. Riley

Spring 2013

Abstract

Microfluidic Modules for Enabling Point-of-Care Biopsy-based Cancer Diagnostics

by

Debkishore Mitra

Joint Doctor of Philosophy in Bioengineering with University of California, San Francisco

University of California, Berkeley

Professor Luke P. Lee, Chair

The analyses of patient tumor biopsy samples and biopsy-based diagnostics have emerged as important tools for cancer diagnostics. However, the techniques employed currently are restricted to centralized laboratories as they are time-consuming, manual labor intensive and vary considerably in their effectiveness amongst institutions and countries. Point of Care testing (POCT) for cancer with the capacity for multiplexed detection of numerous biomarkers in biopsy samples in a rapid, precise and portable manner is emerging as an area with enormous potential to disseminate universal diagnostics to cancer patients. Additionally, POCT can be used as a screening tool, to discern malignant from benign tumors at the physician's office, and lead to reduction in the need for expensive and time-consuming laboratory tests, hence minimizing the cost and anxiety, for patients with benign tumors. A POCT platform for multiple biomarker analysis can not only improve the operational characteristics of assays but can also help ascertain drug efficacy, ushering in personalized medicine for the patients. The reduced volumes and diffusion distances, which enable multiplexed, portable and quick assays, in microfluidic devices makes such devices a promising platform to realize POCT systems. But current microfluidic devices for cancer diagnostics suffer from the lack of a generalized on-chip sample preparation module and a simplified fluid actuation technique.

The overall goal of the reported dissertation research is to develop microfluidic modules that will enable the development of integrated microfluidic diagnostic platforms for the multiplexed detection of cancer biomarkers in tumor biopsy samples. The main focus of the thesis is on the development of novel microfluidic sample preparation modules. The purpose of the sample preparation component is to pre-concentrate cancerous cells, remove background proteins in the sample and to subsequently lyse the cells to release the proteins of interest. The pre-concentration of the adherent cells, including the cancerous cells, in the sample is reported by trapping them using a novel hydrodynamic cell trap. The sample washing methods, to remove extracellular proteins that could interfere with downstream assays, is also optimized. An electrochemical lysis technique is then integrated to the cell pre-concentration module, to effectively lyse the cells without having to add external reagents. Microfluidic modules for the separation of bacterial and mammalian cells from mixed samples are also reported. The immortalized

cancer cell lines used in this research include the human breast cancer cell lines BT-474, known to over express the Her-2 protein, and T47D along with cervical cancer cell line HeLa.

The development of a novel fluid actuation technique, termed Proximal Degas-driven Flow (PDF), is also reported in this thesis. PDF takes advantage of the high porosity and air solubility of PDMS to reduce the pressure inside the fluidic channels leading to fluid flow in the channel. This actuation technique enables bubble-free fluid flow, can be used to fill up dead-end chambers in contrast to traditional pressure (positive or negative) driven flows and does not require the priming of the channels. Unlike degas-driven flow, PDF alleviates the need for pre-degassed and sealed devices, enabling consistent and longer-lasting fluid flow. This portable technique also requires very simple and cheap hardware like a vacuum bulb or membrane pump (thumb pump).

In conclusion, several microfluidic modules to enable Point of Care biopsy-based cancer diagnostics are introduced. The research presented in this dissertation is an effort to transform point-of-care cancer testing and provide universal diagnostics and personalized medicine to cancer patients.

In loving memory of my father and grandmother

DEDICATION

I dedicate this dissertation to my wonderful family and friends. I owe a particular debt of gratitude to my mother and brother for all their support and motivation. I also express my profound appreciation to my partner for her encouragement and patience.

ACKNOWLEDGMENTS

There are a number of people without whom this thesis might not have been written, and to whom I am greatly indebted. I am thankful to my adviser, Prof. Luke P. Lee, for his elemental role in my doctoral research. I am also grateful to my committee members, Prof. Shuvo Roy and Prof. Lee Riley who reviewed the various versions and provided valuable feedback on the same. I would also like to thank the Bioengineering faculty and staff at the Joint Graduate Group in Bioengineering at University of California, Berkeley and San Francisco, especially my graduate advisors Prof. Dorian Liepmann and Prof. Tejal Desai. I am also indebted to Prof. Steven Conolly, Prof. Amy Herr, Paul Lum and Rebecca Pauling, for their considerable support and guidance provided to me over the years.

I am very thankful to the BioPOETS lab for providing an environment conducive to learning and research. In particular I am grateful to John Waldeisen, Brendan Turner, Frank Myers and Charlie Yeh for all the support and help over the years. Several talented undergraduate researchers have assisted me with my projects and I am thankful to them as well. I am especially grateful to Daniel Cohen for the numerous discussions about science, dinosaurs and noodles. I want to also acknowledge and appreciate the various funding sources that have given me the opportunity to conduct the research reported in this dissertation. And finally, I will always be indebted to my mother, brother, partner and numerous teachers and friends who have been instrumental in my achievements, always offering guidance and support.

TABLE OF CONTENTS

CHAPTER 6: PORTABLE AND POWER-EFFICIENT MICROFLUIDIC ACTUATION USING PROXIMAL DEGAS-DRIVEN FLOW

CHAPTER 7: FUTURE DIRECTIONS

APPENDIX

CHAPTER 1

Microfluidic Systems For Point-of-care Biopsy-based Cancer Diagnostics

1.1 ABSTRACT

Tumor biopsy analysis and biopsy-based diagnostics have emerged as one of the most important areas in cancer diagnostic technology today. Point of care testing for cancer is also emerging as an area with enormous potential and demand. As such the application of microfluidic techniques for the development of point of care cancer analysis and diagnostic lab-on-a-chips have been aggressively looked into in recent times. This move is supported by arguments of portability, small sample requirement, faster turnaround time, higher throughput and multiplexing and low production costs. Researchers have been successful in scaling down certain cancer biopsy assay techniques from large laboratories onto small microfluidic chips. However, majority of the work done has mostly involved pre-processed or prepared cancer biopsy samples and have used bulky and non-portable instrumentation. Not a lot of focus has been given to on-chip sample preparation and portable actuation techniques. In this chapter, we explore the importance of Point of care testing in cancer diagnostics and document recent developments and unmet challenges in this field, with the aim of bringing 'all the pieces of the puzzle' together for an integrated micro-cancer analysis system.

1.2 WHAT IS POINT OF CARE TESTING?

In recent times, Point of Care Testing (POCT) has emerged as a sub category of In Vitro Diagnostics (IVD) with an enormous potential to improve healthcare access and delivery in almost every part of the world. The worldwide POCT market is growing at more than 10% annually and is expected to reach US$ 25 Billion by 2016 (Marketresearch.com). This has resulted in a lot of research funding from agencies, like the Bill and Melinda Gates Foundation and DARPA, and an explosion in the number of scientific articles published on POCT. But how do we determine whether a certain diagnostic test can be classified as a Point of Care test or not? There is no easy answer owing to the variety of definitions and opinions that exist on such systems. However, taken together, these opinions can represent the range of possible applications and benefits of POCT systems.

The common theme uniting the various opinions on POCTs is the ability to analyze clinical specimen as close as possible to the patient and to influence medical decisions at the earliest. However the physical realities as to how this is achieved depend on a variety of factors, including operational, geographic and economic, resulting in a variety of definitions. The College of American Pathologists define POCT as being "designed to be used at or near the site

where the patient is located, that do not require permanent dedicated space, and that are performed outside the physical facilities of the clinical laboratories". Willmott and Arrowsmith define POCT as "an analytical test performed at or near the site of a patient, in a setting that is distinct from a normal hospital clinical laboratory" with the aim "to reduce the time required to produce diagnostic test results and, thus, improve clinical care" (1). Kost however defines POCT as "testing at or near the site of patient care wherever that medical care is needed… to facilitate immediate medical decisions that improve patient outcomes… especially during life-threatening crises and emergency resuscitations"(2). Yet another definition is provided by Hirsch et al who define POCT as "laboratory diagnostic testing performed at or near the site where clinical care is delivered" (3).

The fundamental advantage that POCT provides is the ability to influence medical decisions at the earliest, in situations where this was not possible before due to a lack of technology or a lack of resources. Starting from modest beginnings as crude and semi-quantitative 'dipstick' tests, newer POCT systems are emerging rapidly with performance requirements as high as standard clinical IVD tests. Modern POCTs have been used to evaluate patient's physiology and analyze almost any clinical sample (1).

But is technology the only driving factor in POCT? Nichols argues that the vulnerability of POCT results and the resulting treatment implementation on environmental and operational factors necessitates proper management of POCT and "Managing POCT requires dedicated resources, policies, and multidisciplinary commitment and cooperation to ensure the highest quality diagnostic services" (4). Pai et al also claim that the mere availability of technology does not "ensure their adoption and scale up" and that a POCT framework needs to exist to manage the distribution, operation and data management of these systems (5). They even contend that "technology as such does not define a POCT" and that "the focus must be on POCT programs, rather than POC technologies". Although the author agrees with the fact that a proper framework and management of POCT, especially for quality control and data management, is indispensable, we think that technology is still the main driver for POCT. We agree with Soper et al when they say that "POC systems make state-of-art technology platforms accessible to a large population pool" (6). A lot of implementation barriers for POCT can be resolved by improving the test technology rather than changing the framework. Hence, this thesis is focused on technological advancements to POCT technology to increase applicability and versatility of such devices.

So what is an ideal POCT test? The World Health Organization in 2003 coined the acronym ASSURED (Table 1.1) to summarize the ideal characteristics of a diagnostic test that can be used at all levels of the healthcare system (7). As a starting point, therefore, we consider these to be the ideal characteristics of a POCT system. However, Pai et al contend that this ASSURED criteria necessitate contrived restrictions on POCT systems (5). Requiring POCTs to be cheap, for example, can exclude technologies that can be useful under the right circumstances. Rather they suggest looking at POCT systems as a spectrum of technologies, with a diversity of characteristics, which can cater to a large diversity of circumstances (what they refer to as a Target Product Profile or TPP). They propose 5 TPP's, ranging from "at home testing" to tests performed in the central lab (5). Through this range of TPP's a wide variety of POCT systems can be implemented, catering to specific criteria. For example, a POCT to be used in a TPP3 (clinic/health post) scenario can be complicated enough to be used by trained clinic staff, not be as cheap as a dipstick assay and can employ hand-held instrumentation for actuation and readout.

Table 1.1: The ideal rapid test: ASSURED criteria

A = Affordable
S = Sensitive
S = Specific
U = User-friendly (simple to perform in a few steps with minimal training)
R = Robust and rapid (can be stored at room temperature and results available in <30 min)
E = Equipment-free or minimal equipment that can be solar-powered
D = Deliverable to those who need them

1.3 POCT FOR CANCER DIAGNOSTICS

Cancer can be broadly defined as "a group of diseases… (involving the) abnormal growth of cells… evolving into a population of cells that can invade tissues and metastasize to distant sites" (8). Fittingly crowned as "The Emperor of All Maladies" (9), cancer (or rather the more than 100 different malignant diseases grouped as cancer) leads to significant morbidity and mortality all over the world. The global figures (available for the year 2008 from the GLOBOCAN project) show that more than 12 million new cases and 7.6 million deaths due to cancer were recorded globally (10). In the United States alone, more than 1.5 million cancer cases were diagnosed in 2012 and more than 500,000 people are expected to die of cancer (second most common cause of death in the US) (11). Given the global burden (Figure 1.1) and complexity of cancer, a lot of therapeutic developments have taken place ranging from surgery to irradiation to chemotherapy. However, the early and accurate diagnosis of cancer (before the cancer metastasizes) is still crucial in improving the efficacy of the current treatment schemes (8). It is also important to identify and evaluate individual patient variations and responsiveness to therapy before any treatment is started (8). Not surprisingly, there has been a lot of emphasis on early cancer screening and diagnostics via imaging or molecular means; including mammography for breast cancer (12), PAP smear (followed by cytological and DNA testing) for cervical cancer (13), colonoscopy for colon cancer (14) and PSA testing for prostate cancer (15). Such diagnostic techniques have been shown to significantly reduce the mortality due to cancer.

Although traditional cancer screening programs exist all over the world, their efficacy varies between resource-rich developed countries and resource-poor developing countries. Goldie et al looked at cervical-cancer screening (involving PAP smears followed by cytological evaluation) in developing countries and found this strategy, although useful for developed world, to be impractical in the developing world (16). They concluded that multiple clinic visits were the main roadblock for the cervical cancer screening programs in resource poor settings and that alternatives such as HPV DNA tests, which still need at least two clinic visits, were more cost-effective. Okonkwo et al and Anderson et al came to similar conclusion for breast cancer screening in developing countries, where they found the reduction in the number of visits (for example by co-screening for breast and cervical cancer) and the inclusion of pathological and molecular tests (such as cytology) to be important for the cost-effectiveness of the screening programs (12, 17). Hence it is conceivable that POCT systems for rapid cancer detection and diagnosis, where a patient has to make ideally only one clinic visit, will be extremely useful in such situations. The hybrid II HPV DNA test for example if implemented in a POC setting would be very useful in resource-limited settings, where it can be multiplexed and self-contained/automated (to minimize contamination). Molecular POCT systems will also be

practical in resource rich settings, where the focus will be on integration (make the test completely self-contained) and multiplexing (look at multiple biomarkers at once). The need will also be to analyze tissue samples (along with body fluids) and to design the POCT system such that it integrates well into the conventional setup (6). The quick diagnosis provided by a POCT system will be valuable in minimizing psychological stress in patients who receive a suspicious or inconclusive screening result as in the case of mammography for breast cancer (12, 18).

Needless to say, this need for POCT systems in improving healthcare access in developed countries has been identified and is being prioritized. For example, the National Institute of Biomedical Imaging and Bioengineering (NIBIB) under the NIH has also started the Point-of-Care Technologies Research Network to work towards "closing the technology/clinical gap" for POCT technologies, with one of the centers focusing entirely on cancer diagnostics (19). Also POCT products for cancer diagnostics are becoming available like the Alere NMP22® Bladder Check® which is a FDA approved lateral flow assay for diagnosing bladder cancer (20, 21).

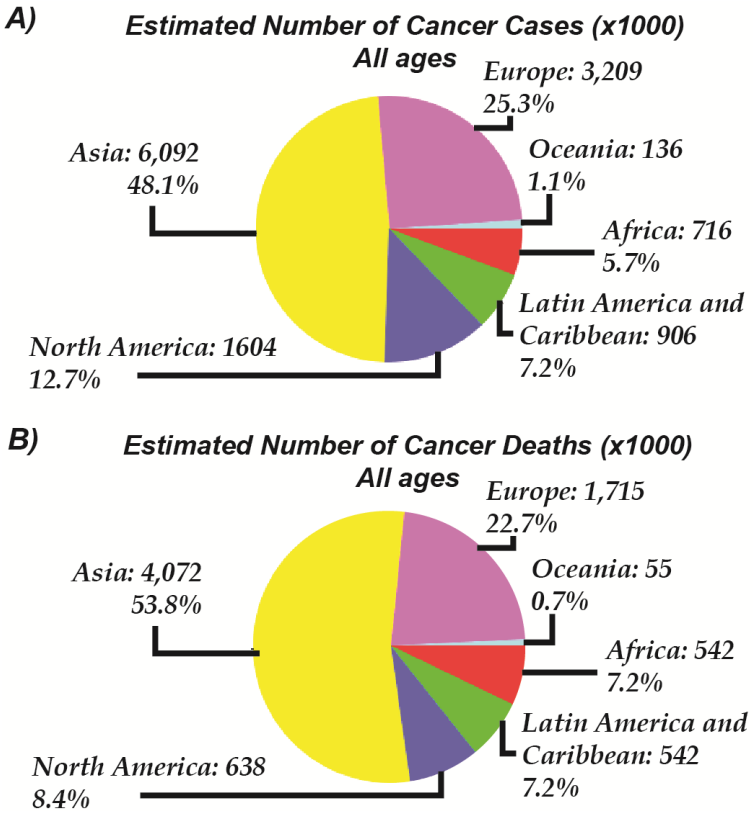

Figure 1.1: **A)** Global statistics on the number of cancer cases diagnosed and **B)** number of cancer deaths in 2008. The global distribution depicts the significant burden of the disease in both developed and developing world. The data represents morbidity and mortality due to all cancers except non-melanoma skin cancer and includes data from all age groups and genders of the population. Data courtesy of GLOBOCAN 2008 project (http://globocan.iarc.fr/)

Another avenue in cancer management where POCT systems will be handy is in therapy monitoring. The evaluation of the effectiveness of a given anti-cancer therapy is challenging

because in the adjuvant and prevention settings, there is no measurable disease. Therefore, there is no way of knowing if a drug or intervention is successful. The longer a patient remains free of disease, the greater the likelihood of cure or prevention. However, this is not an absolute; for certain cancers, for example, breast cancer, disease can recur decades later (22–24). A number of measures are utilized as proxies, among them 5 and 10 year mortality rates, 5 and 10 years disease free survival, median time to progression, cumulative events/1000. For a patient to wait years only to have discovered a systemic and incurable recurrence is unacceptable, especially given that there are other therapeutic alternatives available. POCT systems for proxy biomarkers or in-vitro testing of patient samples can be useful in such circumstances (25). Also, (b) for patients with measurable disease, estimates of efficacy are relatively crude. These measures include physical exam measurements and imaging measurements done using x-ray, ultrasound computerized tomography, magnetic resonance and/or positron emission tomography. Routinely, medications must be administered for weeks or months until an objective measure of response can be observed. A molecular POCT assay done on a regular basis, along with the therapy, can be more useful in giving a quantitative and fast measure of drug effectiveness.

Before we discuss more about POCT technologies for cancer diagnosis, it will be instructive to look at current technologies available or being developed for cancer diagnostics. We have not included imaging techniques in this discussion as imaging-based POCT systems will not have wide applicability especially in resource poor settings.

1.4 SERUM BASED CANCER DIAGNOSTICS

Serum-based cancer diagnostic techniques rely on protein/peptide (Figure 1.2) and nucleic acid biomarkers that have entered the blood circulation through leaky endothelial barriers and have evaded kidney clearance (26, 27). These biomarkers have been touted as being harbingers of early-stage cancer and as such their detection from patient blood samples is being pursued as a minimally invasive and quick cancer diagnostic.

Serum Immunoassays

The landscape of prostate cancer diagnosis was changed by the introduction of the first prostate specific antigen (PSA) immunoassay (28). Since then, multiple isoforms of the antigens and different assay reagent sets have been developed and are available (29). The FDA approved PSA test has a cutoff of 4 ng/mL for triggering prostate biopsies. At this cutoff the assay has a sensitivity of 51% and specificity of 91% (30). The success of the PSA assay has led researchers and companies to develop serum immunoassays for other cancer types such as serum Her-2 assays for breast cancer (31) and ovarian cancer (32), MUC1 serum immunoassay for pancreatic cancer (33) and metalloproteinases for gastric cancer (34). However, a main bottleneck of developing such assays is the identification and validation of serum biomarkers for cancer diagnostics (35). Searching the serum proteome for such biomarkers have emerged as a possible technique to alleviate this drawback (36).

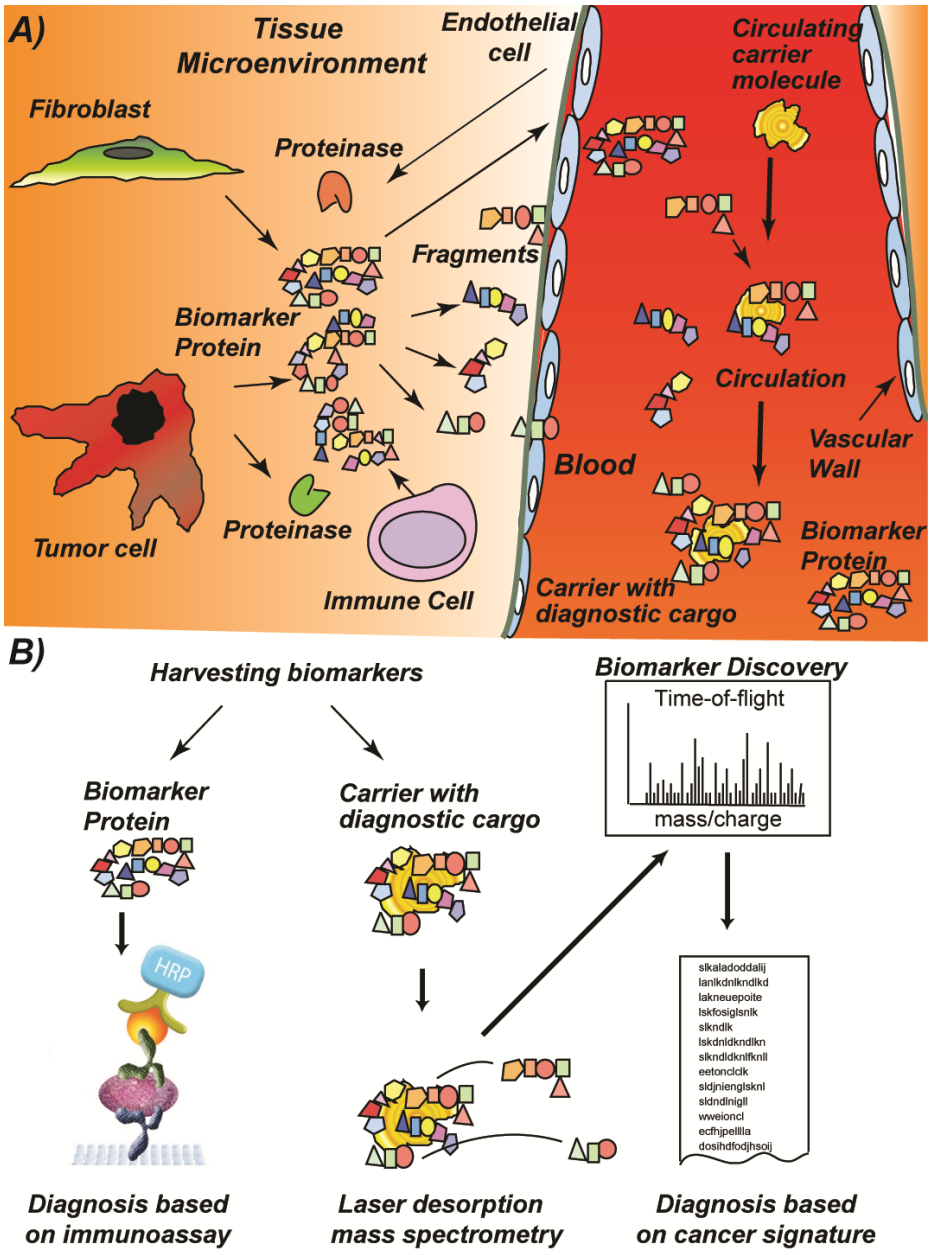

Figure 1.2: **A)** Principle behind serum proteomics and peptidomics for cancer diagnostics. The production of protein and peptide biomarkers within the tissue microenvironment occurs due to all cell types present. The produced protein and its peptide fragments reach the circulation after passing the epithelial vascular wall. Here the peptides bind to carrier proteins (high-abundance proteins) and can be obtained from a serum sample; **B)** These biomarkers from the serum can be found using mass spectrometric profiling and eventually used for diagnosis using either the "Cancer signature" concept or using immunoassays. Reprinted from (26), Copyright (2004), with permission from Elsevier.

Serum Proteomic Profiling

Unlike the direct proteomic or genomic analysis of patient cancerous cells, serum-based biomarkers have to be identified from an overabundant background of other proteins and peptides in serum. Currently, the way to resolve this "needle in a haystack" conundrum is to

evaluate a serum proteomic signature using mass spectrometry techniques, most commonly Surface enhance laser desorption ionization time of flight (SELDI-TOF). SELDI-TOF can be used to evaluate serum proteomic profiles of healthy controls and cancer patients, a "cancer signature" (37), which can be used for finding cancer biomarker. This technique has been used to find biomarkers potentially useful for ovarian, breast (38–40) and lung cancer (41). However these techniques find biomarkers which are very abundant (as compared to proven biomarkers such as PSA) and might not be a good alternative (42). Karsan et al reported that biases from preanalytical and analytical variables, like ex-vivo coagulation and complement cascade activation (43), might be detected through serum proteomic profiling with no clinical indications (44). As a result, they were not able to correlate serum proteome to breast cancer (44). Serum proteome profiles obtained from SELDI analysis have also not been reproducible among the various research groups (45). Hence, serum proteomic and peptidomic profiling for cancer diagnostics, although merits more research, still remains speculative (46) and has not yet become an useful cancer biomarker discovery or diagnostic tool (47). Researchers have also suggested that instead of looking at changes in SELDI-TOF signatures, emphasis should be given to the identification of the biomarkers, which can then we validated independently and detected using conventional immunoassay or microarray platforms (48). Also, more powerful profiling equipment, such as the BioRad's "Lucid Proteomics System" and the use of techniques, other than immunodepletion, for the removal of high abundance serum proteins will help in detecting and profiling higher quality biomarkers in the future (48).

Serum Nucleic Acid Profiling

Human serum contains a variety of nucleic acid molecules, including DNA, RNA and microRNA (miRNA). MiRNA molecules are small non-coding RNA molecules that have an important role in gene expression at a post-transcriptional level (49). As cancer arises essentially from gene dysregulation, changes in the expression profile of miRNA molecules can be correlated to the activation of oncogenes in cancerous cells (50). Recently stable miRNA molecules have been recovered from human serum, although the exact mechanism of their transport from cells into the serum is not clear, and purified either with other RNA molecules (51) or in circulating exosomes (52). The sequences of these miRNA molecules were then evaluated using sequencing technologies (53). The expression profiles of miRNA molecules have been found to be very consistent among healthy individuals (51) and changes in this profile have been observed for many diseases including cancer. Researchers have evaluated these changes for many different types of cancer including ovarian (52), pancreatic (54), breast (55, 56), gastric (57) and lung (58, 59) cancer. For diagnostic purposes, the known miRNA molecules are being assayed using qRT-PCR or oligonucleotide microarrays. Although serum microarray based diagnostics is a very promising candidate for early and non-invasive cancer diagnostics, there are still avenues of concern for this technology. Firstly, is the lack of biological knowledge regarding the source and purpose of these molecules (60). Secondly, the lack of endogenous miRNA controls in these assays makes quantification difficult (61). And finally, clinical studies are still lacking to quantify the diagnostic efficacy of such assays (60). Apart of miRNA in human serum, researchers have also looked at DNA and RNA in human serum and found it to be a promising diagnostic tool (62, 63). However, much like serum miRNA based diagnostic tools, diagnostic assays based on serum DNA and RNA also need to show clinical utility in clinical trials before they can be considered for mainstream use.

1.5 CIRCULATING TUMOR CELL (CTC) BASED CANCER DIAGNOSTICS

Metastases of cancer tumors is the main reason for cancer related mortalities, and the process of metastasis causes tumor cells to enter the patient's peripheral circulation. These circulating tumor cells (CTC's), reported as early as 1869 (64), enter the circulation either during the initial stages of metastasis or through metastatic lesions (Figure 1.3 a). These CTC's are associated with poor patient outcomes (65) and their characterization can provide information useful for diagnosis and treatment (66).

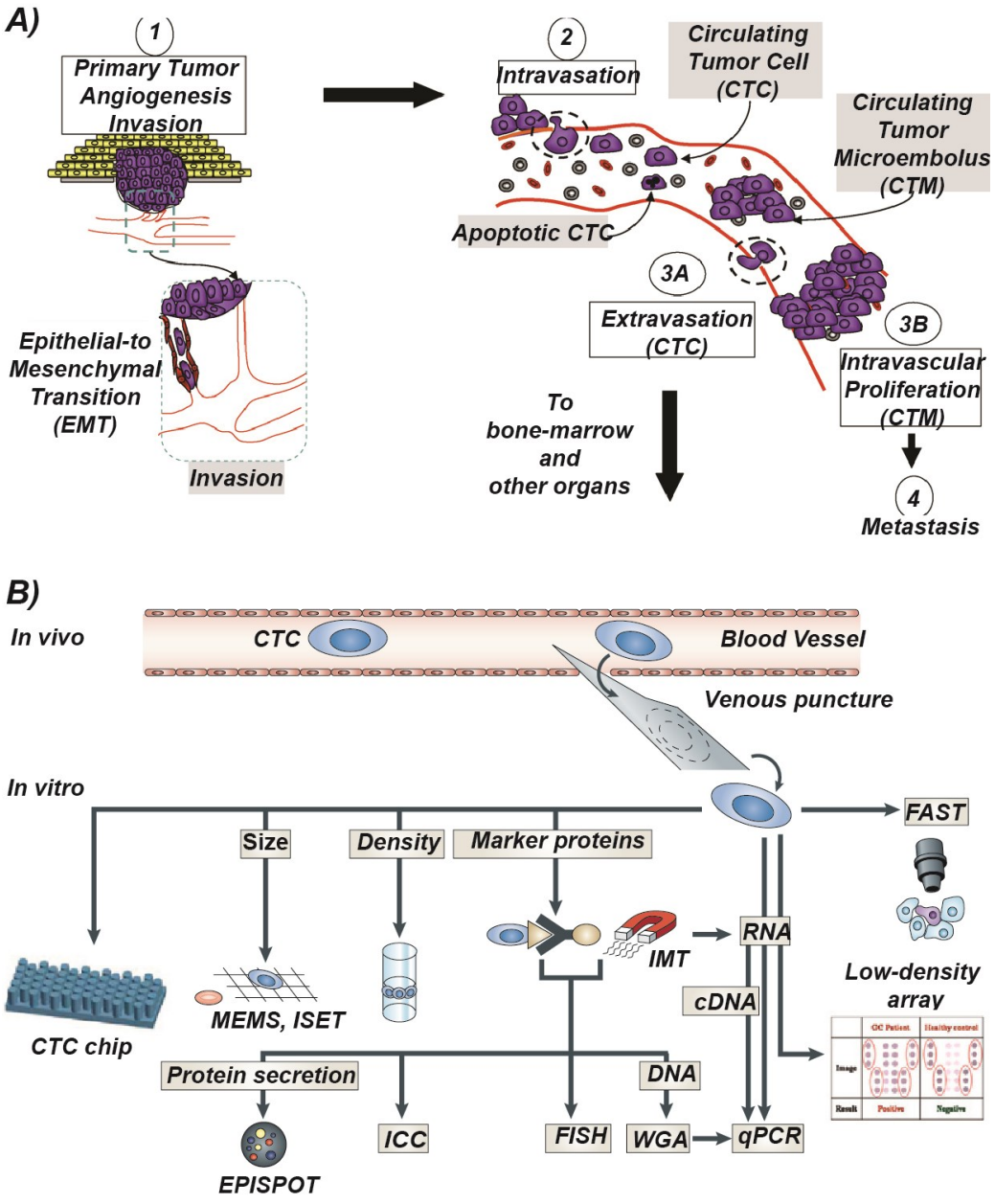

Figure 1.3: **A)** Main steps leading to the entry of circulating tumor cells (CTC) into the peripheral blood circulation. (1) The growing tumor activates angiogenesis due to a lack of oxygen and undergoes the epithelial to mesenchymal transition (EMT) to become more flexible for invasion; (2) The tumor cells enter the blood vessel (intravasation) and

either die or circulate as CTC's; (3A) The CTC's extravasate into distant organs or (3B) proliferate to form circulating tumor microembolus (CTM) both leading to (4) Metastasis. Reprinted from (67), Copyright (2007) with permission from Elsevier; **B)** The various techniques used to enrich, detect and characterize CTC's. The CTC's are enriched using size, density or surface marker proteins (through either immunomagnetic techniques (IMT) or using the CTC chip). The enriched CTC's can be detected and characterize using visual techniques, nucleic acid (RNA, cDNA, DNA) analysis (via qPCR, whole genome amplification (WGA) or FISH), surface protein markers using immunocytochemistry or protein secretion using EPISPOT immunoassays. Reprinted by permission from Macmillan Publishers Ltd: Nature Reviews Cancer (68), copyright (2008)

Healthy controls have been reported to have negligible CTC's (<2 CTC per 7.5 mL of blood) implying a good specificity for a CTC based cancer diagnostic assay (69). However, in cancer patient samples the CTC's are also very rare and occur at a rate of 1 per 10^5 to 10^7 peripheral blood mononuclear cells (or > 2 CTC per 7.5 mL of blood) (70). Hence any diagnostic assay involving CTC's requires a pre-concentration step before the CTC's can be analyzed. A variety of techniques have been developed for the enrichment and/or detection of CTC's in blood samples (Figure 1.3 b). Enrichment of CTC's have been done using physical characteristics such as size (filtration), density (centrifugation) or surface proteins (immunomagnetic separation techniques such as CellSearch (71) or CTC chip (72)) (67). While the size and density enrichment techniques tend to enrich other blood cells (apart from the CTC's); the immunomagnetic enrichment techniques, relying mostly on epithelial surface markers (73), are predisposed to losing CTC's (as CTC's might lose epithelial marker during metastasis due to epithelial-mesenchymal transition (64, 74)). The enriched CTC's can then be detected using either immunological means (such as immunostaining or ELISA) or through nucleic acid amplification means (such as qRT-PCR (66)) (68). The process of detecting and enumerating the CTC's in patient blood samples have been shown to have prognostic efficacy for a variety of cancer types including breast (65, 71, 73), prostate (71) and lung (75) cancer. Since the identification of CTC's much progress has been made in the development of a CTC-based cancer diagnostic assay, including the FDA approval of the CellSearch system. However many challenges still need to be resolved before CTC assays become widely used. Such issues include the improvement of enrichment techniques, identification of biomarkers to distinguish from non-cancerous epithelial cells or hematopoietic stem cells and a thorough evaluation of the clinical utility of such an assay for cancer management and treatment (64, 73). Also, as CTC's enter the bloodstream only after metastasis, this technique is not suitable for early detection of cancer.

1.6 BIOPSY-BASED CANCER DIAGNOSTICS

Tumor biopsy is the process of removal of part of a tissue, suspected to be a tumor and identified by physical examination or imaging, for further analysis to determine its malignancy. Given that a large percentage of such pathologies are benign, being as high as 50% for breast cancer (76), a fast and accurate diagnosis after biopsy is very significant. Also compared to the other diagnostic assays, described previously, biopsy-based diagnostic techniques allow the direct analysis of cancerous cells from the tumor and hence are considered the gold standard for cancer diagnostics. Also confirmatory tissue biopsy for patients with distant metastases is also recommended as it has been seen to alter patient management in 20% of the cases (77). The diversity in cancer types and tumor locations calls for necessary diversity in biopsy procedures as well. The various types of biopsies are listed in Table 1.2.The suitability of a certain biopsy technique depends on the cancer type and tumor location. For example, Fine needle aspiration cytometry (FNAC) is a commonly used minimally invasive diagnostic technique to probe and

sample palpable tumors (Figure 1.4), cysts or lesions (identified by imaging techniques), while deeper tumors or cysts require a surgical biopsy.

Table 1.2: Different biopsy techniques available for cancer diagnostics

S.No.	Name of Biopsy Technique	Description	References
1	Bone Marrow Biopsy	Bone marrow is withdrawn from region of interest with a long needle	(78)
2	Endoscopic Biopsy	Tissue is excised and collected through a flexible endoscopic tube	(79)
3	Skin Biopsy	Skin sample (either epidermal or thicker) are obtained using a blade or punch	(80)
4	Needle Biopsy	Palpable tumors are sample either using a thin (Fine Needle Aspiration) or thicker needles (Core Needle Biopsy)	(81–83)
5	Surgical Biopsy	Surgical procedure to sample or remove tissues in inaccessible regions	(84)

The biopsy samples obtained are then analyzed to enable the prognosis of the cancer patient. The earliest and most common technique for identifying cancerous cells, in the biopsy samples, is histology (for thick tissue samples; or cytology for digested tissue or aspirated samples) which has high sensitivity and specificity (85). The process involves the preparation of fixed tissue/cell slides which are observed under a microscope, by a cytopathologist, to identify malignant cells (86–90). The identification of proteins expressed by cancerous cells led to the development of immuno-histochemistry (Figure 1.4). In this technique, the tissue/cell slides prepared are probed with antibodies, specific against the protein of interest, to improve the contrast and accuracy of the analysis (91). For example the most common proteins studied for breast cancer are Estrogen receptor (ER), Progesterone receptor (PR) and Her-2, with other potential biomarkers like BRCA-1 undergoing clinical validation studies (92). Such biomarkers, apart from establishing malignancy of tumors, also predict drug sensitivities (eg. Herceptin is only effective for Her-2 positive tumors) (93). Flow cytometry has also been used for immunophenotyping aspirate samples (94) or to look at DNA abnormalities like polyploidy (95).

The current histology/cytology techniques, although the gold standard, suffer from the fact that they are labor intensive, need a centralized lab (and hence not suitable for POCT) and can analyze only a limited number of markers. Newer techniques utilizing molecular markers (like gene and protein expression) are important in cases with complex or atypical clinical presentation of histopathology (96–98). Conventional platforms, such as ELISA (99) and RT-PCR (100), or more experimental techniques, such as protein profiling with mass spectrometry (101–104), protein microarray or DNA microarray (96), tissue microarray (105), miRNA profiling (106) or novel amplification technique (107), can be used to profile these molecular markers in patient samples to better diagnose cancer (108). Assays utilizing such molecular markers on tumor samples are also making their way into the market. MammaPrint is a FDA approved 70 gene expression profile assay, utilizing DNA microarrays, which provides metastasis risk assessment (109). OncotypeDX® is a 21 gene expression profile assay, evaluated using RT-PCR, which assesses the risk of breast cancer recurrence (110, 111).

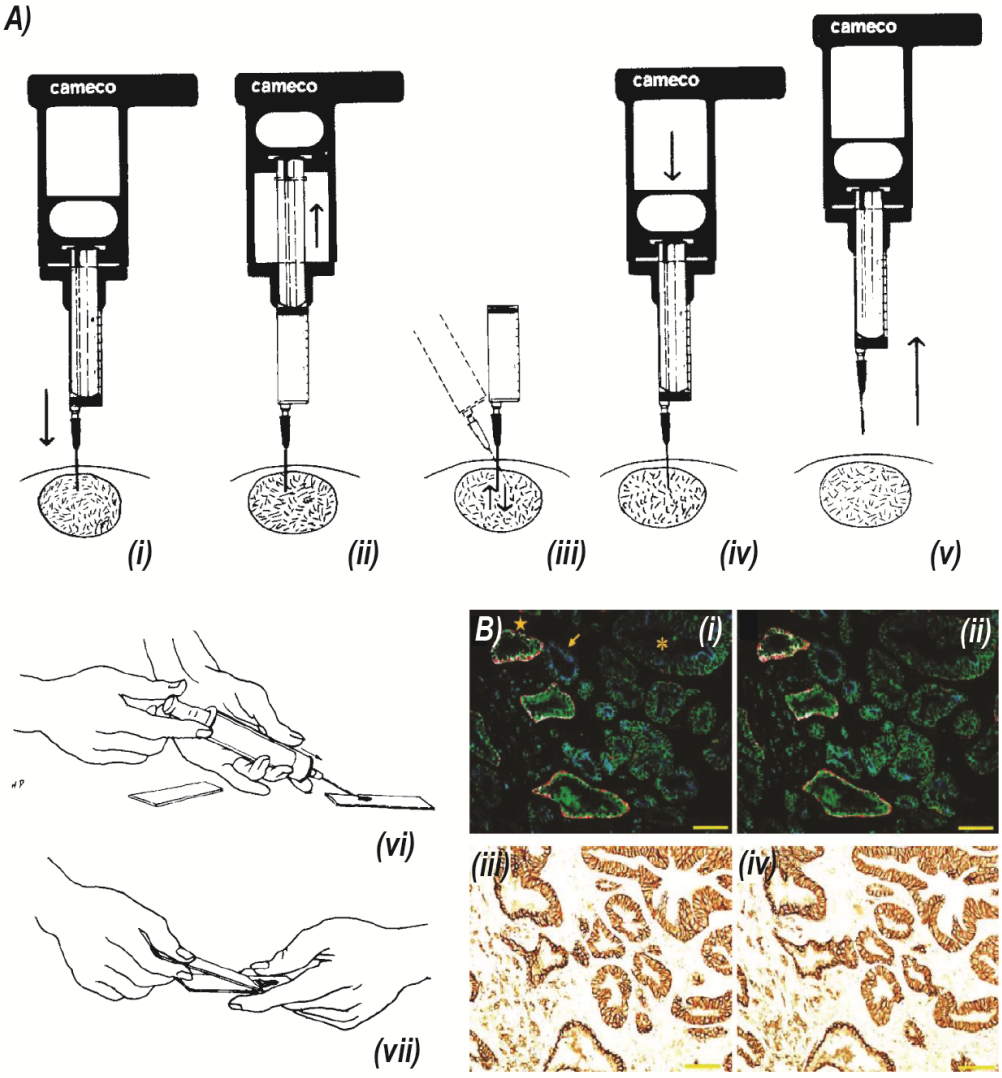

Figure 1.4: **A)** Main steps in the sampling of palpable tumors using fine needle aspiration biopsy and their analysis using immunohistochemistry; the needle is introduced (i) and suction initiated for aspiration (ii). The needle is moved forward and backward under constant suction (iii). The aspiration is stopped (iv) prior to needle withdrawal (v). The aspirated contents are transferred to a slide (vi) and a smear is made (vii) which is immunohistochemically stained prior to pathological observation. Adapted from (87), Copyright (2011); with permission from John Wiley and Sons; and (86), Copyright (2007); with kind permission from Springer Science and Business Media; **B)** Four biomarker multiplexed quantum dot [(i) and (ii)]and one biomarker [(iii) and (iv)] immunohistochemistry stain of prostate cancer tissue section. Adapted with permission from (112), Copyright (2010), American Chemical Society.

1.7 LAB-ON-A-CHIP AS A POCT PLATFORM FOR CANCER DIAGNOSTICS

Microfluidics and lab-on-a-chip (LOC) devices have emerged as a viable technology for point of care analysis systems. Microfluidics promises small size chips capable of performing complicated physical and chemical operations in a time and power efficient way and incurring very low production and operation costs. Micro Total Analysis Systems (μTAS) are systems based on such microfluidic concepts and were introduced for use in chemical and biological analysis systems (113–117). These techniques have a large potential and can also be incorporated

into cancer diagnostic assays resulting in Micro Cancer Analysis Systems (μCAS) (116, 117). The many advantages offered by such devices for cancer diagnostics include the reduction in sample volumes needed, integrated and automated operation (to reduce operator error, sample contamination and exposure of operator to hazardous material), short processing times and fast reporting, and low production and operation costs needed for disposable tests (118). Not surprisingly a lot of work has been done at adapting cancer diagnostic assays onto the microfluidic platform. In this section, focus will be given to microfluidic devices which use tumor biopsy samples, as they are the gold standards for off-chip assays and most likely to be successful in the microscale and also widely adapted. The summary of the technologies described in this section can be found in Table 1.3.

Table 1.3: Microfluidic technologies for biopsy-based cancer diagnostics

S.No.	Name of Technique	Description	References
1	Microfluidic immunocytochemistry platform	Fluorescent antibody based detection of surface protein in micro-sieve enriched cancerous cells	(119)
2	Microfluidic Multiplexed Immunohistochemistry (MMIHC) platform	Independent and parallel microfluidic channels used to probe one sample for multiple proteins	(120–122)
3	Microfluidic Processor for rapid immunohistochemistry of breast carcinoma	Distributed microfluidic channels used to generate uniform antibody concentration in staining region	(123)
4	Micro-immunohistochemistry using a microfluidic probe	Vertical microfluidic probe used to scan and stain tumor samples	(124)
5	Microfluidic Flow cytometer to measure cell deformability	Optical or hydrodynamic shear force used to evaluate cell stiffness to identify and count malignant cells	(125, 126)
6	Electrokinetic Flow cytometer	Integrated device to perform tumor dissociation, fluorescent tagging and electrokinetic transport and cytometry to detect malignant cells	(127)
7	Diagnostic Magnetic Resonance (DMR) device	Flow cytometry device using magnetic nano-particle conjugated antibody tags to detect malignant cells	(128–131)
8	Microfluidic Bead-based Immunoassay (μFBI) platform	Bead-based multiplexed detection of multiple proteins in tumor biopsy lysate to diagnose malignancy	(132)
9	Microfluidic nucleic acid detection assays	Purification, amplification and detection of nucleic acid markers (like DNA, RNA and miRNA) from biopsy lysate to diagnose malignancy	(133–135)
10	Microfluidic genetic mutation and translocation testing	Testing for gene mutation, insertion or deletion in biopsy lysate to predict tumor behavior and drug sensitivity	(136–138)

Microfluidic Immunohistochemistry Platforms

Immunohistochemistry (IHC), as discussed in the previous section, is a method of visually localizing specific antigens, in tissue or cell samples, using labeled antibodies to improve the contrast and information content of conventional histopathological analysis (91). The current IHC process though is time consuming and labor intensive making it unsuitable for POCT. Fully automated IHC stainers have been developed, like the Leica BOND-III and Dako Autostainer Link 48, but they are not portable and still limited by the small sample size available and the lack of multiplexed analysis. The emergence of tissue microarrays (105) further exemplifies the need for IHC techniques to identify multiple biomarkers. Multicolor single-step or sequential staining protocols have been developed for IHC using markers such as quantum dots (112, 139, 140). However these processes suffer from problems such as the low stability of conjugated antibodies, non-specific binding and increase labor and time requirements. Microfluidic immuno histochemistry platforms have been developed to alleviate the concerns of labor, time, portability and multiplexing in conventional IHC protocols. A microfluidic immunocytochemical assay involving cell pre-concentration was reported by Weigum et al. They performed an EGFR assay on oral cancer cell lines captured on top of a micro-sieve embedded in the lab-on-chip device (119). Kim et al developed a microfluidic multiplexed staining platform (Figure 1.5) which can be used for immunohistochemistry (120), immunocytochemical staining (122) or both (121). Their technique utilizes microfluidic channels to divide the surface of the tissue or cell block into independent staining compartments which are exposed to a certain antibody. In this manner they take advantage of the fast diffusion times, in the microfluidic regime, and the small channel footprint for fast and multiplexed staining. This device minimized assay failure rates to less than 1 %, reduced antibody consumption 200 fold, showed only 2% variation from conventional IHC and allowed the simultaneous analysis of 4 or more proteins from the same tissue sample. Ciftlik et al developed a similar microfluidic staining device where they used a distributed microfluidic channel network to ensure that convective diffusion was dominant and ensured more homogenous staining (123). Microfluidic staining techniques involving independent staining chambers also allow for quantitative measurements of protein expression in those chambers. Yeong Won et al developed a microfluidic platform which used a Fc binding aptamer to label primary antibodies, introduced via independent staining channels, and then amplified the number of bound aptamers using an isothermal nucleic acid amplification scheme (141). The above described microfluidic devices still suffer from the possibility of leakage between the channels (especially under high pressures) and tissue delamination from glass slide. Lovchik et al explored an alternate method for immunostaining that rectified these issues. They developed a scanning non-contact vertical microfluidic probe that can confine picoliters of liquid over a region of interest (124). This technique can also be used with tissue microarrays and allow a clinician to perform staining on a specific regions of the tissue sample, interpret the result and reprocess the rest of the sample using adapted conditions.

Microfluidic Flow Cytometry Platforms

Inherent limitations of immunohistochemistry based platforms are the need for visual image analysis and quantitation and the sensitivity to sampling variation (142). Evaluating the biomarker expression of individual tumor cells in an automated fashion can help eliminate these limitations, as is done for example in microfluidic flow cytometry platforms. In such devices, a

single stream of cells, disaggregated from a tumor biopsy sample, are perfused through a microfluidic channel while being counted and analyzed based on either their intrinsic behavior (like mechanical or electrical) or the behavior of labels (like fluorescent or magnetic) attached to them. The simplest platform consists of label free counting and analysis techniques.

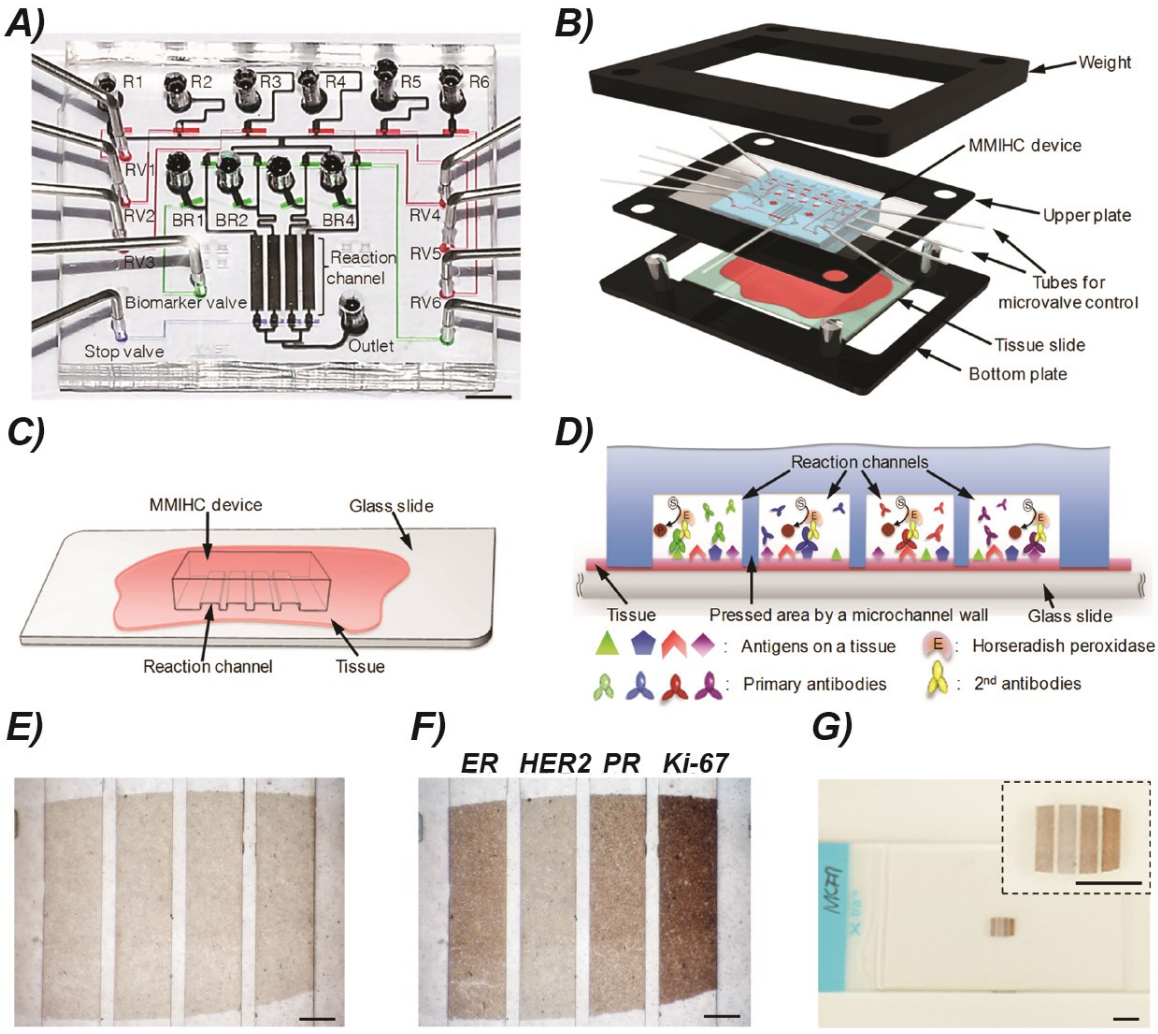

Figure 1.5: **A)** and **B)** Design and configuration of a microfluidic multiplexed immunohistochemistry device. Reagent and biomarker reservoirs with connections to four straight reaction channels were designed. After the device (with the upper plate and weight) was aligned to the tissue sample and a syringe pump was connected to the outlet, the solutions required for IHC were drawn through the reaction channels in the appropriate sequence. Scale bar, 3 mm; **C)** Graphic representation of the interface assembly between the device and a tissue and **D)** Magnified cross-sectional view of the area connecting a tissue and reaction channels of the device and the immuno-histochemical staining process; **E)** Image of an MCF-7 cell block aligned with the MMIHC device. Scale bar, 500 mm. **F)** Image processing DAB reaction. The cell block was stained at discrete sites with ER, HER2, PR, and Ki-67 antibodies. Scale bar, 500 mm. **G)** Completed cell block slide after detachment from the platform. Samples were not damaged by the detachment process. Inset shows a magnified view. Scale bars, 3 mm. Adapted from (120).

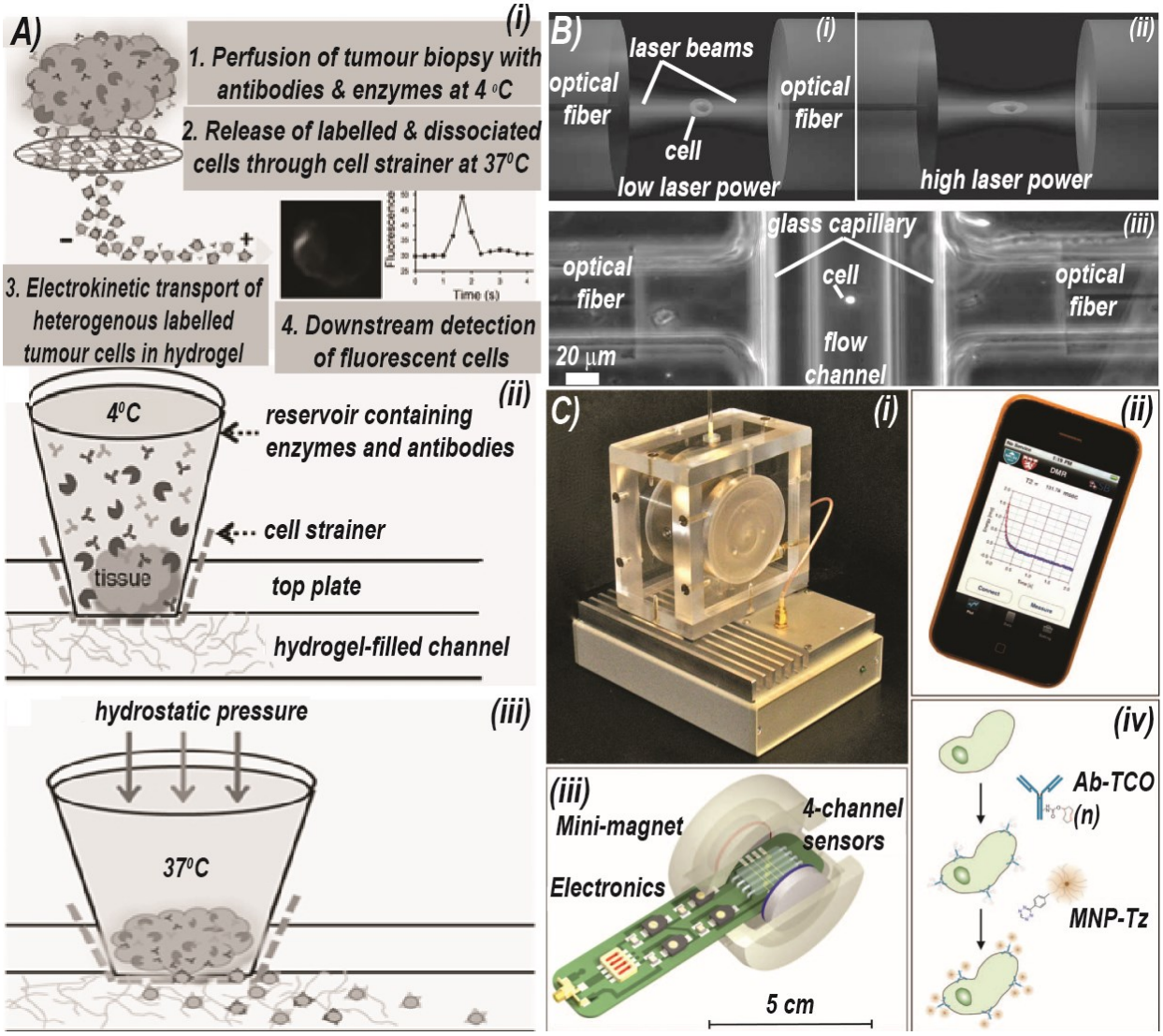

Figure 1.6: **A)** On-chip biopsy dissociation, labeling and transport for fluorescent microflow cytometer; (i) Diagram of the microfluidic processes integrated in the device; 1. Labeling, achieved during in situ interactions with native ECM and neighboring cells, 2.controlled release of labeled tissue cells and 3. Electrokinetic transport in small numbers for detection and imaging; (ii) On-chip digestion of HNSCC tissue placed upon cell strainer in tissue chamber, submerged in enzyme/labeling antibody mixture with the solid hydrogel restricting the fluid to the reservoir; followed by (iii) a combination of melting hydrogel and hydrostatic pressure allowing in situ antibody-labeled, dissociated cells to pass through the cell strainer and hydrogel macropores in the microchannel for detection. Adapted from (127), Copyright (2011), with permission from John Wiley and Sons; **B)** Principle behind "mechanical phenotyping" based microflow cytometry; (i) a cell trapped between two counter propagating divergent laser beams at low laser power shows no measurable deformation; but by increasing the power (ii) the surface stress is sufficient to deform the cell along the laser beam axis; (iii) phase-contrast image of the experimental arrangement where a cell is trapped, against channel flow, inside a glass microcapillary by two laser beams (not visible) coming from opposing single-mode optical fibers. Adapted from (125), Copyright (2009), with permission from AACR; **C)** The Diagnostic Magnetic Resonance (DMR) system and bioconjugation strategy; (i) Complete DMR system for use at the patient's bedside. The base contains all of the NMR measurement electronics, whereas the top enclosure holds a permanent magnet and chip-sized microliter-volume sensors; (ii) a smart phone interface was also developed for operating the system; (iii) An expanded view of the DMR probe used for sensing within the mini magnet and (iv) a bio-orthogonal amplification strategy for ultrasensitive detection of cellular proteins in clinical samples such as fine-needle aspirates. Adapted from (130), Copyright (2011), with permission from AAAS.

Guck et al analyzed cancerous cell types using a microfluidic optical stretcher setup (143), where a deforming force was applied on the cells due to two counter-propagating laser beams and the resultant cellular deformation analyzed to evaluate their deformability (Figure 1.6 b). Their results indicated that cancerous cells had higher deformability than their normal counterparts, suggesting the feasibility of using this "mechanical phenotyping", in the form of deformability, as a label free marker for cancerous cells. A microfluidic hydrodynamic cell deformability measurement device developed by Gossett et al, using hydrodynamic shear forces to deform cells, also reported an enhancement in the deformability of cancerous cells (126). Guck et al followed their work with cells obtained from oral squamous cell carcinoma biopsies and reported a similar increase in deformability for cancerous cells from patient samples (125). Such label free detection techniques however provide no information about the expression levels of certain proteins or genes, which is useful for staging the disease and also for determining therapy. Hence researchers have also developed micro-flow cytometers where labels (mainly antibodies), conjugated with markers, are utilized to count and analyze the cells. Woods et al optimized a technique for using tumor biopsy sample in an electrokinetic flow cytometer using fluorescently-tagged antibodies as labels (127). They report on the integration of the various processes like biopsy dissociation, antibody labeling, cell transportation and fluorescent based cancer cell detection into a single microfluidic platform (Figure 1.6 a). However, optical labels are limited in their multiplexing capabilities. Weissleder et al developed a microfluidic diagnostic magnetic resonance (DMR) device, with a small footprint, which utilizes a planar NMR coil (128) or on-chip solenoidal setup (129) that can be used to detect the surface biomarker expression of cancerous mammalian cells using magnetic nanoparticles conjugated antibodies as labels 9Figure 1.6 c). The magnetic nanoparticles were conjugated to primary antibodies against specific surface proteins of tumor cells. Their aggregation on the cell surface led to changes in their magnetic relaxation properties which were measured and quantified to evaluate the expression level of the biomarker. They improved their design further to enable multiplexed detection of multiple biomarkers from the same sample using multiple detection coils (130). In a study involving 50 patients, a sensitivity of 100% and specificity of 67% was reported with a 4 marker combination using this micro-NMR setup (131).

Microfluidic Platforms for Destructive Testing of Molecular Markers

The microfluidic platforms described until now can be classified as being non-destructive. This term is used to imply that the endpoint of the assay is not destructive for the cells, i.e. they are not lysed. However a lot of the assays looking at molecular markers, such as gene and protein expression, need to performed with biopsy lysate so as to get access to the intracellular contents. With a lot of research being done to find newer molecular markers (both genetic and proteomic) for cancer malignancy and drug sensitivity, a variety of microfluidic platforms are being developed to take advantage of these markers for "personalized" biomolecular diagnostics and therapeutics (144). The evaluation of proteomic biomarkers can be achieved either using immunological or activity-based assays. A microfluidic bead-based immunoassay platform for the multiplexed detection of biomarkers from tissue biopsy lysate was described by Yu et al (132). Beads, conjugated to primary antibodies, were immobilized in a filter region inside a capillary while being exposed to continuously perfused analyte and fluorescently-tagged detection antibody solutions (Figure 1.7 a). Using this platform they also demonstrated the multiplexed detection of seven receptor tyrosine kinases in breast cancer tissue biopsy lysate.

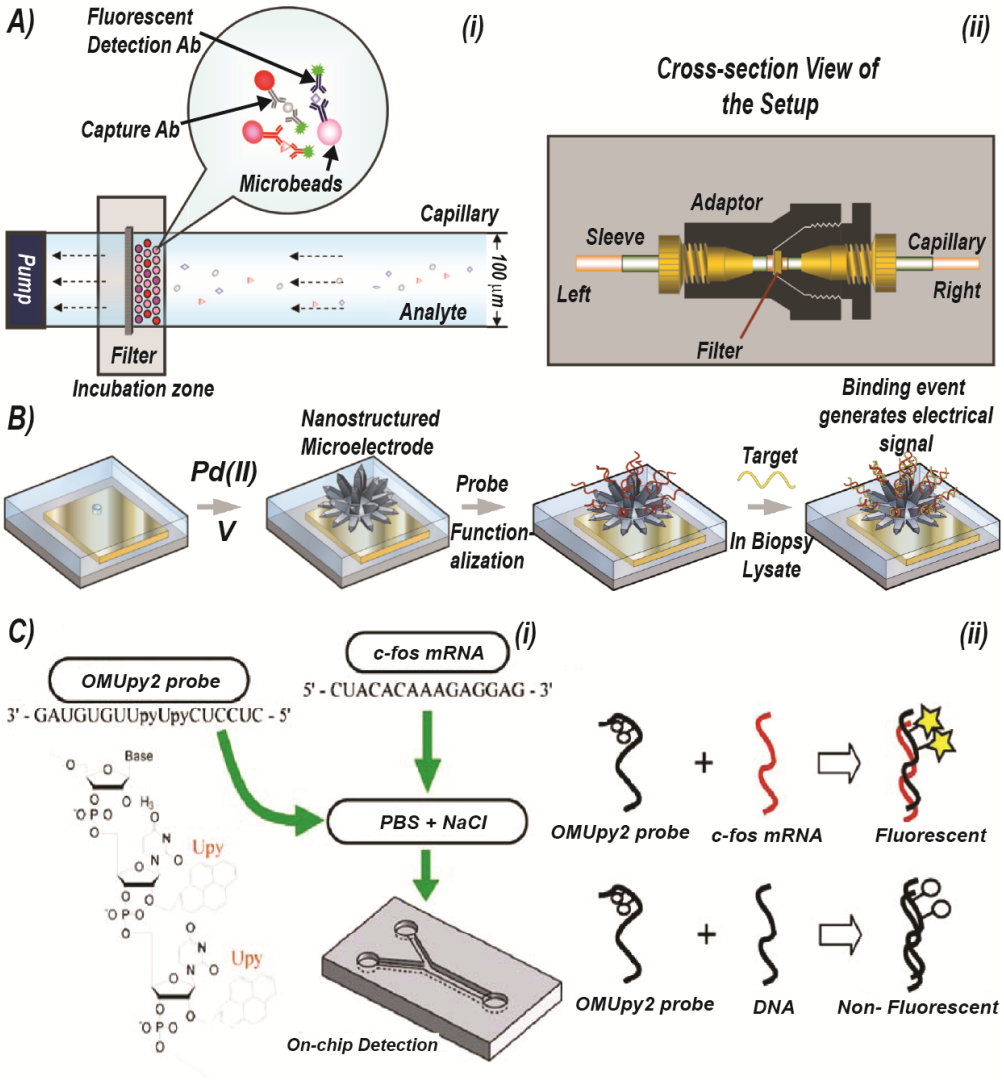

Figure 1.7: **A)** Microfluidic bead-based immunoassay (μFBI); (i) the assay is performed in a capillary using a syringe pump for perfusion. A porous filter is used to keep the capture antibody-coated beads at the incubation site to capture target analytes and to react with detection reagents. After incubation, the beads are collected and the fluorescent signal is measured using a Luminex 100 IS instrument; (ii) The cross section view of the setup showing the incubation zone, which consists of a filter and an adaptor to connect two fused silica-capillaries at both sides. The left capillary is connected to a syringe pump and the right capillary is connected to a sample solution reservoir; **B)** Schematic illustrating steps involved in the sensing of specific sequences in biopsy lysate using nanostructure microelectrodes (NME). NMEs are first plated, in the opening using electrodeposition, and then modified with thiol-derivatized probe sequences. The target sequences from the lysate then hybridize to the sensor and generate a signal using an electrocatalytic reporter system. Adapted with permission from (145), Copyright (2009), American Chemical Society; **C)** mRNA detection using fluorescent oligoribonucleotide probes; (i) Fluorescence is detected when the OMUpy2 probe hybridizes with c-fos mRNA in 10 mM phosphate buffer containing 100 mM NaCl (pH 7.0); (ii) OMUpy2 probe hybridizes with a complementary DNA strand but is not fluorescent hence allowing sensitive mRNA assays without the need to remove DNA. Adapted from (135), Copyright (2007), with kind permission from Springer Science and Business Media.

A non-immunological proteomic assay to evaluate the activity of telomerase enzymes from cancerous cells was achieved within a capillary electrophoresis microdevice by Kim et al (146). There exists a wide variety in the types of nucleic acid biomarkers available for cancer

diagnostics; including DNA, mRNA, miRNA, genetic mutation and gene duplications. Not surprisingly a broad diversity of microfluidic devices has been described to detect these biomarkers. Klapperich et al developed a microfluidic solid phase extraction devices which can be used to purify DNA, mRNA and miRNA from cancerous cell lysate (133) for further analysis. A microfluidic platform for the detection of HPV RNA, instrumental in cervical cancer screening, using isothermal nucleic acid amplification was described by Gulliksen et al (134). Human mRNA, purified from prostate biopsy lysate, were used to detect gene fusion events using a novel nanostructure microelectrode (Figure 1.7 b) functionalized with peptide-nucleic acid probes (145). A on-chip qRT-PCR setup developed by Abruzzo et al allowed the detection of genetic mutations using RNA samples purified from chronic lymphocytic leukemia (137) patient samples. Microsatellite instabilities in colorectal cancer was analyzed in the PCR product of DNA samples, purified from patient biopsies, using a microfluidic capillary electrophoresis device by Odenthal et al (138). A similar setup has also been used for the detection of gene deletion/insertion in Gastrointestinal Stromal Tumors (136). Most of these devices, however, need a nucleic acid purification step before on-chip detection. Yokokawa et al developed a fluorescently tagged oligoribonucleotide probe that can be used to detect mRNA in the liquid phase without the need of purification (135). Using their setup they demonstrated the detection of c-foc mRNA which is an oncogene (Figure 1.7 c).

1.8 UNMET CHALLENGES OF LAB-ON-A-CHIP CANCER DIAGNOSTIC DEVICES

On-chip Sample Preparation

In the previous section we described a selection of microfluidic lab-on-a-chip devices which can be used for Point of care cancer diagnostic testing. Only a small number of these microfluidic devices however include on-chip sample preparation. For example, the microfluidic immunocytochemical assay reported by Weigum et al involved on-chip cell pre-concentration and staining on “micro-sieves” (119). However the immobilized cells could not be released, and had to be observed on the micro-sieve, limiting the throughput of the system. Woods et al reported a more comprehensive sample preparation protocol involving biopsy dissociation, antibody labeling and cell transportation for fluorescent based cancer cell detection (127). A generalized tumor biopsy preparation device using “microfabricated blades” was described by Miller et al and demonstrated to be suitable for flow cytometry analysis (147). However, most of the lab-on-a-chip devices employ off-chip sample preparation processes and work with either purified/concentrated/stained cells or purified protein or nucleic acids. For example, the diagnostic magnetic resonance (DMR) devices discussed previously (130) used cell samples which have been concentrated (and washed using centrifugation and buffer exchange) and stained off-chip. Another example is the microfluidic bead based immunoassay device (132) which requires the off-chip dissociation, concentration and lysis of the biopsy sample. Even the microfluidic devices with nucleic acid purification columns use cell samples which have been purified and lysed off chip (133). Hence a big concern over the clinical adaptation of microfluidic devices is the weak link of sample preparation (146).

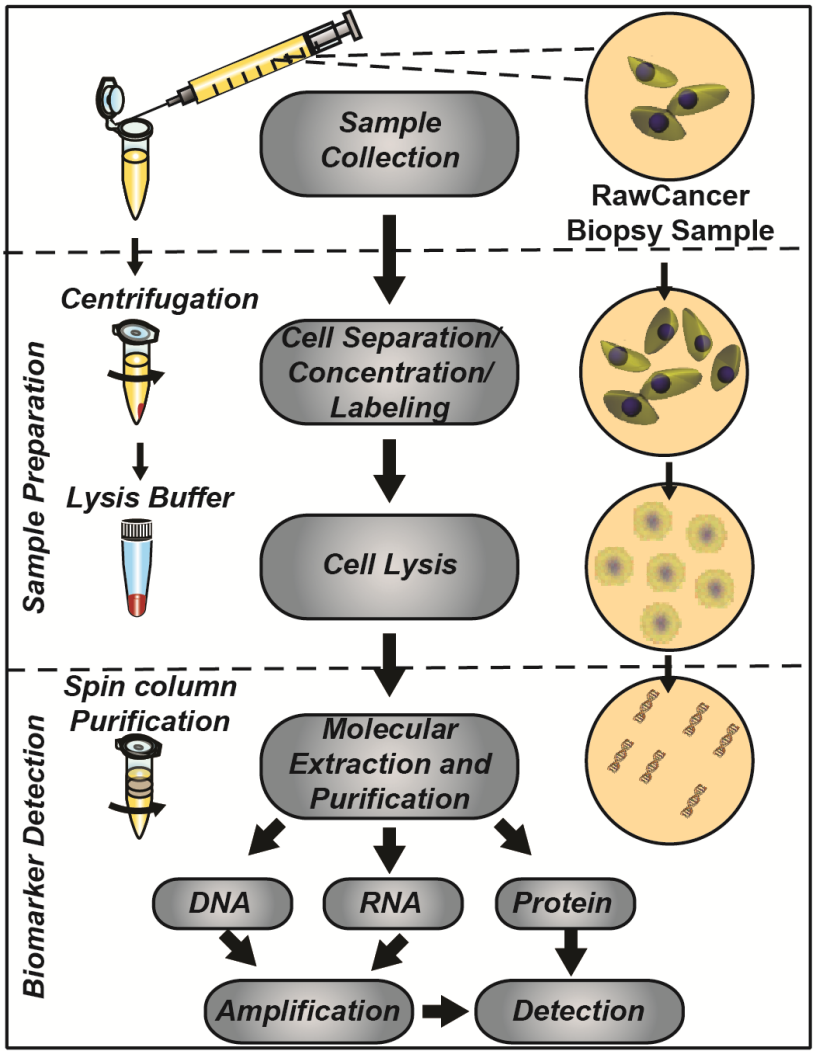

Figure 1.8: Flow chart showing the general sample preparation process involved in molecular diagnostics. The actual sample preparation scheme depends on the assay performed and in the case of immunocytochemical assay, for example, is much simplified and involves only sample concentration and labeling.

Although the sample preparation requirements depend on the assay being performed, some steps are common for a majority of the assays. A generalized sample preparation scheme, adapted from (148), is shown in Figure 1.8. The first step in sample preparation is generally cell separation/concentration which involves the removal and enrichment of cellular components of interest from the biological milieu in the biopsy samples. Traditionally this is done via repeated centrifugation and wash steps which are not suitable for a POCT workflow. The next step is the lysis of the enriched cells, if the assay so requires. Usually this is done using chemical (which might require an additional purification step if the lysis is incompatible with the assay) or mechanical lysis techniques (which need further instrumentation making it ill-suited for POCT workflow) (149). Finally biomarker purification steps might be needed based on the assay type. This workflow is simplified for cytological assays (150), where cell concentration and labeling are required. Microfluidic implementation of these sample preparation steps is important for realizing portable and integrated devices, which need little to no off-chip preparation steps,

which are ideal for POCT use. Such integrated devices will also minimize the number of manual steps (reducing time of assay and manual errors), sites for possible contamination and eventually increase overall efficiency (151).

Microfluidic Actuation for POCT systems

The mechanism of fluidic actuation is often the most important consideration in the design of novel microfluidic systems. A range of active and passive fluid control techniques have been described in the context of microfluidics over the past several decades (152). However the microfluidic devices developed for cancer diagnostics usually rely on a very small subset of these techniques. The most widely used technique is mechanical pumping achieved via a syringe pump (120, 132). In such devices, the POCT systems will require bulky, less portable or energy-inefficient actuation components. The development of micro-pumps, like the diagram deflection pumps utilizing piezoelectric or pneumatic actuation, can improve the portability and energy efficiency of these devices. The i-STAT portable clinical analyzer from Abbott, for example, used pneumatic pumps for mechanical pumping of the biofluids. Other actuation techniques used like electrokinetic (127) or electrophoretic (146) flow still need external actuation components, making them less attractive for POCT systems. While simpler systems, like capillary (153) and degas-driven flow (154), appear attractive due to their portability and ease-of-use, these systems generally lack the functionality required for a complex diagnostic test. Hence the development of simpler microfluidic actuation techniques which can be used for complex microfluidic assays will be instrumental in making microfluidic diagnostics devices accessible for POCT systems.

1.9 CONCLUSION

The current 'standard of care' for cancer diagnostics involves techniques which are time-consuming, manual labor intensive and vary considerably amongst institutions and countries. Point of Care testing (POCT) for cancer, with the capability of multiple-biomarker testing in biopsy samples in a fast, accurate and portable manner, will be an invaluable tool to disseminate universal diagnostics to cancer patients. A portable platform for multiple biomarker analysis will not only improve the operational characteristics of such assays but will also help determine drug efficacy, ushering in personalized medicine for the patients. Given the reduced volumes and diffusion distances, which will enable multiplexed, portable and fast assays, microfluidic devices are poised to be the enabling technology for such POCT systems. However the current microfluidic devices for cancer diagnostics suffer from the lack of a generalized on-chip sample preparation module and a simplified fluid actuation technique.

Organization of Dissertation

The overall aim of the intended dissertation research is to develop microfluidic modules that will enable the development of integrated microfluidic diagnostic systems for the multiplexed detection of cancer biomarkers in the tumor biopsy samples. The thesis is mainly focused on the development of novel on-chip sample preparation modules with a minor focus on simplified fluidic actuation technologies. The purpose of the sample preparation component is to pre-concentrate cancerous cells, remove background proteins in the sample and to subsequently lyse the cells to release the proteins of interest. We report on the pre-concentration of the

adherent cells, including the cancerous cells, in the sample by trapping them using a novel hydrodynamic cell trap. We also optimized sample washing methods to remove extracellular proteins that could interfere with downstream assays. We also integrated electrochemical lysis technique, to the cell pre-concentration module, to effectively lyse the cells without having to add external reagents. We mainly used the human breast cancer cell line BT-474, known to over express the Her-2 protein, and T47D to evaluate the trapping and lysing efficiencies and also the detection efficiency of the released protein.

A novel fluid actuation technique, termed Proximal Degas-driven Flow (PDF), is also reported in this thesis. PDF takes advantage of the high porosity and air solubility of PDMS to reduce the pressure inside microfluidic channels using proximal microfluidic vacuum lines, which leads to fluidic actuation within the channel. This actuation technique enables bubble-free fluid flow and, in contrast to traditional pressure (positive or negative) driven flows, can be used to fill up dead-end chambers. Additionally, priming of channels is not necessary. Unlike degas-driven flow, PDF alleviates the need for pre-degassed and sealed devices, enabling consistent and longer-lasting fluid flow. This portable technique requires very simple and cheap hardware like a vacuum bulb or membrane pump (thumb pump).

1.10 REFERENCES

1. Willmott C, Arrowsmith JE (2010) Point-of-care testing. *Surgery (Oxford)* 28:159–160.

2. Kost GJ (2006) in *Encyclopedia of Analytical Chemistry* (John Wiley & Sons, Ltd).

3. Hirsch J, Wendt T, Kuhly P, Schaffartzik W (2001) Point-of-care testing. *Anaesthesia* 56:760–763.

4. Nichols JH (2007) Point of Care Testing. *Clinics in Laboratory Medicine* 27:893–908.

5. Pai NP, Vadnais C, Denkinger C, Engel N, Pai M (2012) Point-of-Care Testing for Infectious Diseases: Diversity, Complexity, and Barriers in Low- And Middle-Income Countries. *PLoS Med* 9.

6. Soper SA et al. (2006) Point-of-care biosensor systems for cancer diagnostics/prognostics. *Biosensors and Bioelectronics* 21:1932–1942.

7. Peeling RW, Mabey D (2010) Point-of-care tests for diagnosing infections in the developing world. *Clinical Microbiology and Infection* 16:1062–1069.

8. Ruddon RW (2007) *Cancer Biology* (Oxford University Press).

9. Mukherjee S (2011) *The Emperor of All Maladies: A Biography of Cancer* (Simon and Schuster).

10. American Cancer Society A (2011) Global Cancer Facts & Figures 2nd Edition.

11. American Cancer Society A (2012) Cancer Facts & Figures 2012.

12. Humphrey LL, Helfand M, Chan BKS, Woolf SH (2002) Breast Cancer Screening: A Summary of the Evidence for the U.S. Preventive Services Task Force. *Ann Intern Med* 137:347–360.

13. Gunasheela S (2011) *Practical Management of Gynecological Problems* (JP Medical Ltd).

14. Young PE, Womeldorph CM (2013) Colonoscopy for Colorectal Cancer Screening. *J Cancer* 4:217–226.

15. Hugosson J et al. (2010) Mortality results from the Göteborg randomised population-based prostate-cancer screening trial. *The Lancet Oncology* 11:725–732.

16. Goldie SJ et al. (2005) Cost-Effectiveness of Cervical-Cancer Screening in Five Developing Countries. *New England Journal of Medicine* 353:2158–2168.

17. Anderson BO, Jakesz R (2008) Breast cancer issues in developing countries: an overview of the Breast Health Global Initiative. *World J Surg* 32:2578–2585.

18. Lerman C et al. (1991) Psychological side effects of breast cancer screening. *Health Psychology* 10:259–267.

19. Price CP, Kricka LJ (2007) Improving Healthcare Accessibility through Point-of-Care Technologies. *Clinical Chemistry* 53:1665–1675.

20. Lotan Y et al. (2009) Bladder cancer screening in a high risk asymptomatic population using a point of care urine based protein tumor marker. *J Urol* 182:52–57; discussion 58.

21. Grossman H SM (2006) SUrveillance for recurrent bladder cancer using a point-of-care proteomic assay. *JAMA* 295:299–305.

22. Brinkley D, Haybittle JL (1975) THE CURABILITY OF BREAST CANCER. *The Lancet* 306:95–97.

23. Duncan W, Kerr GR (1976) The curability of breast cancer. *Br Med J* 2:781–783.

24. Brinkley D (1977) Curability of breast cancer. *Bull Cancer* 64:585–591.

25. Rusling JF, Kumar CV, Gutkind JS, Patel V (2010) Measurement of biomarker proteins for point-of-care early detection and monitoring of cancer. *The Analyst* 135:2496.

26. Petricoin EF, Liotta LA (2004) SELDI-TOF-based serum proteomic pattern diagnostics for early detection of cancer. *Current Opinion in Biotechnology* 15:24–30.

27. Levenson VV (2007) Biomarkers for early detection of breast cancer: what, when, and where? *Biochim Biophys Acta* 1770:847–856.

28. Kuriyama M et al. (1980) Quantitation of prostate-specific antigen in serum by a sensitive enzyme immunoassay. *Cancer Res* 40:4658–4662.

29. Ishibashi M (2006) Standardization of Prostate-Specific Antigen (PSA) Assays: Can Interchangeability of PSA Measurements Be Improved? *Clinical Chemistry* 52:1–2.

30. Wolf AMD et al. (2010) American Cancer Society guideline for the early detection of prostate cancer: update 2010. *CA Cancer J Clin* 60:70–98.

31. Cook GB et al. Clinical utility of serum HER-2/neu testing on the Bayer Immuno 1® automated system in breast cancer. *Anticancer research* 21:1465–1470.

32. McKenzie SJ et al. (1993) Serum levels of HER-2 neu (C-erbB-2) correlate with overexpression of p185neu in human ovarian cancer. *Cancer* 71:3942–3946.

33. Gold DV et al. (2006) New MUC1 Serum Immunoassay Differentiates Pancreatic Cancer From Pancreatitis. *JCO* 24:252–258.

34. K E et al. (1996) Elevated levels of serum and plasma metalloproteinases in patients with gastric cancer. *Anticancer Res* 17:2253–2258.

35. Sawyers CL (2008) The cancer biomarker problem. *Nature* 452:548–552.

36. Hanash SM, Pitteri SJ, Faca VM (2008) Mining the plasma proteome for cancer biomarkers. *Nature* 452:571–579.

37. Petricoin III EF et al. (2002) Use of proteomic patterns in serum to identify ovarian cancer. *The Lancet* 359:572–577.

38. Powell K (2003) Proteomics delivers on promise of cancer biomarkers. *Nat Med* 9:980–980.

39. Li J, Zhang Z, Rosenzweig J, Wang YY, Chan DW (2002) Proteomics and Bioinformatics Approaches for Identification of Serum Biomarkers to Detect Breast Cancer. *Clinical Chemistry* 48:1296–1304.

40. Kyselova Z et al. (2008) Breast Cancer Diagnosis and Prognosis through Quantitative Measurements of Serum Glycan Profiles. *Clinical Chemistry* 54:1166–1175.

41. Yang S et al. (2005) Application of serum SELDI proteomic patterns in diagnosis of lung cancer. *BMC Cancer* 5:83.

42. Diamandis EP (2004) Analysis of Serum Proteomic Patterns for Early Cancer Diagnosis: Drawing Attention to Potential Problems. *JNCI J Natl Cancer Inst* 96:353–356.

43. Diamandis EP (2006) Peptidomics for Cancer Diagnosis: Present and Future. *J Proteome Res* 5:2079–2082.

44. Karsan A et al. (2005) Analytical and Preanalytical Biases in Serum Proteomic Pattern Analysis for Breast Cancer Diagnosis. *Clinical Chemistry* 51:1525–1528.

45. Ebert MPA, Korc M, Malfertheiner P, Röcken C (2006) Advances, Challenges, and Limitations in Serum-Proteome-Based Cancer Diagnosis. *J Proteome Res* 5:19–25.

46. Diamandis EP, Merwe D-E van der (2005) Plasma Protein Profiling by Mass Spectrometry for Cancer Diagnosis: Opportunities and Limitations. *Clin Cancer Res* 11:963–965.

47. Diamandis EP (2010) Cancer Biomarkers: Can We Turn Recent Failures into Success? *JNCI J Natl Cancer Inst* 102:1462–1467.

48. Gemoll T, Roblick UJ, Auer G, Jörnvall H, Habermann JK (2010) SELDI-TOF serum proteomics and colorectal cancer: A current overview. *Archives Of Physiology And Biochemistry* 116:188–196.

49. Ferracin M, Veronese A, Negrini M (2010) Micromarkers: miRNAs in cancer diagnosis and prognosis. *Expert Review of Molecular Diagnostics* 10:297–308.

50. Brase JC, Wuttig D, Kuner R, Sültmann H (2010) Serum microRNAs as non-invasive biomarkers for cancer. *Mol Cancer* 9:306.

51. Gilad S et al. (2008) Serum MicroRNAs Are Promising Novel Biomarkers. *PLoS ONE* 3:e3148.

52. Taylor DD, Gercel-Taylor C (2008) MicroRNA signatures of tumor-derived exosomes as diagnostic biomarkers of ovarian cancer. *Gynecol Oncol* 110:13–21.

53. Chen X et al. (2008) Characterization of microRNAs in serum: a novel class of biomarkers for diagnosis of cancer and other diseases. *Cell Res* 18:997–1006.

54. Liu R et al. (2012) Serum MicroRNA Expression Profile as a Biomarker in the Diagnosis and Prognosis of Pancreatic Cancer. *Clinical Chemistry* 58:610–618.

55. Asaga S et al. (2011) Direct Serum Assay for MicroRNA-21 Concentrations in Early and Advanced Breast Cancer. *Clinical Chemistry* 57:84–91.

56. Heneghan HM et al. (2010) Circulating microRNAs as Novel Minimally Invasive Biomarkers for Breast Cancer. *Annals of Surgery* 251:499–505.

57. Liu R et al. (2011) A five-microRNA signature identified from genome-wide serum microRNA expression profiling serves as a fingerprint for gastric cancer diagnosis. *European Journal of Cancer* 47:784–791.

58. Chen X et al. (2012) Identification of ten serum microRNAs from a genome-wide serum microRNA expression profile as novel noninvasive biomarkers for nonsmall cell lung cancer diagnosis. *International Journal of Cancer* 130:1620–1628.

59. Hu Z et al. (2010) Serum MicroRNA Signatures Identified in a Genome-Wide Serum MicroRNA Expression Profiling Predict Survival of Non–Small-Cell Lung Cancer. *JCO* 28:1721–1726.

60. Wittmann J, Jäck H-M (2010) Serum microRNAs as powerful cancer biomarkers. *Biochimica et Biophysica Acta (BBA) - Reviews on Cancer* 1806:200–207.

61. Kosaka N, Iguchi H, Ochiya T (2010) Circulating microRNA in body fluid: a new potential biomarker for cancer diagnosis and prognosis. *Cancer Science* 101:2087–2092.

62. Nunes DN, Kowalski LP, Simpson AJG (2001) Circulating tumor-derived DNA may permit the early diagnosis of head and neck squamous cell carcinomas. *International Journal of Cancer* 92:214–219.

63. Schwarzenbach H et al. (2009) Cell-free Tumor DNA in Blood Plasma As a Marker for Circulating Tumor Cells in Prostate Cancer. *Clin Cancer Res* 15:1032–1038.

64. Sleijfer S et al. (2007) Circulating tumour cell detection on its way to routine diagnostic implementation? *European Journal of Cancer* 43:2645–2650.

65. Wülfing P et al. (2006) HER2-Positive Circulating Tumor Cells Indicate Poor Clinical Outcome in Stage I to III Breast Cancer Patients. *Clin Cancer Res* 12:1715–1720.

66. Smirnov DA et al. (2005) Global Gene Expression Profiling of Circulating Tumor Cells. *Cancer Res* 65:4993–4997.

67. Paterlini-Brechot P, Benali NL (2007) Circulating tumor cells (CTC) detection: Clinical impact and future directions. *Cancer Letters* 253:180–204.

68. Pantel K, Brakenhoff RH, Brandt B (2008) Detection, clinical relevance and specific biological properties of disseminating tumour cells. *Nature Reviews Cancer* 8:329–340.

69. Allard WJ et al. (2004) Tumor Cells Circulate in the Peripheral Blood of All Major Carcinomas but not in Healthy Subjects or Patients With Nonmalignant Diseases. *Clin Cancer Res* 10:6897–6904.

70. Ross AA et al. (1993) Detection and viability of tumor cells in peripheral blood stem cell collections from breast cancer patients using immunocytochemical and clonogenic assay techniques. *Blood* 82:2605–2610.

71. Miller MC, Doyle GV, Terstappen LWMM (2010) Significance of Circulating Tumor Cells Detected by the CellSearch System in Patients with Metastatic Breast Colorectal and Prostate Cancer. *Journal of Oncology* 2010:1–8.

72. Sequist LV, Nagrath S, Toner M, Haber DA, Lynch TJ (2009) The CTC-Chip. *Journal of Thoracic Oncology* 4:281–283.

73. Ross JS, Slodkowska EA (2009) Circulating and Disseminated Tumor Cells in the Management of Breast Cancer. *AJCP* 132:237–245.

74. Aktas B et al. (2009) Stem cell and epithelial-mesenchymal transition markers are frequently overexpressed in circulating tumor cells of metastatic breast cancer patients. *Breast Cancer Res* 11:R46.

75. Tanaka F et al. (2009) Circulating Tumor Cell as a Diagnostic Marker in Primary Lung Cancer. *Clin Cancer Res* 15:6980–6986.

76. Frable WJ (1984) Needle aspiration of the breast. *Cancer* 53:671–676.

77. Simmons C et al. (2009) Does confirmatory tumor biopsy alter the management of breast cancer patients with distant metastases? *Ann Oncol* 20:1499–1504.

78. Contreras E, Ellis LD, Lee RE (1972) Value of the bone marrow biopsy in the diagnosis of metastatic carcinoma. *Cancer* 29:778–783.

79. Reid BJ, Blount PL, Feng Z, S Levine D (2000) Optimizing endoscopic biopsy detection of early cancers in Barrett's high-grade dysplasia. *Am J Gastroenterol* 95:3089–3096.

80. Welch HG (2005) Skin biopsy rates and incidence of melanoma: population based ecological study. *BMJ* 331:481–0.

81. Florentine BD, Cobb CJ, Frankel K, Greaves T, Martin SE (1997) Core needle biopsy. *Cancer Cytopathology* 81:33–39.

82. Tiwari M (2007) Role of fine needle aspiration cytology in diagnosis of breast lumps. *Kathmandu Univ Med J (KUMJ)* 5:215–217.

83. Giusti L, Iacconi P, Lucacchini A (2011) Fine-needle aspiration for proteomic study of tumour tissues. *PROTEOMICS – Clinical Applications* 5:24–29.

84. Rimm DL, Stastny JF, Rimm EB, Ayer S, Frable WJ (1997) Comparison of the costs of fine-needle aspiration and open surgical biopsy as methods for obtaining a pathologic diagnosis. *Cancer Cytopathology* 81:51–56.

85. Dennison G, Anand R, Makar SH, Pain JA (2003) A Prospective Study of the Use of Fine-Needle Aspiration Cytology and Core Biopsy in the Diagnosis of Breast Cancer. *The Breast Journal* 9:491–493.

86. Löwhagen T, Willems JS, Lundell G, Sundblad R, Granberg PO (1981) Aspiration biopsy cytology in diagnosis of thyroid cancer. *World J Surg* 5:61–73.

87. Zajdela A, Ghossein NA, Pilleron JP, Ennuyer A (1975) The value of aspiration cytology in the diagnosis of breast cancer: Experience at the fondation curie. *Cancer* 35:499–506.

88. Nussbaum ES, Djalilian HR, Cho KH, Hall WA (1996) Brain metastases: Histology, multiplicity, surgery, and survival. *Cancer* 78:1781–1788.

89. Ursin G et al. (2005) Reproductive factors and subtypes of breast cancer defined by hormone receptor and histology. *Br J Cancer* 93:364–371.

90. Ronco G et al. (2007) Accuracy of liquid based versus conventional cytology: overall results of new technologies for cervical cancer screening: randomised controlled trial. *BMJ* 335:28–28.

91. Dabbs DJ (2010) *Diagnostic Immunohistochemistry: Theranostic and Genomic Applications - Expert Consult* (Elsevier Health Sciences).

92. James CR, Quinn JE, Mullan PB, Johnston PG, Harkin DP (2007) BRCA1, a Potential Predictive Biomarker in the Treatment of Breast Cancer. *The Oncologist* 12:142–150.

93. Baselga J, Norton L, Albanell J, Kim Y-M, Mendelsohn J (1998) Recombinant Humanized Anti-HER2 Antibody (Herceptin™) Enhances the Antitumor Activity of Paclitaxel and Doxorubicin against HER2/neu Overexpressing Human Breast Cancer Xenografts. *Cancer Res* 58:2825–2831.

94. Young NA, Al-Saleem TI, Ehya H, Smith MR (1998) Utilization of fine-needle aspiration cytology and flow cytometry in the diagnosis and subclassification of primary and recurrent lymphoma. *Cancer Cytopathology* 84:252–261.

95. Barlogie B et al. (1983) Flow Cytometry in Clinical Cancer Research. *Cancer Res* 43:3982–3997.

96. Ramaswamy S et al. (2001) Multiclass cancer diagnosis using tumor gene expression signatures. *PNAS* 98:15149–15154.

97. Borczuk AC et al. (2004) Molecular signatures in biopsy specimens of lung cancer. *Am J Respir Crit Care Med* 170:167–174.

98. Symmans WF et al. (2005) A single-gene biomarker identifies breast cancers associated with immature cell type and short duration of prior breastfeeding. *Endocr Relat Cancer* 12:1059–1069.

99. Balasubramanian A et al. (2009) Evaluation of an ELISA for p16INK4a as a screening test for cervical cancer. *Cancer Epidemiol Biomarkers Prev* 18:3008–3017.

100. Crevillén AG, Hervás M, López MA, González MC, Escarpa A (2007) Real sample analysis on microfluidic devices. *Talanta* 74:342–357.

101. Schwartz SA, Weil RJ, Johnson MD, Toms SA, Caprioli RM (2004) Protein Profiling in Brain Tumors Using Mass Spectrometry Feasibility of a New Technique for the Analysis of Protein Expression. *Clin Cancer Res* 10:981–987.

102. Gonçalves A et al. (2008) Protein Profiling of Human Breast Tumor Cells Identifies Novel Biomarkers Associated with Molecular Subtypes. *Mol Cell Proteomics* 7:1420–1433.

103. Johann DJ et al. (2009) Approaching Solid Tumor Heterogeneity on a Cellular Basis by Tissue Proteomics Using Laser Capture Microdissection and Biological Mass Spectrometry†. *J Proteome Res* 8:2310–2318.

104.Shiwa M et al. (2003) Rapid discovery and identification of a tissue-specific tumor biomarker from 39 human cancer cell lines using the SELDI ProteinChip platform. *Biochem Biophys Res Commun* 309:18–25.

105.Simon R, Mirlacher M, Sauter G (2003) Tissue microarrays in cancer diagnosis. *Expert Review of Molecular Diagnostics* 3:421–430.

106.Cummins JM, Velculescu VE (2006) Implications of micro-RNA profiling for cancer diagnosis. *Oncogene* 25:6220–6227.

107.Hoshi K et al. (2007) Rapid Detection of Epidermal Growth Factor Receptor Mutations in Lung Cancer by the SMart-Amplification Process. *Clin Cancer Res* 13:4974–4983.

108.Liotta L, Petricoin E (2000) Molecular profiling of human cancer. *Nat Rev Genet* 1:48–56.

109.Slodkowska EA, Ross JS (2009) MammaPrint™ 70-gene signature: another milestone in personalized medical care for breast cancer patients. *Expert Review of Molecular Diagnostics* 9:417–422.

110.Habel LA et al. (2006) A population-based study of tumor gene expression and risk of breast cancer death among lymph node-negative patients. *Breast Cancer Res* 8:R25.

111.Cobleigh MA et al. (2005) Tumor Gene Expression and Prognosis in Breast Cancer Patients with 10 or More Positive Lymph Nodes. *Clin Cancer Res* 11:8623–8631.

112.Liu J et al. (2010) Molecular Mapping of Tumor Heterogeneity on Clinical Tissue Specimens with Multiplexed Quantum Dots. *ACS Nano* 4:2755–2765.

113.Lee SJ, Lee SY Micro total analysis system (μ-TAS) in biotechnology. *Applied microbiology and biotechnology* 64:289–299.

114.Tudos AJ, Besselink GJ, Schasfoort RB (2001) Trends in miniaturized total analysis systems for point-of-care testing in clinical chemistry. *Lab Chip* 1:83–95.

115.Jakeway SC, de Mello AJ, Russell EL (2000) Miniaturized total analysis systems for biological analysis. *Fresenius' Journal of Analytical Chemistry* 366:525–539.

116.Reyes DR, Iossifidis D, Auroux P-A, Manz A (2002) Micro total analysis systems. 1. Introduction, theory, and technology. *Anal Chem* 74:2623–2636.

117.Auroux P-A, Iossifidis D, Reyes DR, Manz A (2002) Micro Total Analysis Systems. 2. Analytical Standard Operations and Applications. *Analytical Chemistry* 74:2637–2652.

118.Mauk MG, Ziober BL, Chen Z, Thompson JA, Bau HH (2007) Lab-on-a-Chip Technologies for Oral-Based Cancer Screening and Diagnostics. *Annals of the New York Academy of Sciences* 1098:467–475.

119. Weigum SE, Floriano PN, Christodoulides N, McDevitt JT (2007) Cell-based sensor for analysis of EGFR biomarker expression in oral cancer. *Lab on a Chip* 7:995.

120. Kim MS et al. (2010) Breast Cancer Diagnosis Using a Microfluidic Multiplexed Immunohistochemistry Platform. *PLoS ONE* 5:e10441.

121. Kim MS, Kwon S, Kim T, Lee ES, Park J-K (2011) Quantitative proteomic profiling of breast cancers using a multiplexed microfluidic platform for immunohistochemistry and immunocytochemistry. *Biomaterials* 32:1396–1403.

122. Kim MS, Kwon S, Lee ES, Park J-K (2010) in *2010 10th IEEE Conference on Nanotechnology (IEEE-NANO)*, pp 1045–1048.

123. Ciftlik AT, Lehr H-A, Gijs MAM (2013) Microfluidic processor allows rapid HER2 immunohistochemistry of breast carcinomas and significantly reduces ambiguous (2+) read-outs. *PNAS*.

124. Lovchik RD, Kaigala GV, Georgiadis M, Delamarche E (2012) Micro-immunohistochemistry using a microfluidic probe. *Lab Chip* 12:1040–1043.

125. Remmerbach TW et al. (2009) Oral Cancer Diagnosis by Mechanical Phenotyping. *Cancer Res* 69:1728–1732.

126. Gossett DR et al. (2012) Hydrodynamic stretching of single cells for large population mechanical phenotyping. *PNAS* 109:7630–7635.

127. Woods J, Docker PT, Dyer CE, Haswell SJ, Greenman J (2011) On-chip integrated labelling, transport and detection of tumour cells. *Electrophoresis* 32:3188–3195.

128. Lee H, Sun E, Ham D, Weissleder R (2008) Chip-NMR biosensor for detection and molecular analysis of cells. *Nat Med* 14:869–874.

129. Lee H, Yoon T-J, Figueiredo J-L, Swirski FK, Weissleder R (2009) Rapid Detection and Profiling of Cancer Cells in Fine-Needle Aspirates. *PNAS* 106:12459–12464.

130. Haun JB et al. (2011) Micro-NMR for Rapid Molecular Analysis of Human Tumor Samples. *Sci Transl Med* 3:71ra16.

131. Shao H et al. (2012) Magnetic Nanoparticles and microNMR for Diagnostic Applications. *Theranostics* 2:55–65.

132. Yu X et al. (2010) μFBI: A Microfluidic Bead-Based Immunoassay for Multiplexed Detection of Proteins from a μL Sample Volume. *PLoS One* 5.

133. Klapperich CM, Mahalanabis M, Patel SH, Sharma S, Rosen JE (2012) A novel platform for nucleic acid biomarker-based diagnosis of thyroid cancer. *Head Neck Oncol* 4:85.

134.Gulliksen A et al. (2005) Parallel nanoliter detection of cancer markers using polymer microchips. *Lab on a Chip* 5:416.

135.Yokokawa R, Tamaoki S, Sakamoto T, Murakami A, Sugiyama S (2007) Transcriptome analysis device based on liquid phase detection by fluorescently labeled nucleic acid probes. *Biomed Microdevices* 9:869–875.

136.Zamo A et al. (2007) Microfluidic Deletion/Insertion Analysis for Rapid Screening of KIT and PDGFRA Mutations in CD117-Positive Gastrointestinal Stromal Tumors. *J Mol Diagn* 9:151–157.

137.Abruzzo LV et al. (2007) Identification and Validation of Biomarkers of IgVH Mutation Status in Chronic Lymphocytic Leukemia Using Microfluidics Quantitative Real-Time Polymerase Chain Reaction Technology. *J Mol Diagn* 9:546–555.

138.Odenthal M et al. (2009) Analysis of microsatellite instability in colorectal carcinoma by microfluidic-based chip electrophoresis. *J Clin Pathol* 62:850–852.

139.Sweeney E et al. (2008) Quantitative multiplexed quantum dot immunohistochemistry. *Biochem Biophys Res Commun* 374:181–186.

140.Xing Y et al. (2007) Bioconjugated quantum dots for multiplexed and quantitative immunohistochemistry. *Nat Protocols* 2:1152–1165.

141.Yeong Won J, Choi J-W, Min J (2013) Micro-fluidic chip platform for the characterization of breast cancer cells using aptamer-assisted immunohistochemistry. *Biosens Bioelectron* 40:161–166.

142.Sheiman RG, Fey C, McNicholas M, Raptopoulos V (1998) Possible causes of inconclusive results on CT-guided thoracic and abdominal core biopsies. *AJR Am J Roentgenol* 170:1603–1607.

143.Lincoln B et al. (2004) Deformability-based flow cytometry. *Cytometry A* 59:203–209.

144.Shaw KJ et al. (2011) Microsystems for personalized biomolecular diagnostics. *Engineering in Life Sciences* 11:121–132.

145.Fang Z et al. (2009) Direct Profiling of Cancer Biomarkers in Tumor Tissue Using a Multiplexed Nanostructured Microelectrode Integrated Circuit. *ACS Nano* 3:3207–3213.

146.Kim SJ, Choi SJ, Neelamegam R, Seo TS Microchip-based capillary electrophoretic analysis of telomerase activity for cancer diagnostics. *Biochip journal* 4:42–48.

147.Miller AK, Stanton ML, Sanchez CA, Li X, McQuaide SC (2005) in *IEEE International Conference on Automation Science and Engineering, 2005*, pp 1–6.

148.Huang Y, Mather E, Bell J, Madou M (2002) MEMS-based sample preparation for molecular diagnostics. *Analytical and Bioanalytical Chemistry* 372:49–65.

149.Kim J, Johnson M, Hill P, Gale BK (2009) Microfluidic sample preparation: cell lysis and nucleic acid purification. *Integrative Biology* 1:574.

150.Mach AJ, Adeyiga OB, Carlo DD (2013) Microfluidic sample preparation for diagnostic cytopathology. *Lab Chip* 13:1011–1026.

151.Yang S, Rothman RE (2004) PCR-based diagnostics for infectious diseases: uses, limitations, and future applications in acute-care settings. *The Lancet Infectious Diseases* 4:337–348.

152. Iverson BD, Garimella SV Recent advances in microscale pumping technologies : a review and evaluation. *Microfluidics and nanofluidics* 5:145–174.

153. Lu Y, Shi W, Jiang L, Qin J, Lin B (2009) Rapid prototyping of paper-based microfluidics with wax for low-cost, portable bioassay. *Electrophoresis* 30:1497–1500.

154. Hosokawa K, Sato K, Ichikawa N, Maeda M (2004) Power-free poly(dimethylsiloxane) microfluidic devices for gold nanoparticle-based DNA analysis. *Lab on a Chip* 4:181.

CHAPTER 2

Analyzing Hydraulic Jump Phenomenon At The Microscale

2.1 ABSTRACT

The microfluidic study of cellular behavior and function necessitates the easy trap-and-release of microparticles. The observation of microscale hydraulic jump phenomenon led us to envisage a microfluidic device for the hydrodynamic trap-and-release of micoparticles in solution. An increase in the height of microfluidic channel in our device results in a sudden decrease in flow velocity which leads to the sedimentation of microparticles by energy conversion. These particles are thereafter immobilized at the channel floor by friction and adhesion forces, and can be later released by a stronger fluid drag force (resulting from an increase in the flow velocity). Here, we present the numerical analysis and characterization of the microscale hydraulic jump phenomenon and its use for the trap-and-release of microparticles. The effects of geometric effects, such as channel and trap dimensions, and the flow velocity are investigated. This method will have strong implications in precision biology and medical applications since it will provide a platform to observe biological cellular behaviors within the context of physiological conditions and dynamic microenvironments.

2.2 INTRODUCTION

Manipulating microparticles, such as cells, bacteria, and hydrogel particles in microfluidic devices, is important for high throughput and fast cell screening, single cell analysis, and biochemical synthesis (1–5). Currently, such manipulation techniques usually apply acoustic (6), chemical (7), electrical(8) , mechanical (9), magnetic(10), or optical gradients(11). In the microscale, researchers have successfully maneuvered microparticles using techniques such as patch clamp (3, 5, 12), adhesion(13–16), sedimentation(17), size filtration(18), trench separation (19–23), and hydrodynamic trapping (24–31). Microfluidic mechanical manipulation techniques are generally considered to be the simplest and most effective of these methods. They also do not need bulky/expensive instrumentation needed for the other techniques. A frequent implementation of a microfluidic mechanical trap is a dam or a wall, relying on physical entrapment in what can be referred to as constriction based trapping. There are reports that such traps apply excessive pressure onto the immobilized particles (32). On the other hand, expansion based techniques, like Microwells can potentially overcome the deficiencies in constriction based mechanical traps. Molded PEG microwells were used by Khademhosseini et al. for trapping cells in micro channels (33). They introduced cells into their devices having microstructures and let them settle down, capturing cells even in the presence of shear flow (34) . Ochsner et al. used microwell arrays patterned with adhesion proteins to study the effect of ECM shape and flexibility on cell fate (35). Microwells for single cell capture was optimized by Revzin et al (36). Hence, microwells can potentially be a very effective cell trap, which can operate on a wide range of flow rates without putting the cells trapped through a lot of unnecessary forces.

However, microwell techniques have drawbacks such as the absence of releasing capability and the lack of fast mass transport. Here we describe a new microparticle manipulation method that relies on simple microfluidic architecture, possesses trap-and-release capabilities and allows fast mass transport. The hydraulic jump phenomenon observed in nature is applied at the microscale to achieve this (37). The hydraulic jump occurs when a liquid at high velocity discharges into a zone of lower velocity, whereby due to a sudden decrease in fluid velocity, kinetic energy converts to potential energy, causing the fluid to 'jump'. The microfluidic implementation consists of a channel with a hydraulic jump cavity where there is a sudden expansion in height. Because of the sudden expansion of the microfluidic channel height, kinetic energy of the microparticles is converted to potential energy and eventually due to gravitational forces the microparticles settle down. At the channel floor, the microparticles get trapped when the fluid force on them is balanced by surface interaction forces. The trapped particle can then be easily released by stronger inertial force based on simply increasing of flow velocity. The increase in fluid velocity increases the fluid forces which overcome surface interaction forces, leading to particle release. In this simulation study, the geometrical factors, including height and length of the hydraulic jump cavity (for a specific microparticle diameter), and flow velocity are investigated for optimal hydrodynamic trap-and-release device. In addition, adhesion force between substrate surface and particles is considered for the trapping of 0.5 μm sized particles.

Numerical design and modeling are tools that microfluidic researchers can utilize to save upon a lot of time and materials spent in testing all possible device designs (32, 38, 39). Using hydrodynamic simulation researchers have been able to model cell traps and make them efficient. Here we will discuss results from hydrodynamic simulation and optimization of cell traps based on the microscale implementation of the hydraulic jump phenomenon. The main parameters that we optimized were the dimensions of the trap and the flow rate range at which the device can operate. An ideal trap is one which can trap majority of incoming cells and is operable over a range of flow rates.

Another interesting aspect of these traps that we delve into is a basic understanding of the physics behind microparticle behavior in these structures. In the microwell traps, particle trapping takes place by gravity based sedimentation (33, 35, 40). However in the hydraulic jump cell traps, there is interplay between fluid shear, gravity and surface adhesion forces. A further understanding of these forces on the cell can potentially allow us to measure and characterize more intrinsic properties of a particle like its density, shape and surface energy.

2.3 PRINCIPLE BEHIND HYDRAULIC JUMP CELL TRAPS

The principle behind cellular trapping in our device is shown in Figure 2.1. The 'trap' is a region of channel expansion that decreases the fluid flow rate. As a result, the cells initially gain potential energy (and hence height) and, if the flow rate is slow enough, have ample time to sediment downward to the base of the trap due to gravity. The trajectory of the cells caused by this mechanism is shown in Figure 2.1a. Once the cells sediment, friction and non-specific adhesion forces between the cell surface and the base of the trap (plasma treated glass) apply a retardation force, which counters the fluid pressure and drag forces pulling the cells along the flow direction. Glass surfaces are naturally adhesive to certain cell types. It is generally accepted that the natural adhesiveness of such materials come from their ability to support adsorption of extracellular matrix proteins secreted by the cell (41). For trapping, the net fluid drag forces should be less than the net retardation forces. When equilibrium of the forces occurs,

the cells come to rest and become 'trapped' (Figure 2.1a.iii). When the perfusion rate, and hence fluid drag force, is increased the retardation forces are not sufficient to trap the cells and cell release occurs (Figure 2.1 b).

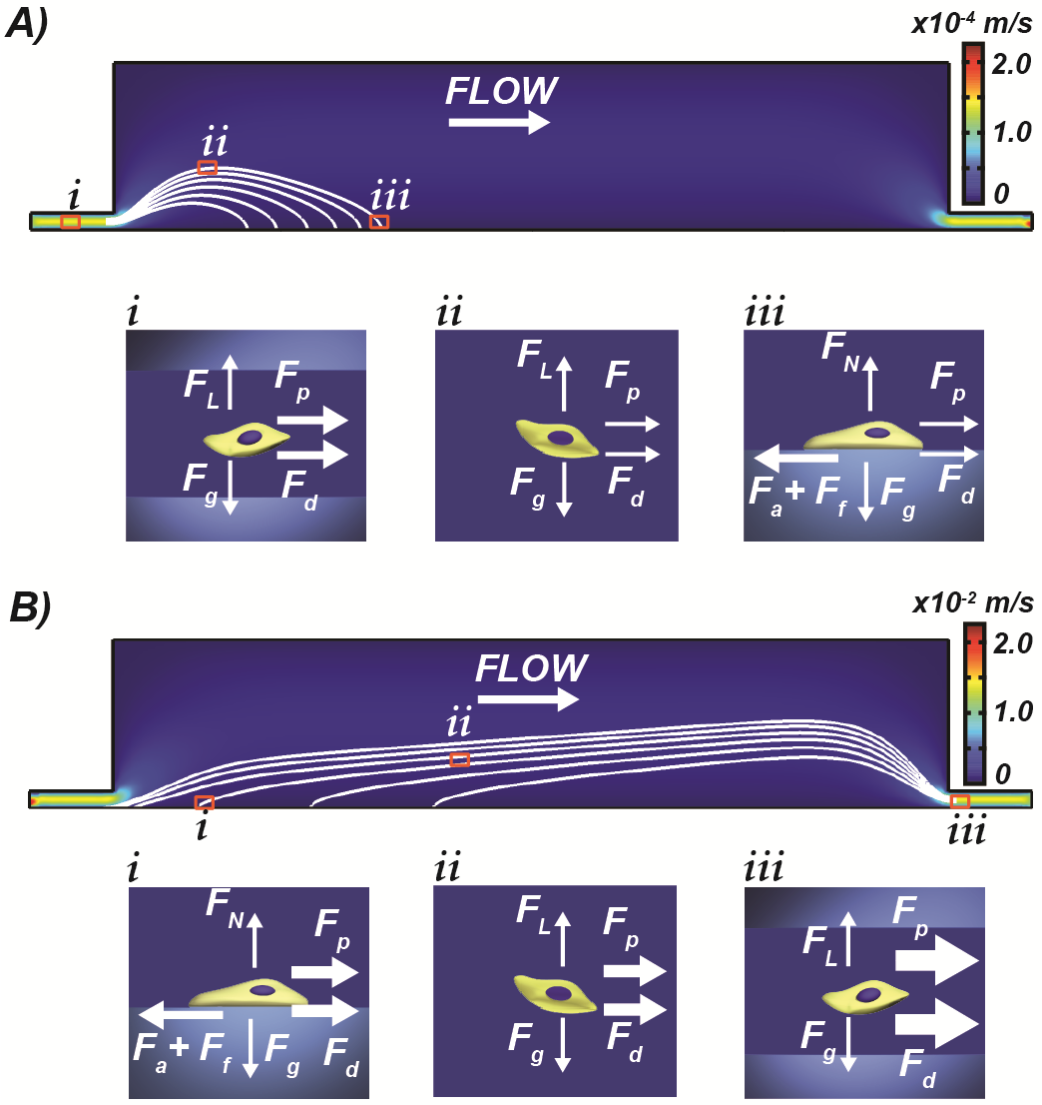

Figure 2.1: **A)** (top) A representative simulation result depicting fluid velocity and cell path lines within the trap region; (bottom) The different forces acting on the cells during the trapping process are shown (flow is from left to right); (i) fluid drag and pressure forces (F_d and F_p) in the channel propel the cells along while the cells experience gravitational (F_g) and lift forces (F_L), (ii) the fluid drag and pressure forces are reduced in the trap region and the cells settle under the action of gravitational force, (iii) once the cells are in contact with the bottom substrate, surface retardation forces (adhesion, F_a, and friction, F_f) overcome the fluid drag forces resulting in cell trapping (F_N is the normal force from the substrate); **B)** (top) A representative simulation result depicting fluid velocity and cell path lines during release of trapped cells; (bottom) The different forces acting on the cells during the release process are shown (flow is from left to right); (i) once the flow velocity in the trap region is increased, surface retardation forces (adhesion and friction) can no longer overcome the fluid drag forces resulting in cell release (ii) and (iii) fluid drag and pressure forces in the channel propel the cells along and out of the trap region. Note, that the fluid drag forces are the only difference from part **(A)**.

2.4 SIMULATION-BASED OPTIMIZATION OF TRAP DESIGN

To optimize the device design for high trapping efficiency, a multiphase 2D numerical model of the system was simulated using the computational fluid dynamics (CFD) package for COMSOL 3.5. Figure 2.2a depicts the 2D simulation model where the width of the trap is assumed to be semi-infinite (very large in comparison to its length and height). Cells were considered a dispersed phased in liquid (continuous phase) to solve for the mixture velocity, pressure, and the phase volume fractions using:

$$\rho(u\cdot\nabla)u = -\nabla p - \nabla\cdot(\rho c_d (1-c_d)u_{slip}u_{slip}) + \nabla\cdot\tau_{Gm} + \rho g \qquad \text{-- (1)}$$

Where u is the mixture velocity, ρ is mixture density, p is pressure, c_d is mass fraction of the solid phase, u_{slip} is the relative velocity (slip velocity) between the two phases, τ_{Gm} is the sum of viscous and turbulent stress, and g is the gravity vector. Slip velocity was used to estimate particle velocity in this multiphase phase model using:

$$(\rho_c - \rho_d)[\nabla\cdot(\phi_d (1-c_d)u_{slip} - D_{md}\nabla\phi_d)] + \rho_c(\nabla\cdot u) = 0 \qquad \text{-- (2)}$$

$$\frac{\partial}{\partial t}(\phi_d\rho_d) + \nabla\cdot(\phi_d\rho_d u_d) = 0 \qquad \text{-- (3)}$$

And the mixture velocity was defined as:

$$u = \frac{\phi_c\rho_c u_c + \phi_d\rho_d\phi_d}{\rho} \qquad \text{-- (4)}$$

Where, ϕ_c and ϕ_d denote the volume fractions of the liquid phase and the dispersed phase, respectively. Here, u_c is the liquid-phase velocity, u_d is the solid-phase velocity, ρ_c is the liquid-phase density, and ρ_d is the solid-phase density. We evaluated the geometrical effects to optimize the trap and release function of the device. However, the particle size limits the possible geometry ranges for the inlet channel height before the hydraulic jump region (h_0) and fabrication methods limit the maximum height of the trap region (h_1). For these reasons, h_0 was selected as the variable to normalize the height of the hydraulic trap: h_1/h_0. The different parameters varied in the simulation are listed in Table 3.1. Also, the boundary and sub-domain conditions used are presented in Table 3.2. A 2D mesh was applied since the hydraulic jump trap is symmetric and a semi-implicit pressure linked equation (SIMPLE) algorithm was applied to solve the momentum equation. Each simulation took ~5 min on an Intel *Xeon* E5420 with a 2.50 GHz processor.

Table 3.1: Parameters

Parameters	Unit	Values
Normalized Height, h_1 / h_0	_	1.5, 2.0, 5.0, 10.0, 15.0, 30.0, 50.0, 70.0
Length of Trap, L	μm	50.0, 100.0, 200.0, 300.0, 1000.0, 1400.0
Re	_	0.445, 4.45 x 10^{-2}, 4.45 x 10^{-3}, 4.45 x 10^{-4}, 4.45 x 10^{-5}
Particle diameter, D_p	μm	15

Table 3.2: Boundary and Sub-domain conditions

Boundary condition	Unit	Value
Initial volume fraction of particles	_	0.0004
Density of liquid	g/cm^3	1.000
Density of cell	g/cm^3	1.033

A simulation snapshot is shown in Figure 2.2a indicating cell trapping (as evidenced by an increase in cell concentration) occurring near the trap entrance. To determine the maximum trapping efficiency (η) for a cell diameter of 15 μm (average diameter of the cells used in this study), the following parameters were varied: the trap length (L), trap height (h_1) normalized to an inlet channel height (h_0) of 20 μm, and operating flow velocity u_0 (within the channel). Figure 2.2b and c shows two representative graphs from the simulation's three-parameter space; showing the dependence of η first on trap length with a fixed normalized trap height (h_1/ h_0) of 10 and second with a trap length of 300 μm with varying normalized trap height. Trapping efficiency increases with decreasing u_0 as is evident in Figure 2.2b, until cell sedimentation upstream of the trap region, within the inlet channel, reduces η at very low u_0 ($<=1.16 \times 10^{-5}$ m/s). Additionally, while throughput of the system suffers at very low u_0 increasing u_0 causes an increase in the fluid drag forces, thus reducing η. Therefore, an optimal u_0 exists that is ~1.16×10^{-4} m/s for maximum cell trapping efficiency. Figure 2.2d depicts the simulated η as a function of the two geometrical factors (trap length and normalized height) at a fixed u_0 of 1.16×10^{-4} m/s. As can be concluded from the simulation data, optimal trapping is predicted for L and h_1/ h_0 equal to or greater than 1,000 μm and 15 respectively at an u_0 of 1.16×10^{-4} m/s ($\eta \sim 1.0$). However, the difference between h_1/ h_0 ratio of 10 and 15 at L of 1,000 μm is found to be experimentally not significant (refer to next chapter). Hence, the optimal design for the trap is a L of 1,000 μm, h_1 of 20 μm and h_0 of 200 μm, operated at u_0 of 1.16×10^{-4} m/s. The trap and release characteristic of these trap are shown in Figure 2.2e. The flow velocity in the trap and stop parts of the graph are the optimal flow velocity, whereas in the release part the flow velocity is increased 100x. The simulation results indicate the hydrodynamic control over trap and release in the hydraulic jump trap design.

Protein transport in the optimal trap design was simulated for an inlet concentration of 0.1 M and a flow velocity in the channel, u_0, of 1.16×10^{-4} m/s. A 2D model of the system was used in the simulations and the convective transport COMSOL 3.5 module was implemented. The flow rate was set at the optimal velocity for trapping and a transient simulation model (with a time step of 1 sec) was executed. The results from the simulation study are shown in Figure 2.3. The results indicate that the convective mass transport in the hydraulic jump traps is very efficient and the desired concentration of the molecule is reached in about 30 seconds (which will be faster for smaller molecules with a larger diffusion constant). Hence, the trapped cells can be easily exposed to different molecules for performing an assay.

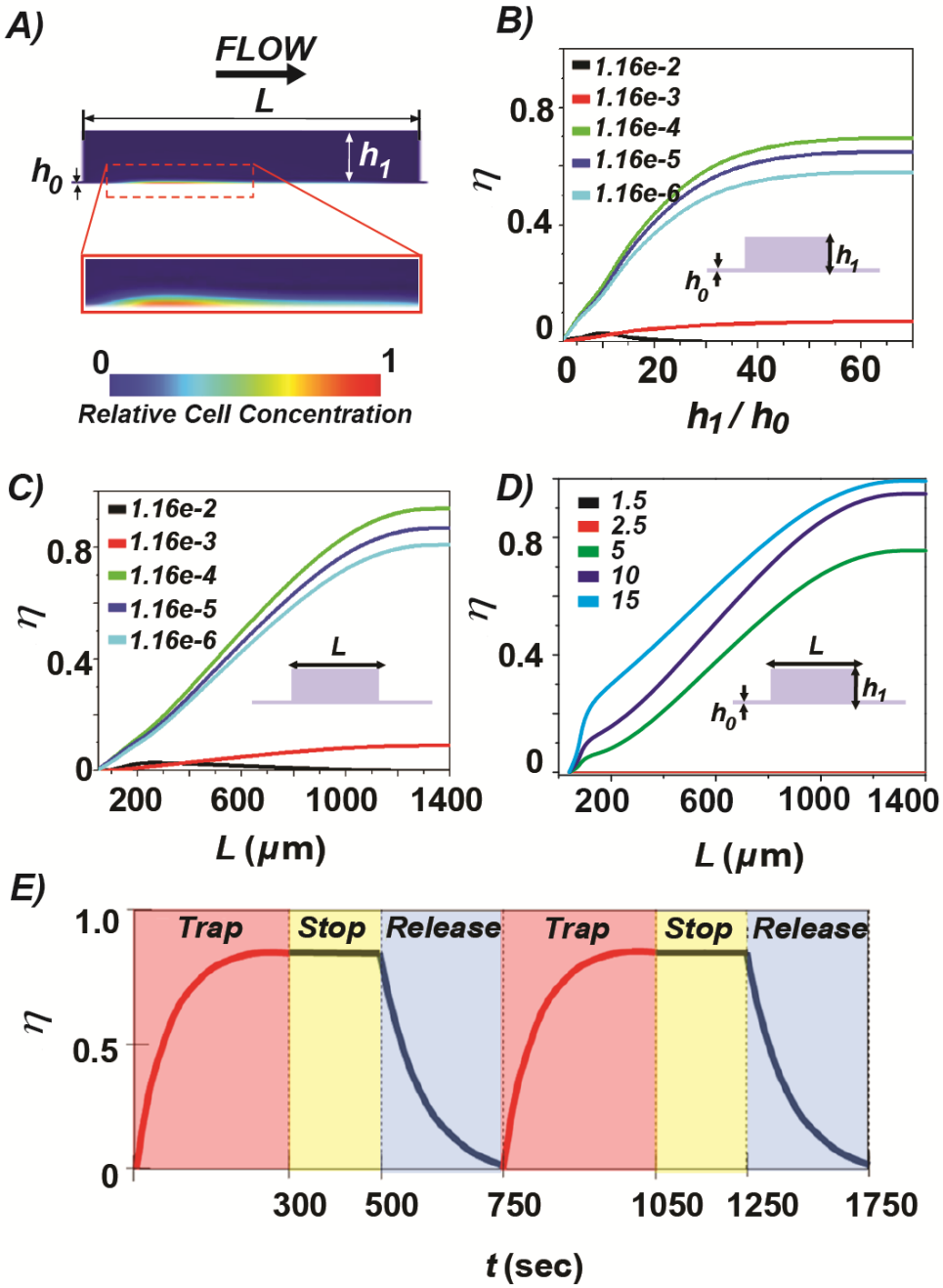

Figure 2.2: Simulation studies on cell trapping in hydraulic jump traps; **A)** representative image of the simulation output, in which the device simulated has a length of 1 mm, a channel height of 20 μm (h_0), and a trap height of 200 μm (h_1) at a u_0 of 1.04 x 10^{-4} m/s. The simulation outputs an increase in the relative cell density in the region where cell trapping occurs. Simulation results are also shown demonstrating trapping efficiency (η) dependence on **(B)** trap length (L), for a normalized trap height (h1/ h0) of 10, and **(C)** on the normalized trap height, for a trap length of 300 μm, for particles with a diameter of 15 μm for various flow velocities u_0 (in the channels). An u_0 of 1.16 x 10^{-4} m/s was found to be optimal for cell trapping in these simulation studies; **D)** Simulation results for cell trapping in hydraulic jump devices. Optimization of trap geometry was investigated using this simulation model by altering two geometric parameters: length (L) and the normalized height (h_1/h_0) of the trap. The simulation results indicate an optimal value of 1,000 μm and 15 respectively at an u_0 of 1.16 x 10^{-4} m/s; **E)** Time resolved cell trapping and releasing steps for h_1/h_0 = 5.0 and L/h_0 = 50, at u_0 (trap) of 1.16 x 10^{-5}m/s, u_0 (stop) of 1.16 x 10^{-5}m/s and u_0 (release) of 1.16 x 10^{-2}m/s, respectively.

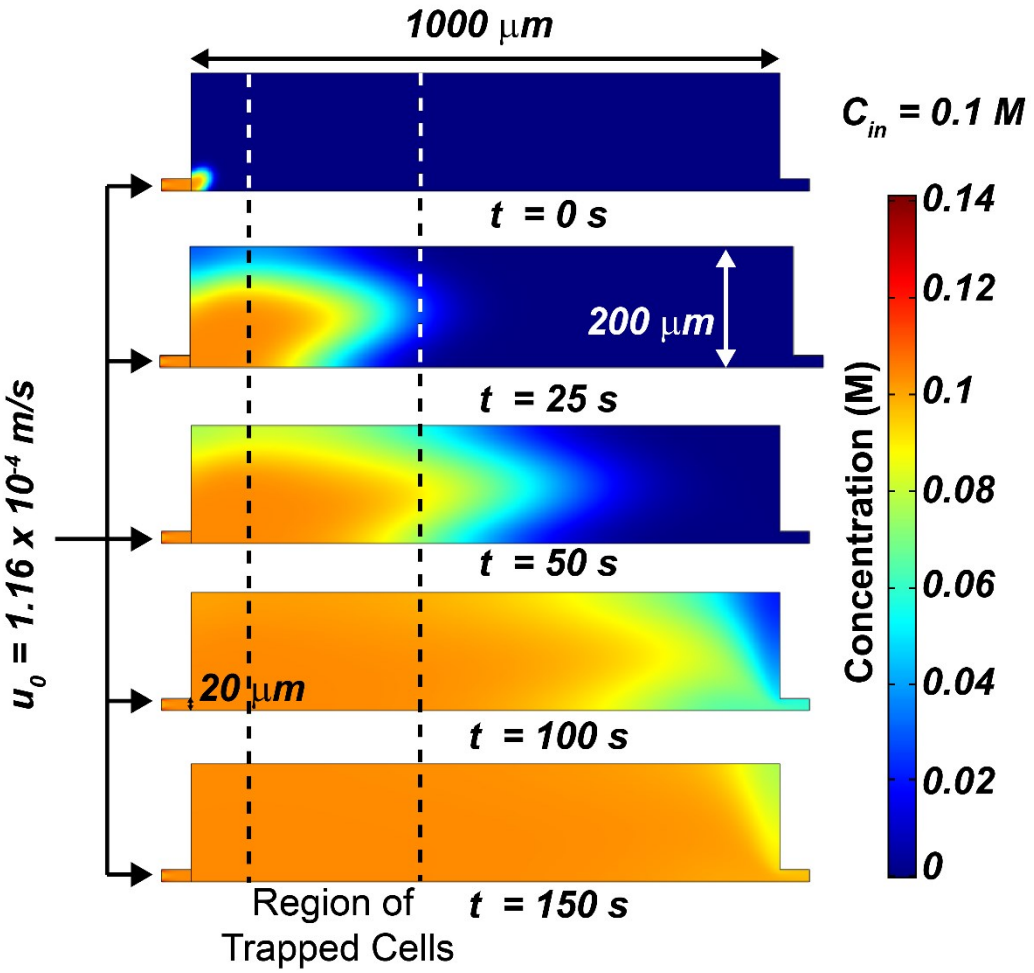

Figure 2.3: Simulation images showing fast mass transport in Hydraulic Jump traps. The time lapse images of the concentration of a molecule (D = 10^{-9} m^2/sec; similar to proteins in solution); being fluxed in from the inlet into the hydraulic jump traps; shows that the desired concentration of the molecule in the microenvironment near trapped cells is reached in about 30 seconds.

2.5 DENSITY EFFECTS ON HYDRAULIC JUMP

The simulation data presented till now assumed that the density of a cell on average is 1.033 g/cm^3. Although the density of the cells does vary around this mean, the results from the simulation (in terms of the optimization of trapping efficiencies) agree well with the bulk behavior of the cells (as shown in the next chapter). Single-cell density, however, is an important indicator of many biological states and can be useful in diagnosing various diseases. The exact value of cell density is dynamic and therefore, it is challenging to definitively state the density of a single cell. Current lab techniques demonstrated to measure single cell density mostly employ a suspended micro-channel resonator (42–46), which requires a small cantilever that resonates at different frequency for single cells with different densities. Some adaptations of this technique also require a combination of two fluids of different density and a silicon cantilever contained within the micro-fabricated device (44). An alternate technique for measuring single cell density that we wanted to explore was with the use of the microscale hydraulic jump phenomenon. The

equations of motion of the cells (Section 2.4) indicate a dependence on the density of the cells. Hence if this dependence can be quantified, then this correlation can be used to back calculate the density of cells provided their motion is measured.

To compute this correlation between the particle path parameters and the particle density, COMSOL 3.5 was used to model several parameters using finite-element analysis. A couple of models were examined for this particular study. One was the two-phase model (particulate phase and continuous phase). The particulate phase represents the particles/cells within the device whereas the continuous phase is the PBS buffer where the particles/cells are suspended in. For this particular model, we were interested in the pathlines of the particles while traversing the hydraulic jump. A range of densities were considered for this study (1000 kg/m^3 to 1100 kg/m^3 with a step size of 10 kg/m^3). The streamlines were plotted in COMSOL and exported into Excel to evaluate the maximum jump height (y_{max}) and the distance (along the trap) where the maximum jump height is achieved (x_{max}). An overlay of representative simulation snapshots are shown in Figure 2.4 a. The different colors of the pathlines indicate the different densities that were simulated. Each family of pathlines represents the average behavior of particles with the same density but different start height in the channel. This was achieved by varying the start height of the pathlines between 7.5 μm and 12.5 μm (the allowable range for the center of 15 μm diameter particles in a 20 μm high channel) with a height resolution between successive heights being 1 μm.

As can be observed from the results, the higher density particles tend to have a lower y_{max} and tend to achieve this height fairly early after entering the trap region. Plots of y_{max} and x_{max} are shown in Figure 2.4 b for different densities and inlet flow velocities. At an u_0 of 1.16x10^{-4} m/s the inverse relationship between density and y_{max}/x_{max} is discernible. Also, the values of x_{max} show a larger range and density resolution (density difference needed to create a statistically significant change in x_{max}) than y_{max}. The differences in the x_{max} values between all the different densities considered here (except between 1090 kg/m^3 and 1010 kg/m^3) were found to be statistically significant with P values (for a one tailed Student T test) less than 0.05. The differences in the ymax values on the other hand were found to be statistically significant only for densities below 1050 kg/m^3. Higher flow velocities were investigated to verify if the density resolution can be increased further (especially in the density range of 1050 to 1100 kg/m^3). Flow velocities, u_0, of 2.32x10^{-4} m/s and 5.8x10^{-4} m/s were considered to evaluate whether an increase in flow velocity can increase the density resolution for densities above 1050 kg/m^3. The simulation results indicate that an increase in flow velocity not only led to an increase in the average values of y_{max} and x_{max} but also to an increase in the variation between the family curves. This in effect reduced the density resolution further. Lower flow velocities were not considered as the reduction in average y_{max} and x_{max} values are going to reduce density resolution irrespective of the variation. Hence this simulation result shows that it is possible to evaluate the density of particles by measuring their motion within the trap region and the density resolution currently is 10 kg/m^3 for densities up to 1090 kg/m^3.

The two-phase model used in the previous work provides the average pathline of the particulate phase, however, in terms of exact particle trajectories; streamline plots are not fully accurate and exact. Therefore, a COMSOL 4.2 a module, Particle Tracing Module along with Laminar Flow Module was used to simulate the exact trajectories of each particle. The Navier Stokes equation for the fluid flow and the particle pathlines were both solved simultaneously in a time-dependent manner to obtain the particle (which is 15 μm in diameter) positions at specific times. The solution was exported to evaluate the x_{max} and y_{max} values for the different densities.

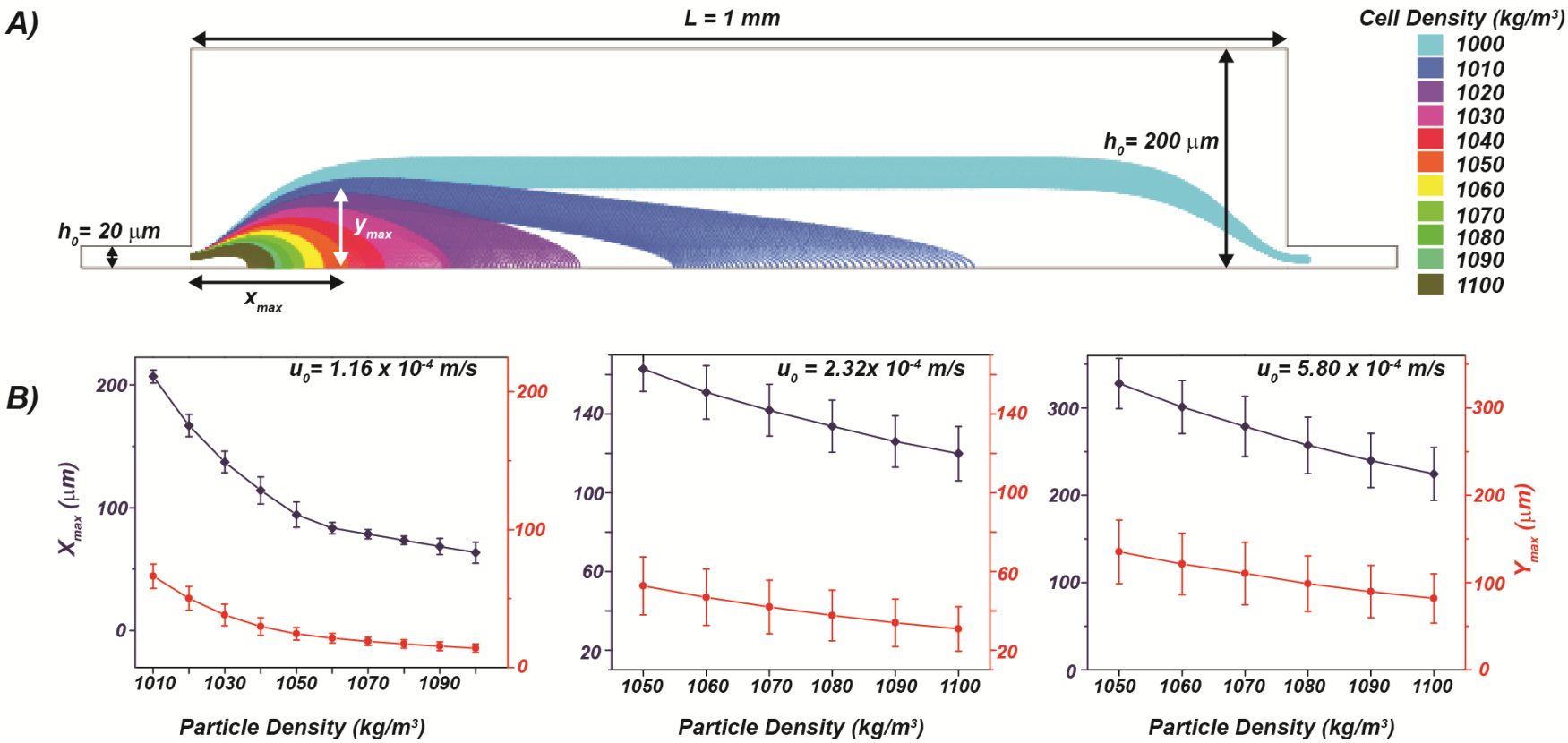

Figure 2.4: Simulation studies on particle motion in hydraulic jump traps using a mixture model; **A)** representative image of the simulation output, in which the device simulated has a length of 1 mm, a channel height of 20 μm (h_0), and a trap height of 200 μm (h_1) at a u_0 of 1.16 x 10^{-4} m/s. The density of the particles (15 μm in diameter) being simulated was varied between 1000 and 1100 kg/m^3. The results indicate a decrease in x_{max} and y_{max} values as the particle density is increased; **(B)** Graphical representation of the simulation results for x_{max} and y_{max} at different inlet flow velocities (u_0). At an u_0 of 1.16 x 10^{-4} m/s a clear decrease in x_{max} and y_{max} values is observed with increasing particle densities. The difference between x_{max} values, between consecutive densities studied was found to be more statistically significant than the ymax values. Higher flow velocities were simulated to evaluate whether higher flow velocities can improve the density resolution at higher densities. However, the results indicate a loss in density resolution at higher flow velocities.

In the particle tracing module, the position of the particle is evaluated by solving the ordinary differential equations in the Newtonian formulation:

$$\frac{d(m_p.\overrightarrow{\boldsymbol{v_P}})}{dt} = \vec{\boldsymbol{F}} \quad \text{-- (5)}$$

$$\frac{d(\vec{\boldsymbol{x}})}{dt} = \overrightarrow{\boldsymbol{v_P}} \quad \text{-- (6)}$$

Where,$\vec{\boldsymbol{x}}$, $\overrightarrow{\boldsymbol{v_P}}$ and $\vec{\boldsymbol{F}}$ are the particle position, particle velocity and external force vectors respectively and m_p is the mass of the particle. The forces on the particle considered in the simulation are the gravity force $\vec{\boldsymbol{F}}_{\boldsymbol{g}}$ and the drag force$\vec{\boldsymbol{F}}_{\boldsymbol{D}}$, which are defined as:

$$\vec{\boldsymbol{F}}_{\boldsymbol{g}} = \frac{m_p\vec{\boldsymbol{g}}(\rho_P - \rho)}{\rho_P} \quad \text{-- (7)}$$

$$\vec{\boldsymbol{F}}_{\boldsymbol{D}} = \frac{18m_p\eta(\vec{\boldsymbol{v}} - \vec{\boldsymbol{v}}_{\boldsymbol{P}})}{\rho_P d_P^2} \quad \text{-- (8)}$$

Where, $\vec{\boldsymbol{g}}$ is gravity vector, ρ_P is the particle density, ρ is the fluid density, $\vec{\boldsymbol{v}}$ is the fluid velocity vector, η is the fluid viscosity and d_P is the particle diameter. The particle fluid interactions were modeled as the momentum force exerted by the particle on the fluid, when the particle experiences a drag force due to the fluid. This net momentum force imposed on the fluid, $\vec{\boldsymbol{F}}_{\boldsymbol{fluid}}$, is distributed over the mesh element corresponding to the particles location. Thus, the momentum force on the fluid is:

$$\vec{\boldsymbol{F}}_{\boldsymbol{fluid}} = \frac{\vec{\boldsymbol{F}}_{\boldsymbol{D}}}{d_{vol}} \quad \text{-- (9)}$$

Where, d_{vol} is the volume of the mesh element where the particle is located.

The results from the simulation using the particle tracing module are shown in Figure 2.5. A representative result for one of the simulation runs depicts the pathlines evaluated by the software (Figure 2.5 a). Plots of y_{max} and x_{max} are shown in Figure 2.5 b for different densities and inlet flow velocities. Both these parameters show an inverse correlation to the particle density similar to that observed using the mixture module. Also, as observed with the mixture model, the x_{max} values gave a better density resolution than the y_{max} values for all the flow rates simulated. At an u_0 of 1.16×10^{-4} m/s, the density resolution for x_{max} values was found to be 10 kg/m^3, for particle densities up to 1050 kg/m^3, and 20 kg/m^3 thereafter till a particle density of 1090 kg/m^3. Higher flow velocities were simulated to evaluate whether the density resolution is improved. Unlike the mixture model, the particle tracing model predicted less variability at higher flow rates and improved the density resolution between 1050 kg/m^3 and 1080 kg/m^3 to 10 kg/m^3 at an u_0 of 5.8×10^{-4} m/s. Hence, the particle tracing model supports the general trend in the results from the mixture model with significant differences. Firstly, it predicts a lower density resolution at higher densities for the lowest flow velocity modeled. Also, it predicts that the increase in flow velocity can improve this lag in density resolution at higher densities.

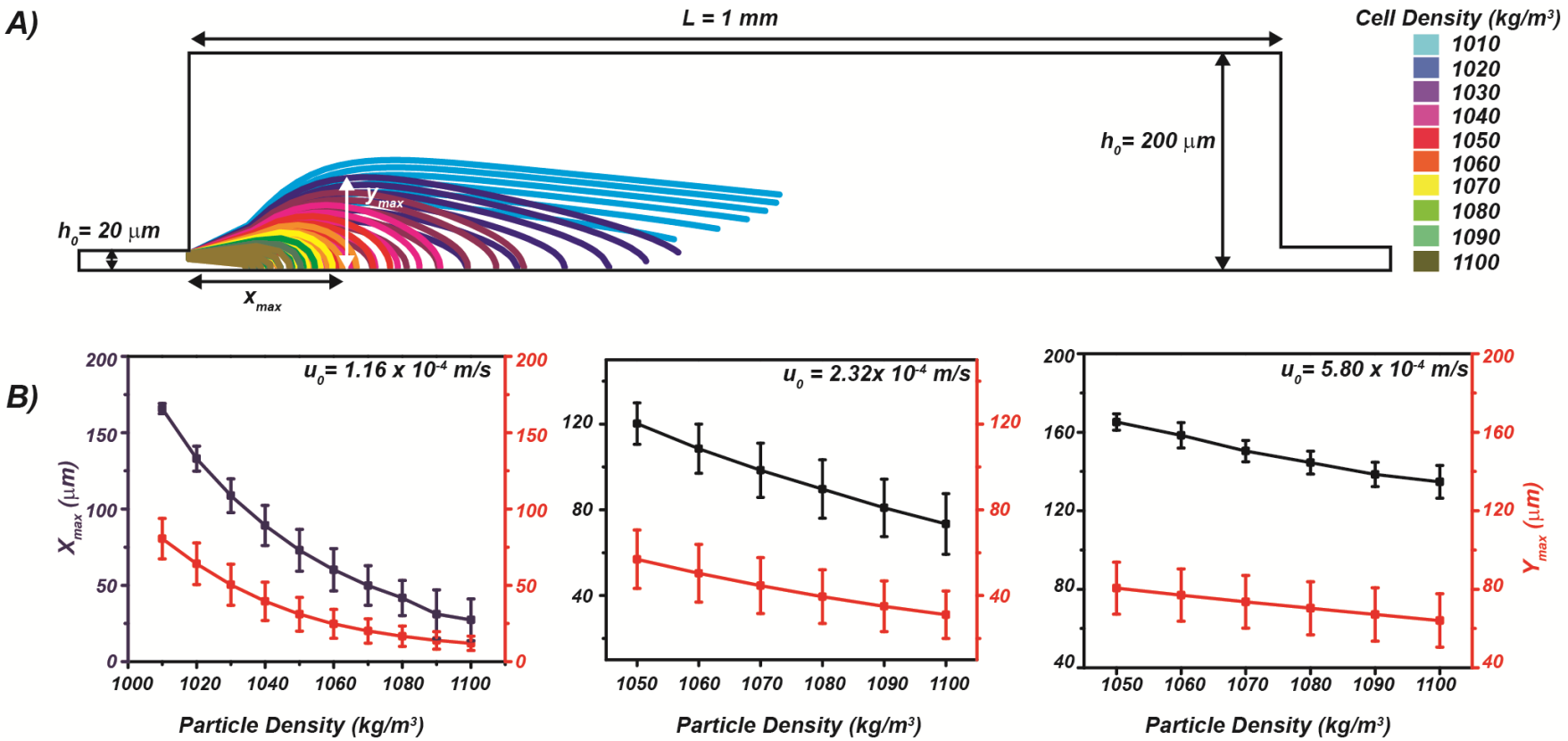

Figure 2.5: Simulation studies on particle motion in hydraulic jump traps using a particle tracing module; **A)** representative image of the simulation output, in which the device simulated has a length of 1 mm, a channel height of 20 μm (h_0), and a trap height of 200 μm (h_1) at a u_0 of 1.16 x 10^{-4} m/s. The density of the particles (15 μm in diameter) being simulated was varied between 1010 and 1100 kg/m^3. The results indicate a decrease in x_{max} and y_{max} values as the particle density is increased. The pathlines for 1010 kg/m^3 do not reach the bottom of the channel during the duration of the time-dependent simulation; **(B)** Graphical representation of the simulation results for x_{max} and y_{max} at different inlet flow velocities (u_0). At an u_0 of 1.16 x 10^{-4} m/s a clear decrease in x_{max} and y_{max} values is observed with increasing particle densities. The difference between x_{max} values, between consecutive densities studied was found to be more statistically significant than the ymax values. The density resolution till 1050 kg/m^3 is 10 kg/m^3 and till 1100 kg/m^3 it is 20 kg/m^3. Higher flow velocities were simulated to evaluate whether higher flow velocities can improve the density resolution at higher densities. The results indicate that u_0 of 5.8 x 10^{-4} m/s can increase the density resolution for higher densities.

2.6 CONCLUSION

In conclusion, we analyzed the hydraulic jump phenomenon at the microscale with applications in particle trap-and-release devices and single cell density measurement. A sudden increase in channel height in the device leads to a significant decrease in flow velocity which in turn causes the trapping of microparticles by energy conversion and force balance at the channel floor. Inversely, the trapped particles are released by increased drag force due to an increase in fluid flow velocity. A systematic, numerical study of microparticle motion in the hydraulic jump cavity is reported here. The trapping efficiency (η_{trap}) increases with trap height (h_1) and trap length (L), while high flow velocity (u_0) resulted in lower η_{trap}. In addition, the motion of the particles within the trap setup was shown to be indicative of the particle density. This provides the possibility of the estimation of particle densities through measurements of the particles pathlines through the trap region. Hydraulic jump-based hydrodynamic trap-and-release method can be integrated into a microfluidic array to selectively control microparticles or living cells for quantitative analysis. It will provide a new platform to manipulate living cells in physiological microenvironments of cell culture media and reagents.

2.7 ACKNOWLEDGEMENTS

I would like to acknowledge Younggeun Park, Yeonho Choi and Bill Kuang for their contribution to this work. I also acknowledge the Biomolecular Nanotechnology Centre (BNC) and Paul Lum for his help and support. Funding for this work was provided by NIH (R01 CA120003-01A2) and the CNMT (2010K000352, 2010K000353, and 2010K000354) of the Ministry of Education, Science and Technology, Korea.

2.8 REFERENCES

1. Nilsson J, Evander M, Hammarström B, Laurell T (2009) Review of cell and particle trapping in microfluidic systems. *Anal Chim Acta* 649:141–157.

2. Lam KS, Liu R, Miyamoto S, Lehman AL, Tuscano JM (2003) Applications of One-Bead One-Compound Combinatorial Libraries and Chemical Microarrays in Signal Transduction Research. *Acc Chem Res* 36:370–377.

3. Neher E, Sakmann B (1976) Single-channel currents recorded from membrane of denervated frog muscle fibres. *Nature* 260:799–802.

4. Toner M, Irimia D (2005) Blood-on-a-Chip. *Annual Review of Biomedical Engineering* 7:77–103.

5. Winssinger N, Ficarro S, Schultz PG, Harris JL (2002) Profiling protein function with small molecule microarrays. *PNAS* 99:11139–11144.

6. Petersson F, Aberg L, Sward-Nilsson A-M, Laurell T Free flow acoustophoresis : Microfluidic-based mode of particle and cell separation. *Analytical chemistry* 79:5117–5123.

7. Abou Neel EA, Palmer G, Knowles JC, Salih V, Young AM (2010) Chemical, modulus and cell attachment studies of reactive calcium phosphate filler-containing fast photo-curing, surface-degrading, polymeric bone adhesives. *Acta Biomaterialia* 6:2695–2703.

8. Schnelle T, Hagedorn R, Fuhr G, Fiedler S, Müller T (1993) Three-dimensional electric field traps for manipulation of cells — calculation and experimental verification. *Biochimica et Biophysica Acta (BBA) - General Subjects* 1157:127–140.

9. Hohne DN, Younger JG, Solomon MJ (2009) Flexible Microfluidic Device for Mechanical Property Characterization of Soft Viscoelastic Solids Such as Bacterial Biofilms. *Langmuir* 25:7743–7751.

10. Gijs MAM (2004) Magnetic bead handling on-chip: new opportunities for analytical applications. *Microfluidics and Nanofluidics*. Available at: http://infoscience.epfl.ch/record/55909 [Accessed March 29, 2013].

11. Ashkin A, Dziedzic JM, Yamane T (1987) Optical trapping and manipulation of single cells using infrared laser beams. *Nature* 330:769–771.

12. Carlo DD, Lee LP (2006) Dynamic Single-Cell Analysis for Quantitative Biology. *Anal Chem* 78:7918–7925.

13. Davidsson R et al. (2004) Microfluidic biosensing systems. Part II. Monitoring the dynamic production of glucose and ethanol from microchip-immobilised yeast cells using enzymatic chemiluminescent micro-biosensors. *Lab Chip* 4:488–494.

14. Kane RS, Takayama S, Ostuni E, Ingber DE, Whitesides GM (1999) Patterning proteins and cells using soft lithography. *Biomaterials* 20:2363–2376.

15. Chang WC, Lee LP, Liepmann D (2005) Biomimetic technique for adhesion-based collection and separation of cells in a microfluidic channel. *Lab on a Chip* 5:64.

16. Basabe-Desmonts L et al. (2010) Single-Step Separation of Platelets from Whole Blood Coupled with Digital Quantification by Interfacial Platelet Cytometry (iPC). *Langmuir* 26:14700–14706.

17. Huh D et al. (2007) Gravity-Driven Microfluidic Particle Sorting Device with Hydrodynamic Separation Amplification. *Anal Chem* 79:1369–1376.

18. Huang LR, Cox EC, Austin RH, Sturm JC (2004) Continuous Particle Separation Through Deterministic Lateral Displacement. *Science* 304:987–990.

19. Khabiry M et al. (2009) Cell Docking in Double Grooves in a Microfluidic Channel. *Small* 5:1186–1194.

20. Manbachi A et al. (2008) Microcirculation within grooved substrates regulates cell positioning and cell docking inside microfluidic channels. *Lab on a Chip* 8:747.

21. Di Carlo D, Wu LY, Lee LP (2006) Dynamic single cell culture array. *Lab Chip* 6:1445–1449.

22. Di Carlo D, Aghdam N, Lee LP (2006) Single-Cell Enzyme Concentrations, Kinetics, and Inhibition Analysis Using High-Density Hydrodynamic Cell Isolation Arrays. *Anal Chem* 78:4925–4930.

23. Wu LY, Di Carlo D, Lee LP (2008) Microfluidic self-assembly of tumor spheroids for anticancer drug discovery. *Biomed Microdevices* 10:197–202.

24. Tan W-H, Takeuchi S (2007) A trap-and-release integrated microfluidic system for dynamic microarray applications. *Proc Natl Acad Sci U S A* 104:1146–1151.

25. Seo J, Ionescu-Zanetti C, Diamond J, Lal R, Lee LP (2004) Integrated multiple patch-clamp array chip via lateral cell trapping junctions. *Applied Physics Letters* 84:1973–1975.

26. Ionescu-Zanetti C et al. (2005) Mammalian electrophysiology on a microfluidic platform. *PNAS* 102:9112–9117.

27. Lau AY, Hung PJ, Wu AR, Lee LP (2006) Open-access microfluidic patch-clamp array with raised lateral cell trapping sites. *Lab on a Chip* 6:1510.

28. Lee PJ, Hung PJ, Lee LP (2007) An artificial liver sinusoid with a microfluidic endothelial-like barrier for primary hepatocyte culture. *Biotechnology and Bioengineering* 97:1340–1346.

29. Lee PJ, Hung PJ, Rao VM, Lee LP (2006) Nanoliter scale microbioreactor array for quantitative cell biology. *Biotechnology and Bioengineering* 94:5–14.

30. Hung PJ et al. (2005) A novel high aspect ratio microfluidic design to provide a stable and uniform microenvironment for cell growth in a high throughput mammalian cell culture array. *Lab on a Chip* 5:44.

31. Lee PJ, Hung PJ, Shaw R, Jan L, Lee LP (2005) Microfluidic application-specific integrated device for monitoring direct cell-cell communication via gap junctions between individual cell pairs. *Applied Physics Letters* 86:223902.

32. Yang J, Li C-W, Yang M (2004) Hydrodynamic simulation of cell docking in microfluidic channels with different dam structures. *Lab on a Chip* 4:53.

33. Khademhosseini A et al. (2004) Molded polyethylene glycol microstructures for capturing cells within microfluidic channels. *Lab on a Chip* 4:425.

34. Kim SM, Lee SH, Suh KY (2008) Cell research with physically modified microfluidic channels: A review. *Lab on a Chip* 8:1015.

35. Ochsner M et al. (2007) Micro-well arrays for 3D shape control and high resolution analysis of single cells. *Lab Chip* 7:1074–1077.

36. Revzin A, Sekine K, Sin A, Tompkins RG, Toner M (2005) Development of a microfabricated cytometry platform for characterization and sorting of individual leukocytes. *Lab on a Chip* 5:30.

37. Park Y, Choi Y, Mitra D, Kang T, Lee LP (2010) Study of microscale hydraulic jump phenomenon for hydrodynamic trap-and-release of microparticles. *Appl Phys Lett* 97. Available at: http://www.ncbi.nlm.nih.gov/pmc/articles/PMC2973986/ [Accessed July 8, 2012].

38. Krishnamoorthy S, Bedekar AS, Feng J, Sundaram S (2007) Simulation-Based Analysis of Fluid Flow and Electrokinetic Phenomena in Microfluidic Devices. *Clinics in Laboratory Medicine* 27:41–59.

39. Kim M-C, Wang Z, Lam RHW, Thorsen T (2008) Building a better cell trap: Applying Lagrangian modeling to the design of microfluidic devices for cell biology. *Journal of Applied Physics* 103:044701–044701–6.

40. Luo C et al. (2007) The combination of optical tweezers and microwell array for cells physical manipulation and localization in microfluidic device. *Biomedical Microdevices* 9:573–578.

41. Mrksich M (2000) A surface chemistry approach to studying cell adhesion. *Chemical Society Reviews* 29:267–273.

42. Bryan AK, Goranov A, Amon A, Manalis SR (2010) Measurement of mass, density, and volume during the cell cycle of yeast. *PNAS* 107:999–1004.

43. Burg TP et al. (2007) Weighing of biomolecules, single cells and single nanoparticles in fluid. *Nature* 446:1066–1069.

44. Grover WH et al. (2011) Measuring single-cell density. *PNAS* 108:10992–10996.

45. Park K et al. (2008) "Living cantilever arrays" for characterization of mass of single live cells in fluids. *Lab Chip* 8:1034–1041.

46. Godin M et al. (2010) Using buoyant mass to measure the growth of single cells. *Nat Meth* 7:387–390.

CHAPTER 3

Microfluidic Hydraulic Jump For Cell Trap And Release

3.1 ABSTRACT

Cell trap and release in microfluidic devices is an important component for the realization of systems capable of studying cellular phenotype and function. Dynamic control of trap and release in microsystems is also critical for the purposes of cell pre-concentration and cell-based microarrays. However, mechanical trapping modalities often lack a 'trap and release' function and most trapping mechanisms are abrasive to cells. Here, a hydrodynamic cell 'trap and release' technique is presented, which employs principles similar to the 'hydraulic jump' phenomenon found in nature. The trap is a region of channel expansion where the interplay between fluidic drag forces, on the cells, and the cellular adhesion forces lead to cellular trapping or release. This modality enables non-abrasive cell trapping, hydrodynamic control of cell trap and release, and provides convection-based mass transfer to the captured cells. Characterization and numerical investigation of the device revealed that both gravity and non-specific cellular adhesion forces have a major role in the trapping of cells. The optimal device design described herein has very high (>90%) cell trapping efficiencies at low flow rates (u_0 = 1.04 x 10^{-4} *m/s*) and releases more than 75% of trapped cells at high flow rates (u_0 = 5.2 x 10^{-3} *m/s*). Additionally, a viability assay was performed and demonstrates the fluid exchange capability of this device and the stability and viability of the trapped and released cells. This 'trap and release' modality provides a new platform to analyze and manipulate living cells in physiologically relevant microenvironments.

3.2 INTRODUCTION

The biophysical and biochemical study of cells is of utmost interest in basic biology and medical science. Microfluidic chips enable complicated physical and chemical procedures in a time- and power-efficient manner while incurring very low production and operation costs. Micro Total Analysis Systems (μTAS) are systems based on such microfluidic designs for use in chemical and biological analysis systems (1–5). While microfluidic cellular research started with analysis of cellular sub-systems and components, it has shifted towards the analysis of living, intact cells and their interactions. A very important component in microfluidic devices designed for these cellomic and biosensor studies is the ability to trap and analyze cells (6, 7). Recently, there also has been interest in cell 'trap and release' devices that enable on-chip cell pre-concentration, dynamic analysis, and post-experimental cell collection (8).

At present, the major techniques used for cell trapping in a microfluidic device are mechanical (e.g. filters), adhesion-based (9), electrical (e.g. dielectrophoresis) and optical (6, 7, 10). Researchers have also developed hybrid electrical-mechanical traps (10) and optical-mechanical traps (11). Of the present techniques, mechanical cell traps are the most common technique to trap cells in microfluidic devices, as they are generally easier to fabricate, use, and require less equipment and materials.

Mechanical trapping can be divided into constriction-based and expansion-based systems. Constriction based mechanical cell traps are quite common and have been used in different forms such as C-shaped rings with micro sieves (12), perpendicular dams, and parallel dams (13). However, constriction-based cell immobilization imposes a high shear stress on the trapped cells. According to a simulation study done by Yang et al., the pressure drop across a dam with a 2 μm constriction, perpendicular to the channel, can be greater than 50% of the total hydraulic pressure difference between the two ends of the micro channels (13). Such high pressures in the constricted regions of the mechanical trap can lead to pressure induced changes in the cells that ultimately can affect the study. Dams parallel to the flow channels do not impose such high pressures; however, no more than a single layer of cells can be trapped due to the cross flow (13). On the other hand, micro-wells are an expansion-based technique for cell immobilization that can potentially overcome the deficiencies in constriction-based mechanical traps (14). Cell trapping in micro-wells occurs by gravity-based sedimentation (15, 16). The sudden expansion in the channel leads to reduced flow rates, allowing cells to sediment and be trapped even in the presence of a shear flow without adverse stresses on the cells (14, 17). Even though micro-wells for single cell capture have been optimized by Revzin et al. (15), the drawbacks of micro-well trapping include the inability to release trapped cells and quickly exchange reagents in the well, as mass transfer properties are diffusion-limited. Warrick et al. have developed a sedimentation-based mechanical cell trap that allows faster mass transfer to the cells and has been demonstrated for use as a cell concentrator (18). Such developments in expansion and constriction-based trapping technologies will advance and enable a number of cell-based applications. A common drawback these trapping techniques have is the lack of a 'release' modality. Recent single cell 'trap and release' work by Tan and Takeuchi utilized constriction based cell trapping and local bubble generation by a laser or heater to release trapped cells (8). However, the various instrumentation and components required hinder ease of use and adaptation. Braschler et al. developed a trap and release modality using alginate hydrogel as the trapping matrix (19). Decreasing the calcium concentration shrunk the hydrogel and enabled release of cells trapped within the hydrogel. However, due to the diffusion limited mechanism of release, the response time of the device is large (~10 min), prolonging the time of the assay. In this work, we have designed and optimized an effective mechanical cell trap and release device that overcomes these drawbacks of the other modalities.

The 'hydraulic jump' phenomena, observed in nature, can be applied at the micron scale for the hydrodynamic trap and release of cells in solution (20). A sudden vertical channel expansion in our microfluidic device leads to a decrease in flow velocity that causes cells to get trapped in the expanded region (Figure 3.1). The trapped cells can then be released by simply increasing the flow velocity, thus allowing hydrodynamic control over the trap and release of cells with high cell viability. This technique is gentle and flow streamlines are in the plane of cell trapping, facilitating rapid mass transfer of nutrients and assay analytes through convective mass transfer. We used two breast cancer cell lines, BT474 and T47D, and one cervical cancer cell line, HeLa, for this study. Notably, the principle of 'trap and release' can also be applied to other adherent cell lines.

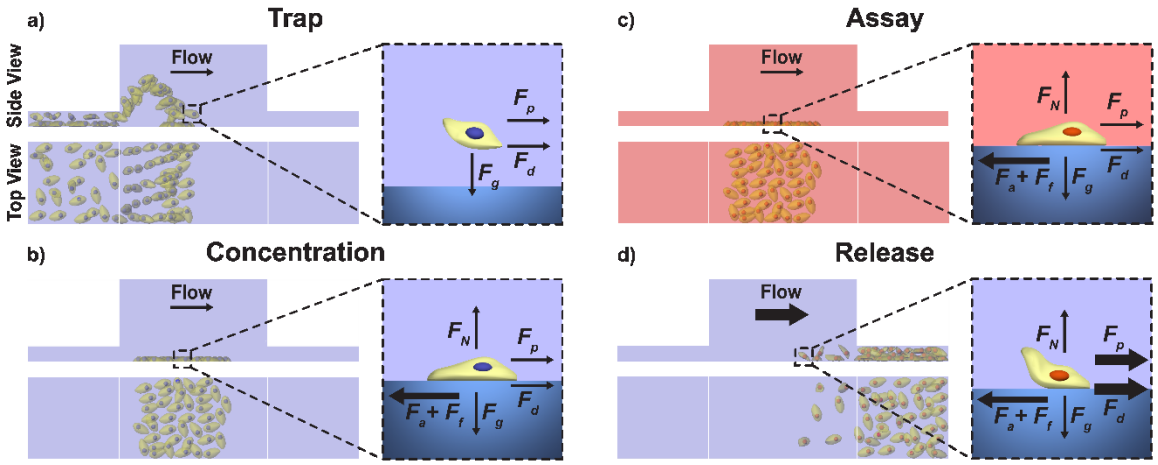

Figure 3.1: Microfluidic hydraulic jump phenomenon for cell trap and release; **A)** Cells are loaded into the microfluidic device where the fluid drag and pressure forces (F_d and F_p) in the channel pull the cells along; **B)** The trap is a region of channel expansion, wherein the fluid velocity and hence the fluid pressure and drag forces get reduced. The cells settle down due to gravitational forces (F_g) and surface retardation forces (adhesion, F_a, and friction, F_f) balance the fluid drag forces and result in trapping of these cells; **C)** The buffer in the device can then be changed to an assay reagent, and as long as the fluid velocity is constant, the trapped cell would remain trapped and exposed to the reagents; **D)** And finally the trapped cells can be released by increasing the fluid velocity, and hence the fluid drag forces, resulting in the release of the treated cells.

3.3 Observing the Microscale Hydraulic Jump

Conventional phase contrast/bright-field microscopy is ill suited for the experimental observation of the "hydraulic jump". These techniques generate a "top-down" view of the microfluidic trap region at a given focal depth and any changes in the height of the microparticles manifests itself in the slight loss in focus of the particles. Hence, the optimal setup for the experimental observation of the microscale hydraulic jump phenomenon will generate a "side" or lateral view of the traps. For this purpose, we built a custom setup for the lateral imaging of the PDMS microchannels and traps through the sidewalls of the PDMS device. Such imaging necessitated very smooth PDMS side walls. This was achieved using a special manifold where polished and smooth silicon pieces were used to mold the sidewalls of the PDMS device (Appendix Figure A.1). The imaging setup was built by rotating the axis of a standard non-inverted microscope by 90° (Figure 3.2 a). A stage, fitted with a slide holder and connected to a micromanipulator, was aligned and situated in front of the objectives. The PDMS device was illuminated using a fiber optic light source positioned in line with the objectives. Images of microparticle behavior were taken with a camera attached to one of the microscope eyepieces and measurements were made by analyzing the images in ImageJ. A representative image of the hydraulic jump trap taken using the lateral viewing setup is shown in Figure 3.2 b. The image consists of three images taken at different parts of the trap region with a 20x objective and stitched in ImageJ. The image shows the capability of the system to image microfluidic structures from the side. Interestingly, the walls of the trap region show ripple like patterns which are commonly seen in thick SU-8 structures like the mold used for making this device. The scale bar was set using a height standard and analyzing its lateral image using ImageJ. Experiments performed using beads of fixed densities exhibited flow profiles similar to simulation results presented in the previous chapter (Appendix Figure A.2).

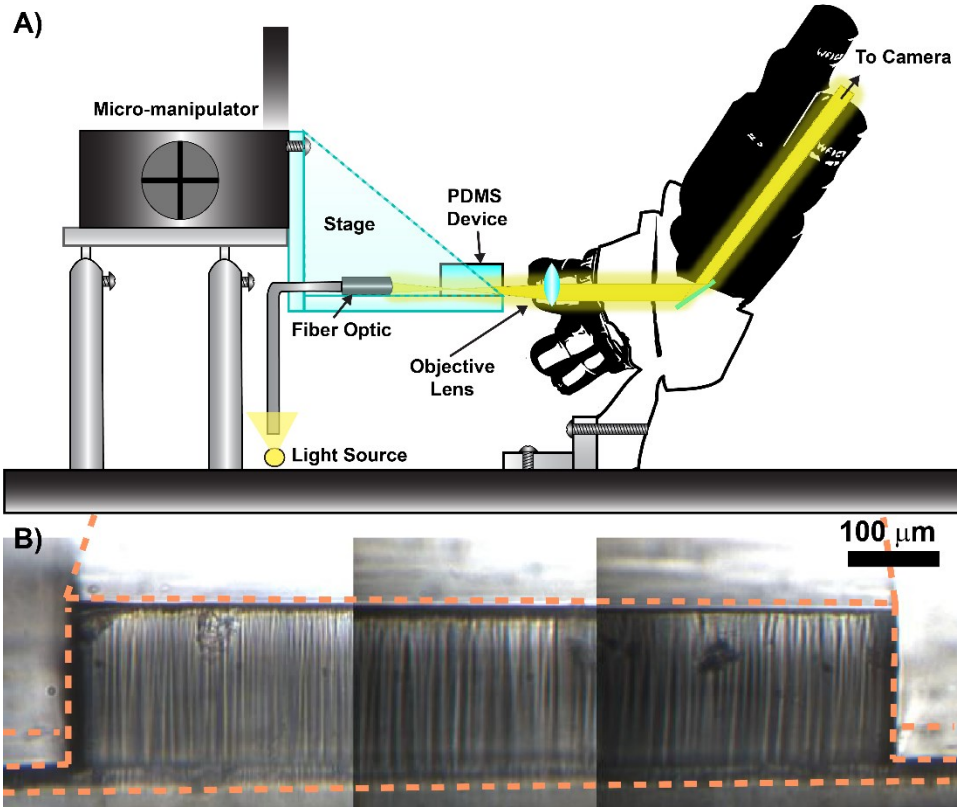

Figure 3.2: Custom setup built for the lateral observation of microfluidic devices; **A)** Sketch showing the setup with the various components. A traditional non-inverted microscope was hacked into two and only the optical elements were placed at a 90° angle on top of an optical table. A micromanipulator (x-y-z motion capable) was modified by attaching to it an acrylic stage (with a slide holder) with a via hole for the fiber optic light source. The micromanipulator was held at the optical table using height adjustable mounting rods and controlled using a joystick console. The light path (shown in the figure) is through the PDMS device and into the microscope optics before finally emerging through the eye piece and captured with a camera; **B)** a stitched image of the hydraulic jump trap imaged using a 20x objective.

3.4 CELL TRAPPING IN HYDRAULIC JUMP CELL TRAPS

The operating principle behind cellular trap and release in the hydraulic jump traps is shown in Figure 3.1. The cell solution being perfused through the device enters the trap, which is a region of channel expansion, where the fluid flow rate is suddenly reduced. Consequently the cells initially rise up and then sediment downward due to gravity (Figure 3.1a). The cells which sediment are immobilized by friction and non-specific adhesion forces, leading to an increase in concentration of the cells near the trap floor (Figure 3.1b). These trapped and spatially concentrated cells can now be exposed to different chemical stimuli by changing the buffer composition (Figure 3.1c). As long as the flow rate in the device is not changed, this buffer exchange will not result in the loss of cells from the trap region. When the perfusion rate, and hence fluid drag force, is increased the retardation forces are not sufficient to trap the cells and cell release occurs (Figure 3.1d). Experimental verification of the simulation results (presented in the previous chapter) was performed using traps with a square cross section ($L = W$), u_0 of 1.04 x 10^{-4} m/s in the channel, and varying L and h_1/ h_0. The 'hydraulic jump' traps were fabricated using standard soft lithography with Polydimethylsiloxane (PDMS) and their capability to trap cells was tested. A two layered SU-8 (MicroChem Corp.) mold was first fabricated on a silicon

wafer using contact lithography processes. The requisite heights were obtained with a tolerance of around 10%. The mold was then hard baked and silanized using Trichloro(1H,1H,2H,2H-perfluorooctyl)silane (Sigma Aldrich). PDMS (Dow Corning Corp.) base and curing agents were mixed in a ratio of 10:1, degassed, and poured on top of the mold. Once the PDMS was cured, it was peeled off and the inlets and outlets were punched. This PDMS device was then bonded to a glass surface using O_2 plasma (20 W, 30 sec, 0.2 Torr). The different mammalian cells to be tested were harvested from confluent cell culture dishes using standard trypsinization protocols. In short, the culture dishes were exposed to 0.25% Trypsin (HyClone) for 5 min. The Trypsin was then inactivated using fetal bovine serum in DMEM media (GIBCO). The solution was then centrifuged to pellet the cells, which were resuspended in Phosphate Buffered Saline (PBS) to the required cell concentration.

To evaluate the trapping efficiency of the cells in the various devices, the bonded devices were first primed using PBS (pH 7.2-7.4). Once the device was completely filled, the mammalian cell solution ($0.25 – 2.5 \times 10^6$ cells/ml) was perfused through the device at various flow rates. Cell trapping was observed and recorded using a Nikon inverted microscope. The recorded videos were later analyzed using the ImageJ software (http://rsbweb.nih.gov/ij/). The trapping efficiency (η) was defined as either:

$$1 - \left[\frac{Average\ Outlet\ Cell\ Density}{Average\ Inlet\ Cell\ Density}\right]_{Over\ 5\ minutes} \quad \text{-- (1)}$$

Or

$$1 - \left[\frac{Number\ of\ cells\ leaving\ trap}{Number\ of\ cells\ entering\ trap}\right]_{Over\ 5\ minutes} \quad \text{-- (2)}$$

The measurement was performed over 5 min to ensure that transient variations were minimal between devices and runs.

Videos of cell trapping were taken with a camera attached to one of the microscope eyepieces in the lateral viewing setup described above and measurements were made by analyzing the videos in ImageJ. The lateral view of the trapping process and the cell trajectory is shown as a series of superimposed time-lapsed images in Figure 3.3a for a device with an h_0 of 20 μm, h_1 of 200 μm and $L = W$ of 1000 μm. The images show the cells 'jump' and gain height as they enter the trap, validating our hydraulic jump hypothesis. Figure 3.3a also shows phase contrast transverse ('bottom-up') images, before and after cell trapping, of the 'hydraulic jump' traps with continuous fluid perfusion. Time lapse transverse images showing cell trapping is available in Appendix Figure A.4. The trajectory of the cells was analyzed for three different cell types (Figure 3.3b). The analysis shows that there is significant differences in the trajectories amongst cells of the same type, which indicates heterogeneity in density, shape, and size within a given cell population. Most of the cells settled down between 100 and 400 μm from the trap inlet forming a band of concentrated cells visible in the transverse view.

Different trap geometries were evaluated for their trapping efficiencies using the HeLa cell line. The experimental data (Figure 3.3c) was found to follow the overall simulation trends, although there were discrepancies most likely due to some of the assumptions made for the simulation studies. We assumed that there is a constant adhesion force at the substrate surface, while such non-specific adhesion forces are more likely to be multi-parametric. Also, the

simulation model was 2D in nature (the width of the trap and channel was assumed to be semi-infinite). However, the actual devices had a finite channel width ($W >> h_0$), which can contribute to deviation between experimental and simulation data. The difference in experimentally observed η between h_1/ h_0 of 10 and 15 was found to not be statistically significant, thus we decided to work with h_1/ h_0 of 10 to decrease fabrication time. We concluded that the optimal trap design (with η > 90%) had L of 1,000 μm, h_1/ h_0 of 10, and an u_0 of 1.04 x 10^{-4} m/s in the channel (or a flow velocity, u_1, of 1.04 x 10^{-5} m/s in the trap region).This optimal geometry exhibited high η (>90%) for both BT474 and T47D cell lines as well.

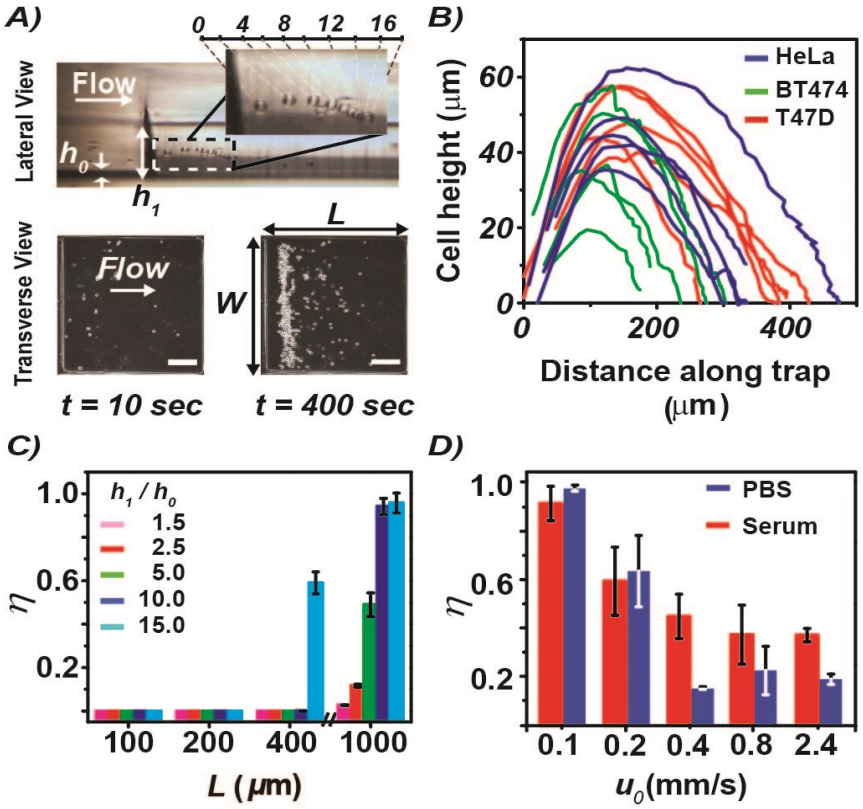

Figure 3.3: Cell trapping in hydraulic jump traps; **A)** Experimental observation of BT474 cell trapping; lateral (side) view of the trapping process was taken in bright-field using a custom microscope and the transverse (bottom-up) view was taken in phase contrast showing cell trapping over ~5 minutes. Time-lapsed lateral images of the cell were superimposed to generate its trajectory (top inset) showing the cells rise upward upon entry into the trap and subsequently settle downward onto the trap floor; **B)** The trajectory of three different cell types generated through lateral viewing of the cell trap; **C)** Optimization of trap geometry for cell trapping; cell trapping efficiencies (η) for different trap lengths (L) and normalized trap heights (h_1/ h_0) at a trapping velocity u_0 (in the channel) of 1.04 x 10^{-4} m/s. The data suggests that the optimal geometry for cell trapping is L of 1,000 μm and h_1/ h_0 of 10; **D)** The inverse relationship between η and u_0 observed for BT474 cell (suspended in PBS or Serum) trapping; device dimensions are the optimal geometries as determined from (C). All error bars in the figure indicate standard deviation for n=3 experiments.

We also tested the effect that the u_0 has on the trapping efficiency (for BT474 cells in Figure 3.3d and HeLa cells in Appendix Figure A.5). As we increased u_0, η decreases in accordance with our hypothesis and verifies the hydrodynamic control on trapping efficiency that we expect with the trap. In Figure 3.3d, Phosphate Buffered Saline (PBS, pH 7.4) and serum (10% in DMEM media) were tested as the suspension solution to compare the effect that crude samples

with excess proteins would have on BT474 cell trapping efficiency. No significant difference was seen at the optimal flow velocity (u_0 of 1.04 x 10^{-4} m/s), but at higher velocities serum improved η. This is possibly due to the presence of higher amounts of non-specific proteins, which make the surface more adhesive for cells. The optimized hydraulic jump trap can hence trap and concentrate >90% of cells in a crude biological sample.

3.5 Effect of Cellular Adhesion on Cell Trapping

To better understand the microfluidic 'hydraulic jump' phenomenon, we verified the importance of non-specific cellular adhesion for cellular trapping in the device. The adhesion forces between HeLa cells and surfaces coated with various concentrations of Bovine Serum Albumin (BSA) were measured using a shear flow assay. A microfluidic device was fabricated with multiple parallel channels 20 μm in height without the hydraulic jump trap. Cells were loaded into these channels and allowed to settle to the floor of the device for 10 minutes. Phase contrast images of the channels were then acquired. Next, PBS was perfused through the channels at different flow rates (different shear rates) for 5 minutes. Images of the channels were taken after perfusion and compared with the images acquired before perfusion. This method analyzes the resistance of the adhered cells to shear stress induced displacement. If a larger percentage of the cells were retained within the channels, the strength of non-specific adhesion forces between the cells and the surface can be deduced to be stronger. O_2 plasma treated glass had the greatest adhesion force at low u_0 (Figure 3.4a). However, 5% BSA treated glass (also plasma bonded) had lower cellular adhesion force. BSA is known to reduce protein adsorption to surfaces (and is used routinely for blocking surfaces); hence non-specific adhesion forces were reduced between the cells and glass. Cell trapping efficiency was measured using BSA treated devices to observe the effect of surface adhesion on hydraulic jump trapping. The results in Figure 3.4b reveal that reduced adhesion forces on the surface reduce cell trapping efficiency at the optimal trapping condition. This affirms the role that non-specific adhesion forces have in cell trapping in the 'hydraulic jump' cell traps. Residual trapping at higher velocities can be attributed to other forces such as friction.

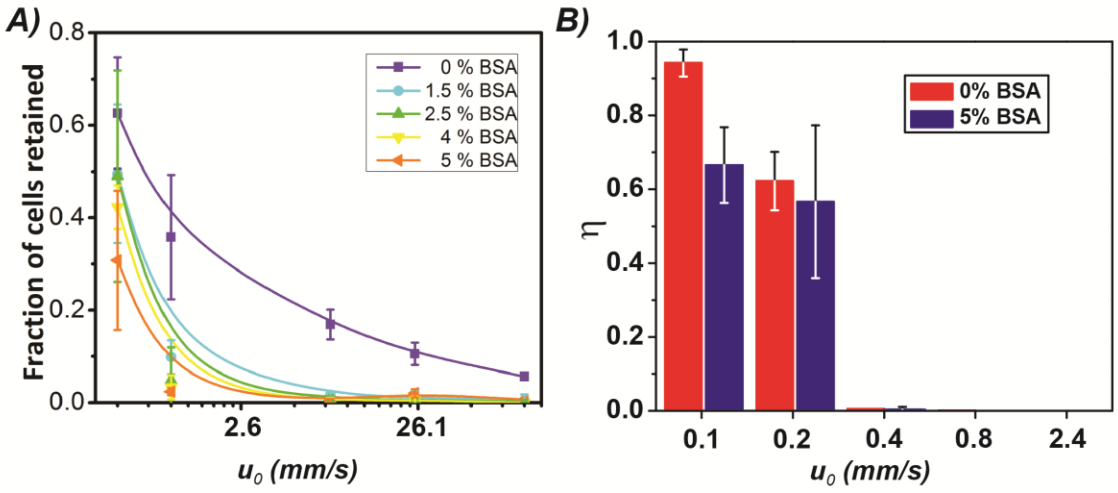

Figure 3.4: Evaluating the importance of non-specific cellular adhesion forces for cell trapping in the hydraulic jump devices; **A)** BSA treatment reduces the non-specific adhesion forces between *HeLa* cells and the glass surface of the device. A microfluidic channel was treated with different concentrations of BSA and cells were loaded into the channel and allowed to settle and adhere to the surface for 5 minutes. Afterwards, buffer at different *Re*

(different shear rates) was perfused through the channels and the number of cells left in the channels was calculated. This ratio would be proportional to the non-specific adhesion forces between the cells and the BSA treated channels. The adhesion force is less for BSA treated devices than for untreated devices; **B)** The graph depicts the trapping efficiency of *HeLa* cells within a microfluidic device bonded to a glass slide at different u_0 for untreated channels (red) and channels treated with 5% BSA. The error bars indicate standard deviation for 3 independent experiments. It was observed at the optimal trapping u_0 that reduction in non-specific adhesion forces due to BSA treatment of the channel surface led to a reduction in cell trapping efficiency.

3.6 CELL TRAP-AND-RELEASE IN HYDRAULIC JUMP TRAPS

Figure 3.5a demonstrates the idea of trap and release in the 'hydraulic jump' traps. The graph plots the percentage of the maximum number of cells in the trap as a function of time. This graph has three distinct regions: the two regions to the left are for lower perfusion rate (u_0 = 1.04 x 10^{-4} m/s) where cell trapping takes place, resulting in an increase in the number of visible cells in the traps, that plateaus in the second region (when the inlet cell concentration was reduced to zero) and the third region depicts a higher flow rate (u_0 ~ 5.2 x 10^{-3} m/s) used for cell release (consequently with a sudden drop in the number of cells to about 10% of maximum). The solid line in the graph indicates simulation results for the same set of conditions, which agrees well with the experimental observation. Figure 3.5b contains images of cell trapping and releasing for the optimized trap design. As can be seen, a higher (10x) initial cell concentration leads to more cells becoming trapped. The trapped cells can also be easily released from the device by increasing the perfusion flow rate (by about 50 times). In the optimal devices we observe the release of more than 75% of the trapped cells. Time-lapsed images showing cell release are available in Appendix Figure A.6.

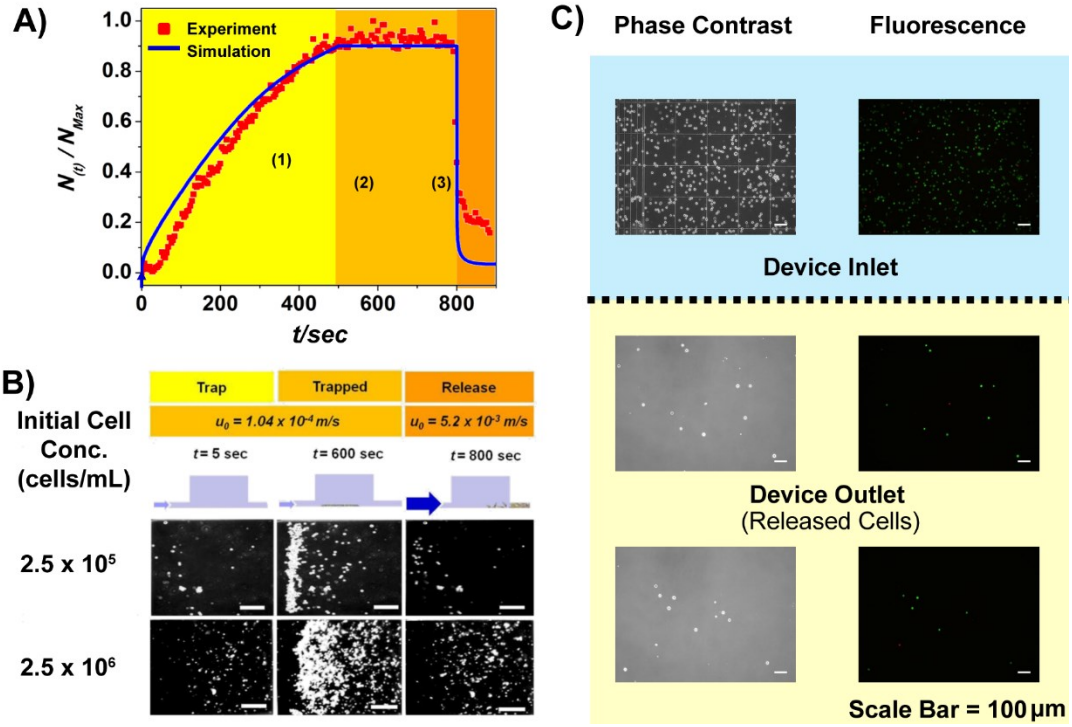

Figure 3.5: Hydrodynamic control of cell trap and release in hydraulic jump traps; **A)** the fraction of the maximum number of trapped cells plotted versus time in a 'trap and release' scenario. The cells were loaded for 10 minutes (yellow region), followed by about 3 minutes of PBS perfusion without cells (light orange region), to demonstrate the stability of trapped cells, and finally release at 50x trapping velocity (dark orange region). The blue line

represents the predicted simulation results for the scenario described above, showing excellent agreement with experimental data; **B)** Capture and release of HeLa cells in the 'hydraulic jump' cell traps at different initial cell concentration. The traps employed were 1 mm in length and width and 200 μm in height (the channels being 20 μm in height). Scale bars are 200 μm in length; **C)** Cells released from Hydraulic Jump trap retain their viability. The top row shows phase contrast (20X) and Fluorescence (600 msec exposure, composite of green and red fluorescent images) of the cells at the device inlet. The green cells are viable while the red ones are non-viable. The bottom two rows show cells released from the traps and collected at the outlet. The released cells show viability of more than 85% (in contrast to cells at the device inlet which are > 95% viable), the reduction in viability resulting from high shear forces at release.

3.7 VIABILITY AND STABILITY OF TRAPPED AND RELEASED CELLS

To test the viability and stability of trapped cells, a live-dead viability assay was performed on cells in the 'hydraulic jump' trap. The bonded devices were first primed using PBS and once the device was filled, the HeLa cell solution was perfused through the device for 5 min at the optimal flow rate for cell trapping. The cell solution was then replaced with the mammalian Live/Dead Cell Viability Assay (Invitrogen) solution containing 2 μM Ethidium Homodimer-1 (EthD-1) and 4 μM Calcein AM. This solution was perfused at the same flow rate as before for 30 min while the device was protected from light. After 30 min, fluorescent images of the trapped cells were taken using a Nikon Inverted Microscope. The same kit was used to assess the viability of the released cells off-chip. Additionally, this assay verified the fluidic exchange capabilities of the cell traps as the procedure replaces PBS with the viability assay reagents. The assay concluded that >99% of the trapped cells were viable (Figure 3.6), thus the cells were not harmed during the trapping process. Also, the assay involved ~ 30 min of continuous perfusion, during which the trapped cells were retained, demonstrating the stability of the cells trapped in the 'hydraulic jump' trap. To assess the viability of the cells after they are released, the released cells were collected off-chip and the viability assay performed on them. The released cells showed a viability of more than 85% (Figure 3.5c), which was lower than the inlet solution (>95%). This reduction in viability can be attributed to the exposure to high shear forces, which can be alleviated by increasing the height of the outlet channels.

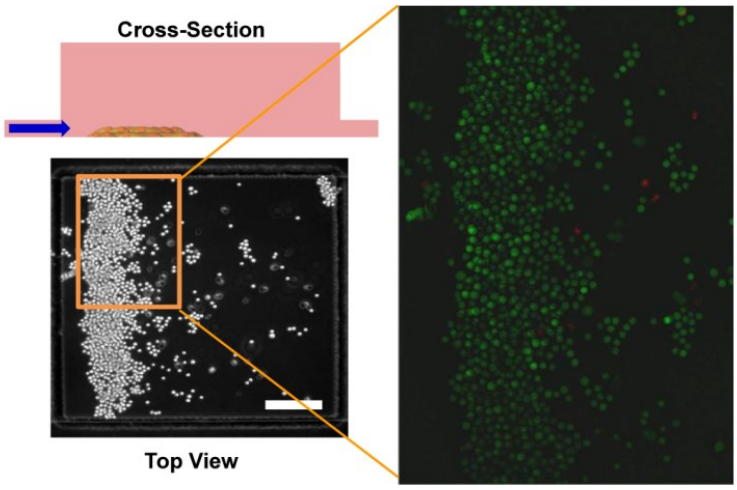

Fig. 3.6: Mass transfer in trap and cell viability of trapped cells. This assay demonstrates the ability to treat trapped cells with different reagents. The cells shown trapped in the figure were treated with a Live and Dead assay and the resultant fluorescence shows that majority of the cells were viable after trapping and treatment. The scale bar is 200 μm in length.

3.8 MULTIPLEXED ARRAY FOR CELL CONCENTRATION PURPOSES

As a demonstration of the utility of a 'trap and release' setup, we fabricated a microfluidic device which utilizes the 'hydraulic jump' to trap and concentrate cell solutions. The concentrated cells were then released and collected off-chip. Using this technique, we can concentrate cells without the need of centrifugation or filtration. While centrifugation has been shown to change the gene expression of the cell (21), filtration is prone to clogging and also exposes the cells to high shear rates. The technique used here can potentially be used to concentrate cells without influencing their gene and protein expression.

The principle behind cell concentration using a 'trap and release' setup is described below. The device first traps a certain volume of cells at a low flow velocity (u_0 = 1.04 x 10^{-4} m/s). If the initial cell concentration (i.e. the concentration of cells in the input fluid) is N_{in}, volumetric flow rate (for trapping) is Q_1, trapping time is t_{in} and the efficiency of trapping is η; the number of cells trapped $n_{trapped} = N_{in} \, x \, Q_1 \, x \, t_{in} \, x \, \eta$. These cells are then released from the trap using a larger flow velocity (u_0 = 5.2 x 10^{-3} m/s). Hence, if volumetric flow rate (for release) is Q_2 and release time is t_{out}, the concentration of cell solution at the outlet $N_{out} = N_{in} \, [1 + \{(Q_1 \text{x } t_{in} \text{x } \eta)/ (Q_2 \text{x } t_{out})\}]$. Therefore, to increase the concentration of the input cell solution, the condition to be fulfilled is $(Q_1 \text{x } t_{in} \text{x } \eta)/ (Q_2 \text{x } t_{out}) > 1$.

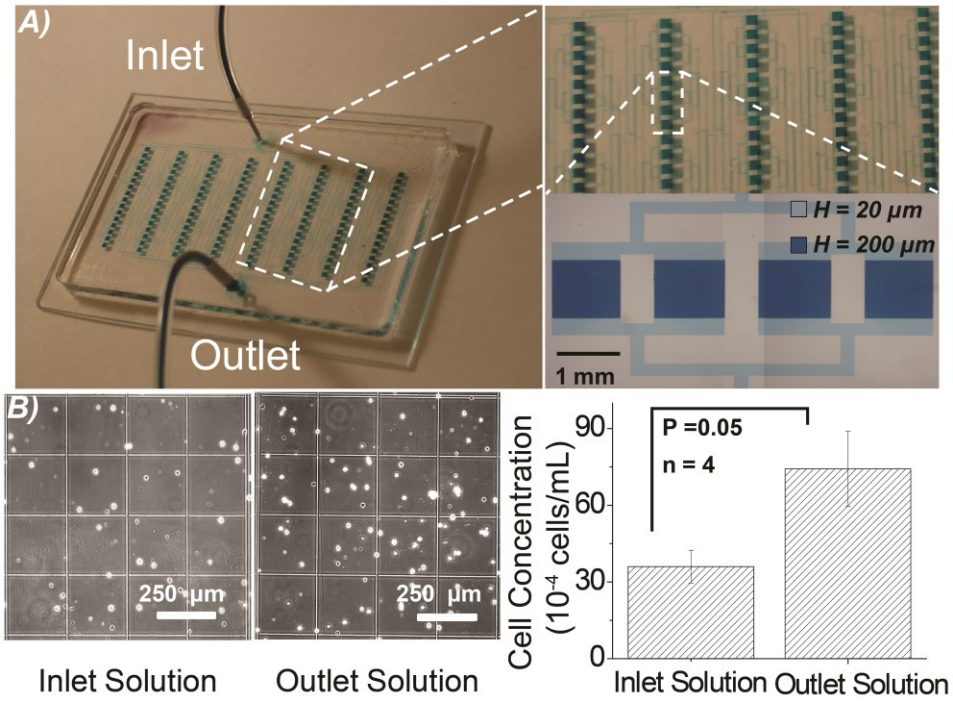

Figure 3.7: Multiplexed microfluidic cell 'trap and release' array for cell concentration; **A)** highly multiplexed microfluidic device having 128 Hydraulic Jump traps. The dimensions of the traps were chosen to be the optimal dimensions for trapping (h_0= 20 µm, h_1= 200 µm) ;**B)** Haemocytometer images and quantification of the cell concentrations of the inlet and outlet solutions. The results show an increase in the cell concentration of around 2X.

The design of the device used for this purpose is shown in Figure 3.7. To improve the throughput of the device, we designed a highly multiplexed microfluidic device as shown in Fig. 3.7a. The device has 128 parallel 'hydraulic jump' traps of the optimal geometry (h_0= 20 μm, h_1= 200 μm). The device was loaded with cell solution at an u_0 = 1.04 x 10^{-4} m/s per trap. The trapped cells were then released at a higher u_0 in an equal volume of the initial cell solution (Q_1x t_{in}x η/ (Q_2x t_{out}) = 1) which led to a 2X increase in concentration. The results from this experiment are shown in Fig. 3.7b, where the haemocytometer images of the inlet and outlet solutions clearly show the increase in cell concentration achieved by the device. A quantification of the haemocytometer images shows a statistically significant increase (~2x) in the cell concentration. Higher increases in concentration can be achieved by using a more multiplexed device, by reducing output volumes or using sequential concentration.

3.9 PAIRED TRAPPING OF CELL TYPES FOR COCULTURE/INVASION ASSAYS

The study of cell to cell communication and complex cellular interactions needs the development of cell co-culture assays which mimic the complex in-vivo microenvironments (22). Such co-culture assays can also be used to analyze the invasion of cancer cells into blood vessels and other tissues during metastasis (23). Microfluidic platforms are suitable for the purpose of co-culture assays because such platforms can be designed to resemble in vivo cellular milieu and be multiplexed to increase the throughput of such assays. In this section, we describe some preliminary work done in adapting the microfluidic hydraulic jump traps as a platform of paired trapping of cell types for use in cell co-culture or invasion assays.

The principle behind paired trapping in hydraulic jump traps is shown in Figure 3.8a. The hydraulic jump traps are isotropic with respect to the inlet and outlet channels. This implies that the trapping efficiency of the trap does not depend on the flow direction within the trap region, as long as the flow velocity is kept at the optimal velocity for cell trapping. Also, under these conditions, such a change in the flow direction within the trap will not affect cells already trapped within that region. Hence it is possible to load two different cell types into the trap region (from two different directions) allowing for cellular co-culture within the trap region. To achieve paired trapping of cell types, we first perfuse one cell type (say, cell type A), at the optimal flow velocity, into the hydraulic jump trap. After sufficient cells are trapped, the flow direction is reversed and a different cell type (cell type B) is perfused into the hydraulic jump trap. This leads to the trapping of the second cell type allowing for the co-culture of these two cell types within the trap region.

Preliminary experimental data of paired cell trapping in the hydraulic jump cell trap is shown in Figure 3.8b. The two cell types used in this experiment were BT474 and MDCK cell lines. The BT474 cells were trapped first and led to the formation of a band of trapped and concentrated cells. The flow direction was then reversed and MDCK cells were trapped in the trap region in the opposite direction. As can be observed from the images, the trapping of the MDCK cells did not lead to any significant changes in the band of trapped BT474 cells. These trapped cells can also be treated with different buffers and media during culture, as long as the flow velocity is kept at the optimal value. The different traps shown were from a multiplexed device platform with multiple trap regions in one device. These trap regions can also be made independent of each other with the use of multiple inlets/outlets. Hence, we can use this platform to generate multiple co-culture regions which can be independently perturbed and studied. Such

studies can be used to analyze the effect of chemicals on cell to cell communication or the action of drugs on the mobility and invasion of cancer cells.

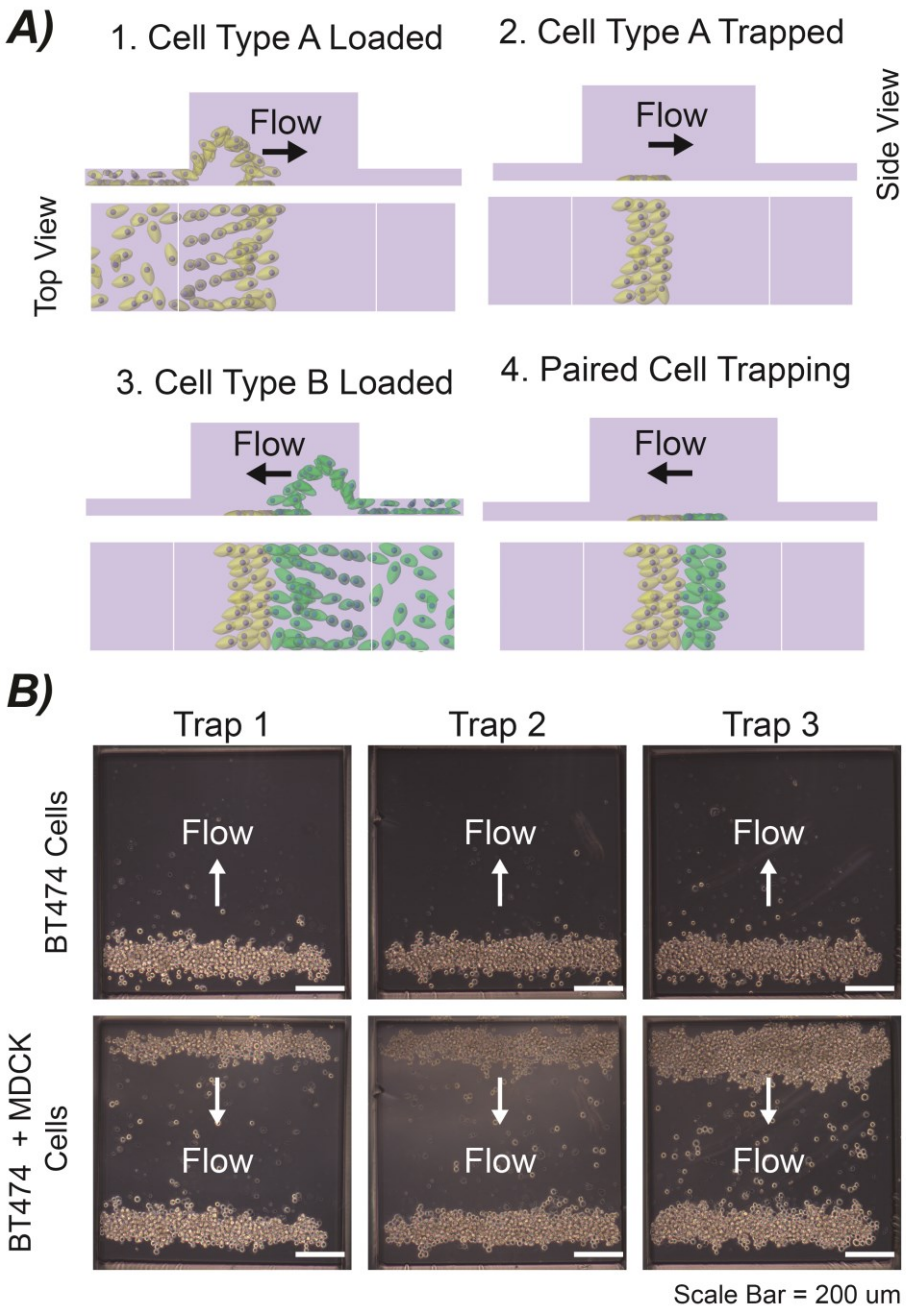

Figure 3.8: Paired trapping of cell types in the hydraulic jump cell traps; **A)** Principle of the paired trapping process. Cell type A is trapped in the trap region by perfusing at the optimal trap velocity from the right. After the first cell type is trapped, the flow direction is reversed and Cell type B is trapped from the left at the same trapping velocity ;**B)** Experimental result of paired cell trapping of BT474 and MDCK cells. BT474 cells are trapped first followed by MDCK cells from the opposite direction. The trapping of the MDCK cells did not lead to any significant change in the band of trapped BT474 cells. This demonstrates the potential of using the hydraulic jump cell traps for paired cell trapping.

3.10 INERTIAL SEPARATION OF BACTERIA FROM MAMMALIAN CELLS

The separation of bacterial cells from mammalian cells (in mixed samples) is an important sample preparation step performed for a variety of biological assays. An example of such an assay is the metagenomic analysis of samples such as gut biopsies. The rapid and efficient sample preparation of these samples for downstream processing remains a significant challenge for both academic and clinical endeavours. This is the first step in realizing microbial analysis of gene and protein regulation with single-cell granularity. Currently, all cells in a sample, including both mammalian and microbial, are lysed prior to DNA analysis. However, the presence of cells other than the microorganisms of interest will give rise to excess DNA which can yield a low Signal to Noise ratio (SNR) in subsequent analysis. Yet basic mechanical filtration remains the state-of-art technique employed in most metagenomic labs (24). This technique has a low throughput and is susceptible to periodic clogging of filters. Hence a technology for continuous and efficient separation of mammalian cells from samples such as the gut sample is needed. Microfluidic devices have yielded promising alternatives to traditional techniques, providing increased efficiency, throughput, and potential for multiplexing. There have been several efforts to separate bacteria from human cells, targeted at a variety of applications. Some techniques that have been applied include soft-inertial separation (25), dielectrophoresis (26) and micromagnetic separation (27). However the current techniques require complex external hardware (such as multiple inlet flows and power sources) or additional sample preparation steps (such as mixing of magnetic nanoparticle conjugates antibodies). Here we take advantage of the high trapping efficiency of mammalian cells and the poor retention of bacterial cells, in the hydraulic jump cell traps, to demonstrate a simple inertial technique for the separation of bacterial cells from mixed cultures.

The principle of this technique is shown in Figure 3.9a. The sedimentation rate (v) of an isolated sphere of radius r and density ρ_s in a liquid of density ρ and viscosity η can be derived, from Stoke's law, to be:

$$v = \frac{2g(\rho_s - \rho)r^2}{9\eta} \qquad \text{-- (3)}$$

Bacterial cells, owing to their small size, have a much lower sedimentation rate than mammalian cells. This leads to a significant reduction in their trapping efficiency in the hydraulic jump cell traps optimized to trap larger mammalian cells (20). Hence if a mixed sample, containing both mammalian and bacterial cells, is introduced into a hydraulic jump trap; the mammalian cells will get immobilized in the trap region leading to a pure sample of bacterial cells in the outlet. There is some loss of bacteria in the trap region (due to non-specific adhesion to channel walls and floor) which can be mitigated by proper device coating and wash steps post sample injection. Experimental verification of this phenomenon was done using a mixed sample of Jurkat and *Escherichia coli* (E.coli) cells. The results of the experiment are shown in Figure 3.9b. The haemocytometer image of the inlet solution shows the presence of both bacterial and mammalian cells. However, the haemocytometer image of the solution at the outlet reveals a pure bacterial sample. This demonstrates the capability of the hydraulic jump trap devices for the inertial separation of bacteria from mixed samples.

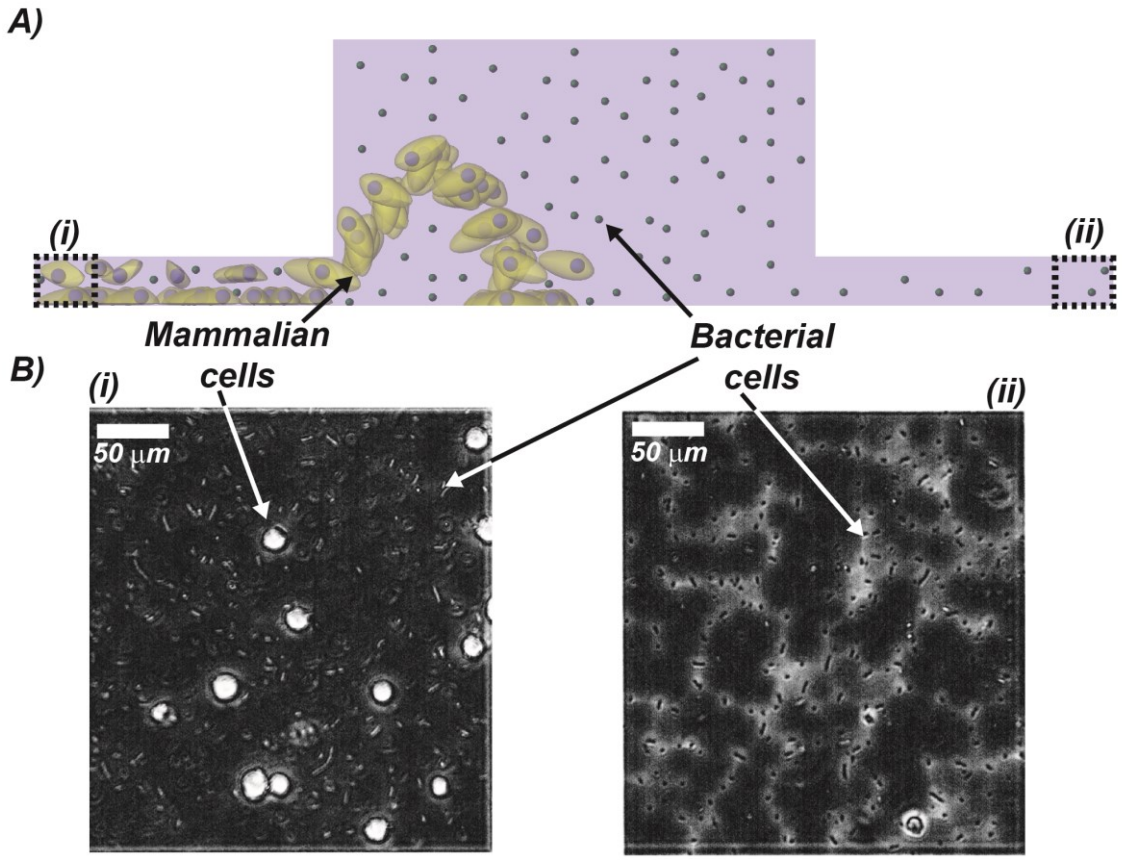

Figure 3.9: Inertial separation of bacterial cells from mixed samples in the hydraulic jump cell traps; **A)** Principle behind the inertial separation of bacterial cells. When a mixed sample (containing mammalian and bacterial cells) enter the hydraulic jump trap, the mammalian cells settle down and get immobilized at the channel floor. The bacterial cells, owing to their slow sedimentation rate, do not settle down and can be collected at the outlet; **B)** Haemocytometer images of the inlet and outlet solutions showing the removal of bacterial cells from the mixed sample (at the inlet). The mammalian cells used for the experiment were Jurkat cells while the bacterial cells used were *Escherichia coli* cells.

3.11 CONCLUSION

In this work, the development of a novel and efficient microfluidic cell 'trap and release' platform that utilizes the 'hydraulic jump' phenomenon, found in nature, is reported. Cell trapping in these structures takes place by the balance of competing forces: the fluidic pressure force, the fluidic drag force, and cellular adhesion forces. We have demonstrated that cell trapping efficiency can be hydrodynamically controlled by altering the flow velocity in the channels (u_0) within the device, thus enabling a cell 'trap and release' system. Trapping efficiencies at low u_0 were found to be greater than 90%, whereas flow at higher u_0 released more than 75% of trapped cells. This device was further used to demonstrate on-chip cell pre-concentration and reagent exchange for cellular analysis. The developed cell trapping mechanism is a simple, efficient, and gentle method to trap and release cells. The described cell 'trap and release' method provides a valuable platform to elucidate cellular behavior in dynamic

microenvironments and enables the downstream post-analysis reclamation of cells. The applicability of these traps for cell concentration, separation and paired trapping was also demonstrated. Hence, this modality will enable micro-devices useful for quantitative biology, drug screening and cell-based diagnostic assays.

3.12 ACKNOWLEDGEMENTS

I would like to acknowledge Younggeun Park, Yeonho Choi, Hinesh Patel, Bill Kuang, Sean M. Torrence, John R. Waldeisen and Taewook Kang for their contribution to this work. I also acknowledge the Biomolecular Nanotechnology Centre (BNC) and the Tissue and Cell Culture Facility at the University of California, Berkeley for their help and support. Funding for this work was provided by NIH (R01 CA120003-01A2) and the CNMT (2010K000352, 2010K000353, and 2010K000354) of the Ministry of Education, Science and Technology, Korea.

3.13 REFERENCES

1. Lee SJ, Lee SY Micro total analysis system (μ-TAS) in biotechnology. *Applied microbiology and biotechnology* 64:289–299.

2. Reyes DR, Iossifidis D, Auroux P-A, Manz A (2002) Micro total analysis systems. 1. Introduction, theory, and technology. *Anal Chem* 74:2623–2636.

3. Auroux P-A, Iossifidis D, Reyes DR, Manz A (2002) Micro Total Analysis Systems. 2. Analytical Standard Operations and Applications. *Analytical Chemistry* 74:2637–2652.

4. Jakeway SC, de Mello AJ, Russell EL (2000) Miniaturized total analysis systems for biological analysis. *Fresenius J Anal Chem* 366:525–539.

5. Tüdõs AJ, Besselink GAJ, Schasfoort RBM (2001) Trends in miniaturized total analysis systems for point-of-care testing in clinical chemistry. *Lab on a Chip* 1:83.

6. Andersson H, Van Den Berg A Microfluidic devices for cellomics: a review. *Sensors and actuators B, Chemical* 92:315–325.

7. Tani H, Maehana K, Kamidate T (2004) Chip-Based Bioassay Using Bacterial Sensor Strains Immobilized in Three-Dimensional Microfluidic Network. *Anal Chem* 76:6693–6697.

8. Tan W-H, Takeuchi S (2007) A trap-and-release integrated microfluidic system for dynamic microarray applications. *Proc Natl Acad Sci U S A* 104:1146–1151.

9. Kwon KW et al. (2007) Label-free, microfluidic separation and enrichment of human breast cancer cells by adhesion difference. *Lab Chip* 7:1461–1468.

10. Le DV, Rosales C, Khoo BC, Peraire J (2008) Numerical design of electrical-mechanical traps. *Lab Chip* 8:755–763.

11. Luo C et al. (2007) The combination of optical tweezers and microwell array for cells physical manipulation and localization in microfluidic device. *Biomed Microdevices* 9:573–578.

12. Lee PJ, Hung PJ, Rao VM, Lee LP (2006) Nanoliter scale microbioreactor array for quantitative cell biology. *Biotechnology and Bioengineering* 94:5–14.

13. Yang J, Li C-W, Yang M (2004) Hydrodynamic simulation of cell docking in microfluidic channels with different dam structures. *Lab Chip* 4:53–59.

14. Khademhosseini A et al. (2004) Molded polyethylene glycol microstructures for capturing cells within microfluidic channels. *Lab Chip* 4:425–430.

15. Revzin A, Sekine K, Sin A, Tompkins RG, Toner M (2005) Development of a microfabricated cytometry platform for characterization and sorting of individual leukocytes. *Lab Chip* 5:30–37.

16. Krishnamoorthy S, Bedekar AS, Feng J, Sundaram S (2007) Simulation-based analysis of fluid flow and electrokinetic phenomena in microfluidic devices. *Clin Lab Med* 27:41–59.

17. Kim SM, Lee SH, Suh KY (2008) Cell research with physically modified microfluidic channels: a review. *Lab Chip* 8:1015–1023.

18. Warrick J, Casavant B, Frisk M, Beebe D (2010) A Microfluidic Cell Concentrator. *Anal Chem* 82:8320–8326.

19. Braschler T, Johann R, Heule M, Metref L, Renaud P (2005) Gentle cell trapping and release on a microfluidic chip by in situ alginate hydrogel formation. *Lab Chip* 5:553–559.

20. Park Y, Choi Y, Mitra D, Kang T, Lee LP (2010) Study of microscale hydraulic jump phenomenon for hydrodynamic trap-and-release of microparticles. *Appl Phys Lett* 97. Available at: http://www.ncbi.nlm.nih.gov/pmc/articles/PMC2973986/ [Accessed March 29, 2013].

21. Kumei Y, Nakajima T, Sato A, Kamata N, Enomoto S (1989) Reduction of G1 phase duration and enhancement of c-myc gene expression in HeLa cells at hypergravity. *J Cell Sci* 93 (Pt 2):221–226.

22. Hwang H, Park J, Shin C, Do Y, Cho Y-K (2012) Three dimensional multicellular co-cultures and anti-cancer drug assays in rapid prototyped multilevel microfluidic devices. *Biomed Microdevices*.

23. Liu T et al. (2009) A microfluidic device for characterizing the invasion of cancer cells in 3-D matrix. *ELECTROPHORESIS* 30:4285–4291.

24. Dinsdale EA et al. (2008) Functional metagenomic profiling of nine biomes. *Nature* 452:629–632.

25. Wu Z, Willing B, Bjerketorp J, Jansson JK, Hjort K (2009) Soft inertial microfluidics for high throughput separation of bacteria from human blood cells. *Lab on a Chip* 9:1193.

26. Lapizco-Encinas BH, Simmons BA, Cummings EB, Fintschenko Y (2004) Dielectrophoretic Concentration and Separation of Live and Dead Bacteria in an Array of Insulators. *Anal Chem* 76:1571–1579.

27. Yung CW, Fiering J, Mueller AJ, Ingber DE (2009) Micromagnetic-microfluidic blood cleansing device. *Lab Chip* 9:1171–1177.

CHAPTER 4

Microfluidic Cell Trap And Lysis Sample Preparation For Biomarker-based Diagnostics

4.1 ABSTRACT

The detection of protein biomarkers in cellular samples has emerged as an important tool for the diagnosis and characterization of many cancer types. Although microfluidic devices for protein biomarker analysis allow highly sensitive multiplexed assays to be performed, most of these devices currently lack on-chip sample preparation modules and cannot work with complex biological samples directly. Here we describe a microfluidic sample preparation module capable of cell concentration, wash, lysis and lysate release for further biomarker detection. Cell concentration and wash in the device is achieved by immobilizing the cells in a region of channel expansion; where the interplay between fluidic drag forces and cellular adhesion forces lead to cellular trapping. The optimal device design described herein has very high (>90%) cell trapping efficiencies at low flow velocities (1.04×10^{-5} m/s) in the trap. The lysis of trapped cells is achieved by the *in situ* production of lytic hydroxide ions using the electrochemical hydrolysis of water present in the sample. The optimized device can accomplish lysis of the trapped cells in less than 3 minutes at low power (<60μW). This integrated device enables gentle cell trapping and concentration while providing the convective mass transfer of lytic agents to the captured cells. Also, an ELISA was performed with on-chip lysates demonstrating that the sample preparation device led to the recovery and detection of cancer biomarkers. This 'trap and lysis' modality provides a preparatory platform that allows microfluidic protein assay systems to interface directly with biological samples and will advance biomarker-based cancer diagnostics.

4.2 INTRODUCTION

The biophysical and biochemical study of cells is of utmost interest in basic biology, disease diagnostics, and therapeutic development. In the field of cancer biology, protein and nucleic acid biomarkers from cells in tumor biopsy samples are important in diagnosing and characterizing many cancer types (1). For example, the cell membrane protein biomarker Her-2 (or ErbB-2) is used in Breast Cancer diagnostics and is also a drug target (2). These cellular biomarkers have been correlated to various aspects of disease including malignancy, drug resistance, and relapse, (3) raising hope that personalized medicine may become a reality for cancer patients. Along with the discovery and validation of new disease biomarkers comes the need for the development of platforms that employ these biomarkers for diagnostics. In this regard, much attention and effort has been devoted to microfluidic 'lab-on-a-chip' devices for disease detection. Microfluidic devices enable complicated physical and chemical procedures in a time- and power-efficient manner while incurring very low production and operation costs (4). In terms of protein

biomarker analysis, the use of microfluidic devices has been shown to reduce the amount of patient sample needed and also the time-to-result (5, 6). Greater specificity of biomarker detection can be achieved by combining multiple markers (7,8) and microfluidic devices have been developed to enable multiplexed detection of analytes from the same sample (9). Additionally, a variety of sensors have been developed for the detection of cancer biomarkers in microfluidic devices using fluorescence, colorimetry, microelectronics (nanowires, impedometry, etc.) (10) and quantum dots (11). All these developments have made microfluidic devices a viable platform for the realization of personalized medicine in cancer.

Although a number of high-throughput multiplexed microfluidic protein assay systems are being developed, most lack on-chip sample preparation (12) and work only with homogenous or cell-free samples (13) such as biopsy lysates. Practical applications in clinical settings, though, involve processing complex samples and the off-chip protocols necessary to prepare these homogeneous samples have emerged as a frequent bottleneck for microfluidic diagnostic devices (12). These bench-top processes generally include centrifugation for cell concentration, followed by cell wash steps. Cellular biomarkers are then released via cell lysis for on-chip analysis (14). An ideal device would operate with unprocessed or minimally processed samples, but the development of microfluidic devices with sample preparation capability is often very complex because of the multiple processing steps involved (15, 16). There is a need for on-chip sample preparation modules to miniaturize the off-chip steps, namely high efficiency cell purification/extraction (as patient sample is limited), concentration, and lysis (17, 18).

It should be noted that cellular purification/concentration can be achieved in a microfluidic device by the continuous trapping of cells in a specific device region. Perfusion flow can then be used to wash these trapped and concentrated cells. At present, the major techniques used for cell trapping in a microfluidic device are mechanical (e.g. filters) , electrical (e.g. dielectrophoresis) (19), optical (20, 21) and hybrid systems (22, 23). Of the present techniques, mechanical cell traps are the most common and can be achieved by either channel constriction or expansion-based approaches. Constriction based mechanical cell traps expose cells to high shear stress (24) and such high pressures can lead to pressure induced changes in the cells that ultimately can affect the study. Micro-wells are an expansion-based technique for cell immobilization where trapping occurs by gravity-based sedimentation (25). The main drawback of micro-well trapping is the diffusion-limited mass transfer, which increases the time required for wash steps. Warrick et al. have developed a sedimentation-based mechanical cell trap that allows faster mass transfer to the cells and its use as a cell concentrator has been demonstrated (26). Such developments in expansion-based trapping have enabled a number of cell-based applications, although features like high trapping efficiency, integrated lysis of trapped cells, and lysate release are still lacking.

Cell lysis of tumor samples are important for any proteomic analysis (27). A variety of microfluidic technologies for cell lysis have also been demonstrated and used. These techniques can be classified, based on the principle mode of lysis, into physical (28, 29), chemical (30, 31), thermal (32, 33), and electrical lysis (34). Of these, chemical methods are the most common as they have high lysis efficiency (in contrast to physical methods), need little to no power (in contrast to thermal and electrical lysis), and can be designed to minimally affect the biomarker of interest (in contrast to thermal methods) (35, 36). However, chemical lysis is limited by the diffusion of lytic agents (in laminar flow regimes), can foul downstream assays and needs either addition of external reagents to the sample or on-chip reagent storage (36).

In this work, we have designed and optimized a microfluidic sample preparation module. The device integrates cell trapping, performed using hydraulic jump cell traps (described in Chapter

3) with an efficiency of more than 90%, and cell lysis, which occurs in less than 3 minutes. The principle behind cell trapping in our device has been described previously in Chapter 3 and 4 (37). A sudden vertical channel expansion in our microfluidic device leads to a decrease in flow velocity that causes cells to become trapped in the expanded region. This technique is gentle and allows for rapid convective mass transfer to the trapped cells. Using electrochemical lysis these trapped cells were then lysed (38). This technique generates lytic hydroxide ions *in situ*, using a low D.C. Voltage, and is non-fouling for downstream detection purposes. We used two breast cancer cell lines, BT474 and T47D, for this study and showed successful off-chip detection of the breast cancer biomarker Her-2 from lysates generated by the microfluidic sample preparation device. This device can be integrated with microfluidic protein detection techniques to enable high throughput biomarker-based cancer diagnostics. Notably, this principle of sample preparation can also be applied to other adherent cell lines.

4.3 PRINCIPLE BEHIND INTEGRATED 'TRAP AND LYSIS' DEVICE

The principle behind the microfluidic integrated 'trap and lysis' sample preparation device is shown in Figure 4.1. This device aims at advancing the conventional sample preparation unit processes (Figure 4.1a) into a multiplexed microfluidic system (Figure 4.1b). The benefits of this device, apart from the minimal sample requirement and small 1"x3" footprint, include centrifugation-free cell concentration, buffer-free lysis, and decreased time for sample preparation. The process flow of the device is shown in Figure 4.1c. The cell solution is loaded into the device (Figure 4.1c.i) and cell concentration is achieved by trapping the cells in a defined 'trap' region (Figure 4.1c.ii). The trapped cells are then lysed using buffer-free electrochemical lysis (Figure 4.1c.iii) and finally the lysate is release (Figure 4.1c.iv) for downstream analysis. The 'trap' in our device is a hydraulic jump cell trap described in Chapter 3. The trap is a region of channel expansion that decreases the fluid flow velocity. As a result, the cell initially travelling upward along streamlines sediments downward to the base of the trap due to gravity. Once the cells sediment, friction and non-specific adhesion forces between the cell membrane and the base of the trap (plasma treated glass) apply a retardation force (39), which counters the fluid pressure and drag forces propelling the cells along the direction of flow. When the net fluid drag forces are less than the net retardation forces, the cells come to rest and become 'trapped'. These trapped and spatially concentrated cells can now be exposed to different washes by changing the buffer composition. As long as the flow velocity in the device is not increased, this buffer exchange will not result in the loss of cells from the trap region. Lysis of the trapped cells is achieved using the electrochemical lysis method described previously by Di Carlo et al. (38). The device includes two platinum planar electrodes (deposited on the bottom glass substrate) upstream and downstream of the trap region. Once the device is filled with cell media/buffer, an application of a suitable voltage will lead to the hydrolysis of water in the media/buffer. By controlling the polarity of the applied voltage we generate hydroxide (OH^-) ions upstream of the trap. These ions are lytic and attack the cell membrane cleaving the phospholipids of the lipid bilayer. The ions generated upstream are transported to the cells immobilized in the traps via convective diffusion, leading to the lysis of the trapped cells. Finally, cell lysate release occurs when the perfusion velocity (and hence fluid shear) is increased. The integrated sample preparation module minimizes the amount of patient sample necessary and yields lysate with a higher concentration of the biomarker of interest. This module is also compatible with microfluidic protein analysis systems.

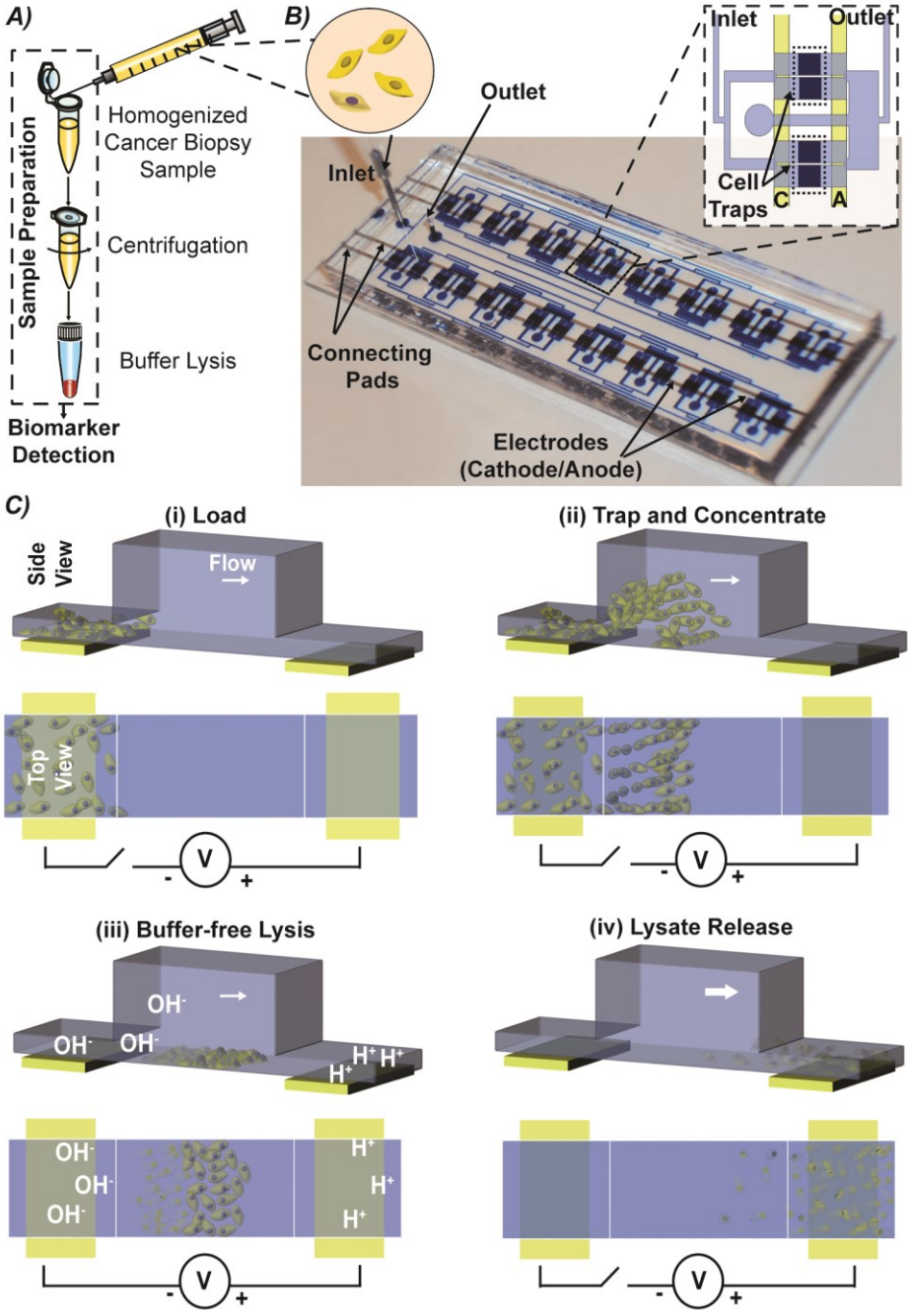

Figure 4.1: Microfluidic trap and lysis sample preparation system for cellular biomarker-based diagnostics; **A)** Processing steps involved in traditional sample preparation; tumor biopsy sample is homogenized (by means of tissue digestion and cell clump breakage), then centrifuged (≥ 1,000 g, > 5 minutes) to concentrate the cells, and the concentrated cells are finally lysed with a lysis buffer; **B)** The high-throughput, integrated sample preparation device developed for performing the traditional sample preparation steps on a microfluidic platform. The device consists of multiple sample preparation units connected in parallel. Each unit (figure inset) is composed of four cell trap regions and electrodes (C stands for cathode and A for anode) for lysis. This platform is amenable to the integration of protein detection systems; **C)** Process flow of the microfluidic sample preparation device; (i) cells are loaded into the microfluidic device, (ii) in the trap region (which corresponds to a channel expansion) the cells settle downward and are immobilized, (iii) the trapped cells are then exposed to lytic hydroxide ions produced upstream by electrochemical hydrolysis, and (iv) finally, the cell lysate is released by increasing the flow velocity.

4.4 CELL TRAPPING IN HYDRAULIC JUMP CELL TRAPS

Cell trapping in Hydraulic Jump Traps was addressed to in the previous chapter. In short, we have optimized the microfluidic trap system to achieve > 90% trapping efficiency (η). This behaviour was seen for all the cell lines tested. For the trap and lysis sample preparation module, a highly multiplexed architecture (as shown in Figure 4.1) was designed. However, cell immobilization was observed sporadically at the optimal u_0 in the channels upstream of the cell trap and lysis region. This even occurred at flow velocities higher than the optimal u_0 due to cell accumulation and clogging of the 20 µm high channel. These clogged cells were not lysed (as described later in the lysis section) and can contaminate the cell lysate if released. To alleviate this problem, the channel height was increased by 10 µm and the trap height was kept at 200 µm. The flow velocity, u_1, in the trap was held at the optimal value of 1.04 x 10^{-5} m/s to maintain a η >90%. The optimized hydraulic jump trap can hence trap and concentrate >90% of cells in a crude biological sample.

4.5 HYDROXIDE ION PRODUCTION AND TRANSPORT FOR ELECTROCHEMICAL LYSIS

Electrochemical cell lysis utilizes the generation of lytic hydroxide ions by applying a voltage to the electrodes in the device greater than the redox potential of water. The equations for the half-cell reactions are:

$$4H_2O\ (l) + 4\,e^- \leftrightarrow 4OH^-\ (aq) + 2H_2\ (g) \qquad \text{At Cathode-- (1)}$$

$$2H_2O\ (l) \leftrightarrow 4H^+\ (aq) + 4\,e^- + O_2\ (g) \qquad \text{At Anode -- (2)}$$

The rate of the reaction (R) can be monitored by measuring the current (i) using Faraday's law of electrolysis (40):

$$R = \frac{i}{nFA} \qquad \text{-- (3)}$$

Where n is the number of electrons involved per hydroxide ion generated (n = 1), A is the electrode surface area, and F is Faraday's constant. The dependence of the current density (i/A) on the surface over-potential (the difference between the applied potential and the constant equilibrium potential) is given by the Butler-Volmer equation (40) as:

$$\frac{i}{A} = i_0\,[e^{(\frac{\alpha nFE}{RT})} - e^{(\frac{\beta nFE}{RT})}] \qquad \text{-- (4)}$$

Where i_0 is exchange current density, which depends on the nature of the electrode, the surface properties of the electrode, and the reactant concentration close to the electrode surface. α and β are the cathodic and anodic charge transfer coefficients, respectively, T is the temperature, R is the universal gas constant and E is the over-potential, which is proportional to the applied voltage. The reactant concentration close to the electrode surface is dependent on the rate of replenishment through convective mass transport. As the convective mass transport rate depends on the flow velocity, hence, the current density and rate of the reaction would also depend on the flow velocity.

Hydroxide ion transport in the microfluidic device was simulated for a Faradaic current of 15µA (corresponding to experimental results described in next section) and a flow velocity in the trap, u_1, of 1.04 x 10^{-5} m/s. A 2D model of the system was used in the simulations and the convective transport COMSOL module was implemented. The interaction between hydroxide ions (produced at the cathode) and hydronium ions (produced at the anode) were neglected within the trap region. This assumption was made because simulation at the anode indicated the absence of hydronium ions upstream in the trap region (i.e. against the flow). The flow rate was set at the optimal velocity for trapping and a transient simulation model (with a time step of 1 sec) was executed. The results from the simulation study are shown in Figure 4.2 and Appendix Figure B.1. The results indicate a lag time before the hydroxide ions reach a critical concentration of 20mM (which corresponds to the hydroxide ion concentration needed for lysis (38)) in the traps. The time required for the hydroxide ions to reach a 20 mM concentration explains the time lag observed before cell lysis begins in Figure 4.3 c. The lag time depended on the distance from the electrode and ranged from 17-44 seconds for the average band of concentrated cells (which lay 100–400 µm from the trap entrance).

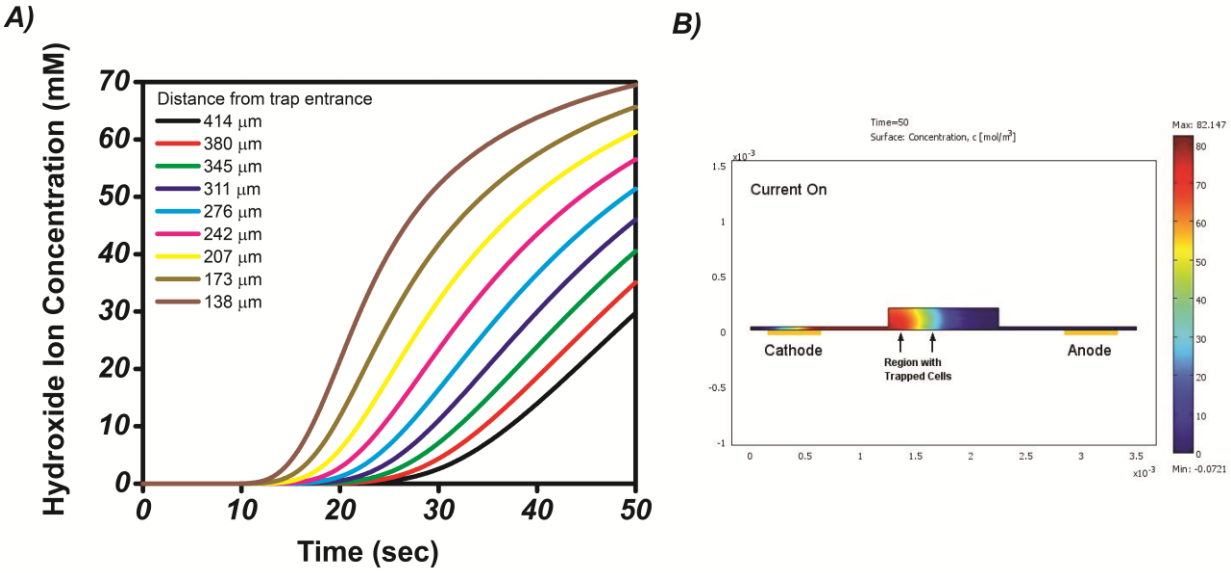

Figure 4.2: Simulation result for the convective transport of hydroxide ions into the trap region; **A)** The hydroxide ions were generated at the upstream electrode at a faradaic current of 15 µA and the fluid velocity in the trap is 1.04 x 10^{-5} m/s. The family curves represent different distances between 100 and 400 µm from the trap inlet; corresponding to the distance of the concentrated cells from the trap inlet. The dashed line indicates the critical hydroxide ion concentration of 20 mM. The length of the trap is 1 mm, the height of the channel is 30 µm (h_0), the height of the trap is 200 µm (h_1), and the length of both electrodes is 500 µm; **B)** A simulation snapshot showing the result of the model. The system simulated had a hydraulic jump trap located between a cathode (upstream) and an anode (downstream).

4.6 INTEGRATED MICROFLUIDIC ELECTROCHEMICAL LYSIS OF TRAPPED CELLS

Integrated PDMS microfluidic chips were fabricated to characterize the performance of the sample preparation module. PDMS devices were fabricated using standard soft lithography processes. The electrodes were patterned on a 2" x 3" glass slide using a lift-off process. S-1818 (Shipley) was patterned on the glass slide, followed by O_2 plasma descumming (100W, 30-60

sec) and metal deposition using an electron beam evaporator (Edwards EB3). A 10 nm thick Titanium adhesion layer was deposited followed by the 100 nm Platinum electrode. The photoresist was then stripped in acetone. Lastly, the PDMS device was bonded to the patterned (with electrodes) glass surface using O_2 plasma (20 W, 30 sec, 0.2 Torr). The PDMS devices were bonded to electrode-patterned glass slides such that the trap was located between the two electrodes with the cathode upstream of the anode (Figure 4.1c). The bonded devices were first primed with PBS and then the cell solution was perfused through the device at the optimal trapping flow velocity. The cells (at an inlet concentration of 10^6 /ml) were trapped for 5-10 minutes and then a PBS wash was performed to remove excess cells from the channels upstream of the trap. External connectors were used to apply a voltage to the upstream and downstream electrodes while phase contrast images of the cells in the traps were acquired. The phase contrast of the cells changed upon lysis allowing evaluation with ImageJ. The lysate was then collected by increasing the flow velocity of the perfused PBS by ~10x. The cell lysate was collected by pipette at the outlet and frozen at -20°C until further analysis.

The hydroxide ions generated by the faradaic current at the cathode (upstream of the trap region) are transported downstream via convective transport (Peclet number of ~100-200, Appendix Figure B.1 and B.2) and lead to lysis of the trapped cells. The change in cell morphology during lysis is easily visualized in a phase contrast microscope (Figure 4.3 a) and was used to enumerate cell lysis rates. Upon initial application of the voltage, a time lag occurs before cell lysis begins as the hydroxide ions are actively transported to the trap region and reach a concentration necessary for lysis. The excess hydroxide ions are then neutralized by the downstream hydronium ions at the anode enabling the non-fouling lysis capability of the device. Time lapsed images of BT474 cell lysis in the integrated trap and lysis system at different voltages are shown in Appendix Figures B.5 and B.6. The temporal current profiles depicted in the images reveal an initial spike in current followed by decay, which corresponds to electrode charging, before the faradaic current reaches steady state. In some experiments an increase in current was observed during lysis, possibly due to the release of ionic species from within the cells increasing the conductivity of the fluid. Hydroxide ions are produced at greater rates with higher voltages, leading to faster lysis and less time necessary to reach the lytic concentration. However, very high voltages produce the gas phase components of the reaction in excess of their solubility limits and bubble formation occurs. Such bubbles can grow to sizes that disrupt cell lysis by insulating the electrodes from the fluid or entering the trap region of the device (Appendix Figures B.3 and B.6). These bubbles generally are produced first at the cathode, which is consistent with the fact that oxygen has higher solubility than hydrogen in water (41).

The experimental results (Figure 4.3b) demonstrate the dependence of time-to-lysis on the applied voltage (2.5 – 4.0V). Voltages below 3.0V took more than 5 minutes for complete lysis and higher voltages (3.75 - 4.0V) resulted in bubbles travelling to the trap before lysis was completed. The inset in Figure 4.3b shows the time to complete lysis for voltages with rapid cell lysis without bubble formation. 3.5V led to fastest lysis with minimal variability. The percentage of lysed cells, as a function of time, for voltages from 3.0-4.0V are depicted in Figure 4.3c and a time lag is evident from the initial application of voltage followed by an exponential increase in lysis. Higher voltages had higher cell lysis rates, however lysis would become inhibited by the formation of bubbles, which entered the trap and/or blocked fluid access to the electrodes. Although the voltage was varied in our experiments, the parameter that correlates directly with the reaction rate is the faradaic current in the system. The optimal operating range in our device is 10-15μA, which corresponds to 3.0 - 3.5V. The integrated trap and lysis system can lyse

trapped cells in less than 5 minutes without the need for an external buffer that can potentially foul downstream detection methods.

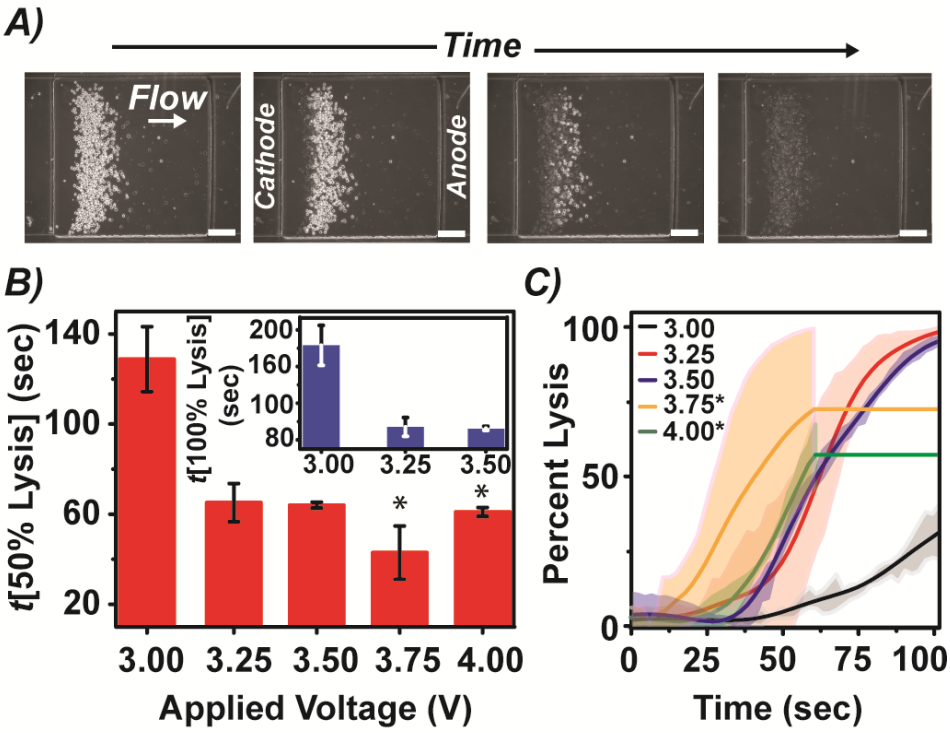

Figure 4.3: Characterization of trapped cell lysis in the integrated sample preparation module; **A)** Time-lapse phase contrast images showing the electrochemical lysis (as manifested by the alteration of the phase properties of the cells) of BT474 cells trapped in the hydraulic jump trap; **B)** Optimization of the voltage needed for electrochemical lysis of BT474 cells; an indirect relationship between the applied voltage and lysis times was observed. At voltages above 3.5V bubble formation occurred at the electrodes and entered the traps, preventing 100% cell lysis (marked by '*'). The inset shows the time to 100% lysis for the three voltages where bubble formation did not interfere with lysis. The error bars indicate standard deviation from 3 independent experiments; **C)** Temporal analysis of lysis performed at different voltages; a lag time was observed between the application of voltage and the onset of lysis. For high voltages (3.75 and 4 V), lysis is inhibited by bubble formation as bubbles can enter the trapping region or insulate the electrode from fluidic contact (marked by '*'). The shaded area represents the standard deviation from 3 independent experiments.

4.7 Off-chip analysis of lysates

Cell lysates were generated on-chip using the optimal conditions for trap and lysis and collected after flushing the device. The lysis voltage was applied for 5-6 minutes to ensure complete lysis and gauge the robustness of the system. The lysates were tested off-chip via immunodetection for protein biomarkers. BT474 (Her-2 positive) and T47D (Her-2 negative) cells were analyzed with an Enzyme-linked Immunosorbent Assay (ELISA) for the Her-2 surface protein. Her-2 is a common biomarker used in the management of breast cancer diagnostics both for diagnostics and therapy selection (2). The on-chip lysate was flushed from the device, collected off-chip, and stored at -20°C until analysis was performed. Each cell line was run in triplicates (in three independent devices with 6 traps per device) where roughly 1000 cells were trapped and lysed at 3.5V. Off-chip cell lysates were collected from a confluent dish of cells using RIPA cell lysis buffer (Sigma-Aldrich). The total protein content was measured using a Bicinchoninic Acid

(BCA) assay to normalize the Her-2 protein data. In short, three dilutions of the lysates were added to the BCA buffer solution (with the addition of copper (II) sulphate for on-chip lysates; to amplify the signal from the small lysate volume). The mixtures were incubated at 60 °C for 60 minutes and their absorbance measured at 562nm. The absorbance values were compared with a standard curve of known BSA concentrations to calculate the total protein content of the lysates. The effect of electrochemical lysis on the immunodetection of proteins was studied using a Total Her-2 ELISA kit (R&D Systems). The Her-2 content of both on- and off-chip lysates of BT474 and T47D cells was measured and compared. For the ELISA assay, 96-well polystyrene microplates (R&D Systems) were coated with the capture antibody overnight and blocked the next day. The lysates were then incubated in separate wells along with a dilution series of Her-2 protein standard. The final sample volume per well used was half the recommended volume and was characterized with standards to verify that the linearity of the assay was not affected in the region of interest (Appendix Figure B.7). The wells were then probed with a detection antibody and peroxidase substrate at 450nm. The ELISA results shown in Figure 4.4 demonstrate that the Her-2 levels in the on-chip lysates of Her-2 positive BT474 cells were detectable whereas the Her-2 negative cell line did not give a positive signal. This experiment verifies that the on-chip sample preparation module used did not inhibit the ability of biomarker proteins to be detected downstream and suggests that the module can be integrated in a diagnostic device. The levels of Her-2 in on-chip BT474 lysates were lower than off-chip lysates which might be due to non-specific protein adsorption within the device or losses incurred during lysate collection. This loss may be overcome by suitable blocking of the devices or the integration of an on-chip detection module. In summary, we have demonstrated the efficiency of the integrated sample preparation module to concentrate, wash, and lyse cells, with minimal sample and time requirement, without impeding downstream immuno-detection.

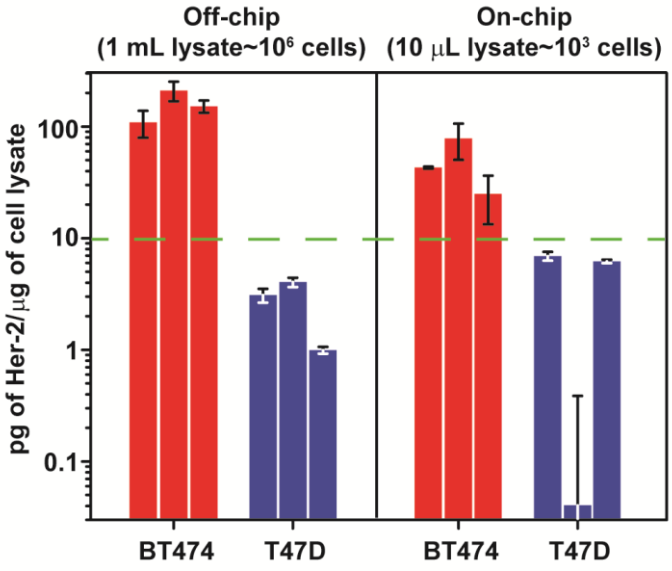

Figure 4.4: Biomarker detection from on-chip lysates was performed to validate the sample preparation module as a platform compatible with downstream protein detection systems. Her-2 biomarker was detected off-chip using an ELISA for two cell types; Her-2 positive BT474 and Her-2 negative T47D and could be used to resolve the difference between the two cells.

4.8 MICRO CHEMOSENSITIVITY ASSAY PLATFORM (μCAP) FOR PERSONALIZED BREAST CANCER THERAPY

Developments in genomics, proteomics, combinatorial chemistry and bioinformatics have considerably increased the number of potential drug targets and candidates for cancer therapy (42, 43). Tumor chemo-sensitivity assays (TCA) allow the in vitro exposure of cultured cancerous cells to these different drug candidates, at varying concentrations, to screen for viable drugs (44–46). The effectiveness of the various candidates can be measured using traditional tetrazolium (MTT) colorimetric assays (47), sulforhodamine B (SRB) protein stain assay (48), Apoptosis-based assays (49), fluorescent assays (50) or label-free techniques (51). In-vitro chemosensitivity assays have also been used to determine drug susceptibilities, of cancerous cells from patients in vitro, and can help discern whether a certain drug regimen will work against a tumor of a certain individual (52, 53). This paradigm of personalized medicine has been explored in breast cancer, where a positive correlation has been shown between TCA guided therapy and successful clinical outcome (47, 54). Results from these in-vitro assays have also been used in basic research, coming full circle, to identify resistance markers and genes (55, 56), providing valuable information for both new drug targets and candidates. Microfluidic platforms can provide clinicians the ability to perform such assays with minimal amount of patient sample, with minimal manual steps and in a high throughput fashion, i.e. with the ability to assay a variety of different therapeutic regimens (57–60). Hence, a lot of microfluidic platforms have been described to perform such in-vitro chemosensitivity assays on cancerous cells. The simplest microfluidic platform involves a tumor biopsy or cells, contained in a micro-chamber, being exposed to a single concentration (61, 62) or a gradient in concentration (63–65) of a drug. To minimize interference between the different drugs/ drug concentrations, microfluidic platforms were designed with compartmentalized cell culture areas which are independent of each other (66–70). The throughput of these assays has also been increased tremendously using high-density microchambers (71) and droplet microfluidics (72). Researchers have also developed three dimensional microfluidic platforms to better mimic in-vivo cellular colonies (73–75). However, current microfluidic assay platforms are limited by the lack of the ability to independently lyse or collect cells exposed to different conditions for analyzing genomic/proteomic causes or resistance/sensitivities. Also these devices suffer from either the absence of on-chip sample pre-concentration or the use of abrasive cell traps. We hence aim here at developing a microfluidic platform, for performing TCA, overcoming these limitations.

We developed a Microfluidic Chemo-sensitivity Assay Platform (μCAP) with non-abrasive on-chip cell pre-concentration and individually addressable assay regions (Figure 4.5). Each independent assay region consists of the Cell Trap and Lysis modules described earlier in the chapter. Cellular pre-concentration was achieved using high efficiency (>90%) hydraulic jump cell trap module. The trapped cells can then be cultured and exposed to different drugs or compounds. The treated cells in the independent assay regions can then be collected, by trypsinization (followed by a fluid flush), and/or lysed using electrochemical lysis. The designed chip has more than 120 cell trap/ analysis areas and can expose cells to two different drugs or drug combinations (with 8 different dilutions) with 8 replicates for each drug condition. The device was adapted to align each assay chamber to a well of a 96 well plate so that it can be streamlined into existing process flow. In this fashion, the cells or lysate released from each assay can be kept isolated and conveniently collected, from the well, for further genomic/proteomic assays. The cells, in this design, would be loaded into the device from each

of the wells via suction flow from the inlet. After the cells are loaded, media can be perfused during the culturing phase and buffer can be perfused during the assay phase. To realize this device design, it was imperative to bond our PDMS-glass devices to the 96 well Polystyrene (PS) dishes. We adapted a silane-based protocol to generate silanol groups on the PS surface (76) as shown in Appendix Figure B.8. The activated PDMS device was then bonded to this modified PS through covalent interaction of the silanol groups. The strength of this bond to retain liquid was tested, for more than a week in a 37°C incubator, and no leakage was observed, indicating a very strong bond.

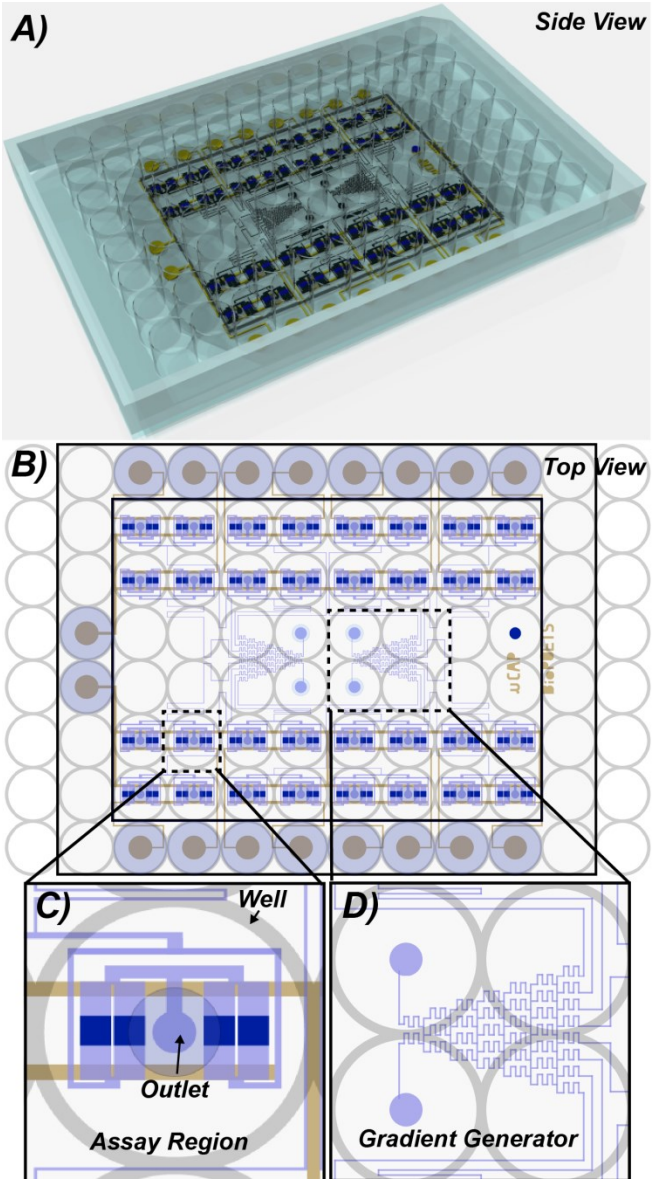

Figure 4.5: A) The μCAP platform; B) The device consists of 120 cell assay area; C) An assay area consists of 4 cell trap regions which are integrated with electrodes for electrochemical lysis. Each assay area is aligned to a well of a bottom-less 96-well dish so that the trypsinized cells/cell lysate of the treated cells can be collected independently from each well; D) The gradient generator setup for exposing cells to two different drugs or drug combinations (with 8 different dilutions) with 8 replicates for each drug condition

4.9 Conclusion

In this work we report the development of an efficient microfluidic cell 'trap and lyse' sample preparation platform that can concentrate, wash, lyse, and release the lysate of adherent mammalian cells. We demonstrate the efficacy of the system using breast cancer cell lines BT474 and T47D. Cell concentration occurs via cell trapping, achieved by the balance of competing forces: the fluidic pressure force, the fluidic drag force, and cellular adhesion forces. Trapping efficiencies for the optimized device were found to be greater than 90%. The trapped cells were further lysed using electrochemical lysis in less than 3 minutes at low power (< 60μW). The cell lysate was probed for the breast cancer biomarker Her-2 off-chip to validate that sample preparation process can be incorporated upstream of protein detection modules. The developed sample preparation module is a simple, efficient, and fast method for concentrating and lysing cells in a microfluidic device. The described cell 'trap and lyse' method provides a valuable module that can be integrated with protein detection platforms to enable complex biological sample analysis without off-chip sample preparation processes. These integrated devices can allow high-throughput biomarker-based analysis of cancer patient tumor samples facilitating personalized diagnosis and therapy.

4.10 Acknowledgements

I would like to acknowledge Brendan Turner, Ritabrata Dhar, Aditya Bandyopadhyay, Hinesh Patel, Jennifer Ni, Connor Landgarf, John R. Waldeisen and Paul Lum for their kind assistance and helpful discussion. I would like to thank the BioPOETS Group, Biomolecular Nanotechnology Center (BNC), and the Tissue and Cell Culture Facility at the University of California, Berkeley for their help and support. I would also like to thank Susan Elizabeth Clare and Rachel J. Blosser at Indiana University for providing T47D cell line and help with the Her-2 ELISA. Funding for this work was provided by NIH (R01 CA120003-01A2), Center for Nanostructured Materials and Technology (2010K000352, 2010K000353, and 2010K000354) of the Ministry of Education, Science, and Technology (Korea).

4.11 References

1. Sidransky D (2002) Emerging molecular markers of cancer. *Nature Reviews Cancer* 2:210–219.

2. Molina R et al. (2005) Tumor Markers in Breast Cancer – European Group on Tumor Markers Recommendations. *Tumor Biology* 26:281–293.

3. Ludwig JA, Weinstein JN (2005) Biomarkers in Cancer Staging, Prognosis and Treatment Selection. *Nature Reviews Cancer* 5:845–856.

4. Jakeway SC, de Mello AJ, Russell EL (2000) Miniaturized total analysis systems for biological analysis. *Fresenius' Journal of Analytical Chemistry* 366:525–539.

5. Choi S, Goryll M, Sin L, Wong P, Chae J (2011) Microfluidic-based biosensors toward point-of-care detection of nucleic acids and proteins. *Microfluidics and Nanofluidics* 10:231–247.

6. Lion N, Reymond F, Girault HH, Rossier JS (2004) Why the move to microfluidics for protein analysis? *Current Opinion in Biotechnology* 15:31–37.

7. Moore RG et al. (2008) The use of multiple novel tumor biomarkers for the detection of ovarian carcinoma in patients with a pelvic mass. *Gynecologic Oncology* 108:402–408.

8. Ren J et al. (2010) Tumor markers for early detection of ovarian cancer. *Expert Review of Molecular Diagnostics* 10:787–798.

9. Yu X et al. (2010) μFBI: A Microfluidic Bead-Based Immunoassay for Multiplexed Detection of Proteins from a μL Sample Volume. *PLoS One* 5.

10. Arruda DL et al. (2009) Microelectrical sensors as emerging platforms for protein biomarker detection in point-of-care diagnostics. *Expert Rev Mol Diagn* 9:749–755.

11. Hu M et al. (2009) Ultrasensitive, Multiplexed Detection of Cancer Biomarkers Directly in Serum by Using a Quantum Dot-Based Microfluidic Protein Chip. *ACS Nano* 4:488–494.

12. Mariella R (2008) Sample preparation: the weak link in microfluidics-based biodetection. *Biomedical Microdevices* 10:777–784.

13. Crevillén AG, Hervás M, López MA, González MC, Escarpa A (2007) Real sample analysis on microfluidic devices. *Talanta* 74:342–357.

14. Tothill IE (2009) Biosensors for cancer markers diagnosis. *Seminars in Cell & Developmental Biology* 20:55–62.

15. Chen X, Cui D-F (2009) Microfluidic devices for sample pretreatment and applications. *Microsystem Technologies* 15:667–676.

16. Liu RH, Yang J, Lenigk R, Bonanno J, Grodzinski P (2004) Self-Contained, Fully Integrated Biochip for Sample Preparation, Polymerase Chain Reaction Amplification, and DNA Microarray Detection. *Anal Chem* 76:1824–1831.

17. Gervais L, de Rooij N, Delamarche E (2011) Microfluidic Chips for Point-of-Care Immunodiagnostics. *Advanced Materials* 23:H151–H176.

18. Yeo LY, Chang H, Chan PPY, Friend JR (2011) Microfluidic Devices for Bioapplications. *Small* 7:12–48.

19. Thomas RS, Morgan H, Green NG (2009) Negative DEP traps for single cell immobilisation. *Lab on a Chip* 9:1534.

20. Andersson H, van den Berg A (2003) Microfluidic devices for cellomics: a review. *Sensors and Actuators B: Chemical* 92:315–325.

21. Tani H, Maehana K, Kamidate T (2004) Chip-Based Bioassay Using Bacterial Sensor Strains Immobilized in Three-Dimensional Microfluidic Network. *Anal Chem* 76:6693–6697.

22. Le DV, Rosales C, Khoo BC, Peraire J (2008) Numerical design of electrical-mechanical traps. *Lab on a Chip* 8:755.

23. Luo C et al. (2007) The combination of optical tweezers and microwell array for cells physical manipulation and localization in microfluidic device. *Biomedical Microdevices* 9:573–578.

24. Yang J, Li C-W, Yang M (2004) Hydrodynamic simulation of cell docking in microfluidic channels with different dam structures. *Lab on a Chip* 4:53.

25. Khademhosseini A et al. (2004) Molded polyethylene glycol microstructures for capturing cells within microfluidic channels. *Lab on a Chip* 4:425.

26. Warrick J, Casavant B, Frisk M, Beebe D (2010) A Microfluidic Cell Concentrator. *Anal Chem* 82:8320–8326.

27. Gromov P et al. (2008) A single lysis solution for the analysis of tissue samples by different proteomic technologies. *Mol Oncol* 2:368–379.

28. Carlo DD, Jeong K-H, Lee LP (2003) Reagentless mechanical cell lysis by nanoscale barbs in microchannels for sample preparation. *Lab on a Chip* 3:287.

29. Kim J et al. (2004) Cell lysis on a microfluidic CD (compact disc). *Lab on a Chip* 4:516.

30. Irimia D, Tompkins RG, Toner M (2004) Single-Cell Chemical Lysis in Picoliter-Scale Closed Volumes Using a Microfabricated Device. *Anal Chem* 76:6137–6143.

31. Sethu P, Anahtar M, Moldawer LL, Tompkins RG, Toner M (2004) Continuous Flow Microfluidic Device for Rapid Erythrocyte Lysis. *Anal Chem* 76:6247–6253.

32. Liu RH, Yang J, Lenigk R, Bonanno J, Grodzinski P (2004) Self-Contained, Fully Integrated Biochip for Sample Preparation, Polymerase Chain Reaction Amplification, and DNA Microarray Detection. *Anal Chem* 76:1824–1831.

33. Waters LC et al. (1998) Microchip Device for Cell Lysis, Multiplex PCR Amplification, and Electrophoretic Sizing. *Anal Chem* 70:158–162.

34. Lu H, Schmidt MA, Jensen KF (2005) A microfluidic electroporation device for cell lysis. *Lab on a Chip* 5:23.

35. Kim J, Johnson M, Hill P, Gale BK (2009) Microfluidic sample preparation: cell lysis and nucleic acid purification. *Integrative Biology* 1:574.

36. Kwapiszewski R et al. (2011) A microfluidic device with fluorimetric detection for intracellular components analysis. *Biomedical Microdevices* 13:431–440.

37. Park Y, Choi Y, Mitra D, Kang T, Lee LP (2010) Study of microscale hydraulic jump phenomenon for hydrodynamic trap-and-release of microparticles. *Appl Phys Lett* 97. Available at: http://www.ncbi.nlm.nih.gov/pmc/articles/PMC2973986/ [Accessed July 8, 2012].

38. Di CarloThese authors contributed e D, Ionescu-Zanetti C, Zhang Y, Hung P, Lee LP (2005) On-chip cell lysis by local hydroxide generation. *Lab on a Chip* 5:171.

39. Mrksich M (2000) A surface chemistry approach to studying cell adhesion. *Chemical Society Reviews* 29:267–273.

40. Bard, Allen J., and Larry R. 1980 Faulkner. *Electrochemical methods: fundamentals and applications*. Vol. 2. New York: Wiley.

41. Wilhelm E, Battino R, Wilcock RJ (1977) Low-pressure solubility of gases in liquid water. *Chem Rev* 77:219–262.

42. Mario Geysen H, Schoenen F, Wagner D, Wagner R (2003) Combinatorial compound libraries for drug discovery: an ongoing challenge. *Nat Rev Drug Discov* 2:222–230.

43. Kramer R, Cohen D (2004) Functional genomics to new drug targets. *Nat Rev Drug Discov* 3:965–972.

44. Caldwell GW, Ritchie DM, Masucci JA, Hageman W, Yan Z (2001) The New Pre-Preclinical Paradigm: Compound Optimization in Early and Late Phase Drug Discovery. *Current Topics in Medicinal Chemistry* 1:353–366.

45. Mestres P, Morguet A (2009) The Bionas technology for anticancer drug screening. *Expert Opinion on Drug Discovery* 4:785–797.

46. Sumantran VN (2011) Cellular chemosensitivity assays: an overview. *Methods Mol Biol* 731:219–236.

47. Xu J et al. (1999) Predictive chemotherapy of advanced breast cancer directed by MTT assay in vitro. *Breast Cancer Research and Treatment* 53:77–85.

48. Keepers YP et al. (1991) Comparison of the sulforhodamine B protein and tetrazolium (MTT) assays for in vitro chemosensitivity testing. *European Journal of Cancer and Clinical Oncology* 27:897–900.

49. Frankfurt OS, Krishan A (2003) Apoptosis-based drug screening and detection of selective toxicity to cancer cells. *Anticancer Drugs* 14:555–561.

50. Fritzsche M, Mandenius C-F (2010) Fluorescent cell-based sensing approaches for toxicity testing. *Analytical and Bioanalytical Chemistry* 398:181–191.

51. Ona T, Shibata J Advanced dynamic monitoring of cellular status using label-free and non-invasive cell-based sensing technology for the prediction of anticancer drug efficacy. *Analytical and bioanalytical chemistry* 398:2505–2533.

52. Cortazar P, Johnson BE (1999) Review of the Efficacy of Individualized Chemotherapy Selected by In Vitro Drug Sensitivity Testing for Patients With Cancer. *Journal of Clinical Oncology* 17:1625.

53. Trojan J et al. (2005) In vitro chemosensitivity to gemcitabine, oxaliplatin and zoledronic acid predicts treatment response in metastatic gastric cancer. *Anticancer Drugs* 16:87–91.

54. Smith HS et al. (1990) Preliminary Correlations of Clinical Outcome with in Vitro Chemosensitivity of Second Passage Human Breast Cancer Cells. *Cancer Research* 50:2943 –2948.

55. Glaysher S et al. (2009) Resistance gene expression determines the in vitro chemosensitivity of non-small cell lung cancer (NSCLC). *BMC Cancer* 9:300.

56. Györffy B et al. (2006) Gene expression profiling of 30 cancer cell lines predicts resistance towards 11 anticancer drugs at clinically achieved concentrations. *International Journal of Cancer* 118:1699–1712.

57. Sung JH, Shuler ML (2009) In vitro microscale systems for systematic drug toxicity study. *Bioprocess and Biosystems Engineering* 33:5–19.

58. Dittrich PS, Manz A (2006) Lab-on-a-chip: microfluidics in drug discovery. *Nat Rev Drug Discov* 5:210–218.

59. Su X et al. (2011) Microfluidic Cell Culture and Its Application in High-Throughput Drug Screening. *Journal of Biomolecular Screening* 16:101 –111.

60. Wen Y, Yang S-T (2008) The future of microfluidic assays in drug development. *Expert Opinion on Drug Discovery* 3:1237–1253.

61. Hattersley S et al. A Microfluidic System for Testing the Responses of Head and Neck Squamous Cell Carcinoma Tissue Biopsies to Treatment with Chemotherapy Drugs. *Annals of Biomedical Engineering*:1–12.

62. Zhang L, Wang J, Zhao L, Meng Q, Wang Q (2010) Analysis of chemoresistance in lung cancer with a simple microfluidic device. *ELECTROPHORESIS* 31:3763–3770.

63. Zhu X et al. (2004) Arrays of horizontally-oriented mini-reservoirs generate steady microfluidic flows for continuous perfusion cell culture and gradient generation. *Analyst* 129:1026–1031.

64. Tirella A, Marano M, Vozzi F, Ahluwalia A (2008) A microfluidic gradient maker for toxicity testing of bupivacaine and lidocaine. *Toxicology in Vitro* 22:1957–1964.

65. Lee K et al. (2009) Microfluidic network-based combinatorial dilution device for high throughput screening and optimization. *Microfluidics and Nanofluidics* 8:677–685.

66. Sugiura S, Edahiro J, Kikuchi K, Sumaru K, Kanamori T (2008) Pressure-driven perfusion culture microchamber array for a parallel drug cytotoxicity assay. *Biotechnology and Bioengineering* 100:1156–1165.

67. Sugiura S, Hattori K, Kanamori T (2010) Microfluidic Serial Dilution Cell-Based Assay for Analyzing Drug Dose Response over a Wide Concentration Range. *Anal Chem* 82:8278–8282.

68. Jedrych E et al. (2011) Evaluation of cytotoxic effect of 5-fluorouracil on human carcinoma cells in microfluidic system. *Sensors and Actuators B: Chemical* 160:1544–1551.

69. Xu Y, Lv Y, Wang L, Xing W, Cheng J (2012) A microfluidic device with passive air-bubble valves for real-time measurement of dose-dependent drug cytotoxicity through impedance sensing. *Biosensors and Bioelectronics* 32:300–304.

70. Gao D et al. (2010) A microfluidic approach for anticancer drug analysis based on hydrogel encapsulated tumor cells. *Analytica Chimica Acta* 665:7–14.

71. Wang Z, Kim M-C, Marquez M, Thorsen T (2007) High-density microfluidic arrays for cell cytotoxicity analysis. *Lab Chip* 7:740–745.

72. Gong Z et al. (2010) Drug effects analysis on cells using a high throughput microfluidic chip. *Biomedical Microdevices* 13:215–219.

73. Liu MC, Tai Y-C (2010) A 3-D microfluidic combinatorial cell array. *Biomedical Microdevices* 13:191–201.

74. Wu M-H et al. (2011) Development of high throughput microfluidic cell culture chip for perfusion 3-dimensional cell culture-based chemosensitivity assay. *Sensors and Actuators B: Chemical* 155:397–407.

75. Wu M-H, Huang S-B, Cui Z, Cui Z, Lee G-B (2008) Development of perfusion-based micro 3-D cell culture platform and its application for high throughput drug testing. *Sensors and Actuators B: Chemical* 129:231–240.

76. Sunkara V et al. (2011) Simple room temperature bonding of thermoplastics and poly(dimethylsiloxane). *Lab Chip* 11:962–965.

CHAPTER 5

Selective Electrochemical Lysis Of Eukaryotic Cells In Mixed Samples

5.1 ABSTRACT

Selective separation of prokaryotic cells from a mixed sample of prokaryotic and eukaryotic cells in the microfluidic regime is essential for many analytical and diagnostic purposes. We report here a method for efficient separation of prokaryotic cells in mixed cultures using the selective electrochemical lysis of eukaryotic cells. We have developed a microfluidic platform that can electrochemically lyse eukaryotic cells, due to the production of hydroxide ions, while show little or no lysis of prokaryotic cells, by virtue of the presence of a highly cross linked peptidoglycan cell wall layer. Using our platform, we report that under an optimal voltage of 3.5 V, HeLa (mammalian) cell lines are completely lysed in about 1 minute. However, under similar conditions the prokaryotic bacterial cells, gram negative *Escherichia coli* and gram positive *Streptococcus lactis* show little to no lysis. We also demonstrate that starting from a mixed culture; one can selectively lyse eukaryotic cells, leaving behind the prokaryotic population. Although the remaining prokaryotic cells are non-viable, they can still be detected and identified using staining or PCR-based methods.

5.2 INTRODUCTION

Prokaryotic bacterial cells are omnipresent. Bacteria interact with human beings very closely by means of mutualism, commensalism, and parasitism. An example of the interactions between bacteria and human can be found in the human gut. Composed of up to 100 trillion cells, [1] the microbiome acts in a very concerted manner to complement the needs of its human host. As such, bacteria have been implicated in disease [2,3] and the well-being [4,5] of host humans. A thorough study of these prokaryotic pathogens or symbionts is therefore necessary for understanding their effects on human health. Earlier bacterial enrichment methods were focused on the culture of bacterial cells found in clinical samples to detectable levels and then performing biochemical characterization to identify the organisms present [6]. Without this culture of bacterial cells, the number of bacteria is often too few to affect a proper diagnosis (particularly in the case of blood sepsis) [7]. Culturing generally takes three days to grow enough bacteria and is vulnerable to contamination [6]. To improve the speed of detection, techniques such as bacterial staining [8], radiometric detection [9] and PCR amplification [2,10,11] have been developed. However, less than 0.1% of Earth's estimated microbial life can be isolated and grown in lab. [12] Hence non-culture based studies were started, which rely heavily on high-throughput DNA sequencing technologies, present in the market today, to develop metagenomic maps of the human gut microbiome.[13]

A common bottleneck that all of the above procedures have is sample preparation. The samples that are studied are generally a complex heterogeneous mixture of human and bacterial cells, and most of these techniques would benefit if the bacteria were separated, concentrated, and purified from the clinical samples before analysis starts [14]. Specifically, bacterial purification might remove unwanted inhibitory compounds in the raw sample [11], reduce gene amplification and sequencing 'noise' [15] and reduce the sample volume and costs for diagnosis [14]. Hence techniques are needed to selectively separate out bacterial cells, in clinical samples, from other components, mainly human cells.

A lot of bacterial separation systems have been reported. Mechanical methods such as centrifugation and filtration are not very efficient when the percentage of bacterial cells is small. To alleviate this, the lysis centrifugation system was developed. In this method, blood cells are loaded in a centrifuge tube with a coating of lytic agents [16,17]. These lytic agents lyse the human blood cells, and after centrifugation sediment containing the microbial cells is formed. This method however leaves the human cell lysate unusable due to prolonged exposure to the lytic agent. Also, immunomagnetic separations have been reported for specific bacterial separation [10,11]. However this technique has to be optimized for each system [14], making it a costly option.

Microfluidics has emerged as a methodology for the development of total analysis systems in biology [18]. Microfluidics provides a promise of small sized chips capable of performing complicated physical and chemical operations in a time and power efficient way and incurring very low production and operation costs. As such researchers have reported microfluidic separation technique like DEP [15], FACS [19] and hydrodynamic separation [20]. However, these techniques require expensive equipments and very precise control of flow rates.

In the previous chapters, electrochemical lysis has been introduced as an effective method for on-chip cell lysis with reduced complexity over traditional methods [21,22]. This methodology involves the on-chip electrochemical generation of hydroxide ions. These hydroxide ions serve as the lytic agent for the mammalian cell lines tested. The hydroxide is generated at low voltages ($< 4\ V$) and acts to generate detergent-like compounds (fatty acids and lysophospholipids) from cellular membrane lipids. Also, unlike the addition of detergents or other chemical lytic agents, excess hydroxide is quenched further downstream when it recombines with hydrogen ions generated at the anode [22]. Interestingly, the membrane architectures of prokaryotes and eukaryotes are very different. The prokaryotes have a highly cross-linked peptidoglycan cell wall protecting their phospholipid bilayer cell membrane. This cell wall provides the rigidity to these cells, which increases their resistance to lysis in the presence of hydroxide ions (as is used during gram staining [23]) for a limited period of time. This difference in the biophysical lysis mechanisms of eukaryotes and prokaryotes suggests that on-chip generation of hydroxide ions by electrochemical means can be used to selectively lyse eukaryotic human cells in a mixed sample (Figure 5.1).

In this study we aimed at utilizing this phenomenon to develop a platform for the selective electrochemical lysis of human cells in a mixed culture with bacteria. The cell line chosen was epithelial HeLa cells to mimic the human cells present in human gut biopsy samples. Gram positive *Streptococcus lactis (S.lactis)* and gram negative *Escherichia coli (E.coli)*, both found in the gut, were used for this report. Using this platform, we demonstrate the complete lysis of human cells within 1 minute, when a voltage of 3.5 V is applied to the device. Under similar conditions the bacterial cells show no lysis, although they exhibit a loss of viability. We finally tested the device with mixed cultures of HeLa and the bacterial cells to demonstrate its

application in the selective separation of bacterial cells from mixed cultures like gut biopsies. Post lysis off-chip amplification of the mixed sample also demonstrates the ability of the system to aid in the selective removal of mammalian DNA (Appendix Figure C.1).

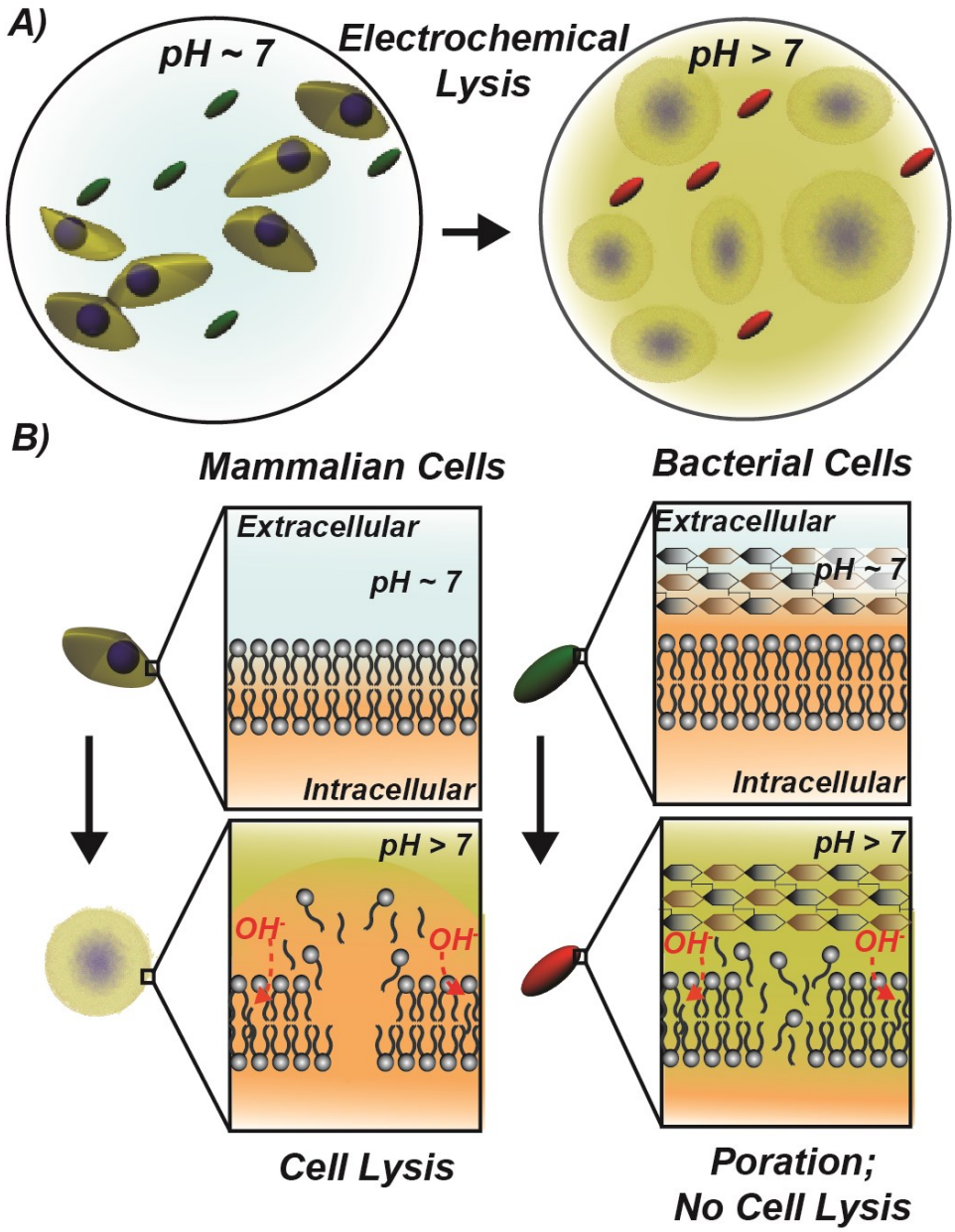

Figure 5.1: Principle behind electrochemical separation of mammalian DNA from mixed samples; **A)** The goal of the technique is to selectively lyse mammalian cells in mixed cultures, so that the mammalian DNA can be removed and the bacterial cells and DNA purified and studied further (Appendix Figure C.1). This will be achieved using on-chip electrochemical lysis, whereby the pH of the buffer is increased, which leads to the lysis of only mammalian cells. The bacterial cells in the process lose their viability (hence the change in their color to red); **B)** The mammalian cells are more vulnerable to an increase in pH as the hydroxide ions generated, during electrochemical lysis, attack the cell membrane. In case of bacterial cells, the cross-linked peptidoglycan cell wall is resistant to hydroxide ions and maintains the rigidity of the cell, hence preventing lysis. The bacterial cell membrane does get porated which makes the bacterial cells non-viable.

5.3 SELECTIVE LYSIS OF MAMMALIAN CELLS IN 20mM [OH^-] SOLUTION

Prior to selective lysis experiments on a microfluidic platform, a series of off-chip experiments were done to verify that electrochemical hydroxide generation could lyse mammalian cells but not bacterial cells. These experiments involved the exposure of the different cells (HeLa, *E.coli* and *S.lactis*) to the pH to which they would be exposed to during the operation of the device. Prior publications [21] have reported that a 20mM [OH^-] solution leads to the lysis of HeLa cells. Therefore all the cell lines were exposed to a 20mM NaOH solution for about 2 min (to ensure complete lysis of HeLa cells) and then microscopically evaluated for the presence or absence of cell lysis. The results (Appendix Figure C.2) show that all HeLa cells are lysed at this pH within 2 minutes. However, in case of the bacterial cells, the control and the treated samples look almost identical. Hence, we proved our hypothesis of selective lysis of mammalian cells via hydroxide attack in a basic solution. At a hydroxide concentration of 20mM (which was known from previous work to be needed for cell lysis), we saw that human eukaryotic cells lysed whereas the bacterial cells showed little or no lysis. This demonstrates the difference in the response of human and bacteria cells to hydroxide ions exposure and the possibility to use this to achieve selective lysis of human cells and isolate the bacterial population in a mixed culture.

5.4 ELECTROCHEMICAL LYSIS OF MAMMALIAN CELLS

The principle behind electrochemical lysis has been discussed in previous chapters. The design of the microfluidic chip used for selective lysis experiments is shown in Appendix Figure C.3. In short, the microfluidic device consists of a sedimentation trap (similar to hydraulic jump traps) with electrodes upstream and downstream. The trap is a vertical channel expansion (channel height = 20 μm and trap height = 200 μm) where the cells sediment down and can be retained under constant perfusion, due to reduced shear stress. The electrode upstream of the trap is the cathode, which produces hydroxide ions by virtue of the electrolysis of water. The hydroxide ions are then transported by convective diffusion over the trapped cells and finally to the anode electrode downstream. Here the hydroxide ions are neutralized by the hydronium ions produced by the electrolysis of water.

The cells are loaded into the device using degas-driven flow technique. This technique depends on degassing the porous PDMS (under an external vacuum) which leads to a reduction in the channel pressure, when the inlet is covered by fluid, and hence to fluid flow into the channels [24]. In our experiments, the PDMS devices bonded onto glass slides (with Platinum electrodes), are put into a desiccator chamber and exposed to house vacuum for 20 minutes, with scotch tape blocking the outlet. Afterwards, a drop of the cell solution (~5 x 10^6 cells/ml) is put atop the inlet. The porous PDMS, which is degassed under vacuum, sucks in the cell solution from the inlet and hence the device gets filled up. Once the device fills up, the cells are allowed to settle for 20 minutes. After that, PBS is constantly perfused at 0.3 μl/min (flow velocity of 1.4×10^{-5} m/s per trap) through the device. At this flow rate, cells in the channels start moving, but the cells settled inside the trap remain stationary. This constant perfusion is important to remove cell lysate from the trap for further downstream analysis.

For cell lysis the electrodes were connected to a constant voltage source. The voltage was applied between the cathode and anode for a duration of up to 5 min. During this period, time-lapsed images of the trap (in phase contrast) were taken. These were analyzed to produce the lysis kinetics curves shown in Figure 5.2 a. As shown in Figure 5.2 a, the time for complete lysis increases with decreasing voltages. This is expected as lower voltage means lower hydroxide production rates. As the applied voltage decreased, the variance in lysis rates increased (shown as Standard Error in the shaded region of graph). The reason for this is the fact that at lower voltages, due to increased lysis time, device and cell variations might play a larger role pushing up population variance.

We observed that for voltages below 2 V, the lysis times were unallowably high, whereas for voltages 4 V and beyond, bubbles of non-dissolved gases (from the electrolysis reactions) started to appear at the electrodes. Hence the experiment was restricted to applied voltages within this range. From the graph in Figure 5.2 b, it is clear that a voltage of 3.5 V is optimal for the lysis of HeLa cells, within 1 minute. Figure 5.2 c shows the time lapsed images of the lysis of HeLa cells. Lysis events led to a change in the phase of the cells in the phase contrast images. The lysis proceeds from left to right, as the hydroxide producing cathode is to the left of the trap.

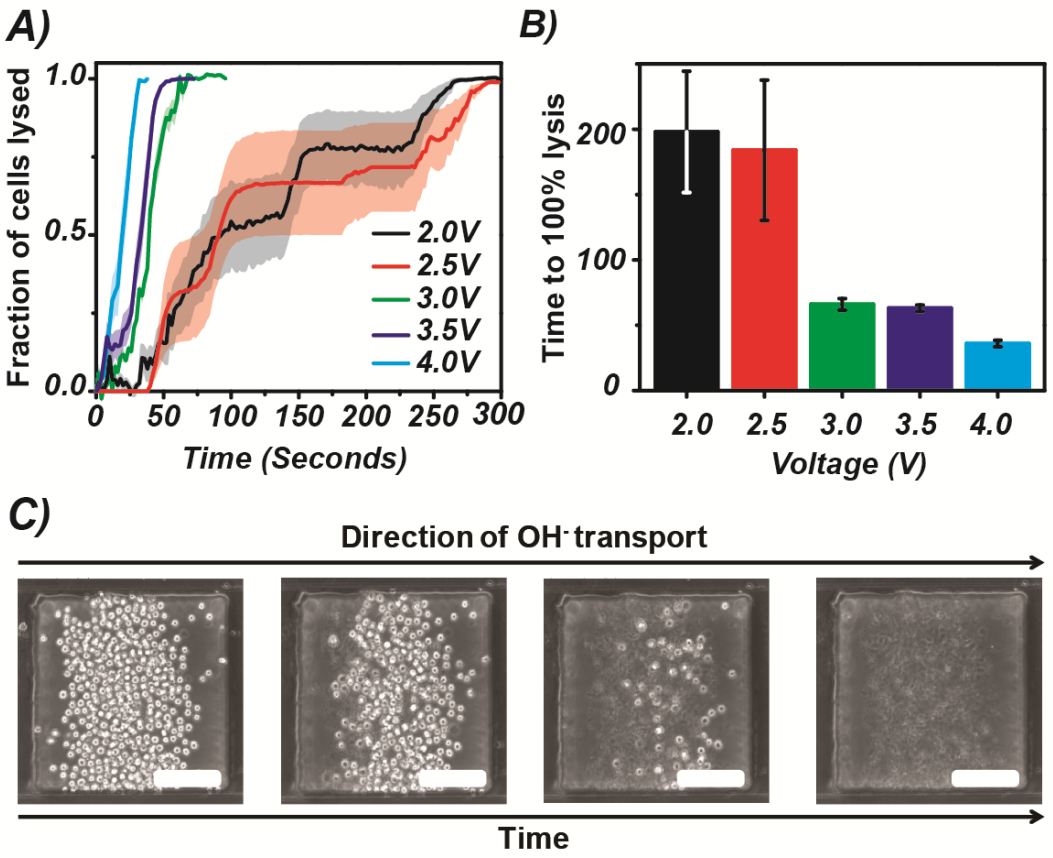

Figure 5.2: Electrochemical lysis of HeLa cells; **A)** and **B)** The dependence of lysis rates on the voltage applied to the system. As can be seen, at higher voltages the total lysis time goes down. However for voltages of 4 V and beyond, the rate of hydroxide ion production exceeds its usage leading to bubbling at the electrodes. For lower voltages, it can be seen that lysis times are prohibitively large. Also at such low voltages, lysis rates start to depend more on experimental conditions, leading to the broad deviation (from mean) that is observed. Hence the device would be run at an optimal voltage of 3.5 V; **C)** Time lapse images showing lysis of HeLa cells in the device. The

hydroxide ions are produced to the left of the trap and move towards the right of the trap. Images are phase contrast taken at 20X. The scale bar shown is 100 μm in length.

5.5 ATTENUATED ELECTROCHEMICAL LYSIS OF PROKARYOTIC BACTERIAL CELLS

The next step was to determine whether the bacterial cells would get lysed at the optimal condition for lysis of HeLa cells. The loading and experimental conditions were similar to what have been described previously for mammalian cells. A voltage of 3.5 V was applied for both 1 minute and 5 minutes. Time-lapsed phase contrast images were taken of the traps during the period the voltage was applied. The results are shown in Figure 5.3 a. For both gram positive *S. lactis* and gram negative *E. coli*, the lysis rates were quite small in comparison to HeLa cells. The range of the fraction of lysed cells was ± 0.1 (10%) indicating little, if any, lysis of bacterial cells. Figure 5.3 b shows time lapsed images of the bacteria during the lysis process. The images show no appreciable difference in number of cells with respect to time of application of the voltage. Also the cells had no apparent visible changes in shape, size or morphology. There were fluctuations in the analyzed lysis data due to noise which prohibited statistical analysis of the lysis rates. The noise in the lysis kinetics data came from image processing limitations and also the fact that the flow was carrying a few bacteria from the channels across the traps. These noise elements prevented further statistical analysis comparing the two cell lines.

A live/dead stain was performed to assess the viability of the bacterial cells before and after lysis. Bacterial viability kit (Invitrogen, BacLight) was used for assessing the viability of the bacterial cells. For this purpose 9 μl of an equi-mixture of Component A and B was added to 3 ml of Phosphate Buffered Saline. This mixture was then perfused through the device at 0.3 μl/min and the device is incubated in dark for 30 min. During this time the device was kept in the dark at room temperature. Afterward, the device was observed under a fluorescent microscope to assess viability of the cells. As can be seen from Figure 5.3 c, the viability drops to almost zero after 1 minute exposure to 3.5 V in the device. This loss in viability is observed in both bacterial cell lines. Figure 5.3 d shows fluorescent images of the bacterial cells showing the loss in viability after exposure to hydroxide ions. This loss in viability is expected from the fact that the hydroxide ions still attack the proteins and carbohydrates on the surface of the cell wall hence denaturing them. These lead to poration of the bacterial cells, which makes them non-viable, but the cell wall helps maintain the rigidity of the cell preventing lysis. The genomic DNA of the bacterial cells (stained by the live-dead stain) was found to be co localized with the non-viable cells (by comparing the fluorescent and phase contrast images) indicating the fact that the DNA of the non-viable cells can still be purified from the mammalian cell lysate.

5.6 SELECTIVE LYSIS OF MAMMALIAN CELLS IN MIXED SAMPLES

We demonstrate the selective separation of bacterial cells from the mixed cultures in our microfluidic devices using phase contrast imaging and nucleic acid amplification. These cultures were prepared by mixing HeLa cells with *S.lactis* or *E.coli*, at different population ratios (HeLa to bacteria ratios) being varied from 1:1, 10:1 and 1:10. These ratios were chosen to test the dynamic range of this method. The different mixed cultures were introduced into the device as described previously. This was followed by the applications of 3.5 V for 1 minute. Phase-contrast images of the traps were taken before and after the application of the voltage. The results are summarized in Figure 5.4. As shown in Figure 5.4, with varying population ratios, we

could still recover the bacterial population from mixed cultures. The mammalian cell lysate was washed away from the device, leaving the settled bacterial cells in the traps. Also almost all the bacterial cells in the traps are retained during the lysis of the human cells. This demonstrates the capability of this system for selective separation of bacterial population from biological samples like gut biopsies.

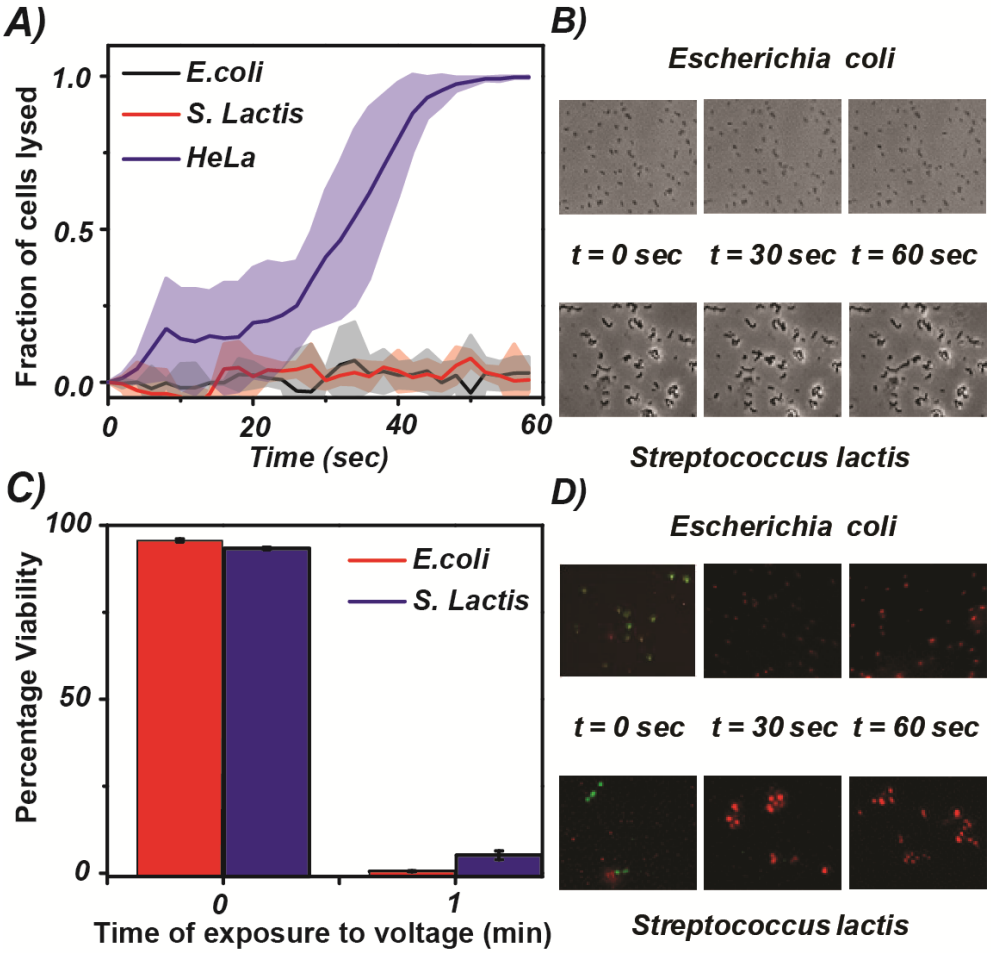

Figure 5.3: Comparison of Prokaryotic and Eukaryotic lysis rates **A)** Graph comparing the lysis times of HeLa, *E.coli* and *S.lactis* cells. As can be seen, the bacterial cells have a very low lysis rate; **B)** Phase contrast images (at 40X) of the bacterial cells showing minimal change in morphology, shape or size due to hydroxide exposure; **C)** The viability of the bacterial cells falls to almost zero with 1 minute exposure to electrochemically produced hydroxide ions; **D)** Live and dead stain results for viability of bacterial cells. A red stain implies a non-viable cell while a green stain implies a viable cell. As can be seen, without exposure to voltage the cells are majorly viable. However after exposure their viability drops to almost zero. The gram positive bacteria show higher viability after treatment, which might reflect their thick peptidoglycan layer.

The main purpose of selective lysis of mammalian cells is to separate bacterial cells, mainly their nucleic acid content. Hence, we attempted to remove mammalian DNA from mixed samples following the selective lysis of the mammalian cells. To achieve this, the mixed sample of HeLa and *E.coli* in a 1:10 (HeLa:*E.coli*) ratio was introduced into the microfluidic device. The sample was lysed in a continuous fashion, implying that the sample was continuously perfused through the device while being lysed. The flow rate was kept at 0.3 µl/min to ensure enough

residence time for the cells to lyse before they left the region in between the electrodes. This was possible because the residence time of the mammalian cells inside the trap region, owing to the low flow velocity in the trap, was more than the time needed for the lysis of the mammalian cells. The outlet was collected and treated with RQ1 RNase-free DNase (from Promega), according to the manufacturer's instructions, to remove mammalian DNA present. The DNase activity was then halted and qPCR was done with the sample using a colony PCR mix (from Strategene with SyBr-green dye) with a primer pair targeted at the 16s rDNA target of *E.coli*.

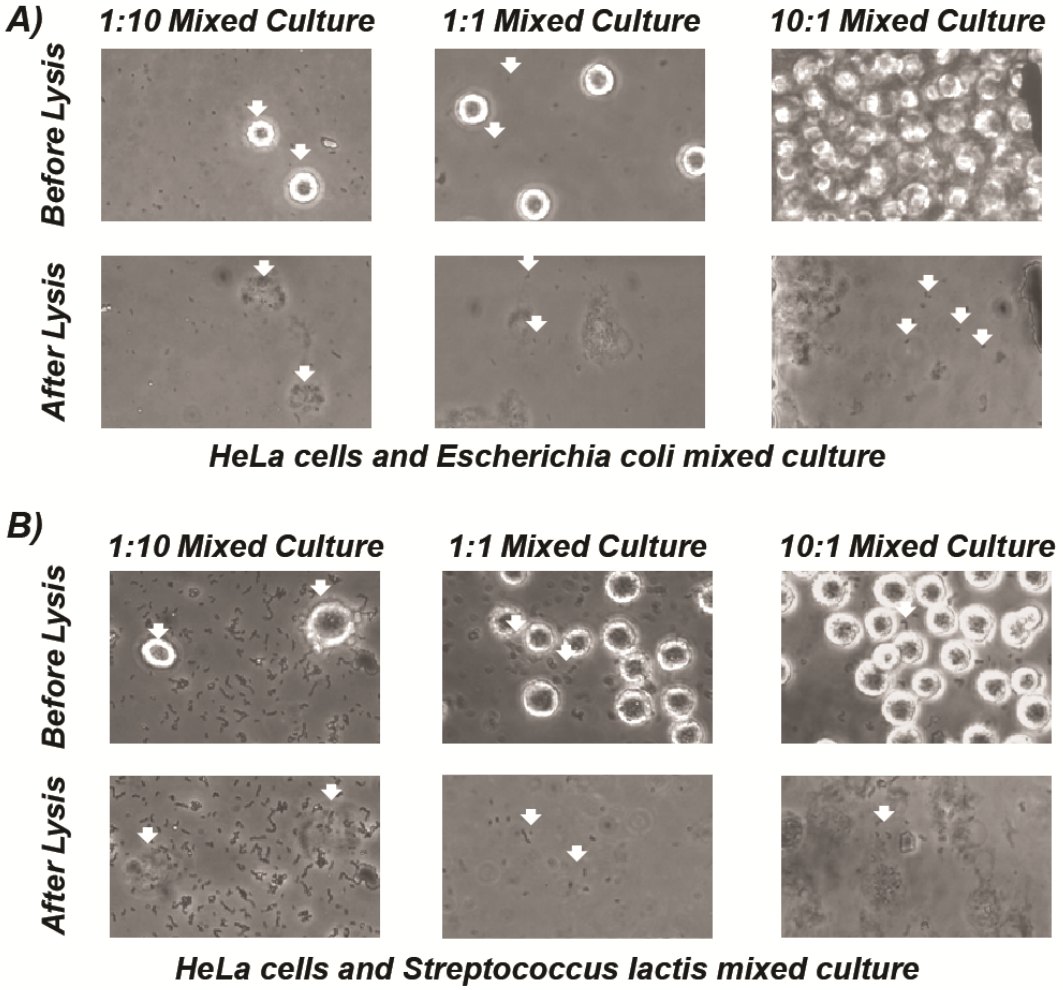

Figure 5.4: Selective separation of bacteria from mixed culture using SEL. Using our device we were able to selectively lyse HeLa cells in mixed cultures with bacterial cells **A)** for *E. coli* and **B)** for *S. lactis.* We tried three different concentration ratios (HeLa: bacteria), 1:10, 1:1 and 10:1, to reflect the range of operation of our device. As can be seen from the image, the HeLa cells were selectively lysed leaving behind the prokaryotic population. These cells can then be used for further downstream analysis. Some markers have been put on the images for comparison purposes.

The result of this real time assay is shown in Figure 5.5. The inlet sample is seen to have very minimal signal arising from the fact that the overabundance of mammalian DNA reduces the binding rate between the primer and bacterial DNA. Other research has also pointed out that

human cells should also be removed from mixed samples prior to bacterial DNA amplification [25] . Main reasons for this are; mammalian DNA would compete with bacterial DNA (which will be present in much lesser quantities) during amplification leading to non-specific amplification noise and hence false positives, prevent the binding of primer with DNA of interest hence leading to false negatives and secondly mammalian DNA would also compete during DNA purification and also lead to false negative results [25,26]. The outlet sample is seen, in contrast, to have a larger signal due to the removal of mammalian DNA. The complete removal of mammalian DNA was confirmed by a RT-PCR assay using a GAPDH primer. The results (Appendix Figure C.4 a) demonstrates the complete removal of human DNA in the outlet sample. The positive controls for both GAPDH and 16s rDNA showed amplification indicating that the primers and the mixture conditions are appropriate for amplification. The 16s rDNA primer negative control (no template) showed a rise in fluorescence intensity, however the Ct values for this set was higher than our positive control and outlet samples.

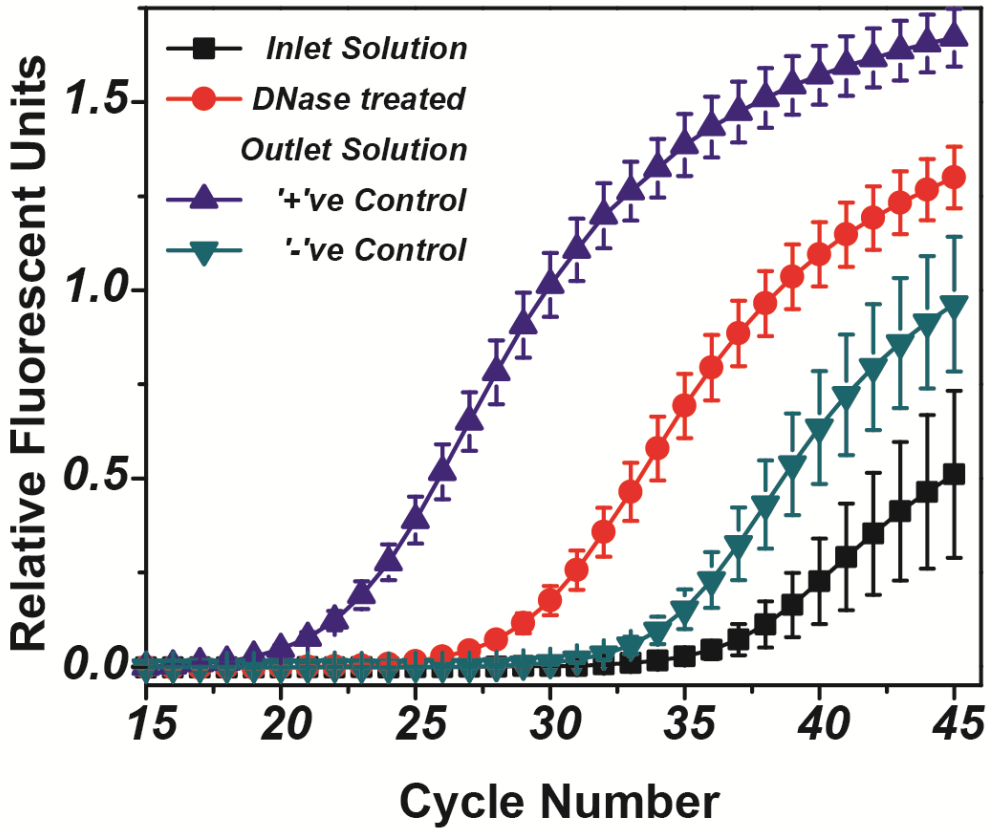

Figure 5.5: Separation of HeLa DNA from a mixed sample. The Inlet Solution contained 10^6 cells/ml HeLa cells mixed with 10^7 CFU/ml *E.coli.* A colony PCR kit was used with primers targeting the 16s rDNA gene of *E.coli*. The DNase treatment of outlet solution led to recovery of bacterial DNA signal, which is masked in the inlet sample due to presence of an excess of HeLa DNA. The Positive Control used had 10^7 CFU/ml *E.coli* and Negative Control was Molecular Grade D.I. Water.

5.7 BACTERIAL PORATION DURING ELECTROCHEMICAL LYSIS

The nucleic acid amplification results of electrochemically lysed bacterial solutions, after DNase treatment, show a distinctive loss in signal. This was observed even in off-chip samples where the bacterial solution was treated with NaOH solution (Appendix Figure C.4 b). However, DNA staining of the cells shows that the bacterial cellular DNA is still associated with the cells and not released into the surrounding. The bacterial DNA content is also not entirely removed, unlike mammalian DNA, supporting the hypothesis that the bacterial DNA is only partially exposed to the surrounding after electrochemical lysis. This implied the possibility that the bacterial cells are getting porated during the treatment and that the diffusion of DNase enzyme into the cells leads to the loss in bacterial DNA content. We decided to visualize and characterize this poration of bacterial cells within our microfluidic device. GFP (green fluorescent protein) transfected *E.coli* was used to visualize this poration and the results are shown Figure 5.6. GFP-*E.coli* were perfused into a microfluidic device where hydroxide ions were generated upstream of the bacteria at an applied voltage of 3.5V. The microfluidic device has an expansion region were flow rate is decreased and the E. coli sediment to the floor the device. Upon application of current, hydroxide ions are convectively transferred into the trap region and leads to the loss of fluorescence of the *E.coli* , as shown in the false color images sequence in Figure 5.6 a, which indicates the poration of the bacterial membranes. The experimental results indicate that over 97% of the GFP *E. coli* are porated, as indicated by a loss in fluorescence (Figure 5.6 b).

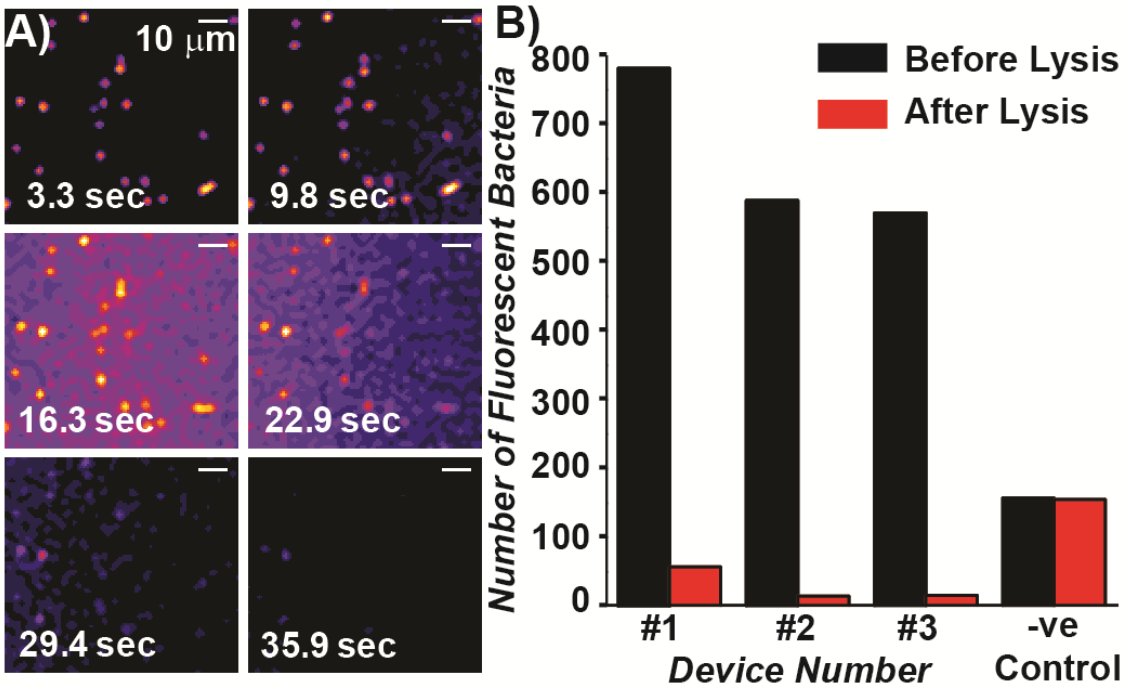

Figure 5.6: Poration of bacterial cells during electrochemical lysis demonstrated using Green Fluorescent Protein (GFP) transfected *E.coli* cells; **A)** False color image sequence of cell poration (evidenced by their rapid loss of fluorescence) as the hydroxide ion wave front (generated via electrochemical hydrolysis) passes through the microfluidic device (from right to left); **B)** Analysis of fluorescent images from the microfluidic devices implies that electrochemical lysis achieves fluorescent loss in over 97% of bacteria cells.

5.8 CONCLUSION

In this chapter we have presented a new technique for the selective separation of prokaryotic bacterial cells from mixed biological samples containing prokaryotic and eukaryotic cells. This is made possible by the fact that bacterial cells (both gram positive and gram negative) have rigid cell walls containing the highly cross-linked peptidoglycan. Cell walls make these cells more resistant to hydroxide lysis. On the other hand, the phospholipid bilayer of eukaryotic cells has a different chemical composition which is prone to nucleophilic attack. As a result, eukaryotic cells, which lack cell walls, will lyse quickly when exposed to hydroxide ions. Hence, when a mixed culture is exposed to hydroxide ions for a limited period of time, the eukaryotic human cells lyse, leaving behind the prokaryotic bacterial population.

This system was realized as an expansion of the microfluidic electrochemical lysis devices already demonstrated in the previous chapters. The final device design had a sedimentation trap to allow immobilizing small bacterial cells in our device and retain the sediment cells even under perfusion flow of Phosphate Buffered Saline. Perfusion flow is important to remove cell lysate for downstream analysis and also to remove residual hydroxide ions after the applied voltage is removed. Each device had six traps and electrodes were designed on either side of the traps, and the flow was along the direction of movement of hydroxide ions, i.e. from cathode to anode. A disadvantage with this device design is the fact that cells also settle along the channels. Those cells may interfere with data collection when they are washed away when perfusion starts. However, the focus of this work was to demonstrate the phenomenon of selective electrochemical lysis and further work involved continuous flow lysis without the need of cell immobilization.

Experiments done with HeLa epithelial cells (to mimic human cells present in gut biopsy samples) confirmed lysis trends observed in our previous studies. With decreasing applied voltage, the lysis rate decreased and hence the time for complete lysis of the cells increased. At very low voltages, it was observed that device-to-device and cell-to-cell variations became more and more pronounced, raising the standard error of the data. This was an interesting observation, and gave the rationale for a lower bound to the optimal lysis voltage. At very high voltages, the rate of hydroxide and hydrogen ion production exceeded their solubility in PBS, leading to the formation of gas bubbles at the electrodes. This observation provided us with the upper bound to the optimal lysis voltage.

The maximum electric field used in our experiments was 18.2 V/cm (which is still an order of magnitude less than that needed for electroporation) confirming the fact that lysis took place due to electrochemically produced hydroxide ions. Also in phase contrast videos, it was clearly seen that the lysis progressed from upstream of the traps towards downstream. This was again a confirmation that lysis happened due to the hydroxide ions produced at the cathode. Once the optimal conditions of lysis for human cells were determined, bacterial cells were exposed to the same conditions. The bacteria chosen were gram positive *S. lactis* and gram negative *E. coli*, both known to colonize the human gut. The two bacteria differed in the presence of an external membrane (in case of *E. coli*) and the thickness of the peptidoglycan layer (thicker in case of *S. lactis*). Surprisingly, both bacterial strains were completely resistant to lysis during the time period of observation. Also, the cells showed a loss of viability after the treatment, possibly due to hydroxide ions attacking the surface proteins. In any case, these cells were still intact and could be analyzed using staining or PCR. To show the applicability of this method, we finally introduced a mixed culture of HeLa and bacterial cells in the device. As expected, after the

application of the lysis voltage, the human cells lysed and their lysate was removed by a continuous perfusion, while the bacterial population still remained in the traps. The lysate collected from these mixed samples was further analyzed using PCR assays which demonstrated the complete release of mammalian nucleic acid. The bacterial nucleic acids were retained within the cells; however poration of cell membrane made these nucleic acids susceptible to enzymes in the buffer. Nonetheless if physical methods of separation of the non-viable bacterial cells are used, this loss in bacterial nucleic acids can be minimized.

5.9 ACKNOWLEDGEMENTS

I would like to acknowledge Tiffany Chen, Frank B. Myers and Supada Sritanyaratana for their contribution to this work. I also acknowledge the Biomolecular Nanotechnology Centre (BNC) and Paul Lum for his help and support. Funding for this work was provided by NIH (R01 CA120003-01A2) and the CNMT (2010K000352, 2010K000353, and 2010K000354) of the Ministry of Education, Science and Technology, Korea.

5.10 REFERENCES

1. D C Savage, "Microbial Ecology of the Gastrointestinal Tract," Nov. 2003.

2. D. De Wit, L. Steyn, S. Shoemaker, and M. Sogin, "Direct detection of Mycobacterium tuberculosis in clinical specimens by DNA amplification.," *J. Clin. Microbiol.*, vol. 28, Nov. 1990, pp. 2437-2441.

3. D.C. Angus, C.A. Pires Pereira, and E.[. Silva, "Epidemiology of Severe Sepsis Around the World," *Endocrine, Metabolic & Immune Disorders - Drug Targets(Formerly Current Drug Targets - Immune, Endocrine & Metabolic Disorders)*, vol. 6, Jun. 2006, pp. 207-212.

4. F. Backhed, R.E. Ley, J.L. Sonnenburg, D.A. Peterson, and J.I. Gordon, "Host-Bacterial Mutualism in the Human Intestine," *Science*, vol. 307, Mar. 2005, pp. 1915-1920.

5. J. Kinross, A. von Roon, E. Holmes, A. Darzi, and J. Nicholson, "The human gut microbiome: Implications for future health care," *Current Gastroenterology Reports*, vol. 10, 2008, pp. 396-403.

6. P. Yagupsky, "Detection of Brucellae in Blood Cultures," *J. Clin. Microbiol.*, vol. 37, Nov. 1999, pp. 3437-3442.

7. "Simple method of monitoring colonising microbial load in chronic bronchial sepsis: pilot comparison of reduction in colonising microbial load with antibiotics given intermittently and continuously.," Aug. 1987.

8. L.R. McCarthy and J.E. Senne, "Evaluation of acridine orange stain for detection of microorganisms in blood cultures.," *J. Clin. Microbiol.*, vol. 11, Mar. 1980, pp. 281-285.

9. H.J. DeBlanc, F. DeLand, and H.N. Wagner, "Automated Radiometric Detection of Bacteria in 2,967 Blood Cultures," *Appl. Environ. Microbiol.*, vol. 22, Nov. 1971, pp. 846-849.

10. "Immunomagnetic separation and PCR for detection of Mycobacterium ulcerans.," Oct. 1997.

11. P. Muir, F. Nicholson, M. Jhetam, S. Neogi, and J.E. Banatvala, "Rapid diagnosis of enterovirus infection by magnetic bead extraction and polymerase chain reaction detection of enterovirus RNA in clinical specimens.," *J. Clin. Microbiol.*, vol. 31, Jan. 1993, pp. 31-38.

12. K. Zengler, G. Toledo, M. Rappé, J. Elkins, E.J. Mathur, J.M. Short, and M. Keller, "Cultivating the uncultured," *Proceedings of the National Academy of Sciences of the United States of America*, vol. 99, Nov. 2002, pp. 15681-15686.

13. P.J. Turnbaugh, R.E. Ley, M. Hamady, C.M. Fraser-Liggett, R. Knight, and J.I. Gordon, "The Human Microbiome Project," *Nature*, vol. 449, Oct. 2007, pp. 804-810.

14. Kelly A. Stevens and Lee-Ann Jaykus, "Bacterial Separation and Concentration from Complex Sample Matrices: A Review," Oct. 2008.

15. Y. Huang, S. Joo, M. Duhon, M. Heller, B. Wallace, and X. Xu, "Dielectrophoretic Cell Separation and Gene Expression Profiling on Microelectronic Chip Arrays," *Analytical Chemistry*, vol. 74, Jul. 2002, pp. 3362-3371.

16. J.C. McLaughlin, P. Hamilton, J.V. Scholes, and R.C. Bartlett, "Clinical laboratory comparison of lysis-centrifugation and BACTEC radiometric blood culture techniques.," *J. Clin. Microbiol.*, vol. 18, Nov. 1983, pp. 1027-1031.

17. H. Richet, M.C. Escande, and P.H. Lagrange, "Lysis centrifugation and slide blood culture systems for diagnosis of bacteremia in immunocompromised patients," *European Journal of Clinical Microbiology & Infectious Diseases*, vol. 6, Feb. 1987, pp. 64-67.

18. S. Lee and S. Lee, "Micro total analysis system (μ-TAS) in biotechnology," *Applied Microbiology and Biotechnology*, vol. 64, Apr. 2004, pp. 289-299.

19. "Micro- and nanotechnology in cell separation," Mar. 2006.

20. Z. Wu, B. Willing, J. Bjerketorp, J.K. Jansson, and K. Hjort, "Soft inertial microfluidics for high throughput separation of bacteria from human blood cells," *Lab on a Chip*, vol. 9, 2009, pp. 1193-1199.

21. D.D. Carlo, C. Ionescu-Zanetti, Y. Zhang, P. Hung, and L.P. Lee, "On-chip cell lysis by local hydroxide generation," *Lab on a Chip*, vol. 5, 2005, pp. 171-178.

22. J.T. Nevill, R. Cooper, M. Dueck, D.N. Breslauer, and L.P. Lee, "Integrated microfluidic cell culture and lysis on a chip," *Lab on a Chip*, vol. 7, 2007, pp. 1689-1695.

23. H. Henry and M. Stacey, "Histochemistry of the Gram-Staining Reaction for Micro-Organisms," *Proceedings of the Royal Society of London. Series B, Biological Sciences*, vol. 133, Dec. 1946, pp. 391-406.

24. Hosokawa, K., Sato, K., Ichikawa, N. & Maeda, M. Power-free poly(dimethylsiloxane) microfluidic devices for gold nanoparticle-based DNA analysis. *Lab Chip* **4**, 181–185 (2004)

25. Handschur, M., Karlic, H., Hertel, C., Pfeilstöcker, M. & Haslberger, A.G. Preanalytic removal of human DNA eliminates false signals in general 16S rDNA PCR monitoring of bacterial pathogens in blood. *Comparative Immunology, Microbiology and Infectious Diseases* **32**, 207-219 (2009).

26. Yang, S. & Rothman, R.E. PCR-based diagnostics for infectious diseases: uses, limitations, and future applications in acute-care settings. *The Lancet Infectious Diseases* **4**, 337-348 (2004).

27. M.A. McClain, C.T. Culbertson, S.C. Jacobson, N.L. Allbritton, C.E. Sims, and J.M. Ramsey, "Microfluidic Devices for the High-Throughput Chemical Analysis of Cells," *Analytical Chemistry*, vol. 75, Nov. 2003, pp. 5646-5655.

CHAPTER 6

Portable And Power-Efficient Microfluidic Actuation Using Proximal Degas-Driven Flow

6.1 ABSTRACT

Portable and miniaturized actuation techniques, for biofluids, in microfluidic chips are essential to realize point of care microfluidic diagnostic devices. Although many fluidic actuation schemes have been developed for microfluidic devices, most of these techniques either are too complex, dependent on external power and bulky or are too simplified and hence not amenable to controlled and complicated flow patterns. In this chapter we report on the development of a novel fluid actuation technique, titled Proximal Degas-driven Flow (PDF), which is portable and can provide controlled fluid pumping using minimal external power. This system also alleviates the need for special device treatment and packaging, is not susceptible to bubbles and can be used for complex geometries, including dead-end chambers and channels. We developed a theoretical model to characterize fluid flow using PDF and have also identified key parameters that determine the flow behavior, achieving flow velocities in the range of 0.8 to 7 mm/sec. These parameters can hence be controlled, to attain a desired flow condition, depending on the device requirements. Also PDF is realized using a portable finger powered membrane pump which will be ideal for microfluidic POCT systems.

6.2 INTRODUCTION

Microfluidic technologies promise to significantly impact the field of point-of-care testing (POCT) by enabling rapid analyses of complex samples while minimizing sample volume and power requirements. The technique to be used for fluidic actuation is often the most important consideration in the design of microfluidic systems. A range of active and passive fluid control techniques have been described in the context of microfluidics over the past several decades (1, 2). A number of these methods have been incorporated into devices specifically designed for disease diagnostics in remote and resource-limited settings (3). However, in many cases, complex microfluidic systems still require bulky or energy-inefficient actuation components, while simpler systems lack the functionality required for a simple field diagnostic test.

Active actuation techniques are the ones that require external power to pump the fluid, while passive actuation techniques use more intrinsic properties, of the fluid and the channels, to actuate the flow with minimal need for external power. The most common active fluid actuation technique used by microfluidic POCT systems is pressure driven flow. This method relies on the difference in pressure between the liquid front, inside the microchannels, and the inlet; with the inlet being at a higher pressure. As such this form of actuation can be divided into positive pressure, with the inlet at a pressure above atmospheric pressure, or negative pressure, with the microfluidic channels at a pressure below atmospheric pressure, driven flow. The main advantages of pressure driven flow is the control over flow and the range of flow rates

achievable. However pressure driven requires exterior equipment such as syringe pump (4, 5) or a pressure/vacuum source (6, 7), and hence the entire setup can become bulky and costly. Also, such actuation is prone to bubbles; which can clog the microchannels (8); lead to oscillatory flow and cannot be used to fill up dead-end channels and chamber, which are useful for digitized and independent assays (9–11). Other active actuation techniques include centrifugal (12), electrokinetic (13) and acoustic (14) pumping. All these techniques provide advantages similar to pressure-driven flow, however they suffer from the same limitations; mainly the need for bulky, energy inefficient and costly external equipments. Centrifugal systems need a stably rotating platform while electrokinetic and acoustic systems need external power sources to either apply an electric or an acoustic field respectively. Hence, although the advantages of active actuation techniques make them attractive for a variety of applications, their limitations restrict their applicability as a portable fluidic actuation method needed for microfluidic POCT devices. Researchers have also developed portable micro-pumps for pressure driven flow which also need minimal power. Such pumps include pneumatic (2), piezoelectric (1), magnetic (1) and finger-operated diaphragm pumps (15–17). Although portable, these techniques are still susceptible to bubbles, require priming of the pump and not amenable to scaling, hence restricting their widespread use and adoption in microfluidic POCT systems.

Passive pumping techniques, with their minimal reliance on external equipments, are poised to overcome the shortcomings of active pumping techniques and provide researchers with an actuation method suitable for POCT systems. As a result, a lot of passive pumping techniques have been developed, which use no external equipment or power, including gravity-driven, surface tension-based, degas-driven and evaporation-based passive pumping. Gravity driven flow uses a liquid pressure head to create a pressure gradient along the microfluidic channel leading to fluid flow (18). However, given the large fluidic resistance of microchannels and the linear dependence of pressure on the height of the pressure head, generally only low flow rates are realizable using reasonable pressure head heights. Also to overcome surface pinning pressures, which can be significant for microchannels, most of the devices need to be primed, i.e. filled with fluid, prior to the use of gravity driven pumping. In surface tension based flow a pressure gradient is produced due to surface tension effects at the leading flow meniscus, as described by the Young-Laplace equations (19). Such flow has been demonstrated in capillaries, micro-patterned channels and paper-based microfluidic devices. Surface tension-based flow is however useful only when the specific liquid-gas-solid condition could provide enough capillary pressure to load the liquid automatically. Also such flow is vulnerable to surface defects and environmental conditions. Degas-driven fluid flow, utilizes the porous nature of poly(dimethylsiloxane) (PDMS), a common material used to prototype microfluidic chips, to store the energy required to pump fluid flow (20, 21). This is done by prior degassing of the device; whereby, during liquid loading, the PDMS bulk can pull air out of the channels leading to fluid flow. While this technique has several advantages such as the ability to pump a variety of fluids into complex geometries including dead end chambers or channels (22), it also possesses disadvantages such as the need for pre-degassing of the devices, device packaging and storage to maintain the degassed state and the susceptibility of the flow on small variations in the operational conditions.

A novel actuation technique, utilizing principles from both active and passive actuation methodologies, is described in this chapter. This actuation technique named Proximal Degas-driven Flow (PDF) can provide power-free, portable and controlled fluid flow in microfluidic devices. PDF takes advantage of the high porosity and air solubility of PDMS to reduce the

pressure inside microfluidic channels, using proximal microfluidic vacuum lines, which leads to fluidic actuation from the inlet (which is at atmospheric pressure). This actuation technique leads to bubble-free fluid flow and, in contrast to traditional pressure (positive or negative) driven flows, can be used to fill up dead end chambers and does not require the priming of channels and pump. Also, unlike degas-driven flow, PDF alleviates the need for pre-degassed and sealed devices and leads to a more consistent and long-lasting fluid flow. This technique requires very simple and cheap hardware like a vacuum bulb or membrane pump and hence is portable.

6.3 PRINCIPLE BEHIND PROXIMAL DEGAS-DRIVEN FLOW (PDF)

Proximal Degas-driven Flow (PDF) is a fluid actuation technique that aims to advance microfluidic device operation by providing an actuation technique that is portable, power-efficient, and tunable. The principle behind PDF and representative device design used for the initial characterization, reported in this chapter, is shown in Figure 6.1.

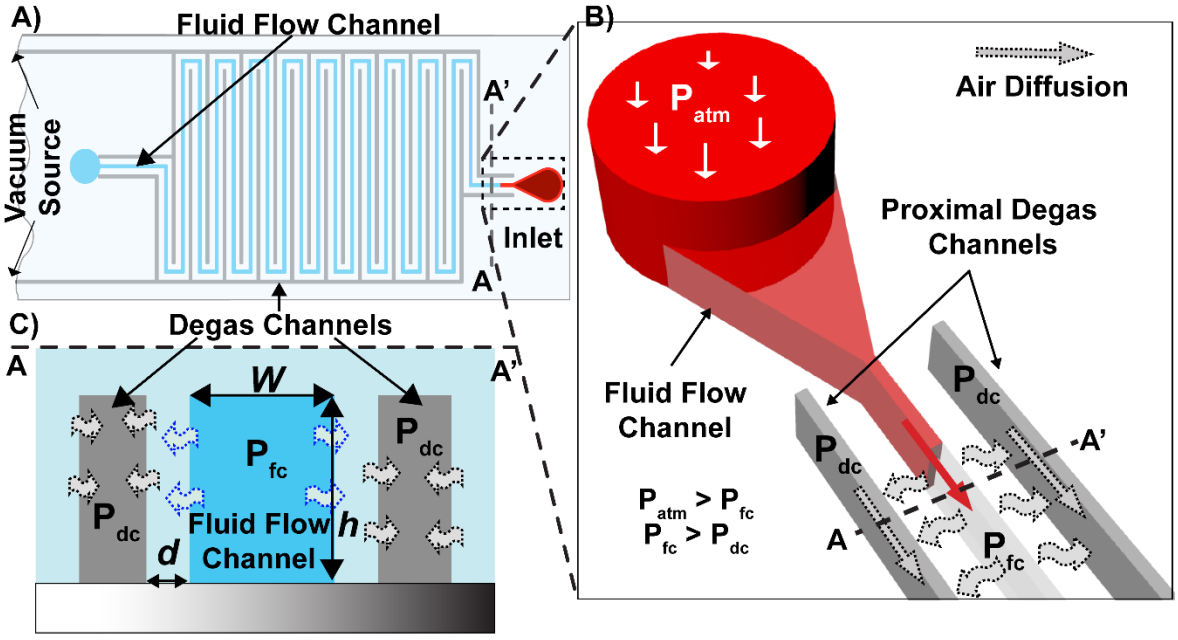

Figure 6.1: **A)** Representative device design of microfluidic devices used for the characterization of PDF. The device design involved a serpentine fluidic channel with proximal vacuum/degas channels surrounding the fluidic channel on both sides. The proximal channels were connected to a vacuum source; **B) and C)** Zoomed in view of liquid loading in the device. The proximal degas channel are at a pressure P_{dc}, which is substantially lower than the fluidic channel pressure P_{fc}. This leads to the diffusion of air out of the fluidic channels and into the degas channels. This leads to the reduction in fluidic channel pressure P_{fc} and hence P_{fc} becomes less than atmospheric pressure P_{atm}. This leads to a pressure gradient across the fluid plug which results in liquid loading into the microchannels.

This technique relies on microfluidic channels, proximal to the fluid channels, which are exposed to a reduced pressure (relative to the atmosphere i.e. vacuum) source. These proximal vacuum/degas lines in turn pull air from the fluid channels (Figure 6.1 b and c), owing to the permeability and solubility of air in PDMS, which leads to a reduction in pressure inside the fluid channels. Hence a pressure gradient is created, between the atmospheric pressure (P_{atm}) at the inlet and the fluid channel pressures, along the fluid column leading to fluid flow from the

inlet into the fluid channels. Many options exist for the reduced pressure source which can be used for PDF. For the initial characterizations we use a vacuum pump (with a bleed valve) to apply a measured and controlled vacuum pressure. This technique is ill suited for POCT applications and other sources such as a handheld vacuum bulb or a membrane diaphragm (thumb) pump can be used for POCT systems.

6.4 THEORETICAL ANALYSIS OF PDF

The driving force behind flow actuation in PDF is the reduction in channel pressure. This reduction in channel pressure is brought about by the diffusion of air out of the fluid channel and into the vacuum/degas channel. From Fick's 2nd law of diffusion, we get:

$$\frac{\partial C}{\partial t} = D\frac{\partial^2 C}{\partial x^2} \quad \text{-- (1)}$$

$$C = C_1 \; at \; x = 0$$
$$C = C_2(t) at \; x = d$$
$$C = C_0 \; at \; t = 0$$

Where, C is the concentration of air in the PDMS, C_1 is the concentration at the wall facing the degas channel, C_2 is the air concentration at the wall facing the fluid channel, C_0 is the initial uniform air concentration in the PDMS and D is the diffusion constant of air in PDMS. The solution for this PDE can be solved as described by Carslaw and Jaeger (23) to get:

$$C(x,t) = \frac{2}{\pi}\sum_{1}^{\infty} sin\left(\frac{n\pi x}{d}\right) e^{\frac{-Dn^2\pi^2 t}{d^2}}\left[\left(\frac{C_0(1-(-1)^n)}{n}\right) + \frac{C_1}{n}\left(e^{\frac{Dn^2\pi^2 t}{d^2}} - 1\right) - \frac{D\pi^2(-1)^n n}{d^2}\int_o^t C_2(\gamma) e^{\frac{Dn^2\pi^2\gamma}{d^2}} d\gamma\right] \quad \text{-- (2)}$$

Where, l is the distance between the two channels (Figure 6.1 c). From Henry's law we get:

$$C_0 = sP_{atm} \quad \text{-- (3)}$$

$$C_1 = sP_{dc} \quad \text{-- (4)}$$

$$C_2(t) = sP_{fc}(t) \quad \text{-- (5)}$$

Where, s is the solubility of air in the PDMS, P_{atm} is the atmospheric pressure, P_{fc} is the air pressure in the fluid channel and P_{dc} is the air pressure in the degas channel. The fluid channel pressure can be described using the ideal gas law and Fick's 1st law to be:

$$P_{fc}(t) = \frac{(n_0 - \int_0^t 2A(\tau)D\frac{\partial C}{\partial x}|_{x=d}\, d\tau)RT}{V(t)} \quad \text{-- (6)}$$

$$P_{fc}(t) = P_{atm} - \frac{\left(\int_0^t 2A(\tau)D\frac{\partial C}{\partial x}|_{x=d}\, d\tau\right)RT}{V(t)} \quad \text{-- (7)}$$

Where, n_0 is the initial number of air molecules in the fluid channel, $A(t)$ is degassing surface area and $V(t)$ is channel volume at time t. Using (7) and (2), we get:

$$P_{fc}(t) = P_{atm} - \frac{4RDT}{WL(t)d}\left(\int_0^t L(\tau)\{\sum_1^\infty [\,(-1)^n e^{\frac{-Dn^2\pi^2\tau}{d^2}}(C_0[1-(-1)^n] + C_1\left(e^{\frac{Dn^2\pi^2\tau}{d^2}}-1\right) - \frac{D\pi^2 n^2(-1)^n}{d^2}\int_o^\tau C_2(\gamma)e^{\frac{Dn^2\pi^2\gamma}{d^2}}d\gamma)]\}d\tau\right) \quad \text{-- (8)}$$

Where, H is height and W is width of channel. Although (8) cannot be solved analytically, we can conclude that the fluid channel pressure is dependent on the degas channel pressure, the distance between the fluid and degas channels, the channel width (which is also related to the degas surface area to channel volume ratio) and the channel length. Here the flux into the channel from the PDMS ceiling is ignored as the device thickness is much larger than distance between degas and fluid channels. Next, to model the flow behavior into dead end channels we used the system shown in Figure 6.2 a. An inlet reservoir of height h is connected to a dead end channel of width w and height h. The inlet is exposed to the atmospheric pressure P_{atm} and the channel pressure is P_{fc}. The surface tension of the fluid is σ and the contact angle is θ. Writing the Navier Stokes equation in 3D we get (neglecting flow in the inlet),

$$\frac{\partial u}{\partial t} = -\frac{1}{\rho}\frac{dp}{dx} + \frac{\mu}{\rho}\left(\frac{\partial^2 u}{\partial y^2} + \frac{\partial^2 u}{\partial z^2}\right) \quad \text{-- (9)}$$

Where the pressure gradient can be written as (ignoring YL forces at the inlet),

$$-\frac{dp}{dx} = \frac{1}{L(t)}\left[-P_{fc} + P_{atm} + \rho g H + 2\sigma\cos(\theta)\left(\frac{1}{w}+\frac{1}{h}\right)\right] \quad \text{--(10)}$$

Also, the Poiseuille flow for rectangular channels can be solved to yield,

$$u(y,z) = \frac{4h^2}{\pi^3\eta}\frac{dp}{dx}\sum_{n,odd}^{inf}\frac{1}{n^3}\left[1 - \frac{\cosh\left(n\pi\frac{y}{h}\right)}{\cosh\left(n\pi\frac{w}{2h}\right)}\right]\sin(n\pi\frac{z}{h}) \quad \text{--(11)}$$

Which when written in terms of the average velocity leads to,

$$u(y,z) = \frac{dL(t)}{dt}\frac{48}{\pi^3(1-0.63\frac{h}{w})}\sum_{n,odd}^{inf}\frac{1}{n^3}\left[1 - \frac{\cosh\left(n\pi\frac{y}{h}\right)}{\cosh\left(n\pi\frac{w}{2h}\right)}\right]\sin(n\pi\frac{z}{h}) \quad \text{--(12)}$$

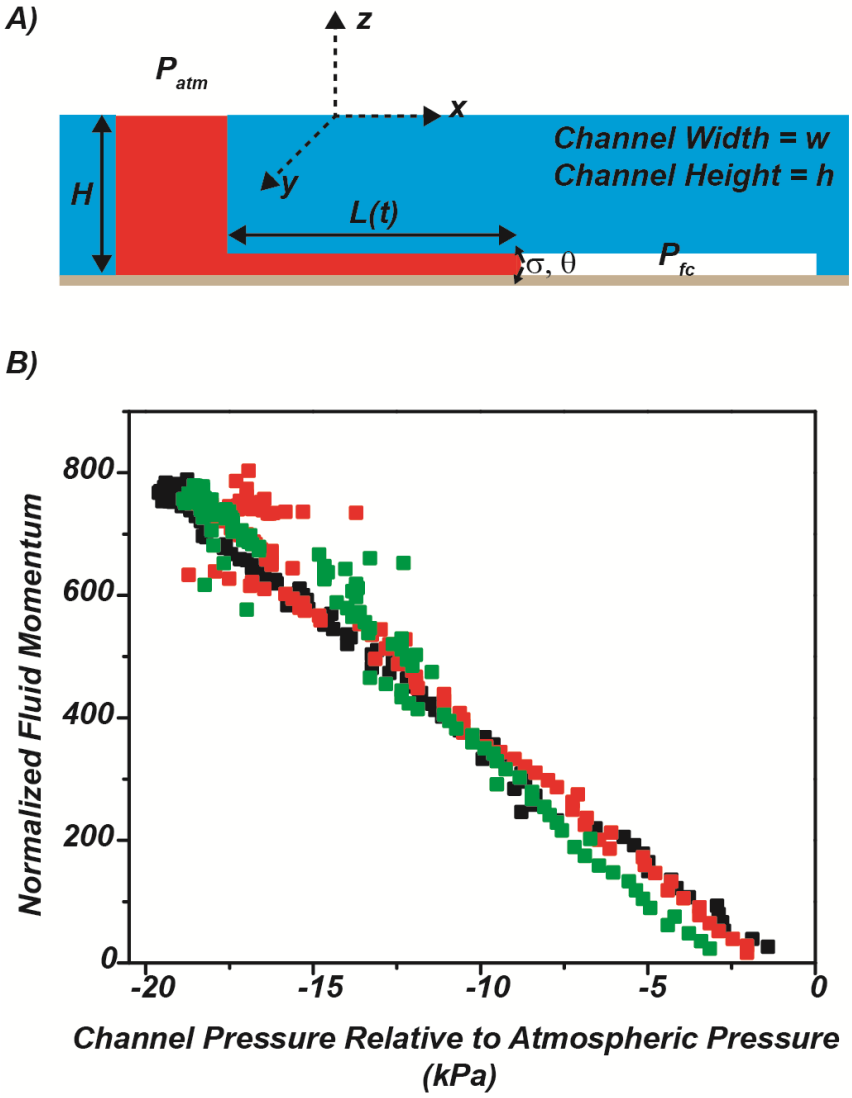

Figure 6.2: **A)** Theoretical model to describe dead-end channel filling with PDF actuation; **B)** Plot showing the linear correlation between relative channel pressure ($P_{fc} - P_{atm}$) and normalized fluid momentum in PDF flow. The different colors represent data from different devices with same design.

The transients in Poiseuille flow last for time scales in milliseconds, and therefore we can assume that the flow profile at any time is identical to the Poiseuille flow profile. Replacing this profile in equation (9) we get,

$$\frac{\partial u}{\partial t} - \frac{\mu}{\rho}\left[\frac{dL(t)}{dt}\frac{48}{\pi^3\left(1-0.63\frac{h}{w}\right)}\sum_{n,odd}^{inf}\frac{1}{n^3}\left\{-\left(\frac{n\pi}{h}\right)^2\frac{\cosh\left(n\pi\frac{y}{h}\right)}{\cosh\left(n\pi\frac{w}{2h}\right)}\sin\left(n\pi\frac{z}{h}\right)\right.\right. \quad \text{--(13)}$$
$$\left.\left. - \left(\frac{n\pi}{h}\right)^2\left[1-\frac{\cosh\left(n\pi\frac{y}{h}\right)}{\cosh\left(n\pi\frac{w}{2h}\right)}\right]\sin\left(n\pi\frac{z}{h}\right)\right\}\right] = -\frac{1}{\rho}\frac{dp}{dx}$$

And then using equation (10), we get;

$$\frac{\partial u}{\partial t} - \frac{\mu}{\rho}\left[\frac{dL(t)}{dt}\frac{48}{\pi^3\left(1-0.63\frac{h}{w}\right)}\sum_{n,odd}^{inf}\frac{1}{n}\left\{\left(\frac{\pi}{h}\right)^2\sin(n\pi\frac{z}{h})\right\}\right] = \frac{1}{\rho}\frac{1}{L(t)}\left[-P_{fc} + P_{atm} + \rho gH + 2\sigma\cos(\theta)\left(\frac{1}{w}+\frac{1}{h}\right)\right] \quad \text{--(14)}$$

Which when simplified gives us,

$$\mu L(t)\frac{dL(t)}{dt}\left(\frac{48}{(\pi h)^2\left(1-0.63\frac{h}{w}\right)}\sum_{n,odd}^{inf}\frac{1}{n^2}\right) = \left[-P_{fc} + P_{atm} + \rho gH + 2\sigma\cos(\theta)\left(\frac{1}{w}+\frac{1}{h}\right)\right] \quad \text{--(15)}$$

The equation (15) indicates that in the case of PDF, the fluid momentum (= ρ*A*L (t)* $\frac{dL(t)}{dt}$; where A is the channel cross section area) is directly proportional to the channel pressure. Hence, we can conclude that the momentum of the fluid (and not only the flow velocity) is the parameter of interest when characterizing PDF flow. The experimental validation of this model was done using the setup similar to that shown in Figure 6.1. The pressure inside the microfluidic channel was monitored, using a miniature pressure transducer (Kulite XCL-080) with a linear pressure-voltage response in the -20 kPa to -70 kPa range (Appendix Figure D.1), while the liquid flow into the microchannels was being imaged and recorded. The image data was processed to evaluate the position of the liquid meniscus which was then used to calculate the velocity and momentum of the liquid plug. The momentum of the fluid was then plotted against the measured pressure data and the result is shown in Figure 6.2. The linear correlation between the fluid momentum (normalized to the fluid density and channel cross section area) and the channel pressure confirms the conclusions of the theoretical model.

6.5 CHARACTERIZATION OF PDF

To characterize the effect of device design on PDF actuation, the various factors influencing fluid flow were varied. The theoretical analysis of PDF implies that the distance between the proximal vacuum lines and the fluid channel (referred to as the proximity or '***d***') should determine the flow behavior. This is because the diffusion of air from the fluid channel to the vacuum lines would depend on the thickness of PDMS between the two channels. Another parameter of interest is the fluid channel geometry which entails from the theoretical analysis presented in the previous section. The other parameters characterized were the thickness of the device, fluid channel length and the pressure applied to the vacuum/degas channels. The various parameters tested in our experiments are listed in Table 6.1.

Table 6.1: Parameters

Parameters	Unit	Values
*Proximity ('**d**')*	μm	50, 100, 200, 300, 400, 500
*Channel Width ('**W**') /SAVR*	μm/ mm^{-1}	50.0 (/40), 62.5(/32), 83.33(/24), 125(/16), 250(/32)
Channel length	mm	262.7, 469.1, 675.5
Device Thickness	mm	< 1 (~180 μm), 2 ,4, 6, 8
Applied Pressure (Relative to P_{atm})	kPa	-30, -40, -50, -60, -70

Appendix Figure D.2 depicts the dependence on the average initial flow velocity on the device thickness. The devices used for these experiments have a fluid channel width of 100 μm, height of 30 μm and a distance of 100 μm between the fluid channels and degas/vacuum channels. It was observed that for device thickness less than 1 mm (~180 μm) the flow velocity was drastically reduced, while a faint dip in flow velocities were observed for thickness more than 4 mm. The reduction in flow velocities for thin devices can be attributed to the diffusion of atmospheric air into the fluid channels through the thin layer of PDMS. The dip in flow velocities observed for device thickness beyond 4 mm are harder to explain and we speculate that air diffusion from the PDMS bulk, into the fluidic channels, might be the cause. Hence, we decided to work with PDMS devices with a thickness of 4 mm for all following experiments.

Figure 6.3 depicts the effect of changing the degas channel proximity on PDF. The devices used for this experiment had varying proximity, while all other parameters were held constant. As expected, an increase in proximity (hence a decrease in '***d***'; refer to Figure 6.3 a) of the degas channels led to an increase in the fluid flow velocity (Figure 6.3 b). The normalized fluid momentum was also calculated from the velocity data and, as mentioned in the previous section, was considered as a measure of the relative channel pressure (P_{fc}-P_{atm}). Figure 6.3 c shows that the normalized fluid momentum increases, or the channel pressure decreases, as the proximity is increased.

Also the time taken to reach the maximum momentum (or minimum pressure) decreases as proximity is increased; due to the increase in the degas flux. It was also observed that the normalized momentum decreased (or the channel pressure increased) after a threshold volume fraction (~0.5-0.6) of the channel is filled with fluid (Figure 6.3 d). This can be explained by the compression of air, left in the channel, as the advancing meniscus of fluid reduces the volume available. This compression should result in an increase in channel pressure similar to our observation.

Figure 6.4 depicts the dependence of fluid velocity on fluid channel width and degas surface area to channel volume ratio (= 2000/fluidic channel width) also referred to as SAVR. The devices used in this experiment had varying SAVR while the fluid channel length and proximity were kept constant. The effect of fluid geometry on PDF consists of two effects; the first one is the pinning pressure at the leading meniscus (due to surface tension) and second is the ratio between the fluid channel volume and degas flux (which depends on the net surface area through which air is being degassed).

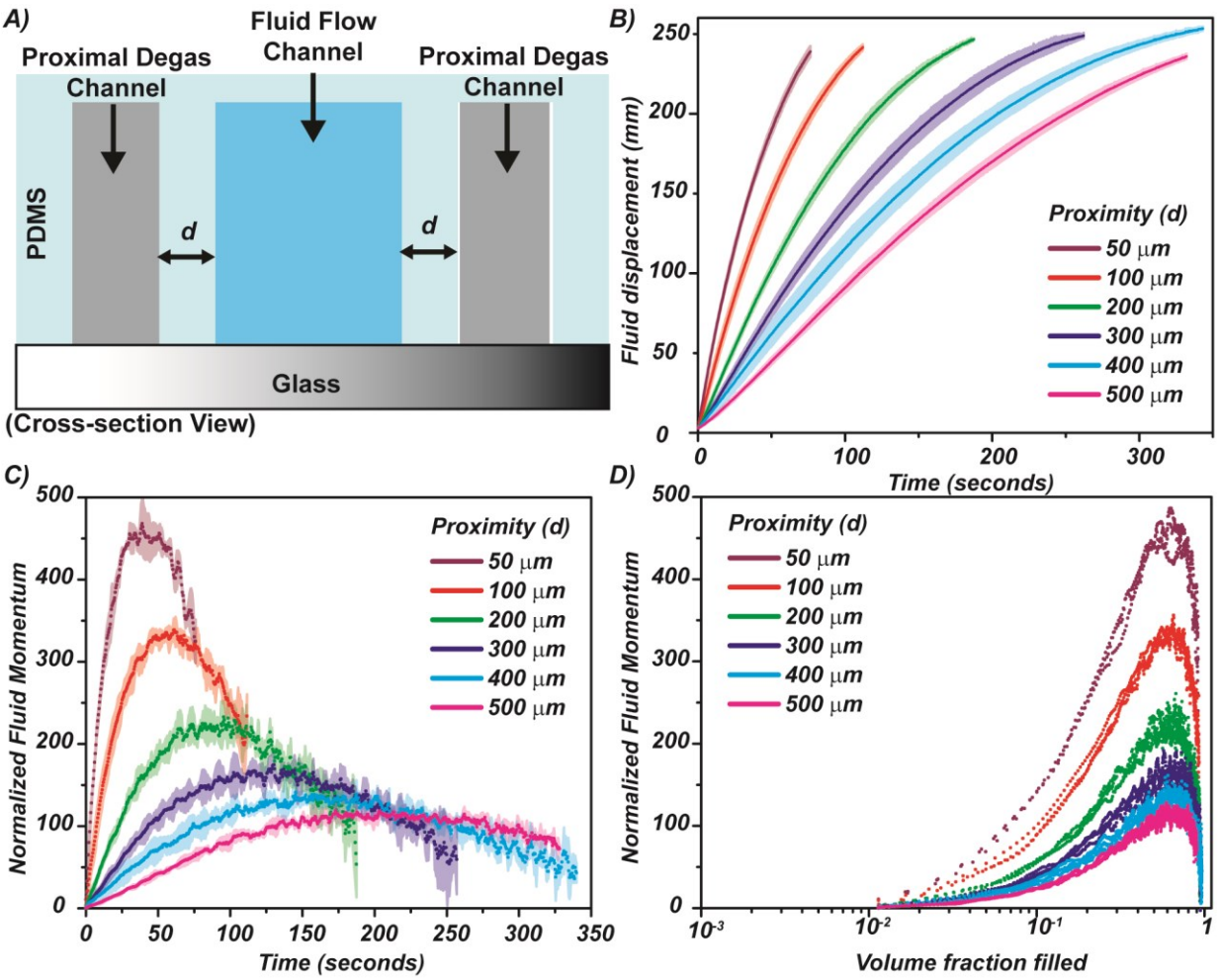

Figure 6.3: The effect of proximity of the degas channels ('***d***') on PDF; **A)** Cross section view of the device used for the experiments. The proximity 'd' was varied while the total volume of the fluid channels and the surface area for degassing were kept constant; **B)** The fluid displacement into the fluid channels is plotted as a function of time for different proximity'd'. The solid line indicates the average and the shaded region indicates two standard deviations from three independent measurements. It was observed that an increase in proximity (or a decreased in'***d***') resulted in an increase in the fluid flow velocity; **C)** The normalized fluid momentum was calculated and plotted as a function of time. The solid line indicates the average and the shaded region indicates two standard deviations from three independent measurements. Using the normalized momentum as a measure of relative channel pressure ($P_{fc} - P_{atm}$), we observe that the channel pressure decrease with an increase in proximity. Also the time taken for the minimum pressure to be realized increases with decreasing proximity (as the flux decreases) ; **D)** The normalized fluid momentum plotted as a function of the volume fraction (of the channel) filled (with the fluid) for different proximity. We observe that while relative channel pressure increases (i.e. channel pressure decreases) with increasing proximity; however after a certain volume fraction of the channel is filled up with the fluid, the compression of the air left in the channel leads to an increase in channel pressure (and hence leads to a decrease in the relative channel pressure and normalized momentum).

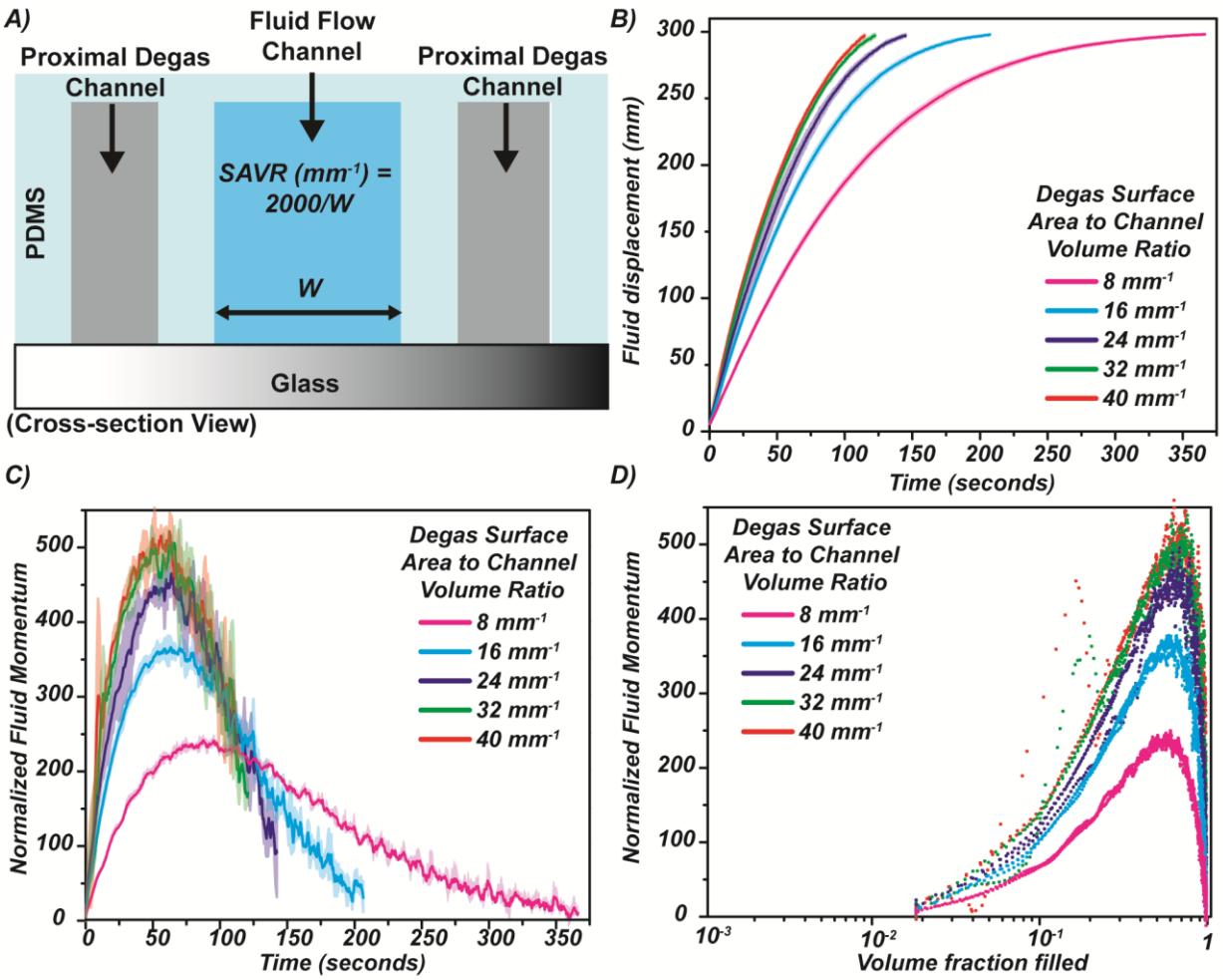

Figure 6.4: The effect of fluid channel width '***W***' (and hence degassing surface area to fluid channel volume ratio; referred to as ***SAVR***) on PDF; **A)** Cross section view of the device used for the experiments. The SAVR (and hence the fluid channel width) was varied while the proximity of the degas channels was kept constant; **B)** The fluid displacement into the fluid channels is plotted as a function of time for different SAVR. The solid line indicates the average and the shaded region indicates two standard deviations from three independent measurements. It was observed that an increase in SAVR resulted in an increase in the fluid flow velocity; **C)** The normalized fluid momentum was calculated and plotted as a function of time. The solid line indicates the average and the shaded region indicates two standard deviations from three independent measurements. Using the normalized momentum as a measure of relative channel pressure ($P_{fc} - P_{atm}$), we observe that the channel pressure decrease with an increase in SAVR.; **D)** The normalized fluid momentum plotted as a function of the volume fraction (of the channel) filled (with the fluid) for different SAVR. We observe that while relative channel pressure increases (i.e. channel pressure decreases) with increasing SAVR; however after a certain volume fraction of the channel is filled up with the fluid, the compression of the air left in the channel leads to an increase in channel pressure (and hence leads to a decrease in the relative channel pressure and normalized momentum).

At very low channel widths, pinning pressures are high and retard the flow. Also, at very large channel widths a decline in fluid velocity occurs due to a reduction in degas surface area-to-channel volume ratio (leading to an increase in the time required to lower the channel pressure). Figure 6.4 b portrays this effect of channel geometry on the fluid velocity. The net trend observed was a decrease in flow velocity with an increase in SAVR. A similar trend is observed for fluid momentum or relative channel pressure (Figure 6.4 c). However the change in channel

pressure, for a SAVR change of 8 mm^{-1}, is less for the higher SAVRs as the surface tension forces dominate at low channel widths (or high SAVR). Also, it was noted that the time needed to reach the minimum channel pressure (or maximum normalized momentum) does not change much between the various SAVRs. Additionally, similar to the experiments done with varying proximity, the channel pressure was observed to increase when the volume fraction, of the channel, filled with fluid increase beyond 0.5-0.6.

Figure 6.5 depicts the dependence of fluid velocity on fluid channel length. The devices used for this experiment had varying channel lengths, while the proximity and SAVR was kept constant. Although the fluid velocity did not change significantly between the different channel lengths (Figure 6.5 b), the maximum fluid momentum increased with an increase in channel length (Figure 6.5 c). Hence the channel pressure reduced further for longer channel lengths as the channels were degassed for a longer time. A decrease in fluid momentum (and hence an increase in channel pressure) was also observed as more than 50% of the channel was filled with fluid (Figure 6.5 d), irrespective of the channel length.

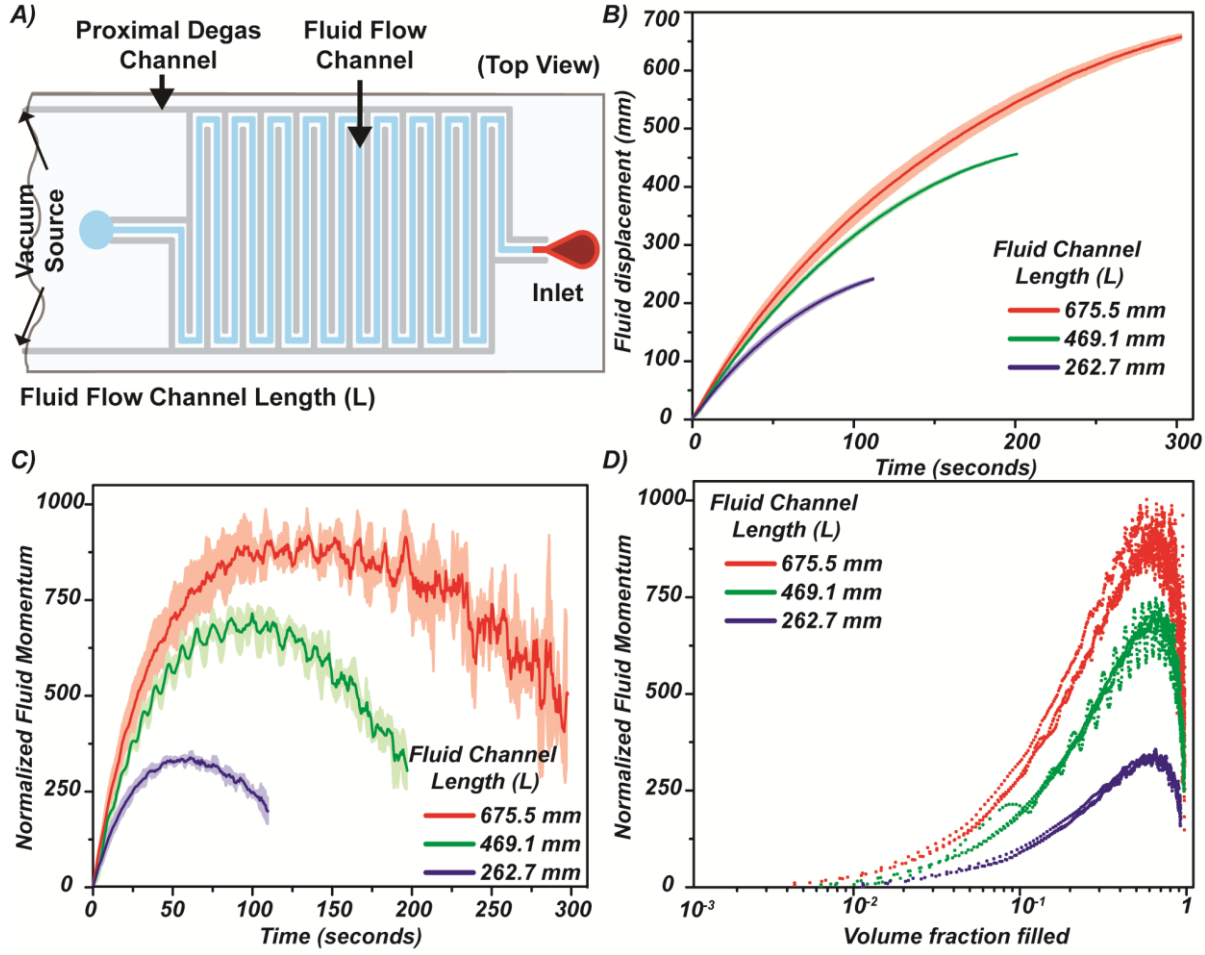

Figure 6.5: The effect of fluid channel length '***L***' (and hence the channel volume) on PDF; **A)** Top view of the device used for the experiments. The fluid channel length '***L***' was varied while the SAVR and the proximity of the degas channels was kept constant; **B)** The fluid displacement into the fluid channels is plotted as a function of time for different channel length. The solid line indicates the average and the shaded region indicates two standard deviations from three independent measurements; **C)** The normalized fluid momentum was calculated and plotted as a function of time. The solid line indicates the average and the shaded region indicates two standard deviations from

three independent measurements. Using the normalized momentum as a measure of relative channel pressure ($P_{fc} - P_{atm}$), we observe that the channel pressure decrease with an increase in channel length; **D)** The normalized fluid momentum plotted as a function of the volume fraction (of the channel) filled (with the fluid) for different channel length. We observe that while relative channel pressure increases (i.e. channel pressure decreases) with increasing channel length; however after a certain volume fraction of the channel is filled up with the fluid, the compression of the air left in the channel leads to an increase in channel pressure (and hence leads to a decrease in the relative channel pressure and normalized momentum).

The effect of the pressure applied, to the degas channels, on PDF is depicted in Appendix Figure D.3. An increase in the applied pressure leads to an increase in the degassing rate for the fluidic channels. Hence we expected that the fluid velocity will increase, while the channel pressure will decrease, with increasing applied pressure. This was confirmed by our experimental data which showed that both the fluid velocity and the normalized fluid momentum increased with an increase in the applied pressure. The effect of varying the coverage of the fluid channel (defined as the fraction of the fluid channel length bounded by the degas channels) on PDF is shown in Appendix Figure D.4. The fluid flow rapidly came to a halt when the bounded length of the fluid channel was filled with fluid, indicating a rapid increase in channel pressure once the degas flux was removed. This also corresponded with the channel pressure, as evidenced by the fluid momentum.

6.6 INTEGRATION OF ON-CHIP MEMBRANE PUMP WITH PDF

Characterization of PDF reported in the previous section utilized an external vacuum source. However, the realization of power-efficient and portable fluidic actuation will entail an on-chip vacuum source for the proximal degas lines. To achieve this we have integrated an on-chip finger operated membrane pump. The membrane deflection (due to pressure applied by the operator's finger/thumb) pushes air from the pump chamber out of a one-way air valve. When the deflecting force is remove, the subsequent relaxation of the membrane pulls out air from the degas lines generating a vacuum in the channels. Using these integrated chips fluidic pumping in a variety of different microfluidic devices has been demonstrated. Images from preliminary experiments done with these chips are shown in Figure 6.6 and Appendix Figure D.5.

6.7 CONCLUSION

In this work we report the development of a power-efficient, portable and tunable microfluidic actuation technique named Proximal Degas-driven Flow (PDF). This technique utilizes vacuum/degas channels, proximal to the fluid channel, to reduce the pressure inside the fluid channels; causing the fluid to be pumped in due to the larger atmospheric pressure acting on the fluid in the inlet. The device design can be tuned to achieve a range of flow velocities from this technique. Also, this technique does not require any prior degassing and can be operated on demand by using a convenient portable diaphragm/membrane pump. PDF hence allows the development of portable microfluidic platforms that can be actuated at the point of care without the need of large, expensive and power consuming pumping systems. This technique also alleviates any need for special device packaging hence reducing the cost of consumable. As the fluid never comes in contact with any of the pumping machinery, this technique is ideal for handling biohazardous fluids without the need of sterilizing the actuators after each run. Hence, this technique can be used for POCT molecular diagnostic platforms and devices.

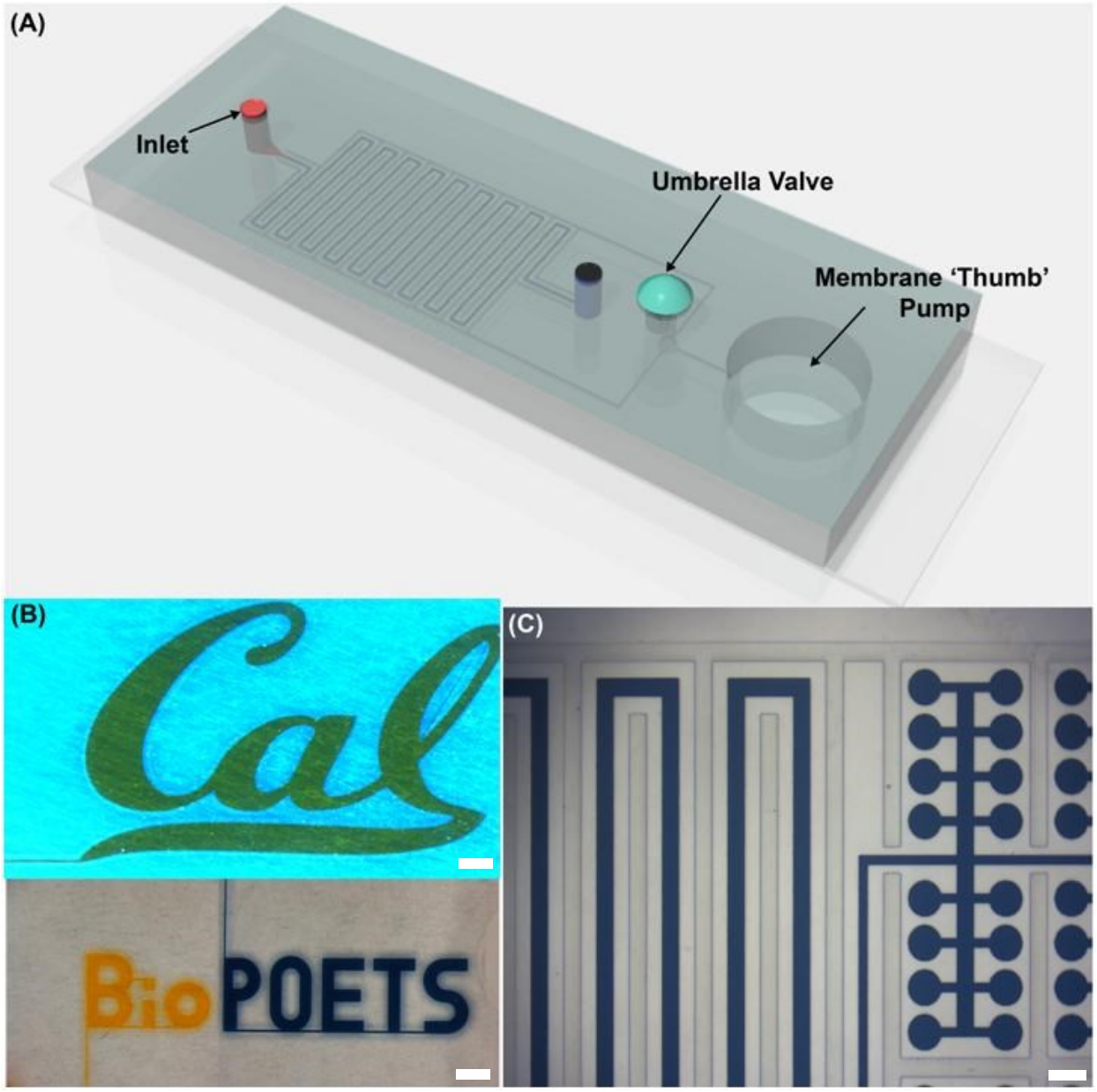

Figure 6.6: A) Device design depicting the on-chip finger operated membrane pump which will be used as a vacuum source for the degas lines. Deflection of the membrane leads to a displacement of the pump chamber air out of the one way air valve. Once the deflecting force on the membrane is remove, the relaxing membrane lowers the pressure inside the chamber and the degas lines; **B)** Preliminary results using the on-chip finger pump for actuating PDF. The devices represent the ability of PDF to fill complex geometries in a bubble-free manner without the need for priming the membrane pump. The scale bars represent 2 mm; **C)** Preliminary results using the on-chip finger pump for actuating PDF. The devices represent the ability of PDF to fill dead end chambers in a bubble-free manner without the need for priming the membrane pump. The scale bars represent 100 μm.

6.8 Acknowledgements

I would like to acknowledge Jixiao Liu and John Waldeisen for their contribution to this work. Funding for this work was provided by NIH (R01 CA120003-01A2) and the Bill & Melinda Gates Foundation (Global Health Grant: OPP1028785). I also thank Center for

Integration of Medicine and Innovative Technology (CIMIT) and Siebel Scholars 2013 program for financial support.

6.9 REFERENCES

1. Iverson BD, Garimella SV Recent advances in microscale pumping technologies : a review and evaluation. *Microfluidics and nanofluidics* 5:145–174.

2. De Volder M, Reynaerts D Pneumatic and hydraulic microactuators: a review. *Journal of micromechanics and microengineering* 20.

3. Gervais L, de Rooij N, Delamarche E (2011) Microfluidic Chips for Point-of-Care Immunodiagnostics. *Advanced Materials* 23:H151–H176.

4. Yu X et al. (2010) μFBI: A Microfluidic Bead-Based Immunoassay for Multiplexed Detection of Proteins from a μL Sample Volume. *PLoS One* 5.

5. Kim MS et al. (2010) Breast Cancer Diagnosis Using a Microfluidic Multiplexed Immunohistochemistry Platform. *PLoS ONE* 5:e10441.

6. Weng C-H, Lien K-Y, Yang S-Y, Lee G-B A suction-type, pneumatic microfluidic device for liquid transport and mixing. *Microfluidics and nanofluidics* 10:301–310.

7. Eddings MA, Gale BK (2006) A PDMS-based gas permeation pump for on-chip fluid handling in microfluidic devices. *Journal of Micromechanics and Microengineering* 16:2396–2402.

8. Jensen MJ, Goranović G, Bruus H (2004) The clogging pressure of bubbles in hydrophilic microchannel contractions. *J Micromech Microeng* 14:876.

9. Shen F, Du W, Kreutz JE, Fok A, Ismagilov RF (2010) Digital PCR on a SlipChip. *Lab Chip* 10:2666–2672.

10. Gansen A, Herrick AM, Dimov IK, Lee LP, Chiu DT (2012) Digital LAMP in a sample self-digitization (SD) chip. *Lab Chip* 12:2247–2254.

11. Zhu Q et al. (2012) Self-priming compartmentalization digital LAMP for point-of-care. *Lab Chip* 12:4755–4763.

12. Gorkin R et al. (2010) Centrifugal microfluidics for biomedical applications. *Lab on a Chip* 10:1758.

13. Guzman KAD, Karnik RN, Newman JS, Majumdar A (2006) Spatially controlled microfluidics using low-voltage electrokinetics. *Journal of Microelectromechanical Systems* 15:237–245.

14. Yeo LY, Friend JR (2009) Ultrafast microfluidics using surface acoustic waves. *Biomicrofluidics* 3:012002–012002–23.

15. Iwai K, Sochol RD, Lee LP, Lin L (2012) in *2012 IEEE 25th International Conference on Micro Electro Mechanical Systems (MEMS)*, pp 949–952.

16. Li W et al. (2012) Squeeze-chip: a finger-controlled microfluidic flow network device and its application to biochemical assays. *Lab Chip* 12:1587–1590.

17. Kallempudi SS, Altintas Z, Niazi JH, Gurbuz Y (2012) A new microfluidics system with a hand-operated, on-chip actuator for immunosensor applications. *Sensors and Actuators B: Chemical* 163:194–201.

18. Laschi S et al. (2010) A new gravity-driven microfluidic-based electrochemical assay coupled to magnetic beads for nucleic acid detection. *ELECTROPHORESIS* 31:3727–3736.

19. Darhuber AA, Troian SM (2005) Principles of Microfluidic Actuation by Modulation of Surface Stresses. *Annual Review of Fluid Mechanics* 37:425–455.

20. Hosokawa K, Sato K, Ichikawa N, Maeda M (2004) Power-free poly(dimethylsiloxane) microfluidic devices for gold nanoparticle-based DNA analysis. *Lab on a Chip* 4:181.

21. Dimov IK et al. (2011) Stand-alone self-powered integrated microfluidic blood analysis system (SIMBAS). *Lab Chip* 11:845–850.

22. Cira NJ, Ho JY, Dueck ME, Weibel DB (2012) A self-loading microfluidic device for determining the minimum inhibitory concentration of antibiotics. *Lab on a Chip* 12:1052.

23. Carslaw, H. S., and Jaeger J. C. (1959) Conduction of Heat in Solids. *Oxford University Press, Great Britain.*

CHAPTER 7

CONCLUSIONS AND FUTURE DIRECTIONS

7.1 CONCLUSIONS

This dissertation describes an effort to transform point-of-care cancer testing and provide universal diagnostics and personalized medicine to cancer patients. In Chapter 1 a review of the current state of cancer diagnostics and the need for point-of-care cancer testing is summarized. Although a variety of minimally invasive cancer diagnostic techniques have been developed, biopsy-based diagnostics are still considered the gold-standard for a variety of reasons. Hence this dissertation concentrated on the development of microfluidic modules to assist point-of-care biopsy-based cancer diagnostics. Microfluidic sample preparation is in focus in many of the chapters, and I believe that developments in microfluidic sample preparation are key to realizing POCT for cancer diagnostics. A main step in sample preparation is the development of a technique for cellular pre-concentration. To this end, we analyzed the hydraulic jump phenomenon at the microscale with applications in particle trap-and-release devices and single cell density measurement. A sudden increase in channel height in the device leads to a considerable reduction in flow velocity which leads to the trapping of microparticles by energy conversion and force balance at the channel floor. Conversely, the trapped particles are released by a surge in drag forces due to an enhancement in fluid flow velocity. In addition, the motion of the particles within the trap setup was shown to be indicative of the particle density. This provides the possibility of the estimation of particle densities through measurements of the particles pathlines through the trap region.

In Chapter 3, the theoretical work from the previous chapter was put to practice and the development of a novel, simple, efficient and gentle microfluidic cell 'trap and release' platform is reported. A setup suitable for imaging the particle pathlines in the trap region is described followed by a characterization of the trap. We have demonstrated that cell trapping efficiency can be hydrodynamically controlled by altering the flow velocity in the channels thus facilitating a cell 'trap and release' system. Trapping efficiencies at the optimal fluid velocity were found to be greater than 90%, whereas higher velocities led to the release of more than 75% of trapped cells. This device was further used to demonstrate on-chip cell pre-concentration and reagent exchange for cellular analysis. The applicability of these traps for cell concentration, separation and paired trapping was also established. Hence, this modality will enable micro-devices useful for quantitative biology, drug screening and cell-based diagnostic assays.

The next important step for sample preparation is the lysis of concentrated cells to release the intra-cellular components for analysis. In Chapter 4, the development of an efficient microfluidic cell 'trap and lyse' sample preparation platform is reported. This platform can concentrate, wash, lyse, and release the lysate of adherent mammalian cells. We demonstrate the efficacy of the system using breast cancer cell lines BT474 and T47D. Cell concentration occurs

via cell trapping in the hydraulic jump traps, described previously, with trapping efficiencies in excess of 90%. The trapped cells were further lysed using electrochemical lysis in less than 3 minutes at low power (< 60μW). The cell lysate was probed for the breast cancer biomarker Her-2 off-chip to validate that sample preparation process can be incorporated upstream of protein detection modules. The developed sample preparation module is a simple, efficient, and fast method for concentrating and lysing cells in a microfluidic device. The described cell 'trap and lyse' method provides a valuable module that can be integrated with protein detection platforms to enable complex biological sample analysis without off-chip sample preparation processes. An additional sample preparation step that arises for specific tumor types or biological analyses is the separation of bacterial and mammalian cells from mixed samples. In Chapter 3, a technique for the inertial separation bacterial cells is reported which is convenient in samples with a large bacterial load and where the goal is to study the mammalian cells. In Chapter 5, a sample preparation module for the selective lysis of mammalian cells in mixed samples is presented. This method is useful for situations where mammalian cells are in excess and the goal is to study the bacterial populations.

The main shortcoming of the techniques previously described is their reliance on regulated flow velocities. Although the hydrodynamic control over trap and release provide us with an opportunity to realize complicated assay systems, the controlled flow velocities are provided in our experiments using syringe pumps. These pumps are not very portable hence limiting the portability of the entire setup. However, a variety of miniaturized pressure pumps have been described which can potentially be used to make the above described platforms portable. Another solution to the problem of portability could be to use a portable vacuum source such as hand-held vacuum bulb, rather than a pressure source, to pull the fluid into the device from the outlet. Also by tuning the vacuum pressure, using a leak valve, the flow rates through the device can be varied at will. A secondary limitation of the integrated sample preparation module, described above, is the need to shield the downstream assay reagents from the biofluids, which can contain extraneous biomarkers possibly confounding measurements, and the hydronium and hydroxide ions, which can denature the detection reagents. However the lysate from the trap region has to be allowed to interact with the assay region. This situation can be resolved by using fluidic valves controlling the access to the detection region. The most common microfluidic valve systems, popularized by work done by Prof. Stephen Quake's group, is not extremely portable due to the need of external pressurized gas sources. In Appendix E, I describe the idea for a magnetically actuated microvalve, which can be used with portable microfluidic devices, without the need of any bulky external equipment. Another alternative is to use a passive valve without any moving parts. In Appendix F, I describe simulation results on such a valve which uses the fact that streamlines in microfluidic flow do not intersect and can be used to shield the detection region.

Finally, the development of a power-efficient, portable and tunable microfluidic actuation technique named Proximal Degas-driven Flow (PDF) is reported in Chapter 6. This method utilizes vacuum/degas channels, proximal to the fluid channel, to reduce the pressure inside the fluid channels leading to fluid flow. The device design can be tuned to achieve a range of flow velocities from this technique. This procedure does not require any prior degassing/special device packaging and can potentially be operated on demand by using a convenient portable diaphragm/membrane pump. The results reported in the dissertation were

obtained using an external controlled vacuum source. Such a setup, however, is not amenable for portable actuation. Further characterization with integrated membrane pump is being carried out currently to make this system ideal for all portable microfluidic applications. PDF hence allows the development of portable, cheap and disposable microfluidic platforms that can be actuated at the point of care without the need of large, expensive and power consuming pumping systems. This fluid actuation approach is also ideal for handling biohazardous fluids without the need of sterilizing the actuators after each run. Thus, PDF can be used for fluid actuation in POCT molecular diagnostic platforms and devices.

7.2 FUTURE DIRECTIONS

Point of Care Testing (POCT) for cancer is poised to be the harbinger of universal and personalized care for cancer patients. Although biopsy-based cancer diagnostics employ procedures which are more invasive than other diagnostic techniques, like imaging or blood-based testing, the ability to analyze cancer cells directly provides this method with a sensitivity and specificity far superior to the other tests. Hence I believe that a viable POCT platform for cancer has to employ biopsy-based analysis, until the other contending techniques have been sufficiently developed. Also, with the advent of newer cancer-associated biomarkers, related to outcomes ranging from metastasis to drug resistance, POCT platforms for cancer with the capacity for multiple-biomarker testing in biopsy samples in a rapid, portable and precise manner will be an invaluable tool to disseminate universal diagnostics to cancer patients. Additionally, the ability to discern malignant from benign tumors at the physician's office will reduce the need for expensive and time-consuming laboratory tests, hence minimizing the cost and anxiety, for patients with benign tumors. Such a platform will not only improve the operational characteristics of such diagnostic assays but will also help determine drug efficacy, ushering in personalized medicine for the patients. I also consider that microfluidic devices with reduced volumes and diffusion distances enable multiplexed, portable and fast assays and are suitable for facilitating such POCT systems. A truly portable microfluidic POCT platform is however realizable only if all unit processes associated with the diagnostic test are integrated together. Current microfluidic devices however rely extensively on off-chip sample preparation steps. The microfluidic sample preparation modules discussed in this dissertation are amenable to integration with most of the current microfluidic detection approaches. I trust that the use of these modules can enable the development of truly integrated sample-to-answer microfluidic POCT platforms. These integrated devices can allow high-throughput biomarker-based analysis of cancer patient tumor samples facilitating personalized diagnosis and therapy.

The modularity of the systems described in these chapters also permits their use as a platform technology for a variety of quantitative biological assays, apart from cancer diagnostics. The cell 'trap and release' method, described in Chapter 3, can be used as a platform to elucidate cellular behaviour in dynamic microenvironments and enable the downstream post-analysis reclamation of cells. The module can also be used to study protein secretion of immobilized cells using a downstream protein immunoassay. Such secretion assays are useful in the understanding of various biological processes including immune response and cell signalling. The paired trapping of cells allows the development of microfluidic invasion and migration assays, instrumental in deciphering cell signalling pathways. The cell 'trap and lyse' sample preparation

module, reported in Chapter 4, can be used for cellular protein and nucleic acid analysis using a range of adherent mammalian cells.

Portable microfluidic actuation is essential for the operation of any microfluidic POCT platform. To this end, there are very few techniques that can provide portability as well as flow control and tunability. I believe that the Proximal Degas-driven Flow (PDF), described in Chapter 6, is apt to fill this niche. The integration of a membrane finger pump to the setup will make this technique portable and can be operated with the use of minimal power.

Before concluding this chapter it would be prudent to consider the materials needed to manufacture the microfluidic modules described in this dissertation. The research reported here was performed using PDMS devices bonded to glass. PDMS provides an excellent material for prototyping microfluidic devices due to the ease of use, high fidelity and bio-compatibility. Another property of PDMS relevant to the research described in this dissertation is its high air permeability, which permits proximal degas-driven flow and also allows the culture of cells on chip. However, PDMS soft-lithography is not suitable for high-throughput industrial manufacturing. The curing process for PDMS is lengthy and not compatible with industry standards such as roll-to-roll manufacturing, injection molding or hot embossing. Not surprisingly, most commercial microfluidic devices are currently manufactured using plastics such as COC, PS etc. But these plastics have low air permeability and are not suitable for some of the modules discussed. A possible solution to this quandary might be the use of hybrid PDMS-Plastic devices, similar to the ones fabricated in Chapter 4. The microfluidic features can be fabricated in the plastic, while silicone elastomeric sheets (currently commercially available) can be used to provide an air permeable surface to the microfluidic channels. Another possible resolution might be the use of Thermoplastic Elastomers (TPE) which are available commercially. These elastomers can be injection molded or hot embossed, but they also possess moderate air permeability which is suitable for the modules reported here. Glass substrates were used in this research due to the ease of bonding PDMS to and patterning metal electrodes on glass. For a cheap disposable device, however, the glass substrate can be replaced by plastic substrates. Bonding these substrates, to plastic chips, can be done thermally or, to TPE chips, using silane chemistry described in Chapter 4. Electrode patterning on these plastic substrates can also be done using screen printing in a roll-to-roll fashion.

In summary, my graduate career allowed me to do research on a variety of topics towards the development of microfluidic POCT platforms for cancer diagnostics. I believe that such POCT systems hold the promise of universal and personalized cancer care. I am thankful to my advisor, fellow lab mates and collaborators for supporting me in my research endeavors and I intend to continue such multi-disciplinary research to bridge the disparity in health care evident in today's world.

APPENDIX A

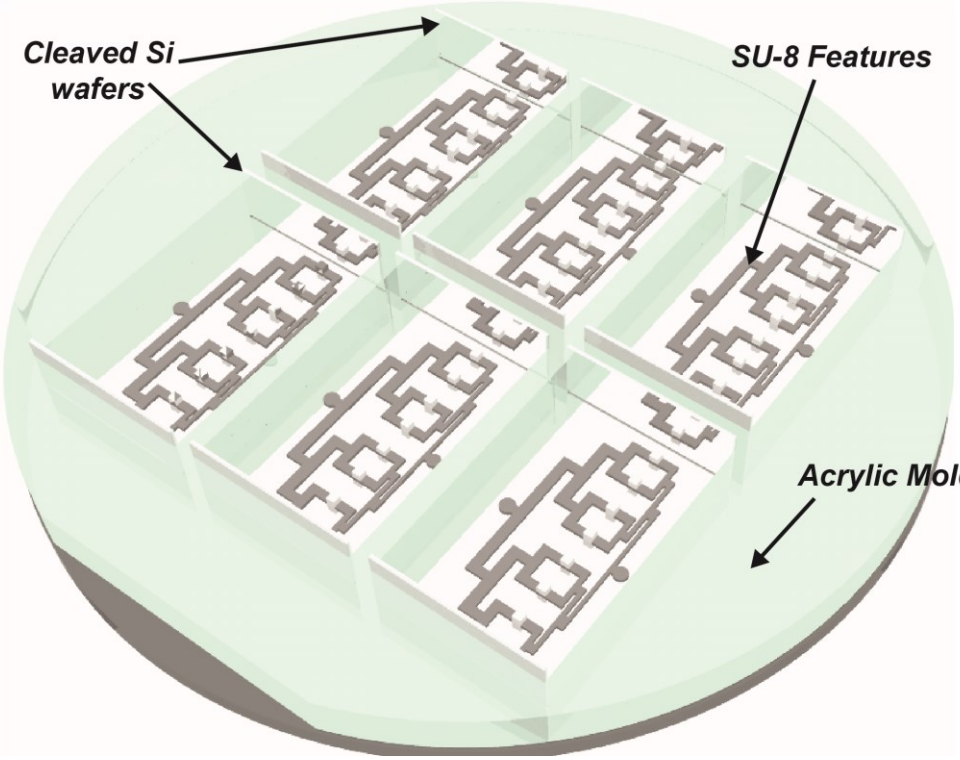

Figure A.1: An acrylic mold, with affixed pieces of cleaved Si wafers, was used when making PDMS devices from the SU-8 mold. The cleaved Si wafer pieces (with their polished side facing the SU-8 features) ensured that the PDMS, poured on top of the features and enclosed by the acrylic mold, had smooth side walls for imaging of the hydraulic jump traps.

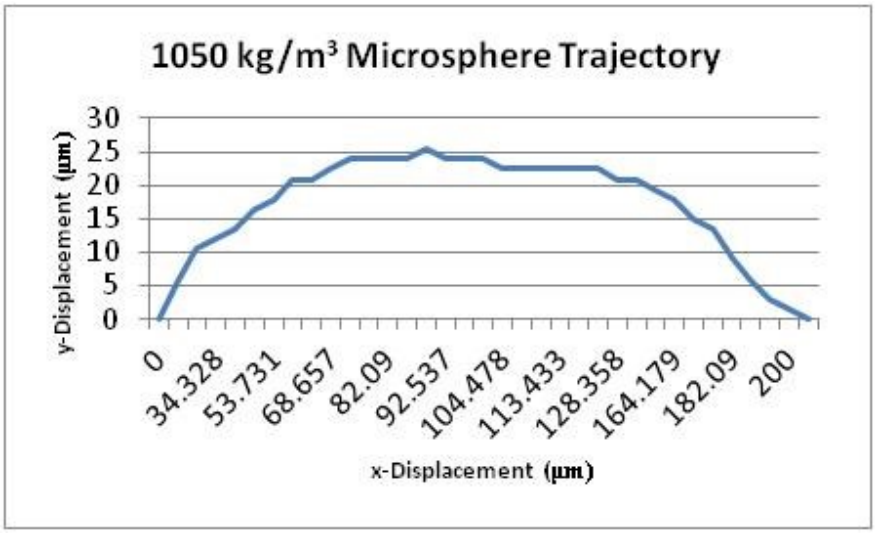

Figure A.2: Trajectory of microsphere with a density of 1050 kg/m^3 observed using the lateral viewing setup. The microspheres were perfused at a flow velocity of 1.04 x 10^{-4} m/s in a PBS buffer.

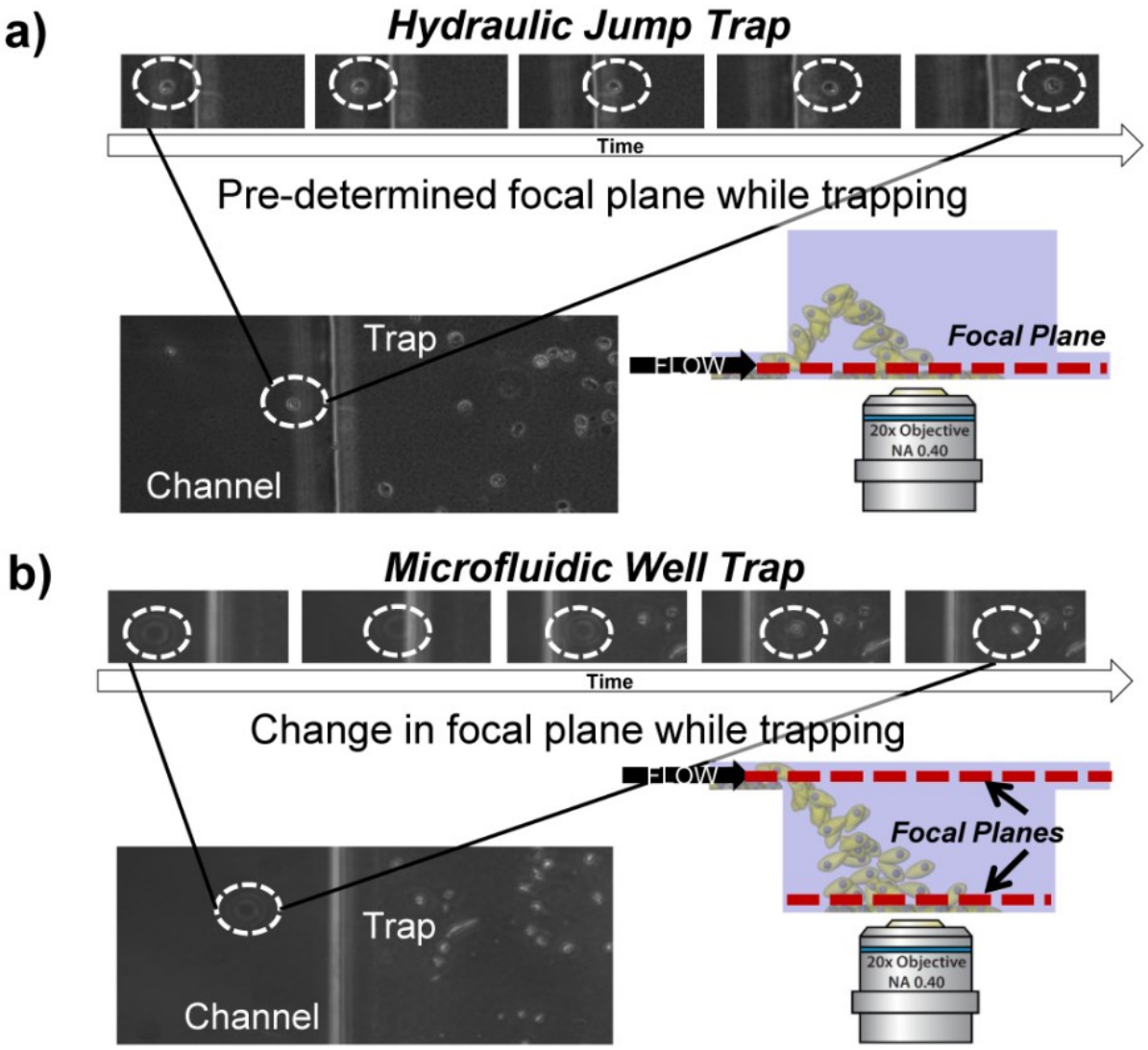

Figure A.3: Comparison of hydraulic jump trap with a microwell cell trap; **A)** Phase contrast images taken for cell trapping in a hydraulic jump device. The focal plane is adjusted so that only the cells becoming trapped are in focus. As can be seen from the time course images taken, the cell (encircled) is in focus in the channel and also as it becomes trapped. Thus the cell does not move much in the focal direction, and is consistent with our hypothesis of the principles behind cell trapping in our devices; **B)** Phase contrast images taken for cell trapping in a microwell device. The focal plane is adjusted so that only the cells becoming trapped are in focus. As can be seen from the time course images taken, the cell (encircled) is initially out of focus in the channel and comes into focus as the cell is trapped. This is consistent with the fact that cells settle downward in the focal direction during trapping.

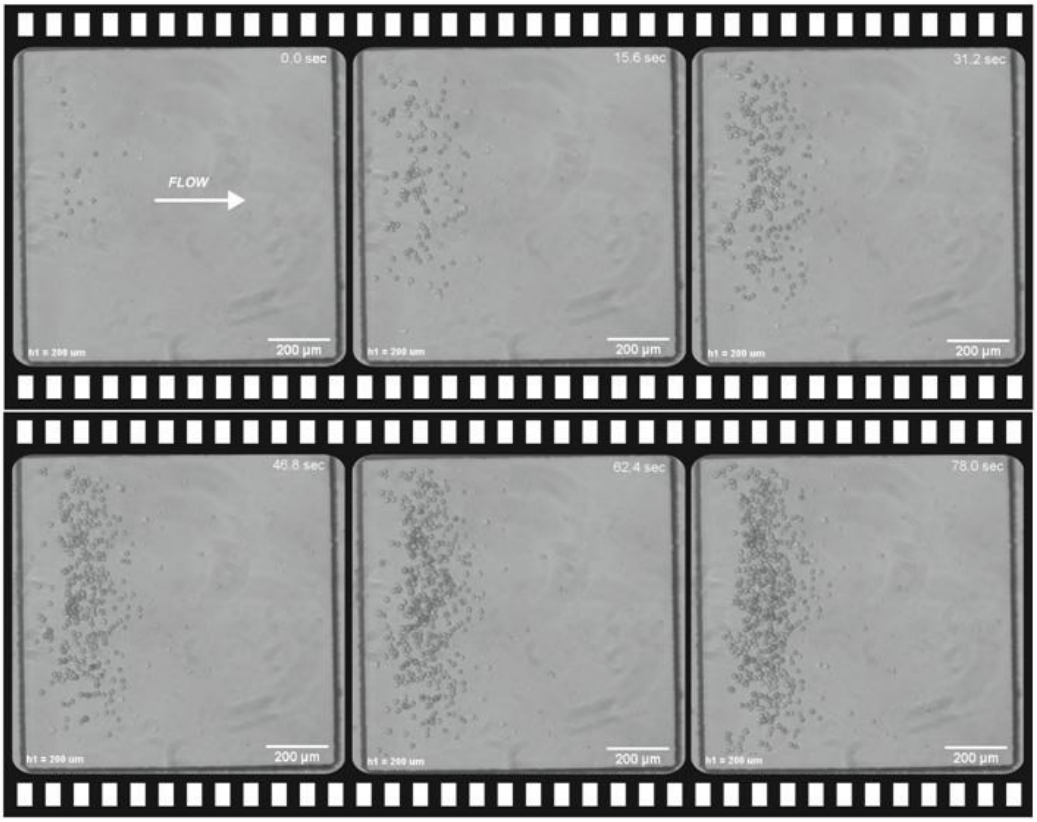

Figure A.4: Trapping of HeLa cells in the optimal hydraulic jump trap design at an u_0 of 1.04 x 10^{-4} m/s. The length of the trap is 1 mm, the height of trap is 200 µm and the height of the channel is 20 µm. The image sequence demonstrates the formation of a band of trapped HeLa cells near the entrance of the Hydraulic Jump Trap

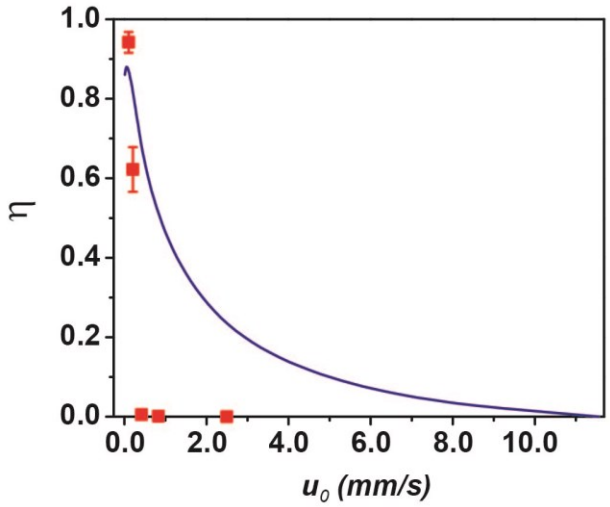

Figure A.5: HeLa cell (D_c = 15 µm) trapping in Hydraulic Jump trap shows flow velocity u_0 (in the channel) dependent trapping efficiency. The trapping efficiency (Solid Square) decreases as the u_0 (and fluid pressure force) increases. This is consistent with our theoretical model and the data from our simulation model (Solid Line). The error bars indicate standard deviation from 3 independent experiments.

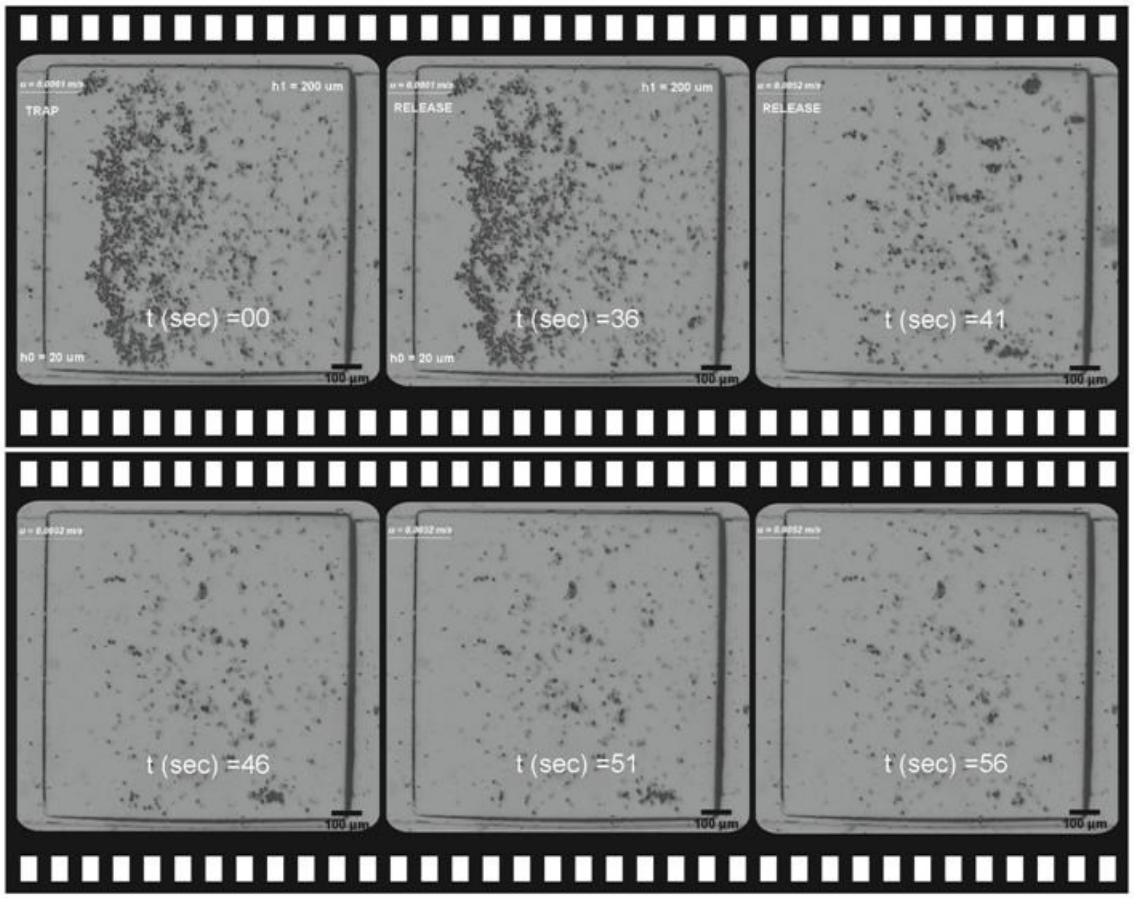

Figure A.6: Release of trapped HeLa cells in the optimal hydraulic jump trap design at an u_0 of 5.2 x 10^{-3} m/s. The length of the trap is 1 mm, the height of trap is 200 µm and the height of the channel is 20 µm.

APPENDIX B

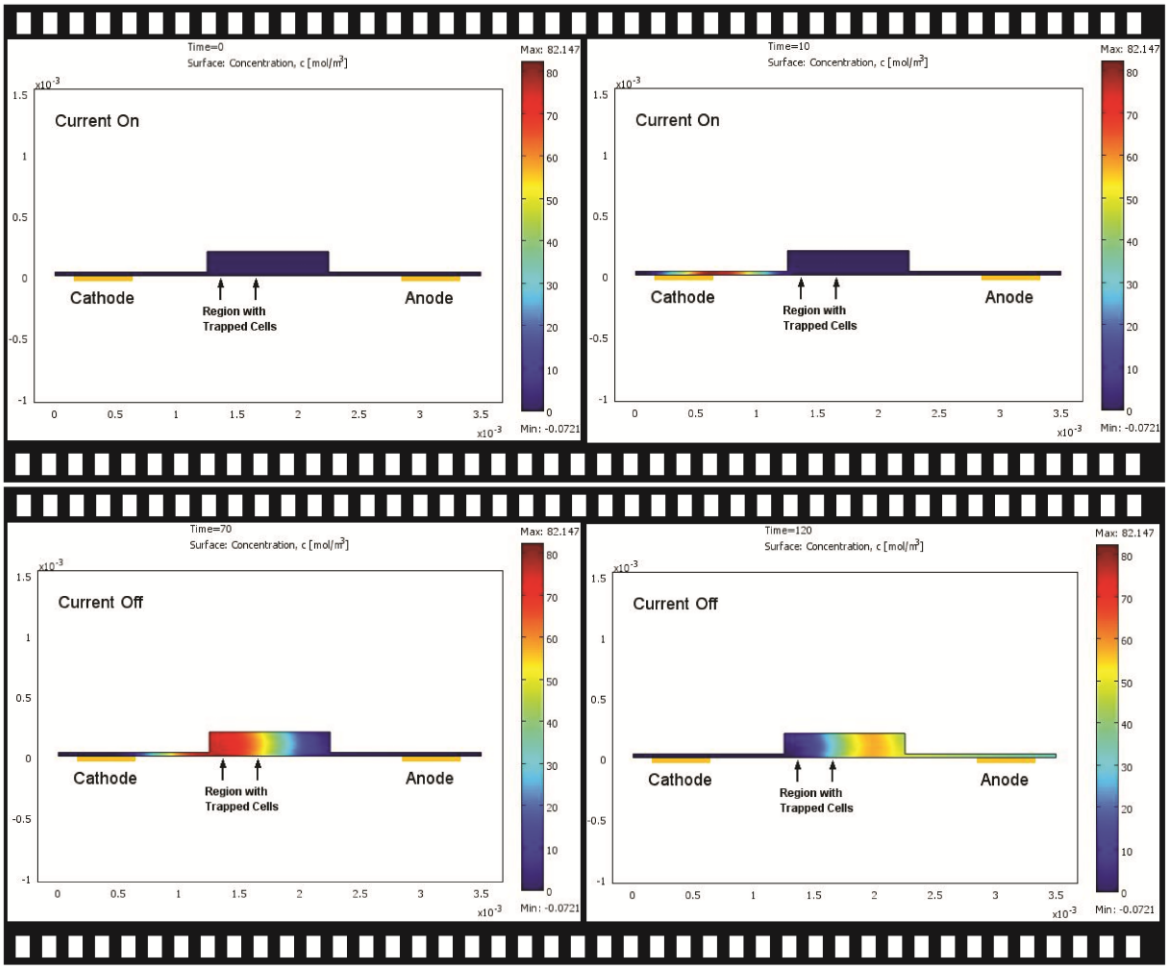

Figure B.1: Simulation of the convective transport of hydroxide ions into the trap region of the device. Hydroxide ions were produced at the upstream electrode at a faradaic current of 15 µA for 60 sec and the flow velocity in the trap is 1.04 x 10^{-5} m/s. The current is stopped after 60 sec and the flow is continued resulting in the flushing of the hydroxide ions from within the cell trap region (100 to 400 µm from the trap inlet as indicated in the video). Hydronium ions were not simulated as they are transported downstream by the flow and do not interact with hydroxide ions upstream of the electrode. The time lapsed simulation results shows the transport of hydroxide ions, represented by the change in concentration, along the flow direction. The length of the trap is 1 mm, the height of the channel is 30 µm (h_0), the height of the trap is 200 µm (h_1), the length of both electrodes is 500 µm and the unit of time is seconds.

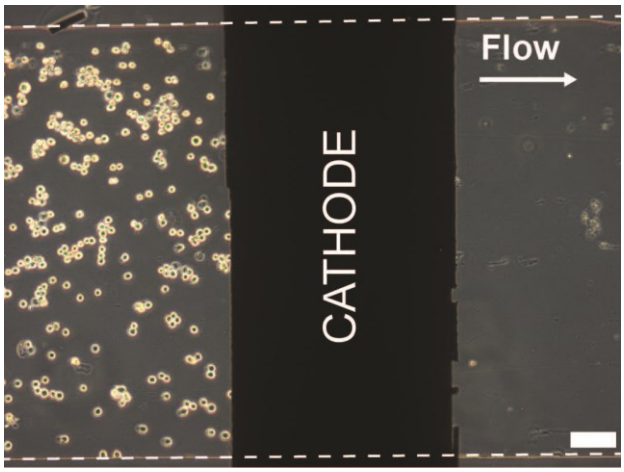

Figure B.2: Visualizing the convective transport of hydroxide ions. The convective transport of hydroxide ions was demonstrated as cells upstream of the cathode failed to lyse while cells downstream of the cathode were lysed. This indicated that convective mass transfer along the direction of flow dominates hydroxide ion transport and that diffusive transfer is negligible. The scale bar is 100 μm in length.

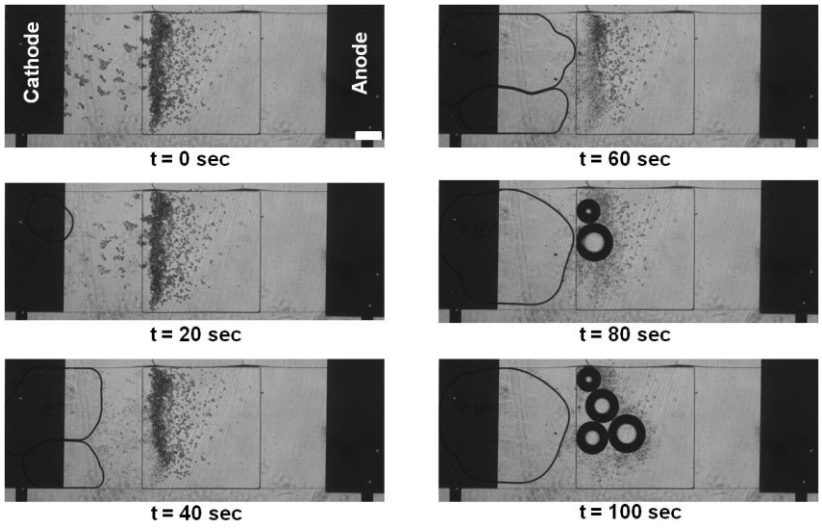

Figure B.3: Bubble generation during electrochemical lysis at high voltages. Electrochemical lysis performed at 4.0V led to the formation of bubbles at the electrodes, which eventually moved into the hydraulic jump trap. Bubble generation occurred due to excessive hydrolysis at the electrodes and the gaseous products exceeding their solubility limits in the buffer. The voltage was started at t = 0 seconds. The scale bar represents a length of 200 μm.

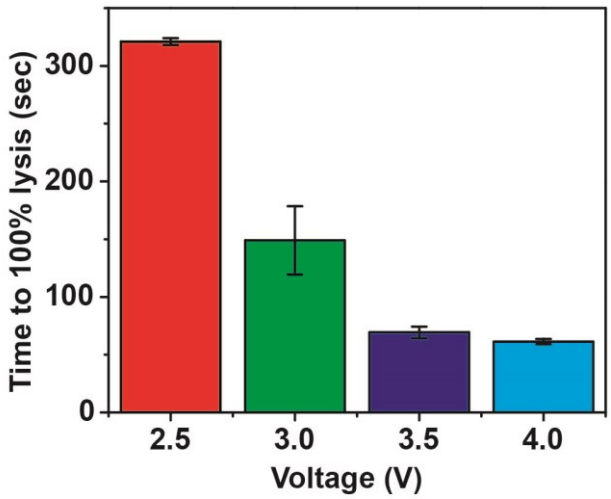

Figure B.4: Time dependence on voltage for complete lysis of BT474 cells in a device with channel height of h_0 = 20 μm and trap height h_1 = 200 μm. As expected, the time to complete lysis decreases with an increasing voltage.

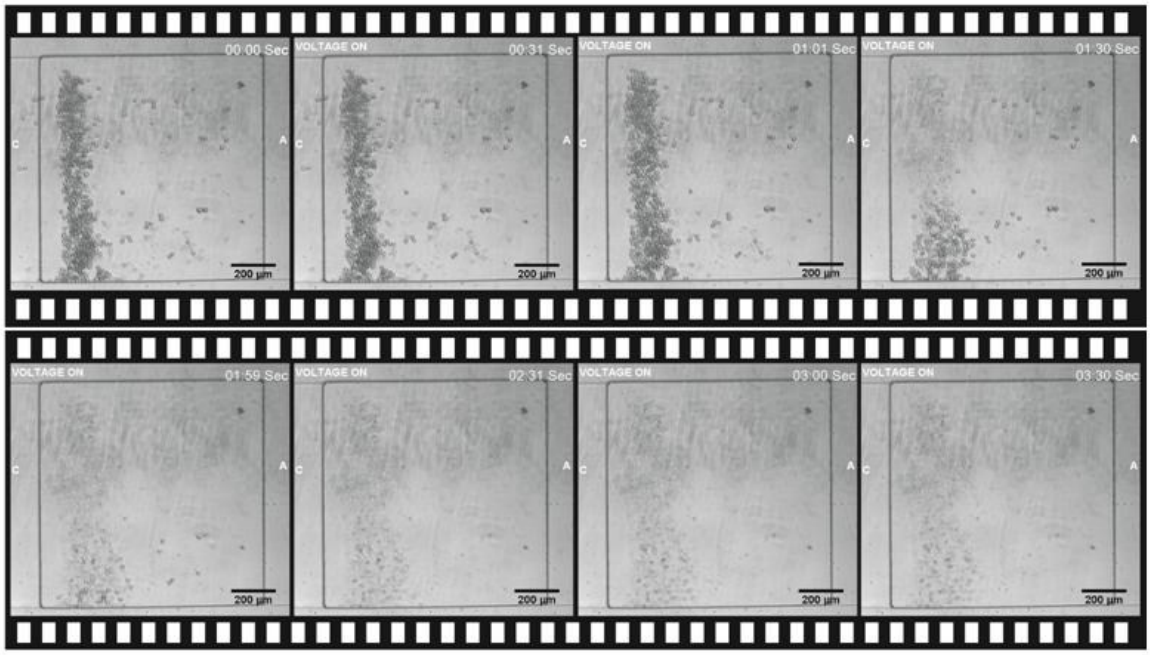

Figure B.5: Time lapse images depicting the lysis of BT474 cells in the integrated trap and lysis system, observed transversely using a phase contrast microscope, at a voltage of 3.5V and perfusion rate (u_1) of 1.04 x 10^{-5} m/s in the trap. The length of the trap is 1 mm, the height of the channel is 30 μm (h_0), and the height of the trap is 200 μm (h_1)

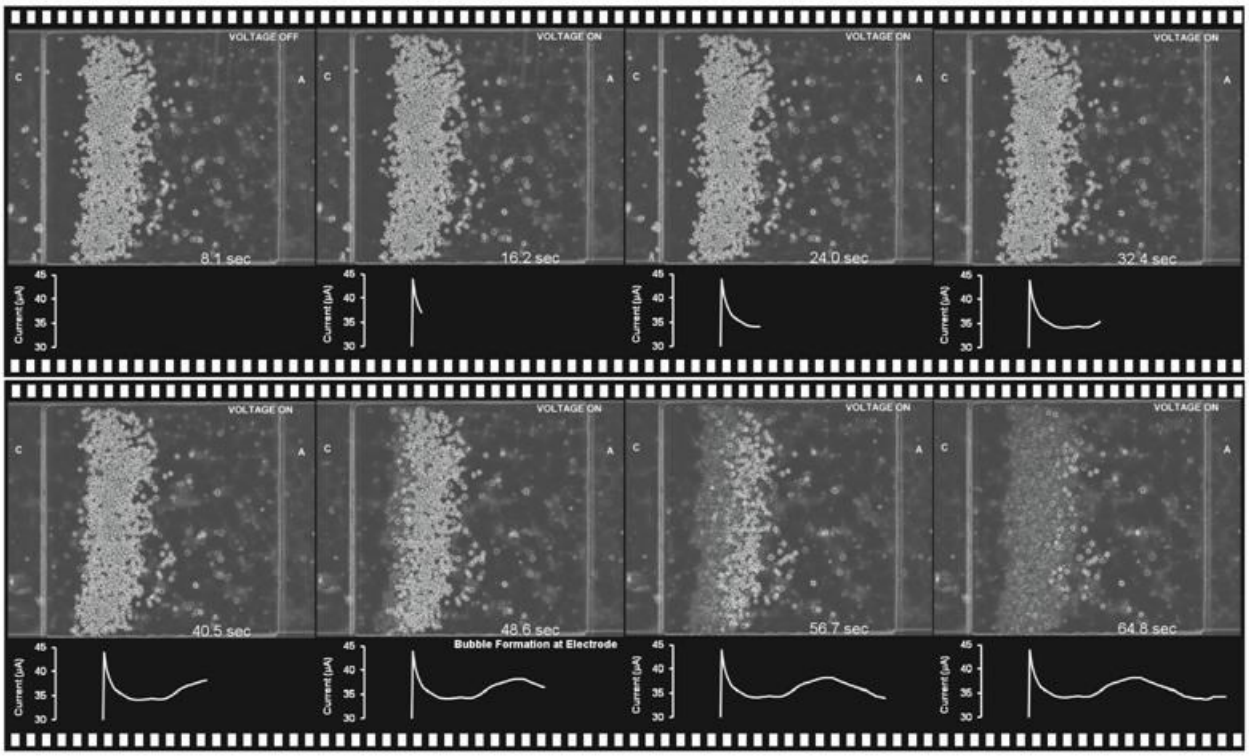

Figure B.6: Lysis of BT474 cells in the integrated trap and lysis system, observed transversely using a phase contrast microscope, at a voltage of 4.0V and perfusion rate (u_0) of 1.04 x 10^{-4} m/s. The length of the trap is 1 mm, the height of the channel is 20 μm (h_0), and the height of the trap is 200 μm (h_1). The temporal current data shows an initial spike in current followed by decay due to electrode charging. The current seems to increase as more cells are lysed, possibly due to the release of conducting species. Bubble formation at the electrode led the decrease in current at the end of the video.

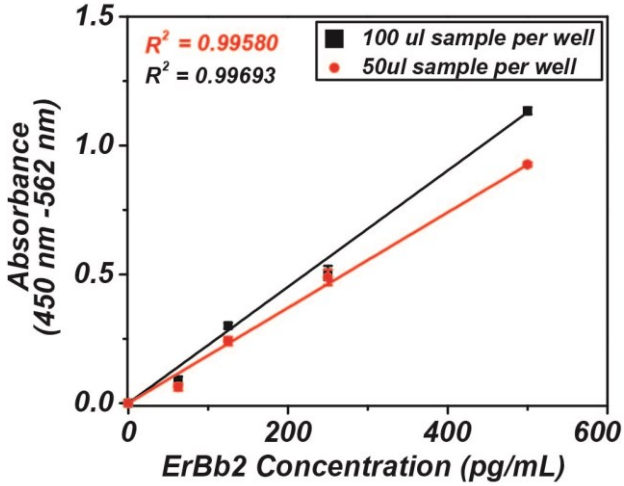

Figure B.7: Optimization of the Her2 ELISA protocol with half the recommended sample volume. The ELISA manufacturers recommended 100 μL of sample volume per well for performing the ELISA. The objective was to determine whether half the recommended amount would adversely affect the assay. The ELISA standards were performed with both sample volumes to determine if there was a deviation in the linearity of the standard curves. No such deviation was observed, which indicated that smaller sample volume per well can be used to perform the ELISA assay.

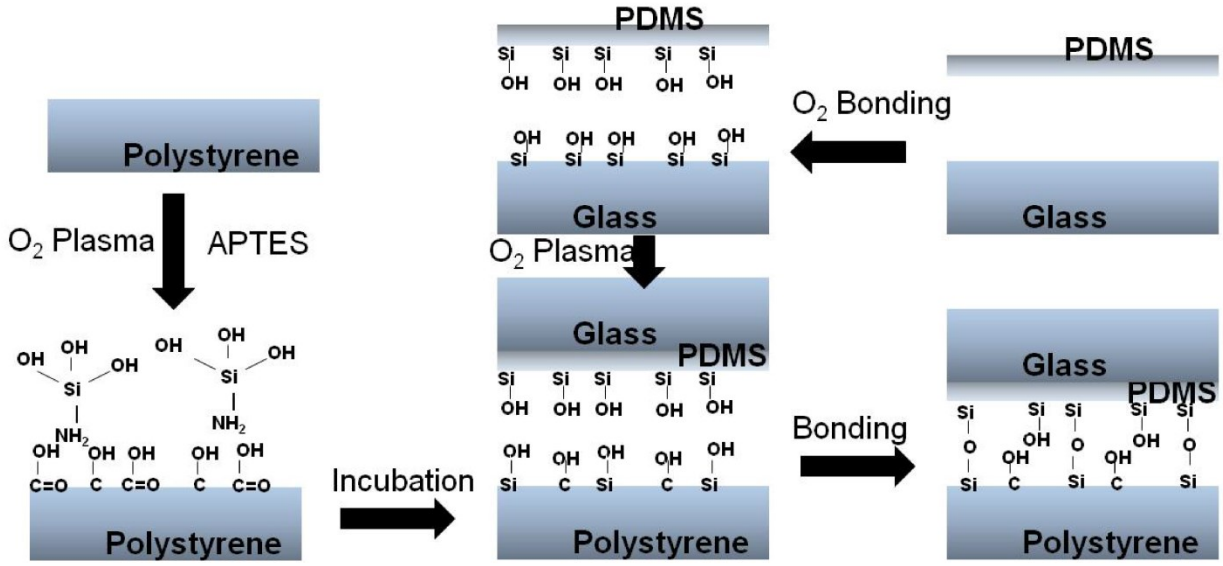

Figure B.8: Bonding of PDMS to Polystyrene to make PS-PDMS-Glass Hybrid devices. The bonding process involves the activation of the Polystyrene surface using APTES and the subsequent bonding of silanol groups on the PS to those on the PDMS.

APPENDIX C

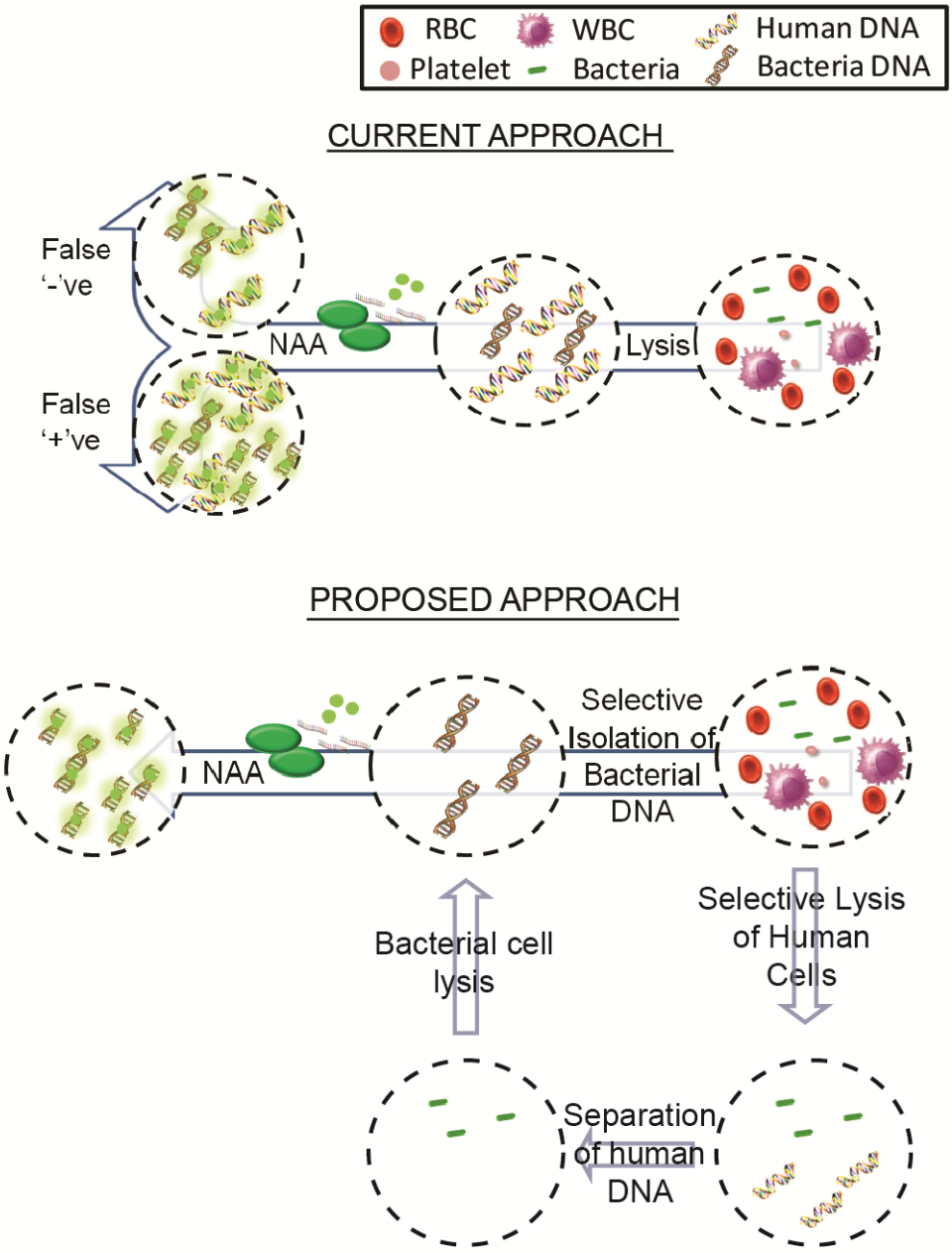

Figure C.1: The current approach in analyzing mixed human samples (for genomic or metagenomic studies) involves the lysis of all cells in the sample, generating a mixture of human and bacterial DNA. The excess amount of human DNA can interfere with these studies generating noise in the form of false negative or positive results. The proposed approach involves the selective isolation of bacterial DNA from such mixed samples. To achieve this, the mammalian cells in the sample are selectively lysed and the human DNA removed. The sample, now containing only bacterial cells, is then lysed to get a pure bacterial DNA sample which can be further analyzed. NAA stands for Nucleic Acid Analysis.

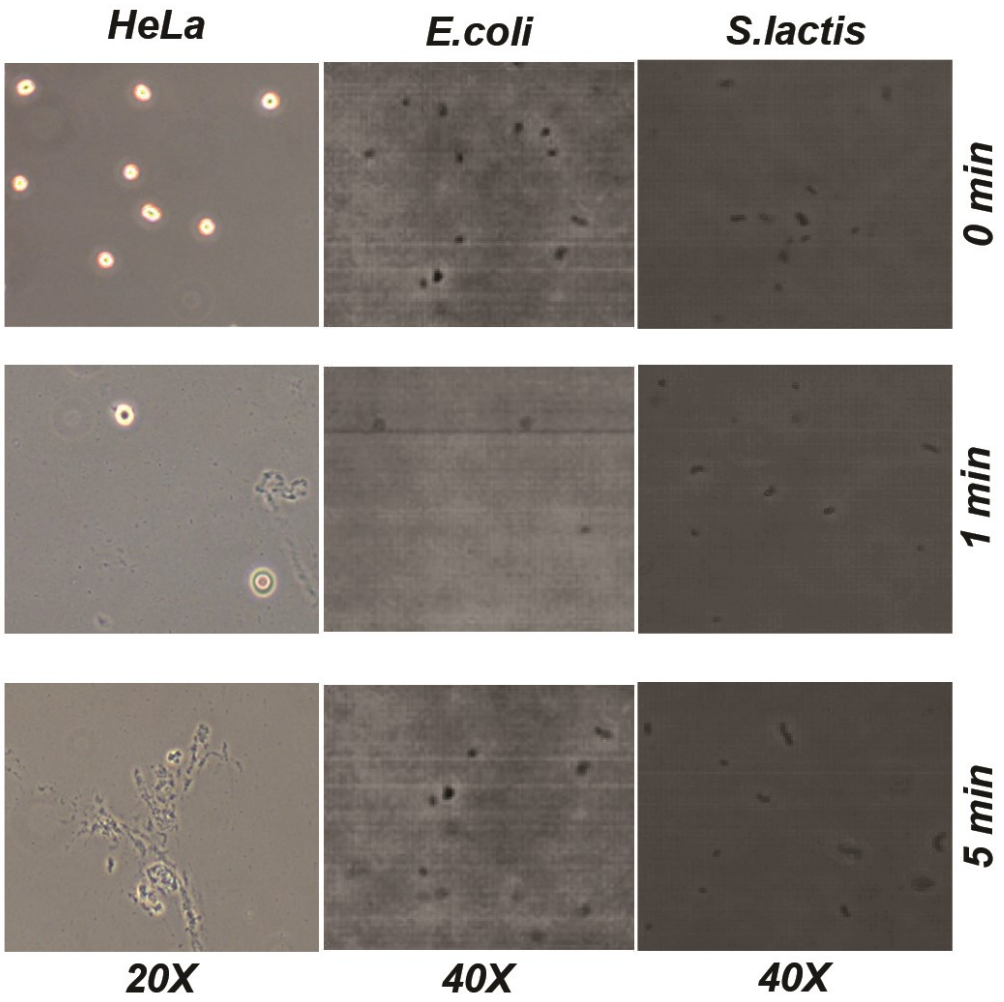

Figure C.2: Proof of concept of selective lysis of bacterial cells using hydroxide ions. Cells were put in 20mM NaOH solutions and images were taken at 0, 1 and 5 minute for HeLa, *E.coli* and *S.lactis* cells. As can be seen, HeLa cells start lysing in 1 minute and are completely lysed by 5 minutes, while the bacterial cells show resistance to lysis.

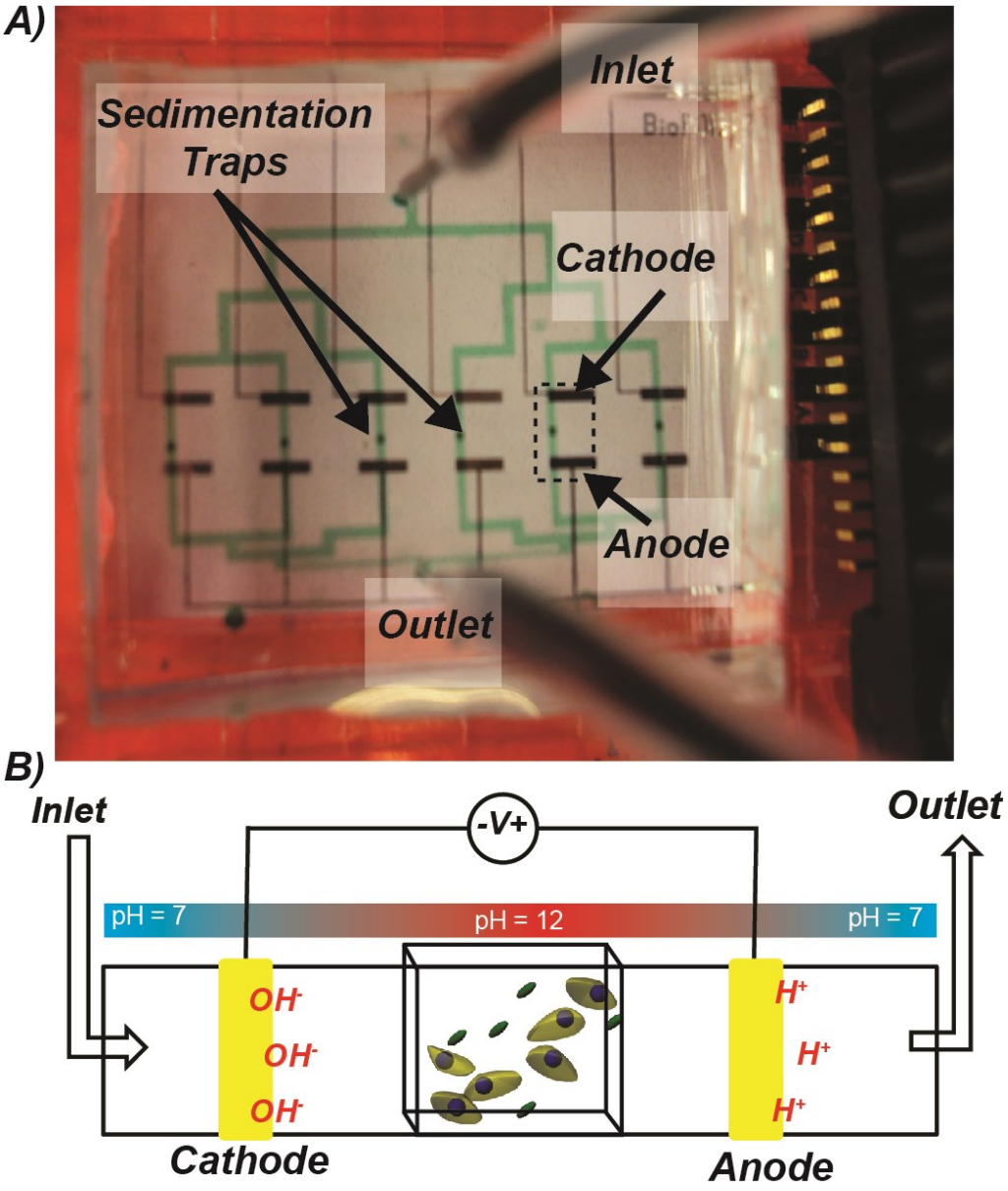

Figure C.3: Device design and layout. The device consists of sedimentation traps realized by channel expansion. The traps are flanked on both sides by electrodes. The cells are loaded and then allowed to settle for about 20 minutes. Afterwards perfusion is started. Cells settled in the channels are washed away, but in the expanded trap region, due to reduce shear stress; the settled cells remain and are used for experiments.

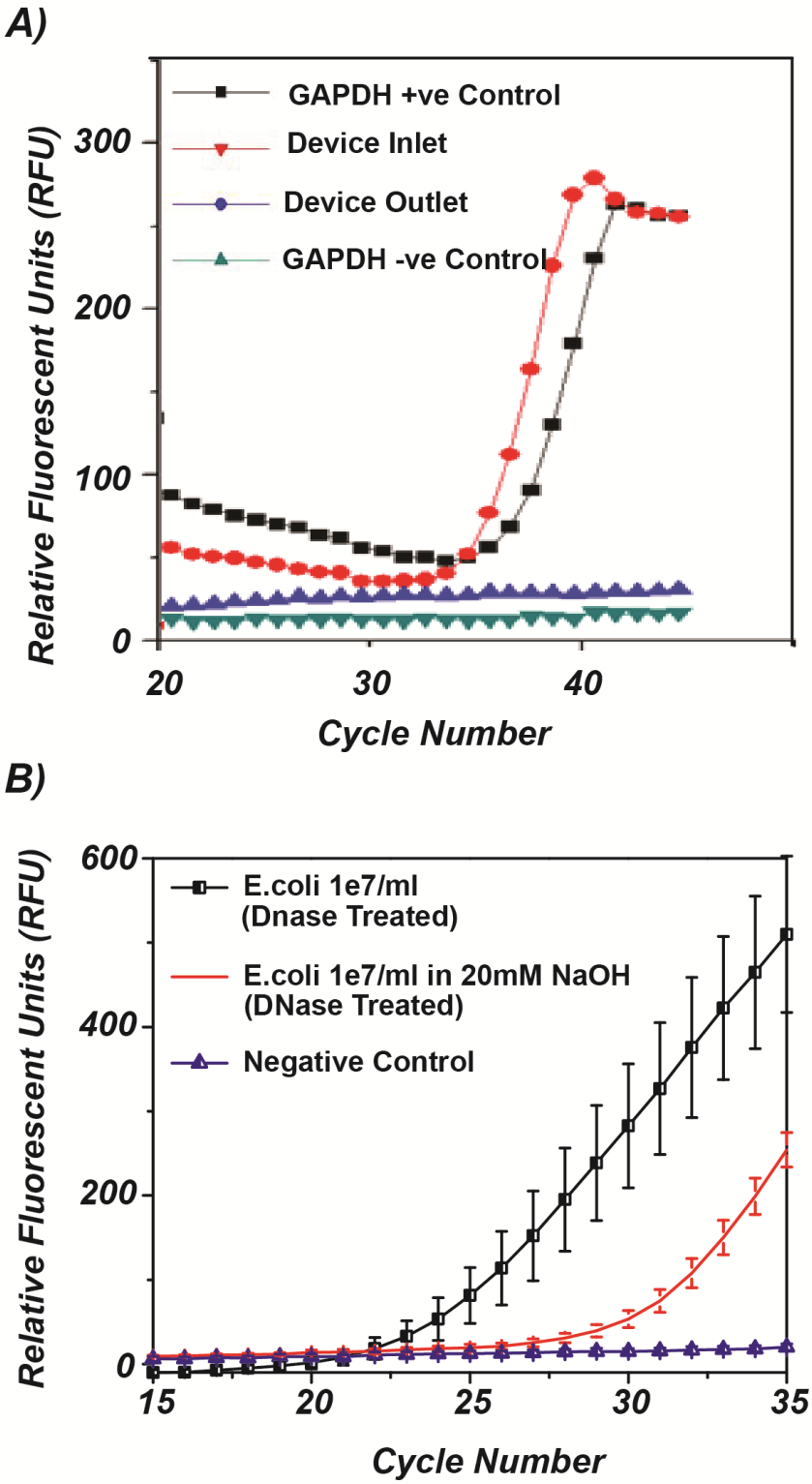

Figure C.4: **A)** Removal of human DNA via DNase treatment after the electrochemical lysis of mammalian cells. The PCR used a GAPDH primer and the absence of a signal in the device outlet (after DNase treatment) indicates the complete lysis of mammalian cells; **B)** The poration of *E.coli* cells off-chip via NaOH treatment shows a loss in signal (after DNase treatment) in comparison to the positive control. This indicates that the poration exposes a fraction of the DNA to external buffer and enzymes.

APPENDIX D

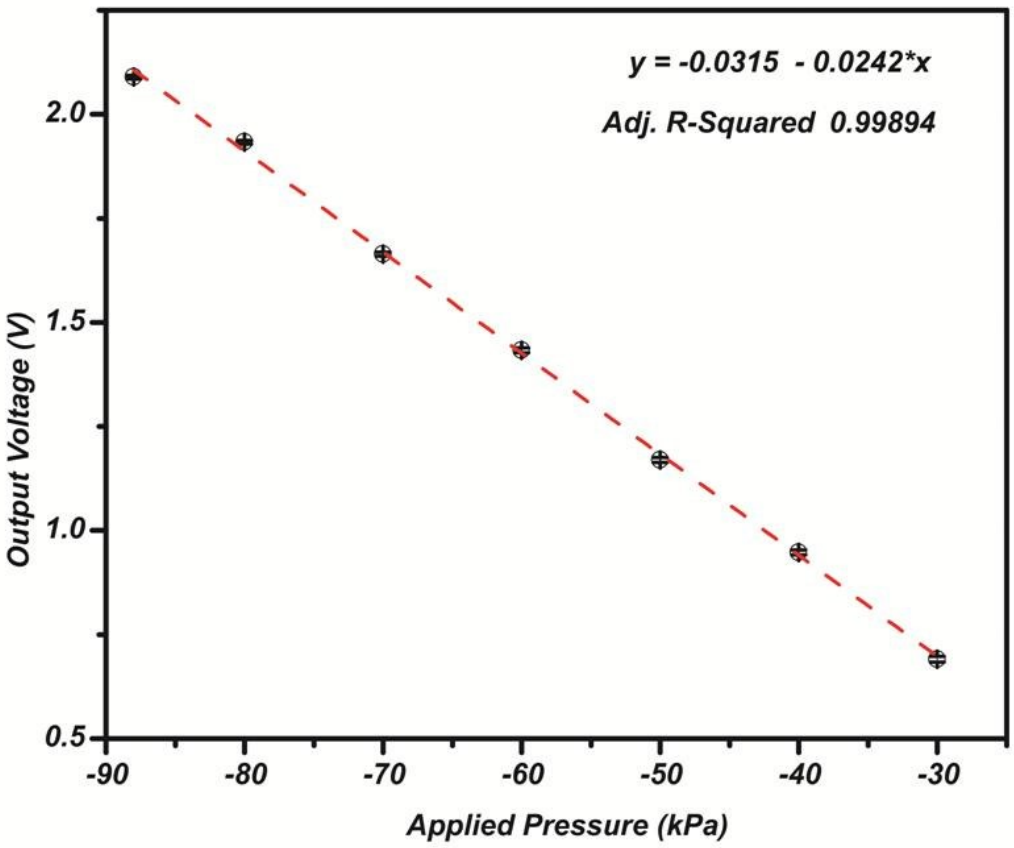

Figure D.1: The calibration curve for the Kulite XCL-080 vacuum sensor. The curve was obtained by the measuring the pressure sensor output for varying applied pressure (relative to atmosphere, negative pressure indicates that a vacuum was applied). The sensor output was amplified > 40X using an OP-AMP circuit and the measured using a sensorDAQ. The curve is linear in the range of interest (-30 to -70 kPa) implying that this sensor can be used in our experiments.

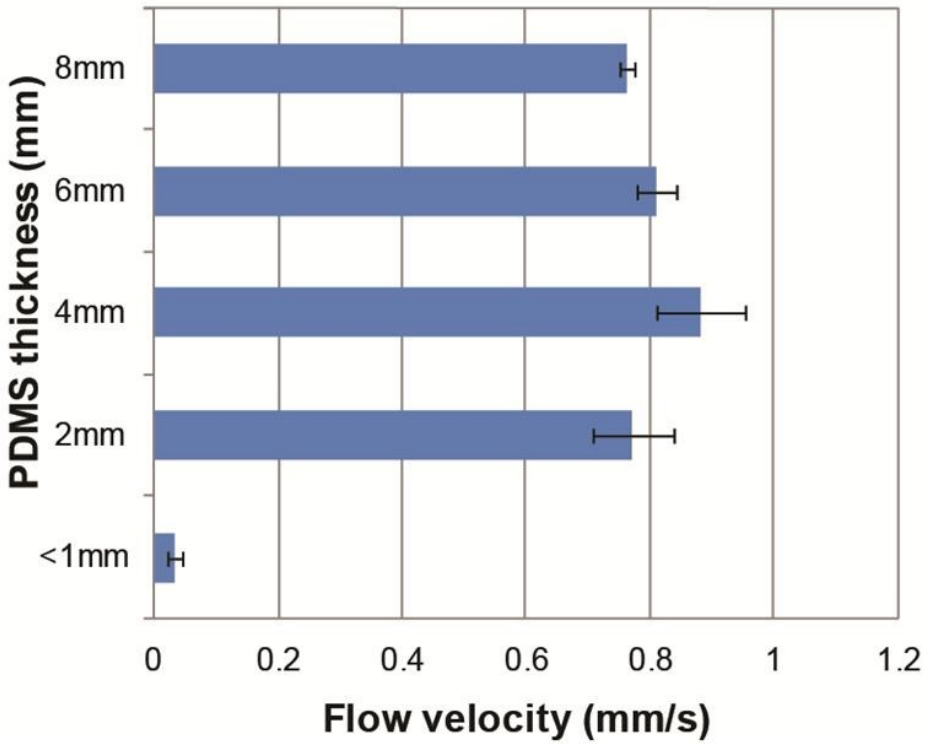

Figure D.2: The effect of PDMS device thickness on PDF. The average initial velocity of the devices was measured for devices with different device thicknesses. It was observed that for device thickness less than 1 mm (~180 μm) the flow velocity was drastically reduced, while a faint dip in flow velocities were observed for thickness more than 4 mm. The reduction in flow velocities for thin devices can be attributed to the diffusion of atmospheric air into the fluid channels.

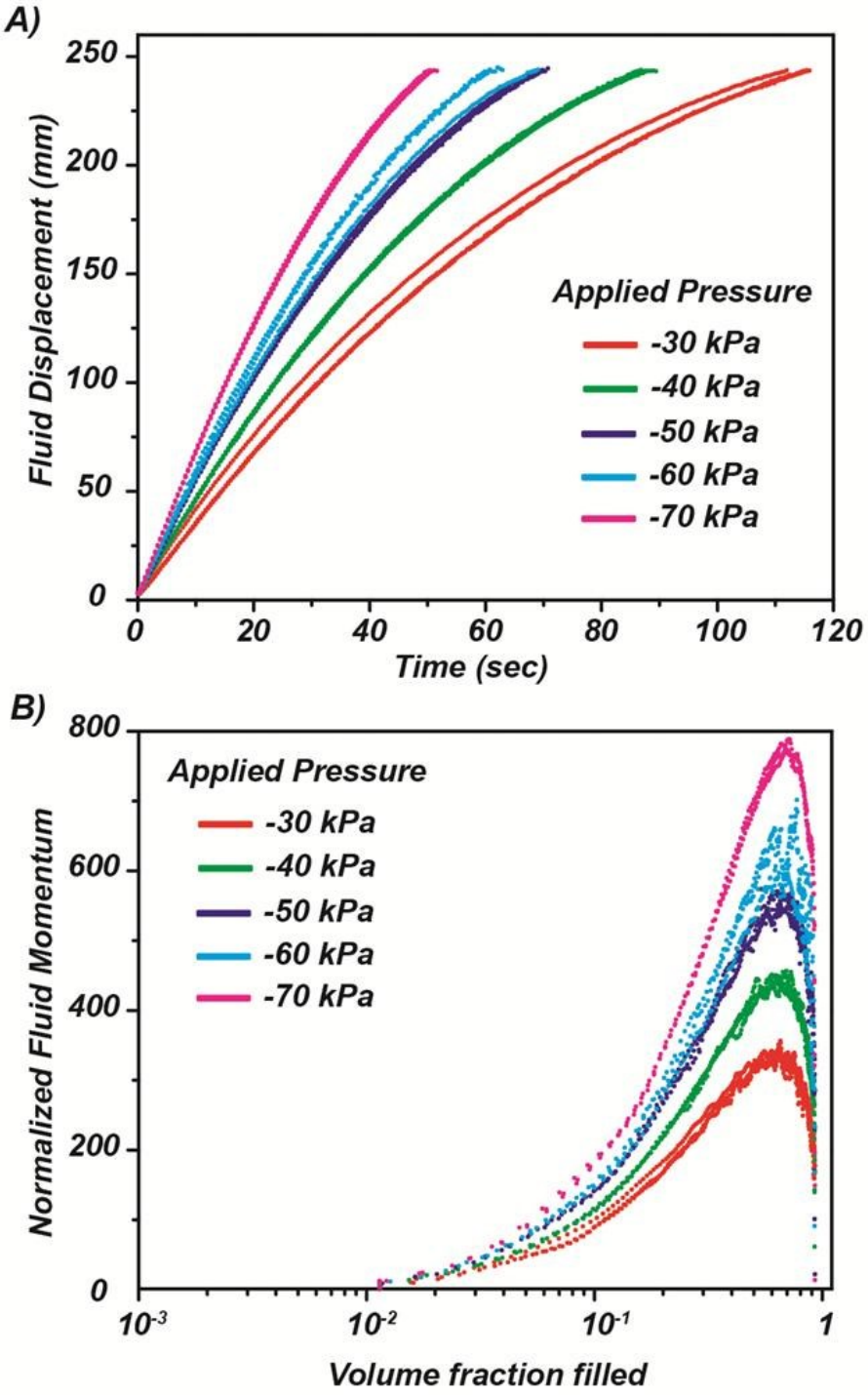

Figure D.3: The effect of applied pressure on PDF; **A)** The fluid displacement into the fluid channels is plotted as a function of time for different applied pressures (relative to atmospheric pressure). Measurements were done in triplicates and are shown as three independent plots for each pressure. It was observed that an decrease in applied pressure resulted in an increase in the fluid flow velocity; **B)** The normalized fluid momentum was calculated and plotted as a function of the volume fraction (of the channel) filled (with the fluid) for different pressures. Measurements were done in triplicates and are shown as three independent plots for each pressure. Using the normalized momentum as a measure of relative channel pressure ($P_{fc} - P_{atm}$), we observe that the channel pressure decreases with a decrease in applied pressure.

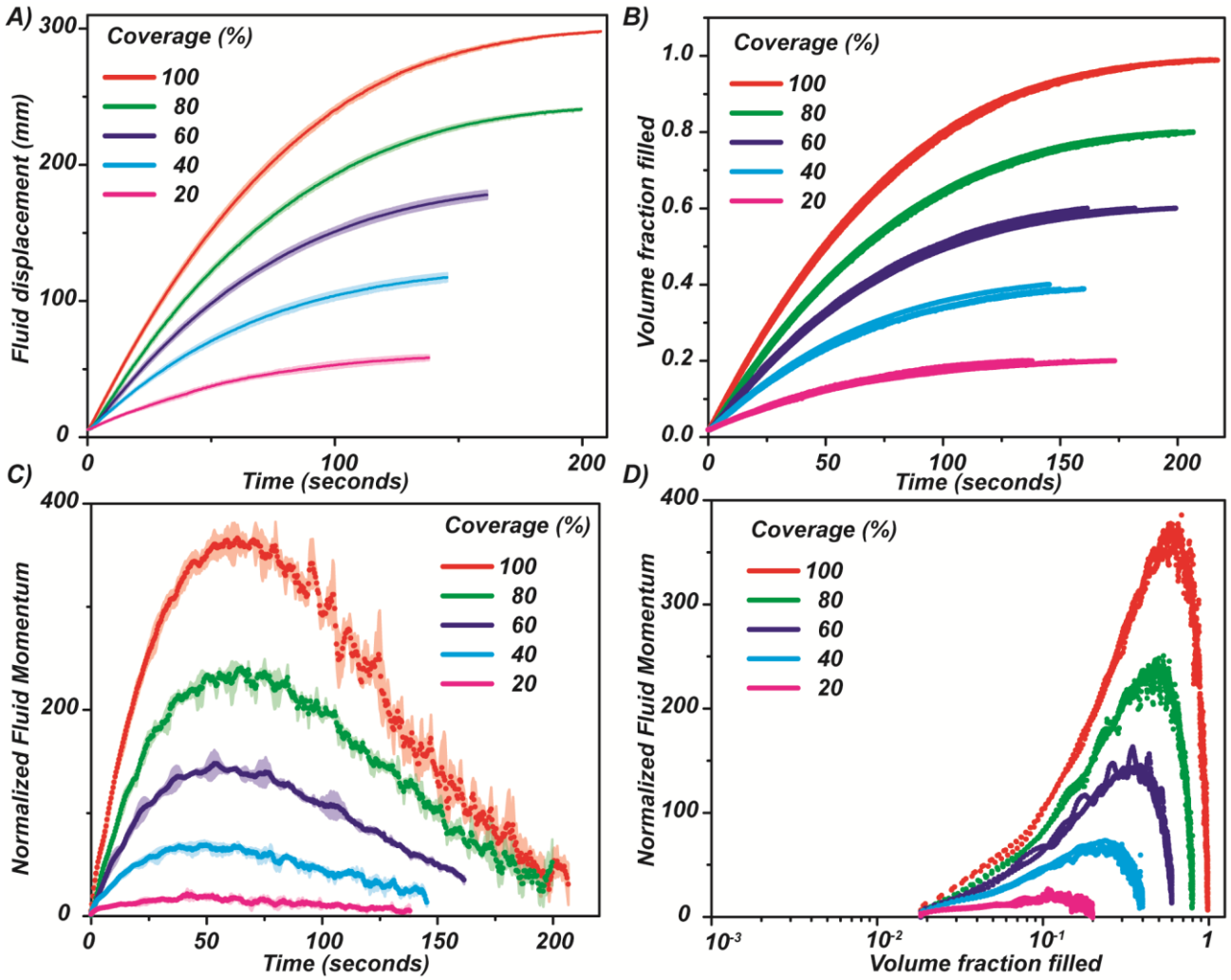

Figure D.4: The effect of the percentage of fluid surface area bounded by degas channels (referred to as coverage) on PDF; **A)** The fluid displacement into the fluid channels is plotted as a function of time for different coverage. The solid line indicates the average and the shaded region indicates two standard deviations from three independent measurements. It was observed that the fluid quickly came to rest once the degas channel bounded fluid volume was filled up; **B)** The volume fraction of the fluid channel filled is plotted as a function of time for the different coverage. The fluid fills up the volume fraction equivalent to the coverage and stops quickly; **C)** The normalized fluid momentum was calculated and plotted as a function of time. The solid line indicates the average and the shaded region indicates two standard deviations from three independent measurements. Using the normalized momentum as a measure of relative channel pressure ($P_{fc} - P_{atm}$), we observe that the channel pressure decrease with an increase in coverage; **D)** The normalized fluid momentum plotted as a function of the volume fraction (of the channel) filled (with the fluid) for different coverage. We observe that while relative channel pressure increases (i.e. channel pressure decreases) with increasing coverage; however after a certain volume fraction of the channel is filled up with the fluid, the compression of the air left in the channel leads to an increase in channel pressure (and hence leads to a decrease in the relative channel pressure and normalized momentum).

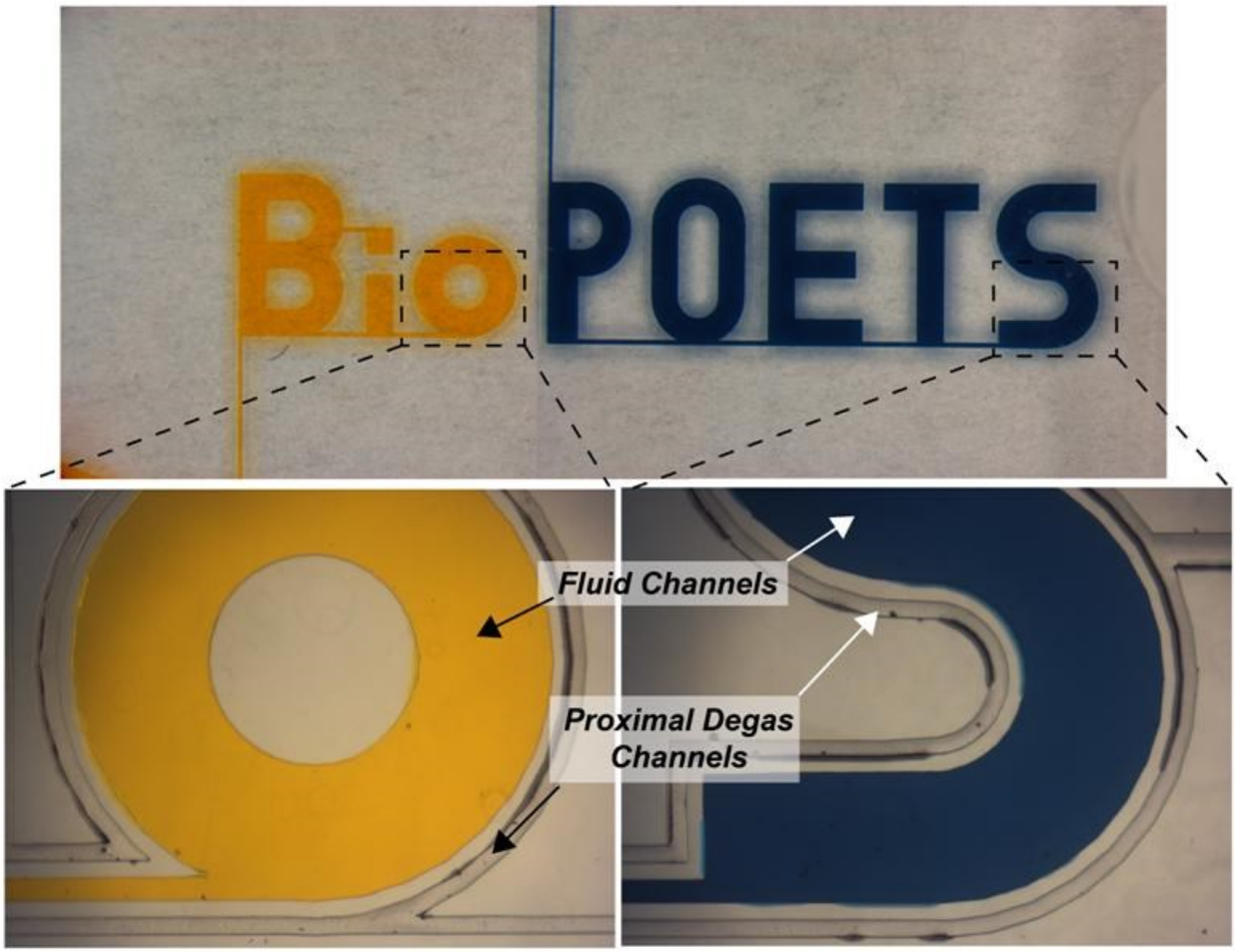

Figure D.5: Dead end channel filling using PDF chips with integrated on-chip membrane thumb pump. The inset shows the location of the fluidic and the degas channels.

APPENDIX E

Magnetically Actuated Microfluidic Valves

PRINCIPLE BEHIND MAGNETICALLY ACTUATED MICROFLUIDIC VALVES

The principle behind magnetically actuated microfluidic valves is shown in Figure E.1. The active component of the valve consists of a PDMS membrane, doped with magnetic particles, which is responsive to an external magnetic field. Such membranes have been described using a variety of magnetic components including carbonyl iron microparticles (1), magnetic discs (2) or magnetic nanoparticles (3, 4). We propose the use of magnetic microparticles due to their low costs and efficient membrane actuation. This magnetic membrane can be deformed, under external magnetic field, to close a channel; hence enabling a "mostly open" valve. Also, this membrane can be used to bridge two fluidically isolated channels, whereby the membrane deformation will connect the channels; hence enabling a "mostly closed" valve. A major limitation of this technology is the optical opacity of the magnetic particles. Hence, to make a viable micro-valve, the magnetic particles need to be patterned to regions where a valve is needed. Figure E.2 depicts a proposed fabrication scheme, which utilizes PDMS capable of being photo-patterned, to generate a PDMS membrane with patterned magnetic particles. These magnetically actuated microfluidic valves can be actuated using a simple electromagnet which will enable these valves to be used in portable microfluidic devices.

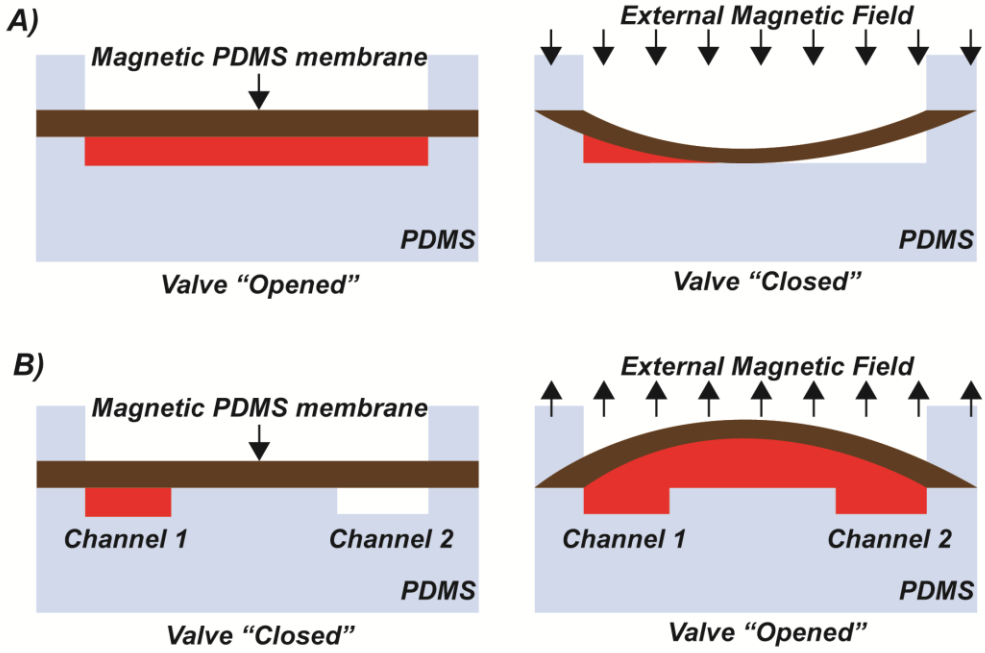

Figure E.1: Principle behind magnetically actuated Microfluidic Valves; **A)** The operation of a "mostly open" valve involves a magnetic membrane placed above the microfluidic channel. The application of an external magnetic field induces the deformation of this magnetic membrane which leads to the obstruction of fluid flow in the channel, hence closing the valve; **B)** The operation of a "mostly closed" valve involves a magnetic membrane bridging two fluidically isolated channels. The application of an external magnetic field induces the deformation of this membrane which connects the two channels, hence opening the valve.

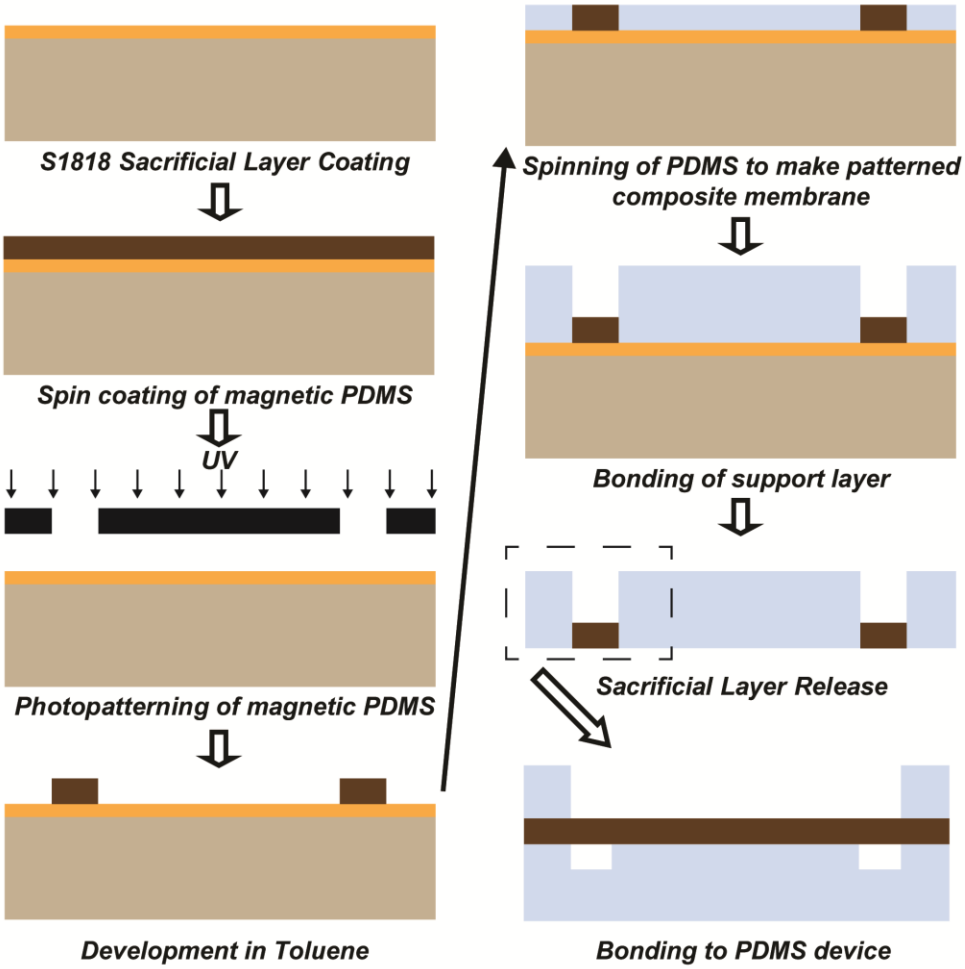

Figure E.2: Patterning of magnetic particles using photo-patternable PDMS. The photo-patternable PDMS is mixed with the magnetic particles and then spun on a wafer, with a S-1818 sacrificial layer. This PDMS layer is then patterned with UV light using the desired mask. The patterned areas are then covered with a layer of transparent PDMS, hence producing PDMS membranes with areas patterned with magnetic particles. This patterned membrane can then be finally bonded to a PDMS block containing the fluidic channels.

REFERENCES

1. Li J et al. Design and fabrication of microfluidic mixer from carbonyl iron—PDMS composite membrane. *Microfluidics and nanofluidics* 10:919–925.

2. Pan T, Mcdonald SJ, Kai EM, Ziaie B A magnetically driven PDMS micropump with ball check-valves. *Journal of micromechanics and microengineering* 15:1021–1026.

3. Pirmoradi F, Cheng L, Chiao M (2010) A magnetic poly(dimethylesiloxane) composite membrane incorporated with uniformly dispersed, coated iron oxide nanoparticles. *J Micromech Microeng* 20:015032.

4. Singh A et al. A magnetic nano-composite soft polymeric membrane. *Microsystem technologies* 19:409–418.

APPENDIX F

Passive Microfluidic Valving Using Flow Rate Control

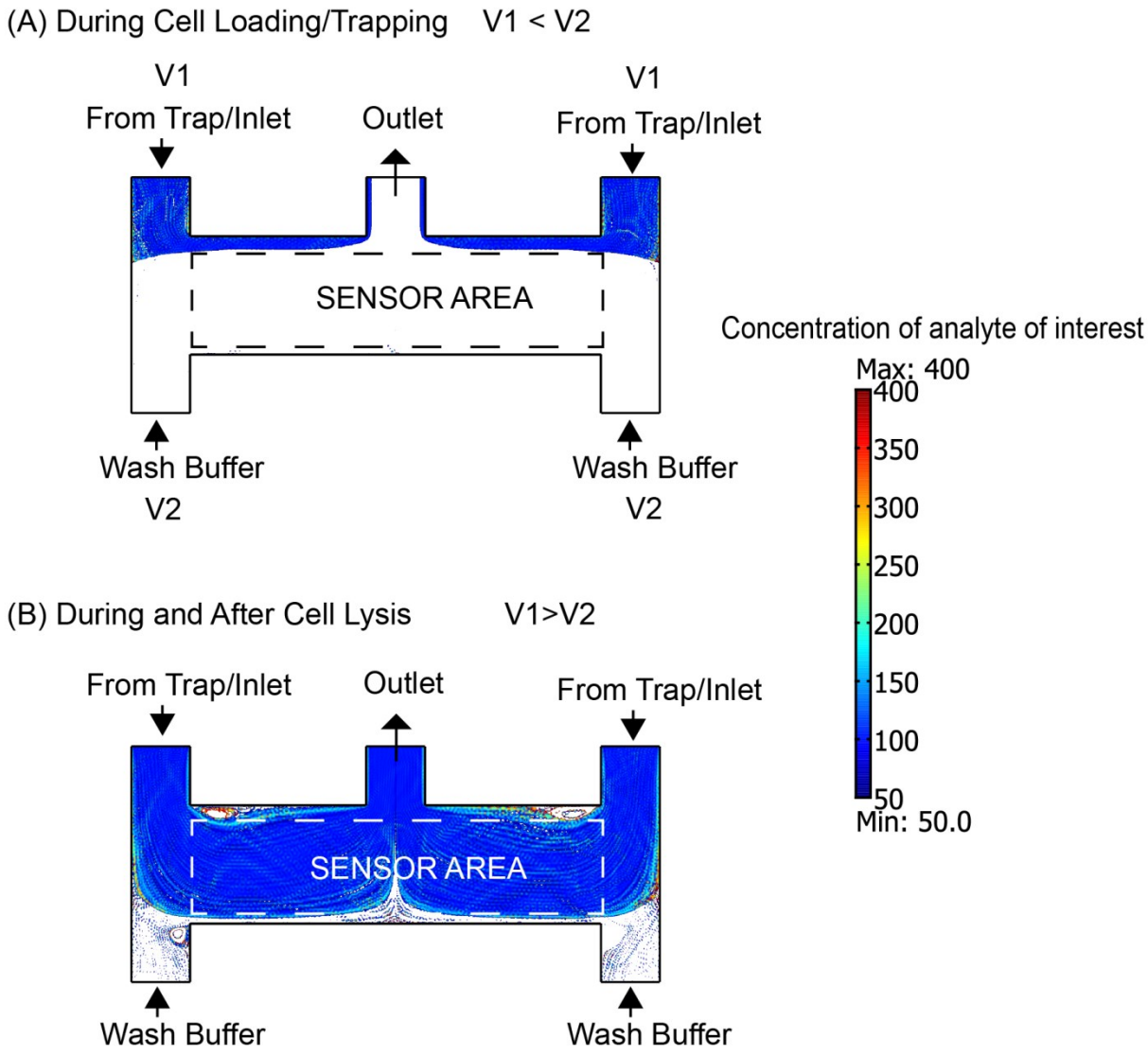

Figure F.1: Principle behind passive fluid valving using flow rate control; **A)** The sensor area is flushed with wash buffer at the flow rate much higher than the flow rate coming from the trap region. As a result, the fluid coming from the trap region, containing extraneous proteins or hydronium/ hydroxide ions, is prevented from coming in contact with the detection/sensor area as the fluid streamlines do not cross. Also the diffusion across the streamlines is minimized due to the large cross flow. The simulation was done for a protein, but similar results are found for smaller hydronium ions.; **B)** To allow the sensor area to be exposed to fluid from the trap regions, the flow rate ratio is reversed. Hence, now the fluid flow rate from the trap is much higher and it covers most of the sensor area.